Fine-Line Printed Contacts on Crystalline Silicon Solar Cells

Dissertation
zur Erlangung des
akademischen Grades
Doktor der Naturwissenschaften
(Dr. rer. Nat.)
an der Universität Konstanz
Fachbereich Physik

vorgelegt von

Matthias Hörteis

Fraunhofer Institut für Solare Energiesysteme
Freiburg

2009

Referenten:
Prof. Dr. Gerhard Willeke
Prof. Dr. Giso Hahn

Tag der mündlichen Prüfung:
16. November 2009

.

Table of contents

1 Introduction

For the past few years the world of energy has been changing, at least in appearance. Catchwords like greenhouse effect, climate change, renewable energy and solar power are broadcasted almost daily; even the idea of supplying Europe with solar energy from the Sahara is currently being re-investigated [1]. However, at present the world is still dependent on fossil fuel. In the current BP statistical world energy review 2009 [2], renewable energies (with the exception of hydroelectricity) are not even included as a significant source of energy, but their rapidly growing share is at least alluded. It appears that people, including politicians, are aware of the finiteness of the traditional hydrocarbon fuels and their negative impact on the environment. The European commission in 2007 set an ambitious target called 20, 20 by 2020 for its future climate and energy policy, with the goal to reduce greenhouse gas emissions by 20%, reduce the overall energy consumption by 20% and to ensure that renewable energy represents a 20% share of total energy use by 2020 [3]. This implies a share of as much as 35% of total electrical consumption. According to EPIA, photovoltaics can provide up to 12% of the European electricity demand by 2020 [4]. This promising prospect of a PV powered future is only possible if the average cost reduction for PV systems, of 8% annually, is continued or even accelerated [4]. PV systems, namely solar cells, are technology driven products and the price decrease is based on new developments and further improvements. The most effective way of reducing the costs is to increase the solar cell efficiency. The optimization of the solar cell metallization, in particular of the front side contacts, is a topic of current research as it has the potential to reduce the material costs combined with an increase in the overall energy conversion efficiency.

The European production capacity for electricity is 3360 TWh (in 2007) [5]. Assuming the same amount for the year 2020, and a 12% share of that being PV energy produced from standard silicon solar cells with an average output power of $4W_p$, 100 billion solar cells are required. For the front metallization of a single solar cell about 0.2 g of silver is required, which accumulates to an amount of more than 20.000 tons of silver, equal to the present annual world silver production. This simple calculation demonstrates that mass production can lead to a material shortage and it is wise to start by now reducing the consumed amount of silver per cell and looking for alternative materials.

Two layer concept

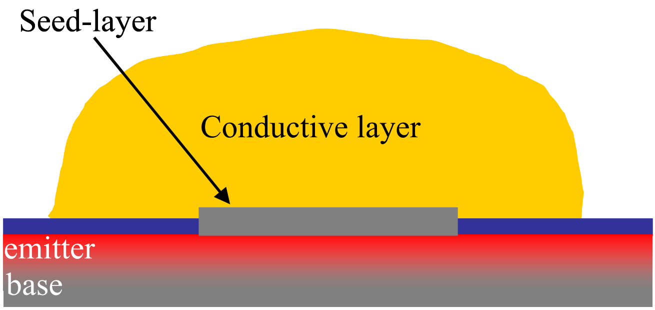

Fig. 1-1: Scheme of two layer front side contact.

At Fraunhofer ISE different promising metallization technologies are currently under investigation, such as electro-less and light-induced plating, evaporation, laser sintering, fine line screen-printing, and aerosol-printing of suitable contact metals [6]. All of these techniques are seed layer processes, where initially a thin metal layer responsible for the contact formation is deposited, and a further thick metal layer is responsible for the current transport [7, 8] as seen in Fig. 1-1. The contact formation is separated from one step into two production steps. This has the advantage, that the contact layer and the conductive layer can be optimized individually.

The formation of the contact layer (seed layer) on silicon solar cells can be distinguished into two types: (i) a low-temperature process where the metal layer is deposited directly on the emitter and a metal silicide can be formed at moderate temperatures T<400°C, and (ii) a high-temperature process where the contact metal is deposited on the anti-reflection or passivation-coating and fired through at temperatures above 650°C. The seed layer is responsible for a low ohmic contact to the semiconductor and a good mechanical adhesion. The second layer, which is responsible for the current transport, can be processed by multiple printings of highly conductive silver inks or by plating of conductive materials like copper or silver. One very promising way to create a high-performance contact under industrially feasible conditions is the combination of the aerosol-printing technology (AP) for seed layer deposition [9] and succeeding light-induced plating (LIP) [8], to produce the conductive layer.

Outline of this thesis

Within this thesis, crystalline silicon solar cells are improved by optimizing the front side metallization with the emphasis on the development of an ink suitable to contact n-type emitters with a reduced doping concentration. The developed inks are deposited as a seed layer on the cell front side and fired in a high-temperature step through the anti-reflection coating and into the emitter. The chemical reaction and the physics behind the contact formation on n-type silicon are studied. The influence of the single ink components and process parameters on the contact is investigated. Based on these results, an optimized seed ink for the metallization of solar cells (SISC) is developed and used to refine the current contact model and to study their performance on different types of solar cells.

In **Chapter 2** and **Chapter 3** the theoretical background for this work is given. The *IV* characteristic of a solar cell and the corresponding two-diode model are introduced, from which cell parameters important for metallization like fill factor, series resistance, shunt resistance and saturation current density can be extracted, and their influence on the cell efficiency is explained. Further on the theory of metal semiconductor contacts, their physical limitations and especially the difference between evaporated contacts and printed and fired contacts are given. The present contact model and the possible current paths for thick film printed and fired contacts are reviewed. **Chapter 4** presents the characterization methods which are mainly used within this thesis. Differential thermo gravimetric measurements (TG-DTA) are used in order to understand and to simulate the high temperature contact formation. The electrical contact quality is studied by contact resistance measurements; here the transfer length model (TLM) is used. Finally the solar cells are characterized by illuminated *IV* curves and by *IV* characteristics determined from SunsVoc measurements.

With **Chapter 5** and **Chapter 6** the experimental part of this thesis begins. In Chapter 5 all important aspects of fine line aerosol printing are summarized. The working principle of an aerosol system is explained. The ink properties, defined by the printing system, are analyzed experimentally and theoretically and the printed line quality with respect to the printing parameters is studied. Chapter 6 highlights the importance of the second layer, the conductive layer, which in this work is deposited by light-induced plating (LIP). The interaction of seed layer and conductive layer and the influence of the conductive layer on the cell performance is experimentally determined and compared to simulations.

In **Chapter 7** the contact formation is shifted form the wafer surface of a silicon solar cell into an alumina crucible of a DTA measurement. The contact formation is simulated under controlled conditions to determine the function of the single ink components. The opening of the dielectric layer, the “etching” of silicon under different atmospheres and the conditions for silver crystallite growth are systematically investigated in order to reveal the secret of high temperature contacts. Based on the results of Chapter 7, different inks are developed and optimized in **Chapter 8**. Relatively basic ink formulations consisting of silver and bismuth oxide or leaded glass are tested on real solar cells. The electrical solar cell and contact parameters, and the contact microstructure, are used to interpret the contact formation.

Front side contacts produced with the developed and optimized seed layer ink for the metallization of solar cells (SISC) are investigated in **Chapter 9**. The current contact model is adopted and the differences between seed layer and thick film contacts are illustrated. This comparison is continued in **Chapter 10**, where the optical properties of fine line printed and plated contacts are studied.

Finally, the results on different substrates obtained during this work are summarized in **Chapter 11**. The simulation tool “GridSim” is used to find the right front side grid. These optimized grids are than applied using aerosol printing and light-induced plating on large area multi-crystalline silicon solar cells and high efficiency float-zone silicon solar cells.

2 Silicon solar cells

All important parameters which can be extracted from *IV* measurements are explained within this chapter. Parameters relating to metallization, e.g. fill factor (*FF*) and series resistance (R_s) are discussed in more detail.

Silicon solar cells are more or less large area diodes with a shallow emitter and a relatively thick base. The simplest way to describe a solar cell is therefore the equation of a ideal diode [10]:

$$j = j_0 \left(\exp\left(\frac{qV}{kT} \right) - 1 \right) - (j_{Ph}) \qquad 2\text{-}1$$

with q being the elementary charge, k the Boltzmann constant, T the temperature and j_0 the saturation current density, which consists of the saturation current density of the base and emitter $j_0 = j_{0b} + j_{0e}$. If the solar cell is illuminated, the photo current has to be taken into account and the *IV* characteristic is shifted to negative values, which means that the current flows in the opposite direction of the forward biased diode. The IV characteristic for both the dark and illuminated states is shown in Fig. 2-2. As a solar cell is not a simple diode, the model needs to be extended by the recombination in the space charge region (j_{02}), the parasitic shunt resistance (R_p), and the losses caused by the series resistance (R_s). The equivalent circuit diagram is given in Fig. 2-1. The second diode represents the saturation current density in the space charge region.

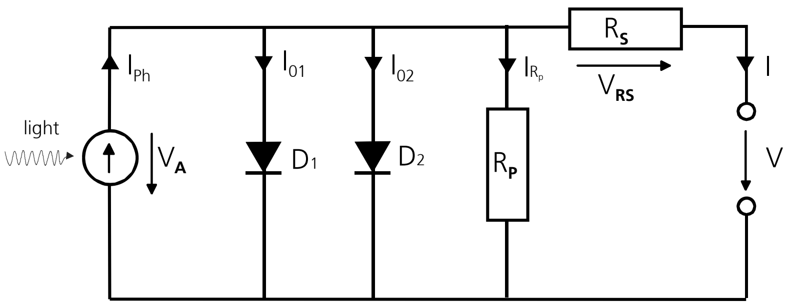

Fig. 2-1: Equivalent circuit diagram (two diode model) of a solar cell

The current generated by a solar cell can better be approximated by the two-diode model [11]:

$$j(V) = j_{01}\left(\exp\left(\frac{q\cdot(V - jR_s)}{n_1\cdot k\cdot T}\right) - 1\right) + j_{02}\left(\exp\left(\frac{q\cdot(V - jR_s)}{n_2\cdot k\cdot T}\right) - 1\right) + \frac{V - jR_s}{R_p} - j_{ph} \qquad \textit{2-2}$$

where j_{01} considers the saturation current density in the emitter and base and j_{02} the saturation current density in the space charge region (SCR). Additionally the factors n_1 and n_2, which are called the ideality factors, describe the quality of the single diodes and should be $n_1=1$ and $n_2=2$. In the ideal case, both are influenced by the recombination mechanism and the injection level. In real solar cells the factors can be quite different from these ideal values.

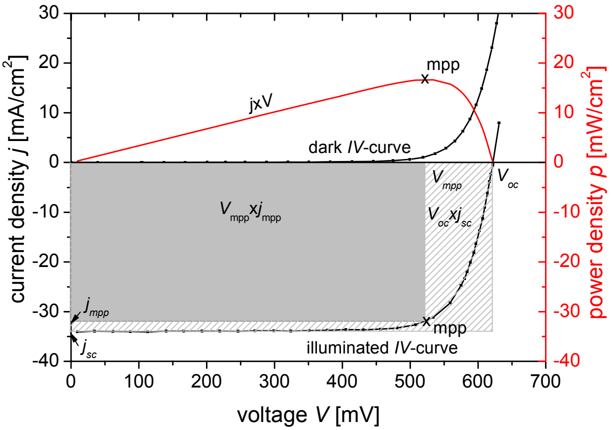

Fig. 2-2: Illuminated and dark IV-curve and the power density vs. voltage of a solar cell, illustrating the IV-parameters.

2.1 Illuminated *IV* characteristic

The efficiency of a solar cell (see, Eq.2-3), which is defined as the ratio of the energy at the maximum power point (P_{mpp}) to the power of the incident light (P_{Ph}), is the main parameter to describe the quality of a solar cell. The efficiency is obtained from an *IV* measurement, while the solar cell is illuminated and kept at defined conditions: temperature: 25°C, light intensity 1000 W/m², spectrum AM 1.5g. From a measured illuminated *IV* curve, as shown in Fig. 2-2. The cell power *P* is the product of current density and voltage and at its maximum defined P_{mpp} and the current density at this point is called j_{mpp} and the voltage V_{mpp}, respectively. Two more important cell parameters are the open-circuit voltage V_{oc} and the short–circuit current density j_{sc}, which can be determined by the intercept of the *IV* curve with the x- and y-axis.

$$\eta = \frac{P_{mpp}}{P_{Ph}} = \frac{V_{mpp} J_{mpp}}{P_{Ph}} = \frac{J_{sc} V_{oc} FF}{P_{Ph}} \qquad \textit{2-3}$$

The ratio of maximum power (P_{mpp}) and the value ($V_{oc}xj_{sc}$) is called the fill factor, *FF*, which is described in Eq.2-4. The fill factor can be regarded as the ratio of two squares, giving rise to the name: the largest square fitting under the IV-curve, and the square defined by V_{oc} and j_{sc}.

$$FF = \frac{V_{mpp} j_{m\,pp}}{V_{oc} j_{sc}} \qquad \textit{2-4}$$

The fill factor is an important factor especially for the metallization of solar cells, as the quality of the formed metal-semiconductor junction influences the shape of the *IV* characteristic and therefore the value of the fill factor. In Fig. 2-3 the influence of R_s and R_p on the fill factor are illustrated. In both cases the maximum power point is shifted and the size of the inner square is reduced, while the values for j_{sc} and V_{oc} are not affected in a certain range. Typical values for the FF are 76-85% [12].

According to Green [10] it is possible to determine an ideal FF_{id} from the measured open circuit voltage, which is free of ohmic and recombination losses:

$$FF_{id} = \frac{v_{oc} - \ln\left(v_{oc} + 0.72\right)}{v_{oc} + 1} \qquad \textit{2-5}$$

with v_{oc} the normalized voltage, $v_{oc}=V_{oc}/(nkT/q)$ an *n* the ideality factor, which should be close to one.

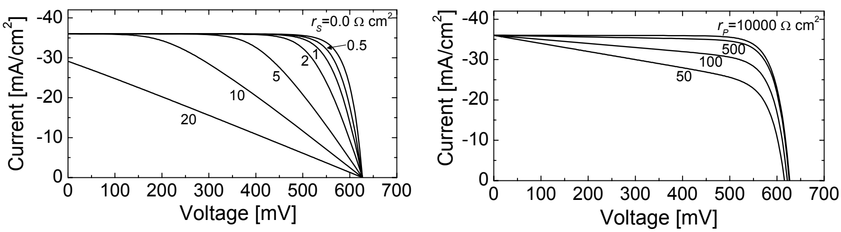

Fig. 2-3: Effect of series resistance (left-hand) and parallel resistance (right-hand) on IV-curve. The maximum power point is directly influenced by RS and RP and hence the fill factor [13].

Another *FF* can be obtained by a *IV* characteristic from SunsVoc measurements: The pseudo *fill factor (pFF)* as it can be determined without a current flow and is therefore free of series resistance losses. The *pFF* can be measured right after formation of a pn-junction, assuming the measurement probes have an ohmic contact to the rear and front sides of the cell [14]. This kind of *pFF* only includes losses due to an inhomogeneous emitter formation, and is close to the ideal FF_{id}. If the *pFF* is measured after the metallization, and the metallization does not influence the pn-junction, both *pFF* have the same value. Usually this is not the case, as the metallization, especially in a firing step, can create additional recombination losses or local shunts and the measured *pFF* is lower than the FF_{id} but higher than the value of the real *FF,* as it is still free of series resistance losses. By measuring the individual *FFs,* the losses introduced during cell fabrication, especially the metallization can be distinguished. Examples are shown in Table 2-1 for an industrially produced large area 15.6x15.6 cm² multicrystalline silicon solar cell and for a 2x2 cm² monocrystalline high-efficiency solar cell. The difference between the ideal FF_{id} and the *pFF* is based on an imperfect junction formation, i.e. recombination in the space charge region, introduced by the metallization (j_{02}) or by local shunts (R_p). By comparing the *pFF* with the *FF* the losses due to the series resistance R_s can be extracted. As the series resistance losses are mainly responsible for a reduced *FF*, see Fig. 2-4 they are described more in detail below. A rule of thumb for the relationship between *FF* and R_s is given by Pysch [15]. He has shown that an increase of 1 Ωcm² in R_s reduces the *FF* by 5% absolute.

In total, by comparing the different *FFs* it can be distinguished whether the metallization creates any shunts or recombination centers in the SCR or if the contact formation is insufficient and the series resistance is increased.

cell type	V_{oc} mV	FF_{id} [%]	pFF [%]	FF [%]	η [%]
multi-Si	622	83.1	81.4	78.8	16.7
mono-Si	645	83.7	83.3	80.7	20.0

Table 2-1: Fill factors for two different types of solar cells. The ideal FF_{id} is calculated from Voc according to [10]. The pseudo FF (pFF) is measured using SunsVoc and the FF is determined from an illuminated IV measurement.

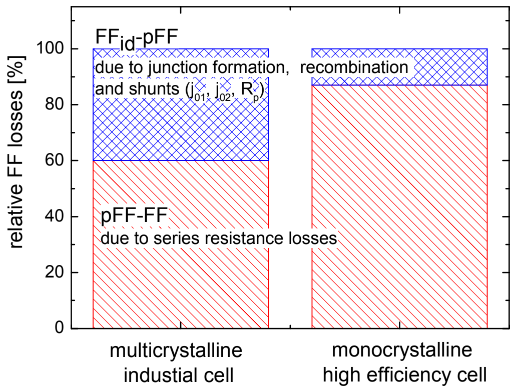

Fig. 2-4: From the normalized differences in the FF, the losses in FF can be allocated to different IV parameters. It is possible to distinguish between them; either the metallization creates shunts in the solar cell, or the contact formation is incomplete, indicated by high R_s.

2.2 Dark *IV* characteristic

The dark *IV* measurement represents directly the diode characteristic of a solar cell and the cell parameters j_{01}, j_{02}, n_1, n_2, and R_s and R_p can be extracted. The measured *IV* characteristic is therefore plotted semi-logarithmic and fitted to the ideal 2-diode equation Eq.2-2, as shown in Fig. 2-5. For the metallization especially the ohmic resistances R_s and R_p and the saturation current density j_{02} are of interest, as they are affected by the contact formation. In order to achieve high efficiencies, R_s should be below R_s<0.5 Ωcm² and R_p>10 kΩcm². The series resistance as extracted from a dark IV curve is always lower as the "real" R_s as the contribution of the emitter is reduced [16, 17]. The dark *IV* fit is therefore not the best way to determine R_s. The most reliable method, according to Pysch, who gave a comprehensive review of the common R_s measurements, is the comparison dark and light fit on the point of maximum power [18].

The influence of j_{01} and j_{02} on the *FF* is shown by Götzberger [19], see Fig. 2-6. For *FF*>80% j_{02} should not exceed a value of 10^{-8} A/cm² while j_{01} is smaller than $j_{01}<10^{-11}$ A/cm².

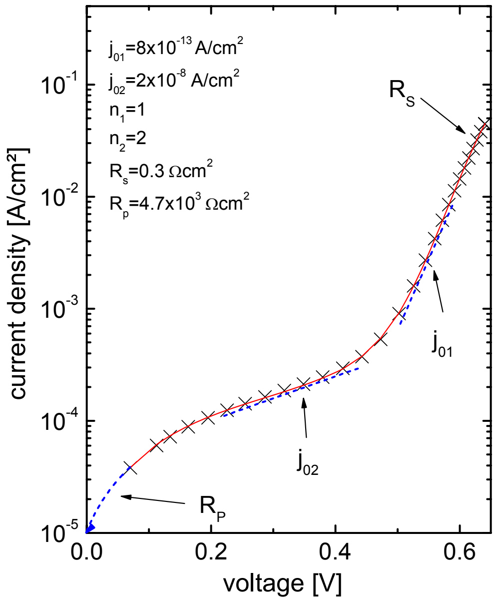

Fig. 2-5: Dark IV measurement together with a 2-diode fit. The sections from which the cell parameters are extracted are labeled.

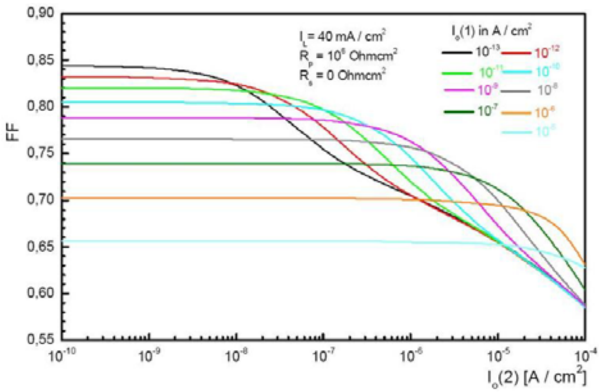

Fig. 2-6: Fill factor as a function of j_{01} and j_{02}. R_p is kept constant at $R_p=10^4$ Ωcm², $R_s=0$, and $n_1=1$ and $n_2=2$ [19].

For some solar cells the ideal 2-diode model is not suitable to fit the measured *IV* characteristic and the value of $n_2>2$. These measurements show a “hump” [20] in the region of the maximum power point, reducing the FF and V_{oc}. This behaviour can be explained by local, nonlinear shunts with a diode characteristic and for a correct fit a third diode is introduced, which represents some local shunts [21]. According to Huster [22], the typical origins of diode shunts in industrial solar cells are point–like Schottky contacts of the silver paste to the base. These contacts can occur due to mechanical emitter damage by handling or printing or due to penetration of the glass frit containing silver through the emitter [23]. They can also be intentionally introduced by damaging the emitter using a diamond scratch [24] or a dicing saw [22].

2.3 Series resistance and optical metallization losses

The motivation behind this work is the reduction of the solar cell losses created by the front side metal grid. Two main loss mechanisms are related to the front side metallization, optical shading losses and electrical series resistance losses. Both have to be balanced, see Fig. 2-7. Finer contact structures reduce the shaded fraction, but when the contact area and the cross section of a conducting finger are reduced, R_s is increased. The optical losses are studied in detail in chapter 10.

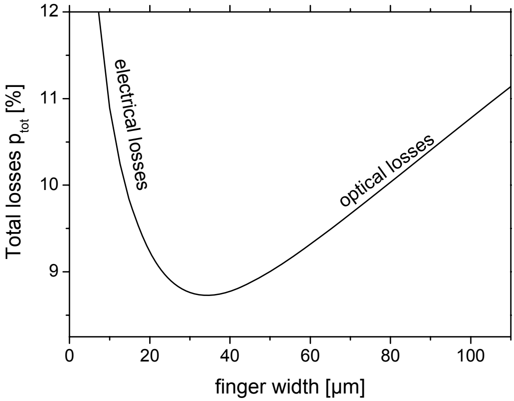

Fig. 2-7: Simulation of the optical and electrical losses of a solar cell.

The series resistance of a standard solar cell with a full metalized rear side and a metal grid on the front side can be separated into eight fractions, summing up to R_s. An overview of the single resistances is given in Fig. 2-8. Within this work the focus is on a further reduction of the contact resistance to the emitter (r_4) and on a reduced line resistance in the finger (r_5), as both are necessary in order to reduce the total losses. The analytical description of optical and electrical losses is summarized by Mette [25].

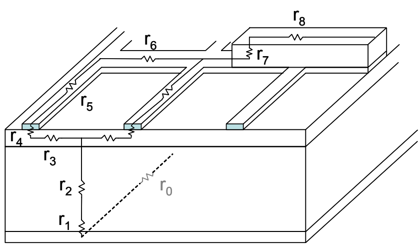

r_0: resistance of rear side layer

r_1: contact resistance of rear side to base

r_2: resistance of base

r_3: resistance of emitter

r_4: contact resistance of front grid to emitter

r_5: line resistance of finger

r_6: line resistance of busbar

r_7: contact resistance soldering joint

r_8: line resistance of tab

Fig. 2-8: Solar cell cross-sectional diagram showing the series resistance contribution [25].

3 Metal – semiconductor contacts

The metal-semiconductor (ms) contact has been a topic of research for more than 100 years and goes back to the early work of Braun (1874), who discovered the asymmetric nature of electrical conduction between metal contacts and semiconductors [26]. This phenomenon was explained decades later by Schottky, who introduced a kind of barrier height which is formed as soon as a metal and a semiconductor are in a close contact, see Fig. 3-1 [27, 28]. In honor of his work, metal-semiconductor contacts are often called Schottky-contacts and the bending in the band diagram the Schottky-barrier. In the 1950s and 1960s the research into ms-contacts was driven by their technical importance in semiconductor technology and later microelectronics. The theoretical understanding of ms-contacts was further increased by the work of Bardeen, Crowell and Sze [29-32]. A summary of the physics of metal-semiconductor contacts is given by Rhoderick and Williams [33].

For solar cell applications, the ms-contact plays an important role: the metallic contact should be as small as possible and the voltage drop over the barrier should be negligible compared to the voltage drop over the total device. The contact should not degrade device performance to any significant extent, it should not inject minority carriers into the device and the contacts should be made in a reproducible manner. A summary of the contact requirements and a review of the contact theory, especially for contacts on solar cells, is given by Schroder and Meier [34].

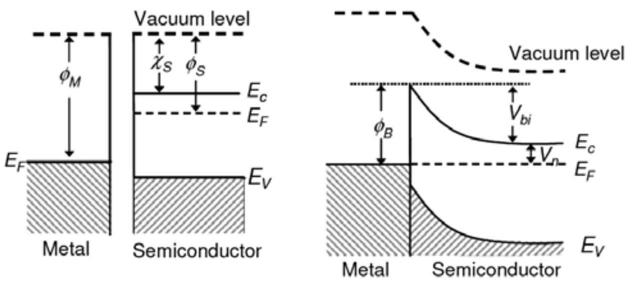

Fig. 3-1: Energy band diagram of a ms-contact on a n-type semiconductor before and after an intimate contact is formed [25].

3.1 Schottky contacts – barrier height

If a metal and a semiconductor are in direct contact a constant electrochemical potential is formed within both materials; in steady-state conditions the Fermi energies E_F in both materials are at the same level – thus the conduction band E_c and valence band E_v of the semiconductor are bended to balance in the difference between the metal work function and the semiconductor electron affinity. The formed Schottky barrier ϕ_B can be described as the difference in metal work function ϕ_M and semiconductors electron affinity χ_s, (see Eq.3-1), where $q\phi_M$ is the potential necessary to excite an electron from the Fermi level to the vacuum level, and $q\chi_s$ is the potential defined by the difference between the conduction band and vacuum level.

$$\phi_{B,n} = \phi_M - \chi_s \text{, n-type} \qquad \phi_{B,p} = E_g - (\phi_M - \chi_s) \text{, p-type} \tag{3-1}$$

For a metal semiconductor junction, the different combinations are possible (see, Fig. 3-2). The metal can be in contact with an *n*-type or a *p*-type semiconductor, where the metal work function is either larger or smaller than the electron affinity. Therefore two kinds of contacts can be distinguished, a rectifying contact (Fig. 3-2a) and d)) and an ohmic contact (Fig. 3-2b) and c)). The difference is visible in the *IV*-characteristic, which is linear for ohmic contacts, where the current can flow in either direction with a negligible small voltage drop, and nonlinear for rectifying contacts, where the current can flow easily only in one direction.

For the contact to an *n*-type semiconductor as shown in Fig. 3-2b) where χ_s is greater than ϕ_M the electron can flow from the semiconductor into the metal without any barrier and ϕ_B becomes zero or negative. A negative or neutral barrier can also be formed on *p*-type silicon when ϕ_M is larger than χ_s. In general, as long as the majority charge carriers are accumulated at the contacts, the contact obtains an ohmic behavior. However, Fig. 3-2b) and c) are very uncommon in practice, and the majority of ms-contacts are of rectifying nature and the *IV*-characteristic is not linear. In fact, for a real contact the direct proportionality between potential barrier and metal work function, and for n-type silicon, could never be measured. Even if a relation between barrier height and metal work function was found experimentally (see Fig. 3-3), it was less strong than expected. The influence of the metal work function seems to be less important. Surface states at the interface layer, acting as donors or receptors, play an important role for contact formation as first proposed by Bardeen [30]. It is also assumed by Tove that the formation of a dipole determines the measured barrier height

[33, 35, 36]. Similar results are found by Cowly and Sze where the role of the dipole is played by an insulating interface layer [31]. With common metals an ohmic contact to n-type emitters seems not to be possible, as common metals like Al, Ag, Au, Pt or Ni form rather high barriers (0.6-0.9 eV). Even if the height of the Schottky barrier is reduced due to image force lowering, which should be less than 0.2 eV for N_D<10^{20} cm^{-3}, relatively high (> 0.5 eV) barriers exist on heavily doped silicon. Therefore, these contacts are ohmic in a different way. A current flow is possible (see below), and according to the definition of an ohmic contact given by Meier and Schroder, "the contact should supply any current that the device requires in its normal mode of operation", therefore rectifying contacts can appear ohmic.

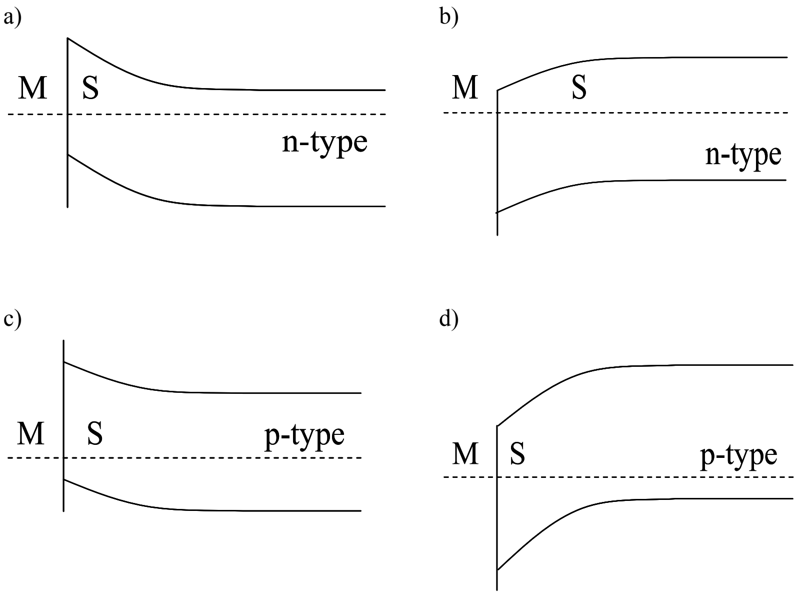

Fig. 3-2: Contact barriers for semiconductor of different types and work functions.

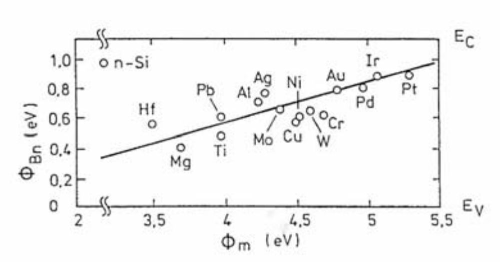

Fig. 3-3: Measured barrier heights as a function of metal work function for different metals, evaporated on n-type silicon [34].

Image force lowering

The height of the Schottky barrier is lowered due to the electrical field in the semiconductor at the contact interface. The different potentials on a Schottky barrier are shown in Fig. 3-4. The applied potential is overlaid by the image-force potential, the shape of which is equal to a coulomb potential. An electron q^-, located at the position x above a metal surface, forms an image charge q^+ inside the metal at the position $-x$. The image force $F(x)$ of the coulomb potential of both carriers attracts the electron above the metal surface. The same principle can be applied for a metal-semiconductor interface and leads to a reduction of the barrier height for both electrons and holes [33]: The conduction band bends downward and the valence band bends upward respectively. To account for this effect, the barrier height ϕ_B must be modified by $\Delta\phi_B$.

$$\Delta\phi_{B,n} = \left(\frac{q^3 N_D \left(V_{bi} - k_B T / q\right)}{8\pi^2 {\varepsilon_s}^3} \right)^{\frac{1}{4}} \tag{3-2}$$

The image-force lowering is proportional to the electrical field, which depends on the doping concentration N_D and the built-in potential V_{bi} and ε_s is the dielectric constant of the semiconductor.

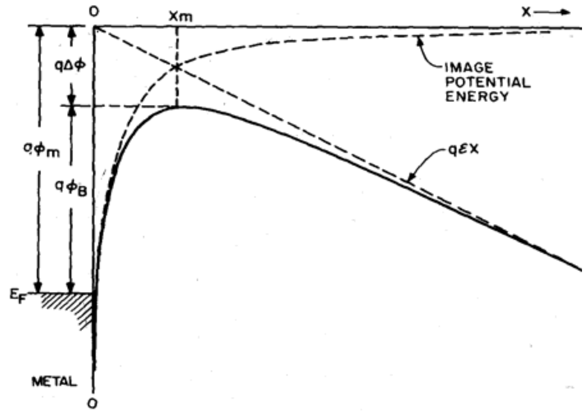

Fig. 3-4: Image force barrier lowering on a ms-contact [32].

3.2 Current transport mechanism and contact resistance of a Schottky barrier

An overview of the current transport in metal-semiconductor junctions is given by [32, 33, 37-39]. For the transport of charge carriers in the metal-semiconductor junction, three mechanisms can be distinguished: (i) the thermionic emission (TE), which describes the thermal activation of charge carriers over the barrier and is valid for low doping concentrations $N_D < 1\times10^{17}$ cm^{-3}, (ii) the field emission (FE), which describes the tunnelling of charge carriers through the barrier, and is valid for high doping concentrations $N_D > 1\times10^{20}$ cm^{-3}, and (iii) the thermionic field emission (TFE), which is a combination of both and is valid for doping concentrations in between [32, 37, 38]. For silicon solar cells in general, with typical emitter doping concentrations of 1×10^{18} cm$^{-3} < N_D < 5\times10^{21}$ cm^{-3}, the dominant transport mechanism for the charge carriers are the TFE and the FE; for industrially fabricated solar cells in particular, where the surface doping concentration is generally far above $1\text{x}10^{20}$ cm^{-3}, the dominant mechanism is the tunnelling process (FE). Both theories predict mainly a dependence on the doping concentration (N_D) and the barrier height (ϕ_B) of the metal-silicon or silicide-silicon junction. The higher the doping concentration and the lower the barrier height, the better the electrical contact. A simulation of the contact resistance as a function of N_D corresponding to different theories for silver as a contact metal with a barrier height of 0.78 eV [32] is given in Fig. 3-6 [23].

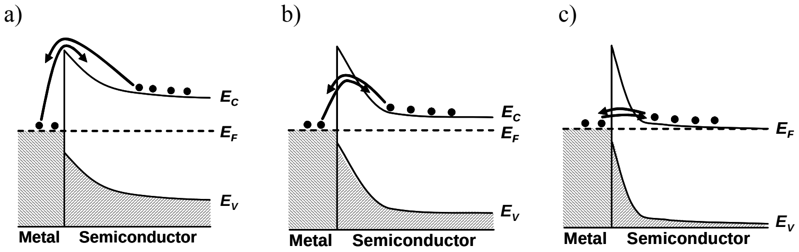

Fig. 3-5: Current flow mechanism on a metal semiconductor junction – a) thermionic emission, b) thermionic field emission, c) field emission [25]

For the different current transport mechanisms a current density, dependent on the applied voltage and the barrier height, can be given and the specific contact resistance can be subsequently calculated by [38]. In all given equations the lowering in the barrier height due to image forces is considered.

$$\rho_c = \left(\frac{\partial j}{\partial V} \right)^{-1}_{V \to 0} \qquad \textit{3-3}$$

Thermionic emission (TE)

The current transport in a ms-contact on a lowly doped silicon with moderate barrier height is dominated by the thermionic emission, which means the thermal activation of the charge carriers over the barrier and only electrons from the n-type emitter with energy larger than the barrier can contribute to the current transport. If the Schottky barrier is too high, the contact changes its behavior from ohmic to rectifying. The current density can be given by [32]:

$$j_{TE} = A^* T^2 \exp\left(-\frac{q(\phi_{Bn} - \Delta\phi_{Bn})}{k\,T} \right) \left(\exp\left(\frac{qV}{kT} \right) - 1 \right) \qquad \textit{3-4}$$

With $A^* \approx (m^*/m_0) \cdot 120\ \mathrm{Am^{-2}K^{-2}}$ being the effective Richardson constant, m^* the effective electron mass and m_0 the free electron mass.

Using Eq. 3-3 the resistivity can than be calculated as:

$$\rho_c(TE) = \frac{k}{qA^*T}\exp\left(\frac{q(\phi_{Bn} - \Delta\phi_{Bn})}{k\,T}\right) \qquad \textit{3-5}$$

Thermionic field emission (TFE)

When the doping concentration is high, the depletion region width becomes smaller. Therefore, electrons can tunnel through the barrier, in addition to the thermionic emission process. Electrons with sufficient energy are activated over the barrier and electrons with less thermal energy are then able to tunnel through the thinner barrier. The TFE therefore is a combination of the field emission and the thermionic emission [38, 40, 41] and the current density can be expressed as:

$$j_{TFE} = A^*T^2\frac{1}{C_1}\exp\left(-\frac{2\sqrt{\varepsilon_s m^*_{tunnel}}}{q\hbar}\frac{(\phi_{Bn} - \Delta\phi_{Bn})}{\sqrt{N_D}\cosh\left(\frac{E_{00}}{kT}\right)}\right)\left(\exp\left(\frac{qV}{kT}\right) - 1\right) \qquad \textit{3-6}$$

And the specific contact resistance is given as:

$$\rho_c(TFE) = C_1\frac{k}{qA^*T}\exp\left(\frac{q(\phi_{Bn} - \Delta\phi_{Bn})}{E_{00}\cosh\left(\frac{E_{00}}{kT}\right)}\right) \qquad \textit{3-7}$$

with

$$C_1 = \frac{kT\cosh\left(\frac{E_{00}}{kT}\right)\sqrt{\cosh\left(\frac{E_{00}}{kT}\right)}}{\sqrt{\pi(\phi_{Bn} + E_F)E_{00}}}\exp\left(\frac{E_F}{E_{00}\cosh\left(\frac{E_{00}}{kT}\right)} - \frac{E_F}{kT}\right) \qquad \textit{3-8}$$

and the characteristic energy E_{00}:

$$E_{00} = \frac{q\hbar}{2}\sqrt{\frac{N_D}{m^*_{tunnel}\varepsilon_s}} \qquad \textit{3-9}$$

E_{00} represents a characteristic energy which is related to the tunnelling probability and depends on the doping concentration. The increase in E_{00} with N_D reflects the barrier becoming thinner at higher doping levels, leading to increased carrier tunnelling.

Field emission (FE)

The tunnelling of charge carriers through the barrier is described by the field emission, which is the case either for very high doping concentrations or very low temperatures. The tunnelling is now possible without any thermal activation, as the barrier is thin enough and the current can be given by:

$$j_{FE} \propto \exp\left(- \frac{4\pi \sqrt{N_D}\left(V_{bi} - \frac{kT}{q} \right)}{h\sqrt{m^*_{tunnel}\varepsilon_s}\left(\phi_{Bn} - \Delta\phi_{Bn}\right)} \right) \left(\exp\left(\frac{qV}{kT} \right) - 1 \right) \qquad \textit{3-10}$$

and the resistivity for the field emission is equal to [38]:

$$\rho_c(FE) = C_2 \frac{k}{qA^*T} \exp\left(\frac{q(\phi_{Bn} - \Delta\phi_{Bn})}{E_{00}} \right) \qquad \textit{3-11}$$

with:

$$C_2 = \left(\frac{\pi}{\sin\left(\frac{\pi kT}{2E_{00}} \ln\left(\frac{4\phi_B}{E_F} \right) \right)} - \frac{2E_{00}}{kT\ln\left(\frac{4\phi_B}{E_F} \right)} \right) \exp\left(\frac{E_F \ln\left(\frac{4\phi_B}{E_F} \right)}{2E_{00}} \right) \qquad \textit{3-12}$$

The ratio kT/E_{00}, used in C_1 and C_2, is a measure of the relative importance of the thermionic process in relation to the tunnelling process [38]:

- For $kT/E_{00} >> 1$ the thermionic emission (TE) dominates the current transport on a barrier (N_D<10^{17} cm^{-3})

- For highly doped semiconductors or very low temperatures, $kT/E_{00} << 1$ the current transport can be described by the field emission (FE), which is the main transport mechanism (for $N_D \geq 10^{20}$ cm^{-3}).

- In the case that the thermionic and tunnelling processes are comparable, $kT/E_{00} \approx 1$ the current transport on a Schottky barrier is described by the thermionic field emission (TFE) (10^{17} cm^{-3}<N_D<10^{20} cm^{-3})

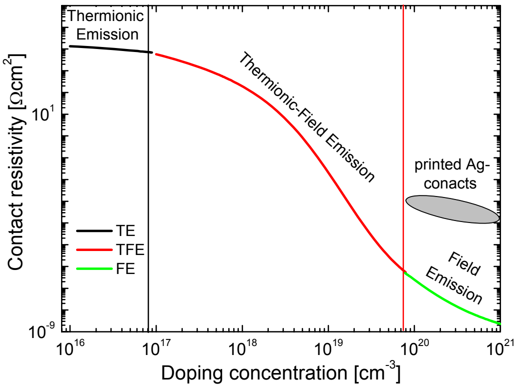

Fig. 3-6: Simulation of the theoretical resistivity ρ_c as a function of doping concentration (N_D) [23] for silver as a contact metal with a barrier height of ϕ_b=0.78 eV. The areas for the different current transport mechanism are marked and the region for contact resistivities for printed and fired contacts on silicon solar cells is illustrated.

The contact resistivities for all three current transport mechanisms are summarized as a function of doping concentration in Fig. 3-6. All are dependent on N_D and the different areas where they are valid are marked. The resistivity is strongly reduced for higher doping concentrations (N_D>10^{18} cm^{-3}), which is the doping level of n-type silicon emitters. As the resistivity of industrially produced silver contacts – printed and fired – (area labeled in Fig. 3-6) is reduced due to a reduced contact area, the doping level has to be very high (N_D>10^{20} cm^{-3}) to guarantee an ohmic contact behavior. In general, the experimentally determined values for the resistivity fit very well to the theory. In Fig.

3-7 ρ_c is plotted over N_D for Al-n-Si contacts, measured at RT additionally to the theoretically expected values for ϕ_B=0.7 eV and ϕ_B=0.6 eV [38].

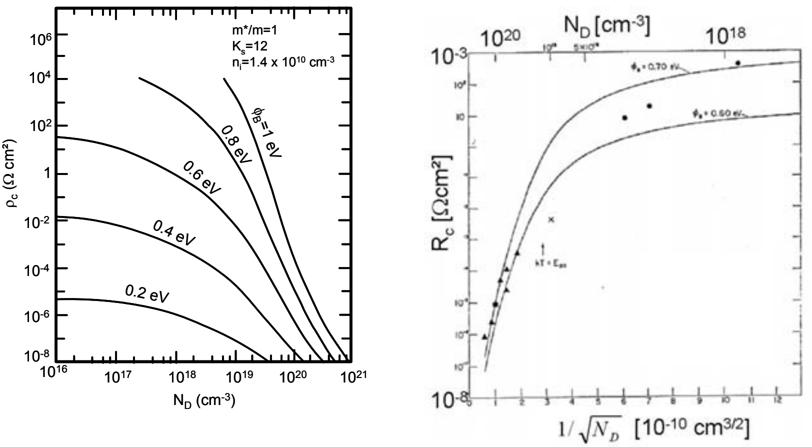

Fig. 3-7: Resistivity as a function of the doping concentration for different barrier heights (left) and in combination with experimentally determined values for Al contacts on n-doped silicon (right), taken from [38].

The influence of the barrier height on the resistivity is shown in Fig. 3-7 [34], where ρ_c is plotted as a function of N_D for different barrier heights. For common materials, the barrier height varies from 0.5 eV<ϕ_B< 0.8 eV. Some average values are given in Table 3-1. The reported barrier heights are widely scattered e.g. for Ni between 0.55 eV and 0.74 eV, depending on the experiment. Half of the data are around 0.6 eV, therefore, the given values are average values taken from [42]. The results for silver vary between 0.62 eV and 0.78 eV and are only slightly higher than for nickel. The contact formation using metals which form silicides is supposed to be preferred. However, the difference in barrier height between metal-silicon or silicide-silicon contacts is negligible; sometimes higher, sometimes lower and rarely exceeding 0.05 eV [35, 42]. The formation of silicide has therefore only a minor impact on the electrical contact parameter. The advantage of silicide is more a mechanical aspect, as the metal, if it forms a silicide, is chemically connected with the semiconductor and the adhesion is increased. That is also the reason why silver contacts evaporated on silicon do not adhere, as silver does not form silicides in this case. Additionally, it should be mentioned that the barrier height on p-type silicon is, in general, lower than on n-type.

ϕ_B [eV]	Ag	Al	Au	Cr	Cu	Mg	Ni	Pd	Pt	Ti
n-type	~0.7	~0.7	~0.8	~0.55	~0.65	~0.55	~0.60	~0.75	~0.8	~0.5
p-type	~0.5	~0.5	~0.3		~0.5		~0.5			~0.5

Table 3-1: Barrier heights for selected metals which are used for the metallization of semiconductors. Metals, commonly used for the metallization of silicon solar cells are highlighted [42].

3.3 Printed and fired contacts

Industrially fabricated solar cells are mainly metalized by printed contacts. The reason for this is based on the simplicity and process speed of printing systems. The time frame for the contact formation on a solar cell is currently about 1.5 s per wafer with the trend to even shorter processing times. Therefore, metallization processes using photolithography, as it is commonly used in microelectronics, is too time consuming and can not be used to process solar cells. Currently several metallization methods are under discussion, see below. The most promising are fine line printing of silver contacts, which have to be fired, or the electroless plating of e.g. nickel. Regardless of all new metallization concepts, the dominant technology is still screen-printing of a metal paste and subsequent contact firing in a furnace at temperatures between 600°C<T<900°C. The high temperatures are necessary to open the ARC and to support the reaction between the ink components and the silicon. The paste consists of a solvent system, which is defined by the printing system, and inorganic powders, metal powder and glass frit, responsible for the actual contact formation.

The first printed and fired contacts on silicon solar cells were studied by Ralph 1975 [43] and Frisson 1978 [44]. In the same year, Lin [45] evaluated the contact quality on n^+-Si and p-Si and Riemer [46] measured the contact resistance and gave a still valid overview of the requirements of printed and fired contacts: low contact resistance to silicon, low line resistance, negligible effect on the silicon substrate, good line resolution, good solderability, good adhesion and low cost. Riemer additionally mentioned the complexity of the contact formation in a firing step: "The evaluation of thick film materials is complicated, by the infinite number of variables that can be considered…"[46]. He separated the problem of contact formation into three areas: the composition of the ink, the processing conditions, and the properties of the silicon wafers. According to Mertens and Cheek, the firing of the front silver contacts is the most critical processing step in the cell manufacturing [47, 48]. Today, firing is still a critical process step and the right process parameter has to be carefully evaluated: when a new contact ink or paste is tested, or the substrate layout or structure has been changed, the firing sequence needs to be optimized each time. Several process steps are combined in a firing step: the front contacts are formed (see below and chapter [49]); at the rear side and next to an ohmic contact, a highly doped p^+-region, a so-called aluminium BSF is formed, which reduces the surface recombination at the rear side [50]. Finally, the bulk carrier life time is increased, especially for mc-Si, due to an enhanced hydrogen passivation by the fired SiN_xH_y-ARC coatings [51-53]. During the 1980s, two types of cell metallization were distinguished [47]: first, the ARC is initially deposited on the wafer and the Ag front metallization is fired through the dielectric coating, or second, the ARC is deposited after the firing of the front side contacts. Only the first sequence, the firing through the ARC, is used today. It has the advantage that the cell is protected by the dielectric layer and impurities can not diffuse into the cell while it is exposed to high temperatures. The thermal budget of a solar cell was reduced over the years, while Mertens 1984 [47] used 10-12 min, Prudenziati 1988 [54] produced his cells with a reduced peak time of about 4 min. At present, belt furnaces are generally used, where the wafers are exposed to the peak temperature for less than 3 s. A typical firing profile is shown in Fig. 3-8.

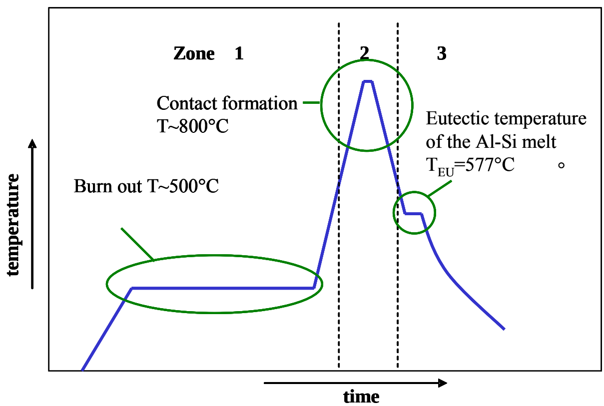

Fig. 3-8:Typical temperature profile for a printed silicon solar cell.

It starts with a burn out where all organic paste ingredients which are not volatile are thermally decomposed. During the peak zone, where the wafer is heated within seconds up to temperature of T~800°C, the actual contact formation occurs. The cooling is usually as fast as the heating process and the wafer is rapidly cooled to RT. A step in the measured temperature profile during cooling indicates the re-crystallization of an aluminium-silicon phase at the eutectic temperature of T_{Eu}=577°C.

3.4 Review of the current contact model

The contact formation of printed and fired silver contacts has been investigated during the last few years [55-64]. The interface between front contact and silicon surface was studied in detail by analyzing fired front contacts. Mainly scanning electron microscopy (SEM), transmission electron microscopy (TEM) and atomic force microscopy (AFM) images together with electrical parameters of solar cells were used to explain the role of the glass, the grow of silver crystallites and the possible current flow. The dissolution or etching of silicon by the liquid lead-silver-glass melt and the growth of the silver crystallites is dependent on the crystal orientation of silicon. Solar cells processed by Cheek et al. performed better on (111)-Si than on (100)-Si and had a considerably reduced contact resistance [45, 48]. The results were explained by the fact that (111)-silicon oxidizes three times faster than (100)-silicon. The silicon oxide, formed during the firing under oxygen, is etched by the molten glass. Cheek's results were confirmed by Khandilkar, who took SEM-images of different contact interfaces on (111)-Si and (100)-Si. The crystal orientation of the substrate also defines the silver-crystallite shape.

On (111)-silicon, the crystallites are quite shallow and lens-shaped, whereas on (100)-Si the crystallites are pyramidal. Ballif proved the epitaxial growth of the Ag-crystallites along the Si-lattices by high resolution TEM studies, again on contacts fired on (111)-Si and (100)-Si. The shape of the crystallites fits very well to the crystal orientation as modeled by Pysch [65].

Most of the studies were performed using commercially available pastes. Mertens et al. were one of the first who reported in the mid-1980s cell results with "homemade" pastes. It took more than 20 years before Schubert investigated the contact formation by studying the reactions between the single ink components, silver, glass and silicon in different combinations, with the aim to understand the reaction mechanisms and to develop, together with a paste manufacturer, a lead-free front contact paste [23]. Within his work, he suggested a contact model which is based on his results and on the investigation of the authors mentioned above:

The contact formation is separated into several sections defined by the temperature. During the burn out step at temperatures T<550°C, the glass frit melts and wets the contact interface. At temperatures between 550°C<T<700°C the ARC is removed by the molten glass. The actual contact formation occurs at temperatures of 700°C<T<800°C. Here the lead oxide, incorporated in the glass frit, reacts with silicon at the same time lead is formed, which is able to melt surrounding silver grains. The liquid lead-silver phase dissolves the (100)-Si planes and the formation of inverted pyramids starts. Schubert proposed that the presence of lead lowers the temperature for the interaction between silver and silicon. During cooling, silver and lead separate according to the phase diagram. Silver recrystallizes on the (111)-Si planes of the inverted pyramids and lead is found at the bottom side of the silver fingers.

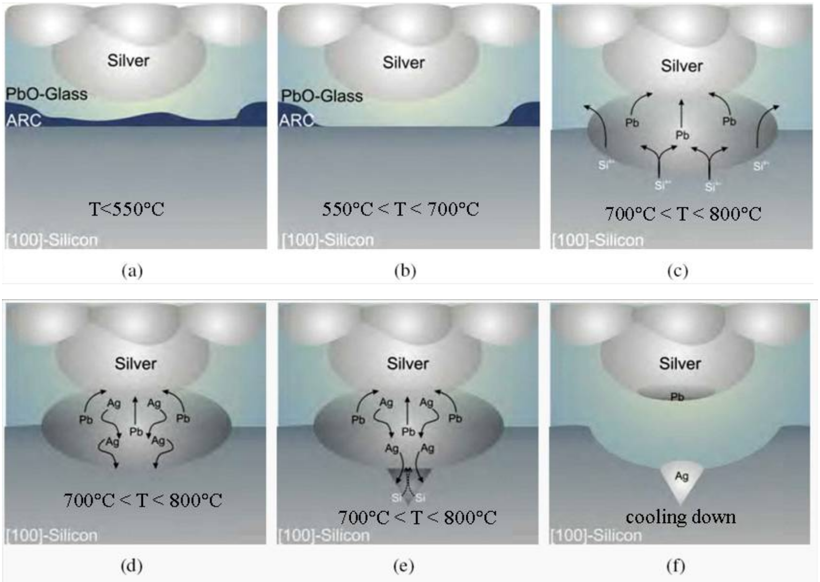

Fig. 3-9: Model of the contact formation as published by Schubert [23].

The contact model also reveals the main difference between an evaporated and printed/fired contact: in the case of an evaporated contact, the metal is in an intimate contact with the silicon and the metalized area is equal to the contact area. Both are unfortunately not the case for printed/fired contacts. The silver crystallites are separated by an insulating glass layer and the effective contact area is reduced to the area covered by the crystallites. In Fig. 3-6 the resistivity for printed and fired silver contacts is marked. The difference from the theoretically assumed resistivity and the measured resistivity can be explained by the reduced contact area, (see chapter 9)

3.5 Possible current paths on printed contacts

Another controversially discussed topic is the current transport mechanism. Several possible current paths between emitter and front side grid are explained by [57, 66], and were extended for light-induced plated (LIP) contacts by [25, 65]. The following mechanisms are proposed: first, the current transport between emitter and front side contact is possible via single Ag-crystallites, which are either in direct contact with the bulk silver or covered by a thin glass layer, and tunnelling is the transport mechanism for the charge carrier. It is also possible that current flows between the emitter and the bulk silver on contact areas where the ARC is opened and the bulk silver is in direct or indirect contact with the emitter, and again, a direct or a tunnelling contact can be imagined. These main transport mechanisms are enhanced if the printed and fired contacts are additionally plated. Mette and Pysch measured a reduced contact resistance for plated contacts [25, 65]. This reduced contact resistance leads to the assumption that current flow between LIP-silver and silver crystallites/emitter is likely. Detailed SEM studies have shown that in the surrounding of a screen printed and fired contact, a narrow glass layer was found. During the firing process either glass leaks out of the printed contact structure and exceeds the actual contact width, and/or a layer of glass is left behind as the contact shrinks in width. The LIP-silver is grown on this narrow glass layer and further contact points and additional current paths are possible. Again, the current can flow via crystallites formed under the glass layer, and also directly from the opened emitter into the LIP-silver, either direct or via tunnelling trough the thin glass layer. The tunnelling is likely, as a large number of metal precipitates were found in the narrow glass layer. Another advantage of LIP is the increasing density of the initially porous sintered bulk-silver, which leads to a reduced distance between emitter and bulk silver, and therefore to a reduced contact resistance.

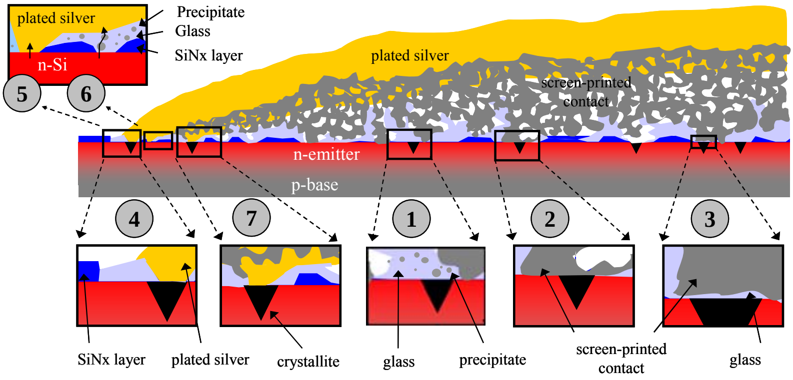

Fig. 3-10: Possible current paths on a fired and plated, screen printed front side contact [25]

The main current path is still under discussion. Most of the above shown current paths are related to Ag-crystallites grown into the emitter. The theory of a high quality contact formation due to the epitaxial growth of the Ag-crystallites is generally accepted [56, 57, 67]. However, it is suggested that the formation of silver crystallites indicate an over-fired contact with a reduced contact and cell quality [58]. It is suggested by Li and Young to keep the firing temperature in a range where the ARC is opened by the glass frit, but the emitter is not affected and no silver crystallites are formed. This "smooth" contact formation has the advantage that the pn-junction is not affected by the penetration of metal impurities. In this case, the proposed current path is defined by a multiple tunnelling process between the opened emitter and the bulk silver, as shown in Fig. 3-10 (current path 6). Metal that precipitated within the glass layer formed during the firing step is responsible for the effective tunnelling through a >15 nm thick glass layer. Improved glass conductivity due to the presence of metal precipitates was reported by Roy [68].

It is therefore not entirely clear in what way the contact inks and the firing process should be optimized, and the open question is: is it preferable for the current transport to have a large contact area by a widely opened SiN_x coating and the contact is based on a tunnelling process, or is it advantageous to have local contact points (Ag-crystallites) where a direct connection between silicon and silver is possible?

4 Characterization methods

Within this chapter, the characterization methods used to understand the contact formation, the electrical contact parameters, and the contact influence on the solar cell are introduced. Information on the chemical reaction behind the contact formation can be gained by thermal gravimetric - differential thermo analysis (TG-DTA). The measurement was used to study the reaction between the individual ink components with silicon. In order to describe the electrical contact quality, the contact resistance and resistivity were determined using the transfer-length method (TLM). The influence of the metal contacts on the solar cell, especially on the pn-junction, was tested with SunsV_{oc} measurements, an easy and fast method to determine the solar-cell IV-characteristic without the influence of the series resistance. Further on, the processed contacts were analyzed by several imaging methods like optical microscopy, confocal microscopy, scanning electron microscopy (SEM), transmission electron microscopy (TEM), and atomic force microscopy (AFM).

4.1 Contact resistance measurement (TLM-method)

The best values to describe the electrical quality of an ms-contact are the contact resistance or the resistivity (the specific contact resistance). The contact resistance can be determined in several ways [69-71], All methods are based on a 4-point measurement, where a current is applied between two points and the resulting voltage is probed on two further points. The resulting resistance is overall independent of the measurement. Different structures have been proposed to construct a test: the Kelvin structure [72], Meier Schroder structure [34], square metallization pattern [46], a dotted pattern [73], and finally the TLM or ladder structure [69, 74], (see Fig. 4-1). Most measurements are developed for planar, evaporated contacts. In this work, most contacts to be analyzed are printed and fired contacts on a rough surface. A suitable measurement, especially for these contacts, is the transfer length method (TLM) as it is a relatively simple test structure where equidistant fingers are cut out of a solar cell. However, for a reliable result, the contact geometry must be known exactly and the voltage measurement needs to be quite accurate, as the contact resistance is only a small fraction of the measured resistance, see below. The method was originally introduced by Shockley [74] and further refined by Berger and Murrmann [69, 75, 76], who developed a test structure from which the front (R_c) and end (R_e) contact resistance can be measured; both are necessary to determine the resistivity (ρ_c).

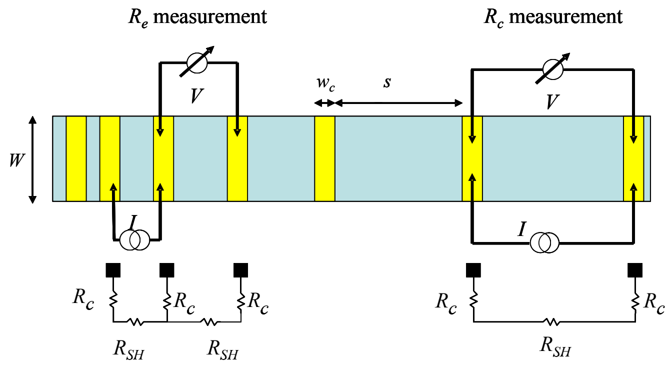

Fig. 4-1: TLM-structure with the resistor network for the front contact resistance (right) and the end contact resistance measurement (left).

4.1.1 Measurement of R_c and the normalized contact resistance $R_c \cdot W$

The applied constant current I has to overcome two times the ms-junction (2xR_c) and the emitter in between (R_{em}). The measured resistance R_{TLM} is therefore equal to:

$$R_{TLM} = \frac{V_{i,i+1}}{I_{i,i+1}} = 2R_c + R_{em} = 2R_c + R_{SH}\frac{s}{W} \tag{4-1}$$

with R_c the contact resistance and R_{SH} the emitter sheet resistance.

If the measurement is repeated for varying distances between the contacts (s), the values for R_{TLM} can be plotted on a linear curve. From the intercept R_c, and from the slope R_{SH} can be extracted. An example for a TLM-measurement on a sample with equidistant contact pads is shown in Fig. 4-2. The measured value of R_c is only the total contact resistance for this specific structure. For the determination of a global value, the specific contact resistance ρ_c, i.e. the electrical contact geometry needs to be known. That means in addition to the contact width (W), the length of the contact, within which most of the applied current has entered the contact, the so-called transfer length (L_T) are required (see Fig. 4-3). However, for a comparison of similar contact structures e.g. printed silver contacts of similar contact length (w_c), a useful value is the normalized contact resistance $R_c \cdot W$, which is the actual contact resistance multiplied by the contact width [37]. In this work, both values are used in parallel.

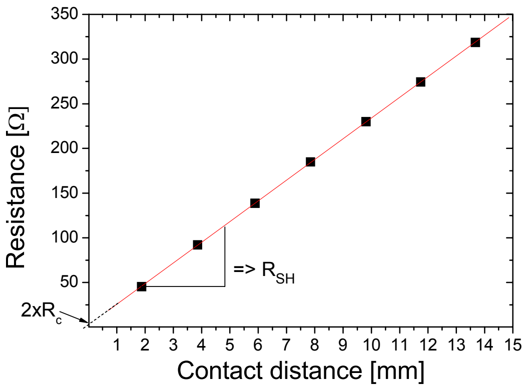

Fig. 4-2: TLM-measurement, where the measured resistance R_{TLM} is plotted as a function of the spacing (s) between the contact pads. From the slope the emitter sheet resistance R_{SH} and from the intercept the contact resistance R_c can be determined.

4.1.2 Determination of the specific contact resistance ρ_c

The specific contact resistance, the resistivity ρ_c which is independent on the contact geometry can be determined if the effectively used contact area is known. The current enters the contact laterally and is not homogenously distributed over the contact area, but concentrated at the edges. If the current would be homogenously distributed over the contact area, ρ_c could be easily calculated by weighting the measured contact resistance R_c with the contact area $w_c \cdot W$. Unfortunately this is not the case and the resistivity is dependent on the current flow under the contact, the *current crowding* [76, 77]. The distance at which the current density has dropped to 1/e from the initial value is called transfer length (L_T), (see Fig. 4-3).

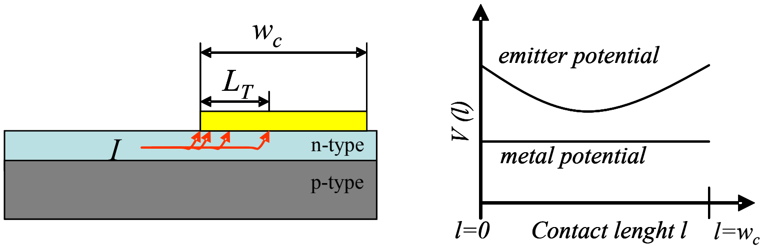

Fig. 4-3: Schematic drawing of the current entering the metal contact (left) and the potential distribution over the contact, assuming the current is entering the contact from both sides (right).

The distribution of the current and the according potential under the contact can be described by: [78]

$$\frac{dI(l)}{dl} = \frac{W}{\rho_c} V(l) \qquad \text{und} \qquad \frac{dV(l)}{dl} = \frac{R_{sk}}{W} I(l). \tag{4-2}$$

with R_{sk} the emitter sheet resistance under the contact.

Both equations can be combined to a differential equation of the second order:

$$\frac{d^2V(z)}{dz^2} - \frac{R_{sk}}{\rho_c} V(z) = 0. \tag{4-3}$$

As a constant current I_0 is applied between two contacts, the equation can be solved using the following boundary conditions: The current at the contact position l=0 is I_0 and all current enters the contact within the contact length l_c, the current at the end of the contact $I(l_c)$=0 and the contact width $w >> l_c$ and L_T and the line resistivity of the contact metal is negligible. The differential equation can then be solved and R_c can be calculated to:

$$R_{\mathrm{c}} = \frac{V(0)}{I(0)} = \frac{R_{\mathrm{sk}} L_{\mathrm{T}}}{W} \coth\left(\frac{w_{\mathrm{c}}}{L_{\mathrm{T}}}\right) = \frac{\sqrt{\rho_{\mathrm{c}} R_{\mathrm{sk}}}}{W} \coth\left(l_{\mathrm{c}} \sqrt{\frac{R_{\mathrm{sk}}}{\rho_{\mathrm{c}}}}\right). \tag{4-4}$$

with:

$$L_{\mathrm{T}} = \sqrt{\frac{\rho_c}{R_{sk}}}. \tag{4-5}$$

Assuming the sheet resistance under the contact R_{sk} is the same as next to the contact R_{SH}, the resistivity and the transfer length can be calculated as R_c and all the geometrical values are known. However, it is very likely that the emitter concentration under the contact changes, either by the formation of silicides or due to the etching of the paste components into the emitter. Therefore an additional measurement where the end contact resistance R_e is determined is necessary. The voltage drop is measured between a finger of the current – circuit and an adjacent finger, as illustrated in Fig. 4-1. The end resistance is defined as:

$$R_{\mathrm{e}} = \frac{V(w_{\mathrm{c}})}{I(0)} = \frac{R_{\mathrm{sk}} L_{\mathrm{T}}}{W} \frac{1}{\sinh\left(\frac{w_{\mathrm{c}}}{L_{\mathrm{T}}}\right)}. \tag{4-6}$$

If R_e and R_c have been measured experimentally, the transfer length can be determined by the ratio of R_c and R_e:

$$\frac{R_{\mathrm{c}}}{R_{\mathrm{e}}} = \cosh\left(\frac{w_{\mathrm{c}}}{L_{\mathrm{T}}}\right). \tag{4-7}$$

Furthermore, the sheet resistance under the contact R_{sk} from Eq.4-6 and finally the resistivity ρ_c using Eq.4-5 can be calculated:

$$\rho_c = L_T{}^2 R_{sk} \qquad 4\text{-}8$$

Two limiting cases are useful to simplify Eq.4-4 [37]

1) $w_c \geq 1.5L_T \Rightarrow R_c \approx L_T R_s/W = \rho_c/L_T W$
2) $w_c < 0.5L_T \Rightarrow R_c \approx \rho_c/w_c W$

For the first case, where the contact structure exceeds the transfer length, R_c is dependent on L_T or put another way, R_c is independent of the contact length l_c as all the current enters the contact metal near the edge and the rest of the contact is inactive. In the second case, where L_T is larger than the contact length l_c the entire contact area is used for the current transfer and the transfer length L_T is substituted by the l_c. The relation between R_c, ρ_c and contact length l_c is illustrated in Fig. 4-4. With increasing contact length l_c the contact resistance R_c is strongly reduced in the beginning, in the range where L_T is the important factor for the current transfer, approaching a constant value as soon as l_c exceeds L_T (case 1). The resistivity ρ_c is steadily increased, as it is always weighted by the contact area, which is increased for wider contacts. For small contact length l_c the resistivity increases almost at a constant rate due to the additional contact area being almost compensated by a more effective current transfer, rising with a constant slope as soon as $l_c >> L_T$. The contact length can therefore be reduced until it is in the range of the transfer length before the contact resistance, which is the limiting parameter for the solar cell, is increased. This is assuming the series resistance is constant, which is the case for the two layer contact concept in particular.

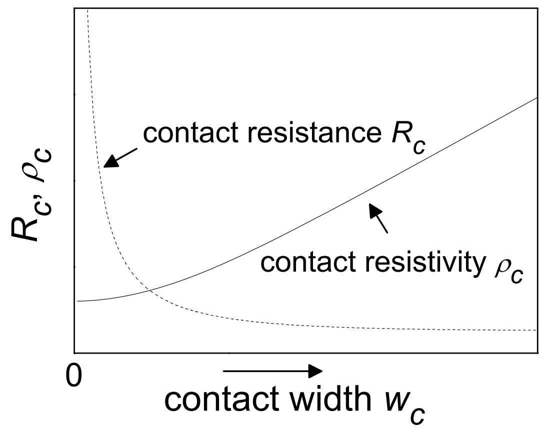

Fig. 4-4: Illustration of relationship between contact length w_c and contact resistance and resistivity for a constant transfer length, taken from [25].

4.2 I_{sc}-V_{oc} characteristic - SunsV_{oc} – measurement

I_{sc}-V_{oc} curves measured independent of the light intensity are a versatile tool to investigate the physics of silicon solar cells. Since I_{sc}-V_{oc} curves are unaffected by the series resistance R_s [79], the pseudo fill factor pFF, and the pseudo efficiency as an upper limit for the cell performance can be determined. Especially the series-resistance-free pseudo fill factor of the I_{sc}-V_{oc} curve is an excellent measure for the diode quality determined by shunts and junction recombination. It is the upper limit when optimizing the series resistance of silicon solar cells.

The standard IV-curve measured under constant illumination can be described by a single diode:

$$I = I_0\left[\exp\left(\frac{q}{nkT}(V - IR_s)\right) - 1\right] - I_{Ph} \qquad \textit{4-9}$$

The cell is connected to an external resistive load which is varied between short circuit and open circuit conditions. The current flow and the resulting voltage are measured.

In this case, the series resistance influences the measurement and follows all cell parameters, like FF and efficiency.

In the case of an I_{sc}-V_{oc} characteristic where the light intensity is varied, the measurement is free of series resistance losses, as the voltage is measured under open circuit conditions and alternating the current is measured under short circuit conditions:

$$I = I_0\left[\exp\left(\frac{q}{nkT}V_{oc}\right)-1\right]-I_{Ph} \qquad \textit{4-10}$$

An elegant way to measure a I_{sc}-V_{oc} characteristic is the $SunsV_{oc}$-measurement as proposed by Cuevas and Sinton [80]. The measurement, called the quasi-steady state open-circuit voltage method ($qssV_{oc}$), is a fast and easy method to measure the I_{sc}-V_{oc} characteristic of a solar cell under varying illumination, Fig. 4-5. To illuminate the solar cell, a flash light is used. The short-circuit current of the cell is not actually measured at every light intensity. Instead, the incident light intensity is measured with a calibrated reference solar cell. This incident light intensity can be converted to a measure of current by using the short-circuit current or the modelled photogeneration of the test sample ($j_{SunsVoc}=j_{sc(1\text{-}suns)}$). The light is varied in a way that the resulting voltage at the solar cell can be measured in a quasi steady state. The IV-curves of a solar cell measured under a constant light intensity (IV-curve) and under a varying light intensity ($SunsV_{oc}$) are shown in Fig. 4-6. From the comparison of both curves at the point of maximum power voltage, the series resistance R_s can be determined [79]. Cuevas and Sinton have described the observation of a SunsVoc measurement with a reversal point [80]. For illumination densities above this reversal point, the voltage is *decreasing* with *increasing* illumination densities. They attributed this to the Schottky-barrier formed between the p-type silicon and the rear-side aluminium. This effect was investigated in detail by Glunz [7], who studied the cell response (V_{oc}) at very high illumination for different rear sides. He found the $SunsV_{oc}$ measurement to be a helpful tool in order to qualify of the back contact junction. It is further proposed by Cuevas to use the $SunsV_{oc}$ method to acquire useful cell data, directly after pn-junction formation. As long as it is possible to form an ohmic point contact on the cell, e.g. by a sharp probe, an IV-curve can be measured without any metallization. It is therefore possible to use the $SunsV_{oc}$ measurement to quantify the influence of the contact formation on the solar cell efficiency.

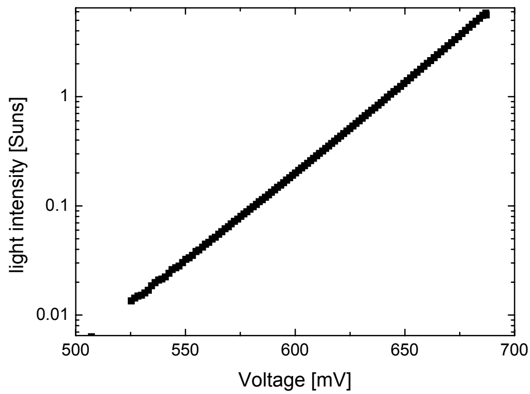

Fig. 4-5: SunsVoc as a function of the light intensity

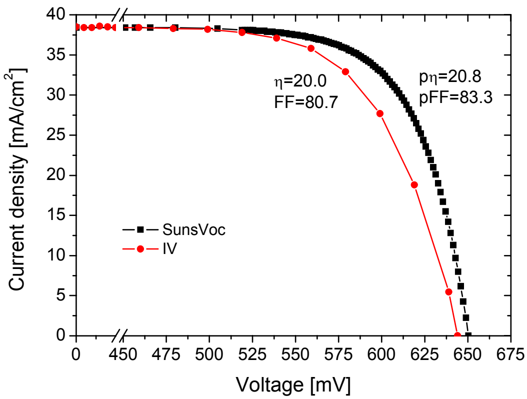

Fig. 4-6: Comparison of a $j_{sc}V_{oc}$-curve and a standard IV-curve.

4.3 Thermal gravimetric - differential thermo analysis (TG-DTA)

The combination of thermo-gravimetric (TG) and differential-thermo analysis (DTA) was used to study the reaction mechanism behind the front-contact formation in a firing step. The thermo-gravimetric measurement is used to determine the mass and the mass variation respectively of a sample, in dependence on the temperature and/or time. A schematic diagram is shown in Fig. 4-7 (TG-curve). The sample is heated up in a thermally stable crucible, e.g. platinum or ceramic. The sample holder is connected to a sensitive balance which measures the mass changes. A thermocouple close to the sample measures the temperature (see Fig. 4-8a). The mass of a sample can change by evaporation, combustion and chemical reaction e.g. oxidation or reduction processes. Important for the measurement is the used atmosphere, the reaction gas. Chemical reactions can be studied in oxidizing- (O_2), reducing- (N_2/H_2), or under inert- (N_2, Ar) atmospheres. The evolving reaction gases from the sample can be additionally analyzed if the exhaust of the TG is coupled e.g. with a mass spectrometer (MS). The reaction information gained from a TG-measurement is the mass loss, the reaction temperature and the reaction kinetics. From this information one can draw a conclusion on the reaction that has occurred.

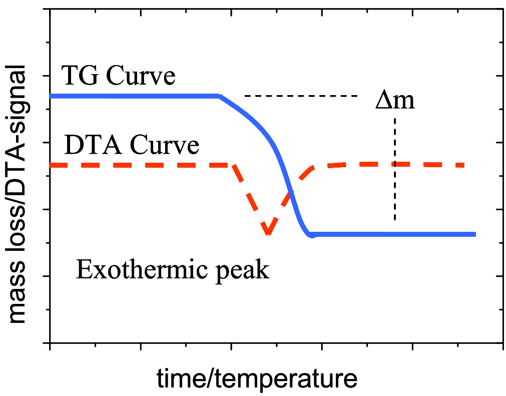

Fig. 4-7: Signals, determined from a TG-DTA measurement.

Additional information on the reaction characteristics can be given by the differential-thermo-analysis (DTA). The DTA uses the temperature difference between sample and reference during a controlled temperature program. The measurement system is the same as for a TG-measurement, aside from the sample holder. A DTA-sample holder, shown in Fig. 4-8b), consists of two cups where each is connected to a thermocouple. The sample holder again is placed in a furnace on a sensitive balance. During a controlled temperature program, the measured temperature on reference, usually an empty cup and sample, can be different and is dependent on the chemical reactions or phase changes of the studied sample. It can be distinguished between exothermic reactions where additional reaction heat is produced (e.g. due to condensation energy) or endothermic reaction, where reaction heat is "consumed" (e.g. during melting). The difference in thermal voltage, as measured by the thermocouples, is plotted as a function of temperature/time (see Fig. 4-7 DTA-curve). A signal including some characteristic temperature points is shown in Fig. 4-9.

a) b)

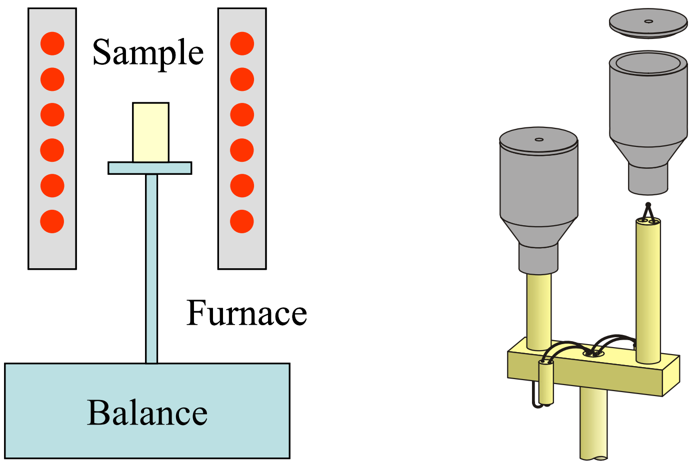

Fig. 4-8: Schematic setup of a thermo gravimetric (TG) measurement (left) and a DTA-sample holder (right) [81].

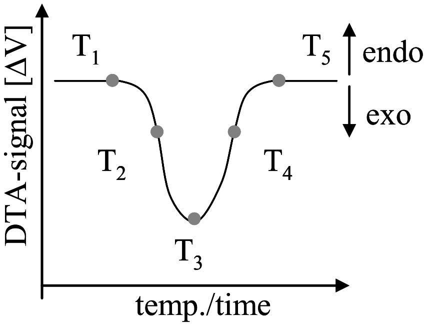

T_1: starting point of the reaction

T_2: highest reaction speed

T_3: effective reaction temperature

T_4: end of the reaction

T_5: temperature adjustment

Fig. 4-9: Characteristic points in a DTA-signal

5 Aerosol printing technique

The metal aerosol printer is a Maskless Mesoscale Material Deposition (M3D) technique from Optomec INC., USA. The system was designed to close the gap between photolithographically defined structures (<100 nm) and thick film printed features (~100 µm) for microelectronic applications. Using a well designed ink, features as small as 10 µm can be deposited contactless on flexible and thin substrates [82]. The technology became available in 2004 and was designed for the rapid prototyping of electronic equipment, legacy repair and for laboratory experiments [83].

In 2004, one of the first systems was installed at Fraunhofer ISE by A. Mette and P. Richter [9, 84] to deposit front side contacts on silicon solar cells. This was the first time that an aerosol system was used to process solar cells. The system was chosen due to its flexibility and its ability to perform contactless fine line printing. The deposition of different line widths and line distances, front side grids and test patterns is straighforward, as CAD-drawings can be translated into machine code and be directly printed. Additionally, the system is used to study the contact formation of fine line printed contacts on silicon solar cells. A variety of different materials and inks can be tested, as it is relatively easy to change the ink. Nevertheless, before we could start the processing and printing of solar cells, some obstacles had to be overcome. The main problem, beside some minor hardware issues in the beginning, was the lack of a suitable ink. As soon as the right ink parameters like particle size, viscosity, and solid load were determined, we were able to study a variety of different ink compositions in order to optimize the contact formation with a shallow, thin ink layer. After optimization of both, contact ink and printing parameter, lines with below 20 µm could be deposited.

5.1 Printing system

The main parts of the system are illustrated in Fig. 5-1-Fig. 5-4. The deposition of material is a two step procedure. Initially an aerosol is created in a nebulizer, concentrated in a virtual impactor and finally focused and deposited using a printing head.

An aerosol can be generated from an ink, either by compressed air nebulizers or by ultrasonic nebulizers. The utilized atomization technique depends on the ink parameters, or to put it another way, the atomization technique defines the ink requirements. Inks with a low viscosity μ<10 mPas and a small particle size distribution d_{50}<50 nm can be atomized ultrasonically. Slurries and suspensions, as mostly used for contact inks, can be atomized by compressed air. The diameter of the aerosol droplets may range from less than d_{drp}<10 µm up to 100 µm or more, depending on the nebulizer. Different compressed air atomization techniques are available, like Collison, DeVilbiss, Lauterbach, Laskin, Wright, or Lovelace nebulizers; an extended list and description of the different atomizer types is given by Raabe [85]. They are characterized by aerosol parameters like output rate, aerosol density, air volume, droplet size and size distribution. In general, the application determines the choice of a nebulizer. For an aerosol printer, the requirements are: a high aerosol density (10^{16} m^{-3}) [86] produced with small gas flow rates (50-120 ml/min), and a mean droplet size in the range of 1-3 µm. These requirements can only be fulfilled by an ultrasonic atomizer, as the gas flow rates are too small for any pneumatic atomization. In order to allow the use of a pneumatic atomizer, an additional device, called a virtual impactor, is used to concentrate the aerosol. In our aerosol printing system, the nebulizer used for slurries with viscosities up to 1000 mPas is a so-called Collison atomizer. It was introduced in 1932 by W. E. Collison [87], mainly for medical purposes. The working principle is illustrated in Fig. 5-3. The atomizer consists of one or more orifices of various diameters, e.g. 0.3 mm, set at right angles to a vertical liquid feed channel within a cylindrical metallic rod. Compressed air is accelerated by the orifice over the liquid feed channel, and due to the Venturi effect, ink is pressed into the channel and atomized by the air stream. Most of the liquid, including large droplets, is collected by impaction and remains in the ink jar. The produced droplet size distribution depends on the requirement and is in the range of 2 µm. Since the atomization gas is used as a transport gas for the aerosol and the flow rates with 1-4 l/min are too high for a direct deposition, the aerosol has to pass a virtual impactor; about 95% of the gas is separated from the aerosol. A schematic drawing of the virtual impactor is given in Fig. 5-4.

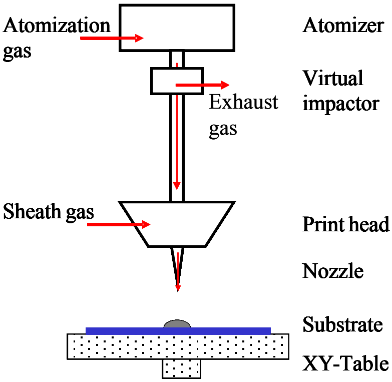

Fig. 5-1: Schematic drawing of an aerosol printing system with its main components and gas flows.

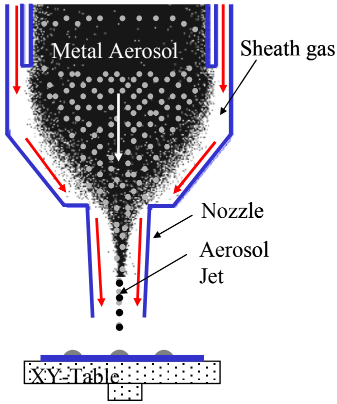

Fig. 5-2: Simulation of the print head. The aerosol is focused by the sheath gas to a dense aerosol jet.

Virtual impactors are technically used to separate small particles or droplets from large ones [88]. In principle, they consist of two oppositely directed funnels called jets. The jets are separated by a small gap. The jet diameter and the jet distance define the particle separation. Larger droplets, which possess a higher inertial momentum, follow the main gas stream and overcome the gap between the two jets, whereas small droplets, or in this application simply air (atomization gas) with a small initial momentum, is guided out of the system. The two jets are encapsulated and a vacuum pump helps actively to separate the gas from the droplets. The remaining concentrated and condensed aerosol is forwarded into the deposition head, Fig. 5-2.

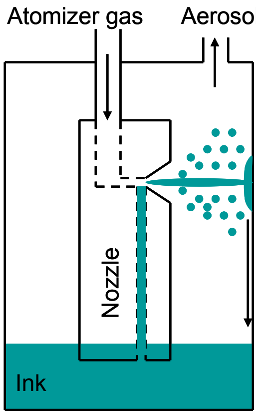

Fig. 5-3: Schematic drawing of a pneumatic (Collison) atomizer.

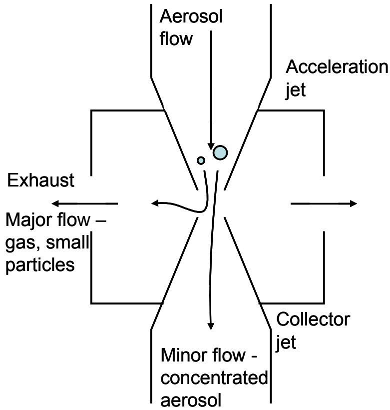

Fig. 5-4: Schematic drawing of a virtual impactor as it is used to concentrate the aerosol flow.

Inside the deposition head, the condensed aerosol is focused and forwarded into the nozzle. The technique is based on a principle which is used in optical aerosol particle counters [89]. The print head consists of two interconnected tubes ending on top of a nozzle. The aerosol flows through the inner tube with a low velocity. A second gas stream, called sheath air, flows laminar in the outer tube having a higher velocity. On top of the nozzle, the sheath gas surrounds the aerosol and streams through the nozzle. The sheath gas focuses the aerosol and prevents it from touching the wall. As a result, a narrow and dense aerosol jet exits the tip and is deposited as a thin line on the substrate. The line width can be influenced by the ratio of sheath gas flow to condensed aerosol flow. By increasing the sheath gas flow rate, the line becomes narrower. The simulation, see Fig. 5-5, which is based on water vapour (aerosol) and nitrogen gas (sheath gas), shows this tendency. The optimum for the ratio (generation gas:sheath gas) was found at 1:4, which is quite consistent with the experimentally determined ratio. If the sheath gas rates getting too high, no significant change in line width is observed; on the contrary, the aerodynamic behaviour of the gas streams changes and sheath gas and aerosol are partly mixed. The result is a very narrow line with a broad overspray. The material output is reduced as well and if the sheath gas rates are too high, the aerosol flow can be totally stopped. For a good line definition, the ratio should be kept in the range of 1:3 – 1:5. The line width can be effectively influenced by the nozzle diameter. A set of nozzles with openings between 100 µm and 300 µm are available. The jet diameter is more than 10 times smaller than the nozzle opening itself. Depending on the ink and the substrate, the line width can be 3-10 times smaller than the nozzle opening. For the metallization of textured solar cells, a factor of 5 is typical, as the inks tend to wet the textured substrate. The wetting is more distinct for an alkaline texture than for an acidic texture. The structured pyramids present no barrier to the ink; the wetting is even reinforced by the pyramids as the liquid ink is driven into the valleys by capillary forces. The wetting and the broadening of printed lines can be minimized if hot melt inks are used [90]. These inks condensate as soon as the ink droplets touch the cold solar cell surface. Another option to avoid wetting is the evaporation of ink solvents directly on the wafer surface by heating the substrate. Both methods give similar results, and line width below w_c<20 µm can be achieved on textured solar cells using a 100 µm nozzle opening (see Fig. 5-7).

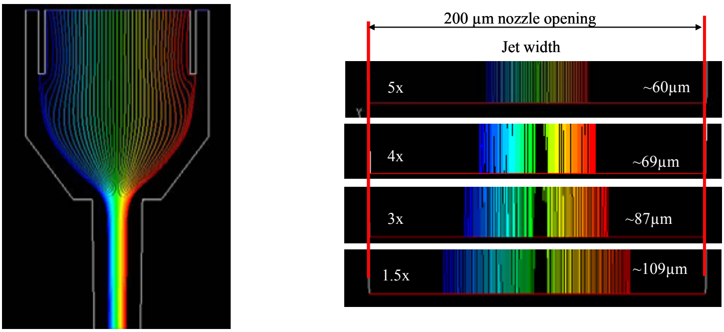

Fig. 5-5: Simulation of the aerosol flow in a single head dependent on the gas flow rates, 1.5 – 5 (sheath gas:aerosol gas). The simulated aerosol is water vapor and the nozzle opening was 200 µm.

Currently there are two printing systems available at ISE: one for laboratory use and one for industrial fabrication. In 2004 only a single nozzle system was available. The metallization of a single 15.6×15.6 cm² cell took about 20 min, which is by far too long. Currently, the industrial requested printing time for a solar cell is about 1-1.5 sec. Therefore, an upscale of the system was necessary. Instead of printing the whole front side grid with one nozzle, one nozzle for each contact finger should be applied. For a proof of concept, a 10-nozzle head was successfully tested at ISE, with a nozzle distance of about 4 mm. The reduced printing time to 1-3 min per wafer is in a range where the lab fabrication makes sense. Process times below 1 min are possible, if only the fingers are printed; the double process time can be estimated if additionally the bus bars are aerosol printed by multiple path printing. The front side grid and the inks can then be optimized on a sufficiently large number of wafers. For an industrial use it is still too slow and further improvements were necessary. Since the number of nozzles could be increased from one to ten without problems like clogging, a further increase to 40 nozzles was realized as well. The printing principle is still the same, instead of ten, 40 nozzles are switched in parallel in a single print head. All nozzles are fed by one aerosol chamber. The construction is more compact, the aerosol paths are shorter, the atomizer works more efficiently and the printing speed can be increased up to 100 mm/s, resulting in a process time of about 3 sec for a large wafer. The company Manz Automatisation has recently begun to deliver a fully integrated aerosol printer for mass production.

By increasing the number of nozzles, the system became faster; however, it lost one very important feature, its flexibility. Only straight lines of fixed distance can be printed. For experimental use, the single or the ten nozzle system is still preferred. An often-requested application is the filling of laser groves or the ink deposition on predefined structures, like an opened dielectric layer or a selectively diffused emitter.

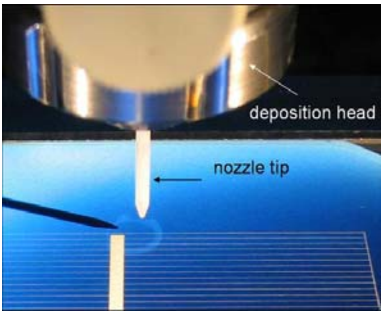

Fig. 5-6: Picture of a single-nozzle deposition head. It is used for the flexible deposition of front side grids or test structures and to print on predefined structures like selective emitters or laser grooves, as the alignment with a single nozzle is quite accurate.

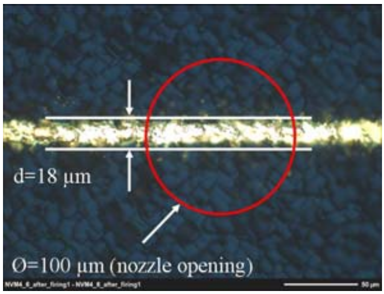

Fig. 5-7: Microscopic picture of an aerosol printed line. The 100 µm wide nozzle opening is symbolized by the red circle. The deposited line is, as expected, about 5 times thinner than the nozzle opening.

Fig. 5-8: Picture of a ten nozzle print head. The upper tube supplies the head with aerosol; the lower is the sheath gas inlet.

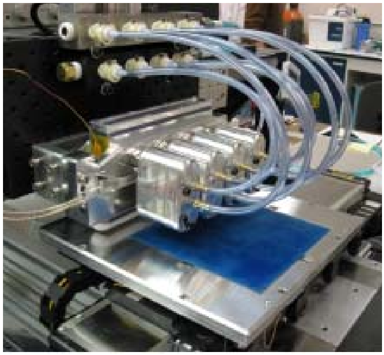

Fig. 5-9: Picture of a 40 nozzle head, as it is principally used in the aerosol printer offered by Manz Automatisation.

5.2 Ink requirements

The ink requirements had to be determined before we could start with the ink preparation and especially before different inks could be tested and optimized. When we started working with the aerosol printer, there was no ink available which could be used in an aerosol printer to contact a solar cell. Due to the lack of a suitable ink, our first promising solar cell results could be achieved using commercially available screen-print paste as it is used in a standard production process. Such a paste has solid loads up to 80m% and viscosities higher than 10 Pas. To transfer a screen-print paste into an aerosol ink, it has to be diluted to reduce the dynamic viscosity below μ<1 Pas. The solid load drops due to the dilution from 80m% to approximately 60m%, which is still sufficient for a seed layer print. With such an ink we could already achieve very good solar cell results [9]. However, printing uptime and especially printing speed were limited. Printing was stopped about every 10-20 min due to clogging of the nozzle. The line definition was also quite poor and line widths below 80 µm were hardly possible. After adapting the viscosity according to specification, the particle size had to be adjusted as well to guarantee a stable printing process and the deposition of fine, well defined lines.

5.2.1 Particle size

The particle size is crucial for both, the aerosol generation and the deposition. During the pneumatic aerosol generation, large particles are separated from small ones. The larger particles are atomized against the wall of the jar and remain in the ink vessel, whereas smaller droplets, loaded with smaller particles are carried by the gas flow towards the deposition head (see Fig. 5-3). To find the optimum particle size for a highly silver loaded aerosol ink, a diluted screen-print paste with a wide particle size distribution, and a second paste with a narrower and smaller particle size distribution were analyzed in a laser particle analyzer before and after printing, (see Fig. 5-10 and Fig. 5-11). The size distribution of the diluted screen print ink originally contained particles from under 100 nm up to diameters of more than 6 µm. However, the printed and deposited material contains only particles smaller than 2 µm, with an average particle size of around d_p=500 nm. Only small particles are atomized, whereas the large particles remain in the ink vessel. Obviously, larger particles are atomized incidentally, as clogging was one of the main issues when using a diluted screen print ink. If an ink with an original particle size distribution below 1 µm is atomized, no separation in particle size and no clogging were observed. Whether the particle size is in the right range or not can easily be controlled by measuring the solid load of the ink, which should be the same before and after deposition. The diluted screen print ink lost about 1/3 of solids after printing; only small particles and solvents were atomized. Therefore, the ink composition, i.e. the ratio of silver:glass, has changed as well, as the silver and glass particles are probably not homogenously distributed. In case of the monodisperse sub-micrometer ink, the solid load before and after printing and the size distribution remain constant with an average value of d_p= 250 nm. For an efficient atomization, the particle size should be as small as possible, at least <1 µm. Furthermore, a narrower particle size distribution or the use of monodisperse particles is preferred, as the aerosol generation and the material deposition are more homogeneous under these conditions. This has the beneficial effect of generating more aerosols without any ink deposition in the system – clogging can be avoided, thus the printing speed can be increased as well as the system uptime.

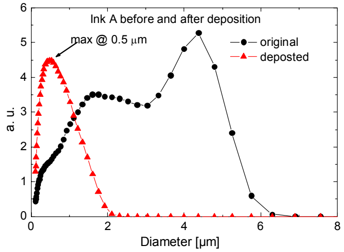

Fig. 5-10: Particle size distribution before and after printing of a diluted screen print ink.

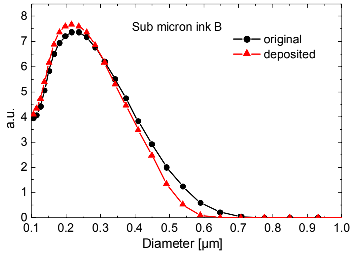

Fig. 5-11: Particle size distribution before and after deposition of an almost monodisperse ink with a maximum of d_{90}<0.5 µm.

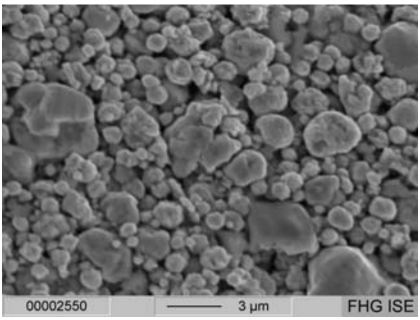

Fig. 5-12: Silver particles in a standard screen print paste

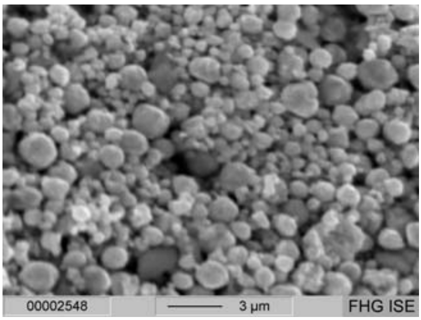

Fig. 5-13: Silver particle of a standard screen print paste after deposition, using an aerosol print system

The deposition head requires the right particle/droplet size distribution. Whereas for the aerosol generation, a lower limit in particle size does not exist; the smaller the particles are, the more aerosol is generated; the droplet size in the deposition head is limited, (see Fig. 5-15). For the simulation, steel particles of different sizes (5 µm, 1 µm and 0.1 µm) were assumed at optimized gas flows. Particles that are too large cannot be focused by the sheath gas, resulting in contact with the print head and the nozzle. The particles are deposited inside the printing head, making piling up and clogging of the tip unavoidable. For particles/droplets far smaller than 1 µm, the diameter of the aerosol jet is increased. The motion of a particle, and the forces which interact between the carrier gas and the particle, especially in a slowly converging micro-capillary as it is the case in an aerosol tip, were studied by Akhatov [91, 92]. The aerosol flow can be described in total by seven forces: the Stokes drag force, which represents a steady viscous drag force; the Basset force, which represents a non-steady viscous drag force; virtual mass force, which represents the inertia of the fluid around a particle added to that particle; fluid pressure gradient force, gravity force, the Magnus force, which represents a steady lift force of a viscous fluid on a rotating particles; and the Saffman force, which represents a steady lift force induced by the local shear flow of a viscous fluid. The dominant forces are the Stokes and Saffman force. Especially the Saffman force is responsible for the formation of a collimated aerosol beam [93]. It describes a force perpendicular to the direction of flow and was first observed by Poiseuille [94] for red blood cells, which tend to avoid vessel walls when flowing trough capillaries. That means, that particles/droplet in an aerosol system tend to move towards the centre of the aerosol beam. As the Saffman force is proportional to the square of the particle size, larger particles (~1 µm) are more affected than smaller particles (~0.2 nm) and are therefore more focused than smaller ones [91]. Schulz [95] showed theoretically and experimentally the influence of the Saffman forces on the diameter of the aerosol beam. He built a nozzle which enforces the Staffman forces, consisting of converging and diverging nozzle and he could reduce the diameter of the aerosol beam and consequently the deposited line width below w_c<10 µm [95].

The optimum was found for particles/droplets in the range of 1 µm. The motion of small particles in gasses such as aerosol can be described theoretically by Stokes' law. The Newtonian resistance law is generally used to describe the motion of spheres passing through a gas, and is primarily used for spheres with high inertial forces and high Reynolds numbers Re>1000. The Reynolds number is the ratio of initial to viscous forces. For an aerosol where the Reynolds number is rather small Re<1 (laminar flow) and made up of quite small particles, the forces on a particle are dominated by viscous forces and can be described by Stokes' law:

$$F_D = 3\pi\mu V d_p \qquad \textit{5-1}$$

with the viscosity μ, the velocity of a spherical particle V and its diameter d_p.

A special application of Stokes' law is the description of curvilinear particle motion, which is characterized by a dimensionless number called Stokes' number (*Stk*). It describes the motion of a particle around an obstacle. When *Stk*>>1, particles continue moving in a straight line when the gas turns; when *Stk*<<1, particles follow the gas streamlines perfectly. The Stokes number is dependent on the geometry and for the special case of inertial impaction, (see Fig. 5-14), it is given by:

$$Stk = \frac{\tau U}{D_j / 2} = \frac{\rho_p d_p^2 U C_c}{9 \mu d_{noz}} \qquad \text{5-2}$$

where τ is called the *relaxation time* of the particle, characterizing the time required for a particle to adjust or "relax" its velocity to a new condition of forces. C_c is the *Cunningham correction factor* and corrects the assumption in Stokes' law that the relative velocity of the gas at the surface of a sphere is zero, which is especially not the case for small particles <1 µm. ρ_p is the density of the particle, d_p is the particle diameter and μ is the viscosity. U is the particle velocity at the nozzle exit and d_{noz} is the nozzle diameter. Detailed information is given by Hinds[96]

The inertial impaction finds many applications in the collection and measurement of aerosol particles. In an aerosol printer it is used twice: the virtual impactor and the aerosol deposition can be described as inertial impactions. All inertial impactors operate on the same principle, as shown in Fig. 5-14, where an aerosol is passed through a nozzle and the output stream (jet) directed against a flat plate, called the impaction plate. The gas flow represented by the stream lines is deflected by the impaction plate and is bent by 90°. Larger particles, i.e. particles with a large inertia momentum, are unable to follow the streamlines and collide (impact) on the plate, whereas small particles (with small inertia momentum) can follow the streamlines and remain airborne and flow out of the impactor. In the case of the virtual impactor, the impaction plate is replaced by a jet, which collects and separates the larger particles from the smaller particles and the major gas flow (see Fig. 5-4). The remaining larger particles at this point have the right size distribution for the next impactor, the deposition on a substrate. Here they are supposed to be deposited in a possible straight motion.

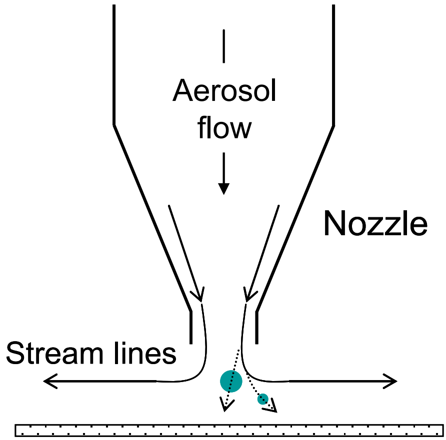

Fig. 5-14: Schematic drawing of an inertial impactor.

The trajectory at the nozzle orifice is determined by the particle/droplet size. Large particles with a large inertial momentum and a high Stokes number (>>1) tend to maintain a straight line from the nozzle opening to the substrate. Particles with a low Stokes number predominately follow the gas stream lines. Instead of impacting on the substrate they follow the shear flow tangent to the substrate. As a virtual impactor is used right before the deposition, all droplets should be in the right range for being deposited; however, it can happen that the droplets change their diameter. The critical lower limit in droplet size <0.5 µm can be reached, if particles are used which are smaller than 0.5 µm together with volatile solvents. If the droplets dry during printing, the initial nano-sized particles determine the deposition quality. To avoid the contamination of air with metal aerosols, non-volatile solvents like glycol ether are used for the ink preparation.

In conclusion, the deposition of well-defined fine lines on silicon solar cells is possible, if droplet size is in the right range; around 1 µm. For an efficient atomization, the particles should be as small as possible, and a non-volatile solvent is required to avoid both the drying of the ink inside the atomizer jar and the drying of the droplets on their way from the atomizer towards the deposition head.

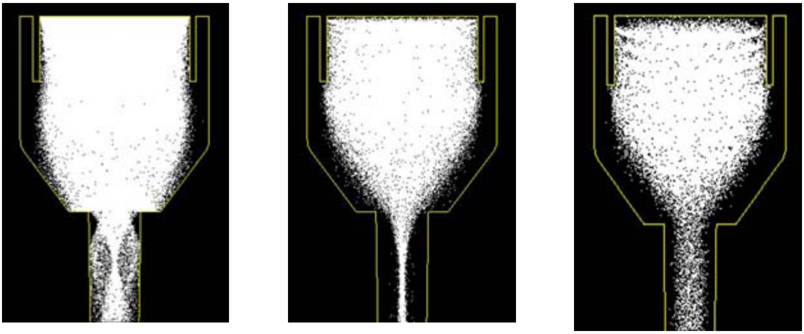

Fig. 5-15: Simulation of aerosol flow inside the deposition head for different particle sizes. Monodisperse spherical steel particles were assumed for the simulation with a diameter of a) 5 µm, b) 1 µm, c) 0.1 µm.

5.2.2 Viscosity and throughput

The viscosity predominately determines the amount of ink which is atomized and therefore deposited on the substrate. The viscosity is only of interest for atomization, and for the definition of the deposited line. In general, the lower the viscosity, the more ink is deposited and the higher can be the printing speed.

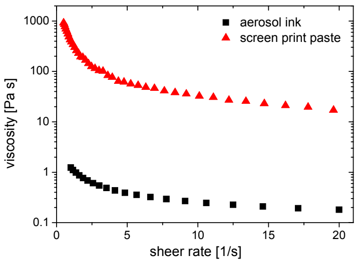

Fig. 5-16: Viscosities, for a screen print paste and an aerosol ink, measured with a rheometer from Malvin instruments CVO 010 using a 60 mm cone with an angle of 2°.

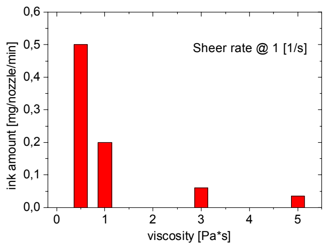

Fig. 5-17: Throughput, dependent on the ink viscosity.

It is difficult to determine a limit for the viscosity, as the atomization is also dependent on the rheology. Ideally the inks should behave Newtonian or sheer thinning. For these liquids the viscosity should be below 1 Pas, better <0.5 Pas at small sheer rates <10 s^{-1}, measured with a rheometer with cone-plate geometry.

The deposited amount of ink is given by the throughput of dry material and has the unit [mg/nozzle/min]. It is strongly dependent on the ink viscosity, as shown in Fig. 5-17. All ink parameters related to the ink, like throughput or ink density, are determined for the deposited and dried ink, as only the solid ink components are of interest for the contact formation. The solid load of inks is not constant and can vary during the deposition. The ink amount is determined by measuring the ink mass after printing on a glass plate for a defined period of time. The ink on the glass plate is dried at a temperature of about T=250°C for 5 min. In addition to the throughput of wet and dry material the solid load of the ink is known. From the dry throughput, the ink density per area ρ_A with the unit [g/m²] can be determined from the line width and printing speed. The minimum amount of ink per area (the ink density) has to be experimentally defined for each contact ink by printing at different speeds or by multiple path printing. As soon as the required ink density is known, the printing speed can be adjusted according to the throughput. The throughput is a strongly ink-related parameter, whereas the ink density is more dependent on the printer settings.

$$\rho_A = \frac{\phi_d}{w_c \times v} \qquad \textit{5-3}$$

where ϕ_d is the dry throughput, w the line width and v the printing speed.

For example, if a new ink is tested, the maximum throughput for a stable aerosol printing process is measured. In the next step, the necessary ink density is determined by multiple layer printing and finally the optimum or maximum printing speed is defined. There are inks which require a density less than 3 g/m² (see chapter 9), but there are also inks where 6 g/m² is still too little. In Fig. 5-18 an area is marked for different, successfully tested ink densities. The results are based on experimental data from more than 30 tested inks. The ink densities in this graph are calculated based on a printing speed of 100 mm/s, as it is required for an industrial production. By changing the line width, the necessary throughput can be drastically reduced. The highest throughput measured at ISE was 1.0 mg/min for an ink which demands an ink density of about 6 g/m². According to Fig. 5-19, the printing speed for this ink is limited to 50 mm/s. With a proper ink, printing speeds of 100 mm/s and more are possible.

The maximum printing speed can be assumed as follows:

For example, the necessary ink density is set at ρ_A=4 g/m² and the line width at w_c=50 µm. To get the maximum possible printing speed, we need to calculate the theoretically possible throughput. Therefore, the volume of aerosol passing through a nozzle is calculated (ϕ_{aero}) as well as the density of the aerosol (ρ_{aero}) and multiplied with each other.

$$\phi_d = \phi_{aero} * \rho_{aere} = \left(\frac{d_{jet}}{2}\right)^2 \pi v_{gas} * n_{drp} \frac{4}{3}\left(\frac{d_{drp}}{2}\right)^3 \pi \rho_{ink} \qquad \text{5-4}$$

with $v_{gas} = \dfrac{\phi_{gas}}{\left(\dfrac{d_{noz}}{2}\right)^2 \pi}$

The diameter of the aerosol jet inside a 200 µm wide nozzle is assumed to be d_{jet}=10 µm. The gas flow rates for the 200 µm nozzle are set at 100 ml/min (sheath gas) and 25 ml/min for the aerosol gas, which gives a total gas flow of ϕ_{gas}=125 ml/min. With the nozzle opening, the gas speed can be calculated as v_{gas}=66 m/s. The aerosol jet d_{jet}=10 µm can transport a volume of ϕ_{aera}=0.3 ml/min. The aerosol density can be calculated with the droplet density ρ_{drp}=10^{10} cm^{-3}. The droplet diameter d_{drp}=1 µm and the ink density ρ_{ink}=2.3 g/ml and gives a value of ρ_{aero}=12 mg/cm^{-3}. If we now multiply the aerosol density of 12 mg/cm^{-3} by the aerosol volume of 0.3 cm^{-3}/min, we get the desired ink throughput of ϕ_d=3.7 mg/min. The ink has a solid content of about 60m%, therefore the throughput is reduced to the dry throughput of 2.2 mg/min. With the desired ink density of 4 g/m², the line width of w_c=50 µm, and the calculated throughput of 2.2 mg/min, the theoretically possible printing speed is v_{print}=180 mm/s.

The uncertainties in this calculation are the aerosol density, and especially the aerosol jet diameter and the droplet size. In theory, a printing speed of above 100 mm/s should be possible.

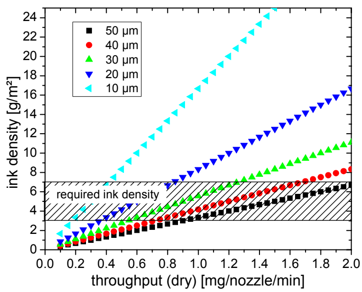

Fig. 5-18: Calculated ink density plotted versus throughput for different line widths, deposited at v=100 mm/s. The hatched area marks a confidence band, within a contact formation is possible.

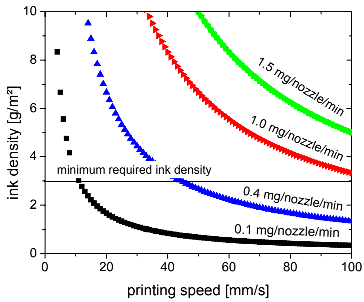

Fig. 5-19: Ink density plotted versus printing speed for different throughputs. The line width was kept constant at 50 µm.

5.2.3 Ink preparation

The aerosol inks used for this study are mixed according to the properties determined above. The main components of a metal ink for a contact formation on silicon solar cells in a fast firing step are silver, which acts as a contact and conductive metal, a glass frit, which promotes the contact formation and improves the adhesion, and/or a low melting oxide, such as lead oxide or bismuth oxide, which can substitute the glass. The advantages or disadvantages of using the pure oxide or a glass frit are described later in chapter 8. Besides the inorganic ingredients the ink contains: organic solvents, dispersant agent, and eventually additives to adjust the rheology. The size distribution of all used solids should be below 1 µm. Small particles can in general be produced in two ways (see Fig. 5-20): In a so-called top-down method or in a bottom-up method. The first one means the mechanical grinding of large particles until the required size distribution is achieved, and the bottom-up method describes the wet chemical formation of solids from solutions.

The contact promoter, lead oxide or bismuth oxide, was either added directly to the ink or in the form of a glass frit. The pure oxides were purchased whereas the glass was manufactured. The mixture of oxides is filled in an alumina crucible heated in a furnace to 1000°C (above the melting point of lead oxide or bismuth oxide). The reactive oxide melt solves the further metal oxides, silicon dioxide and boron oxide, and a glass is formed. The hot liquid glass is poured into cold water and fritted. The solid glass frit of about 1 mm in size is grinded in a ball mill down to a particle size distribution of a $d_{90}<1$ µm. The milling of particles in the sub-micrometer range is not easy and often agglomerates are formed. We used a zircon oxide jar, 1-3 mm ZrO balls and milled the glass in a dispersion of glycol ether, the same solvent as used for the ink fabrication, to minimize the agglomeration. Milling times of about 4 hours are necessary to achieve the desired size distribution.

Small metal particles, e.g. silver from a few nanometers up to around 1 µm can be produced wet-chemically with bottom-up methods [97]. These syntheses are either based on the precipitation of metal particles from a metal salt solution using reducing agents, or on electrochemical pathways or the controlled decomposition of metastable organometallic compounds. Quite well-defined nano-sized crystallites can be formed by the use of reverse micelles [98]. The chemical reduction of transition metal salts in the presence of stabilizing agents to generate metal colloids in aqueous or organic media, was first published in 1857 by Faraday [99]. The formed nano-sized particles and colloids can be protected from agglomeration by two methods:, electrostatic stabilization and steric stabilization [100]. The electrostatic stabilization is based on the Coulombic repulsion between the particles, caused by the electrical double layer formed by ions adsorbed at the particle surface. The electrostatic stabilization is effective in media with high dielectric constants like water. In our ink, the steric stabilization is more effective. It is achieved by the coordination of sterically demanding organic molecules that act as protective shields on the metallic surface. This way, nano-metallic cores are separated from each other and agglomeration is prevented. Silver particles, sterically stabilized in the size range of 0.1-1 µm, as required for aerosol printing, were produced in a method described by Velinkov [101]. The metal source, silver nitrate ($AgNO_3$), was solved in water and added to a variable amount of stock solution of gum arabic (stabilizer). The reducing agent citric acid was also solved in water and added to a solution of gum arabic. Under vigorous stirring, the silver solution was quickly added to the acid solution. As a result of the size-dependent extinction of the silver particles, the colour of the solution turned from transparent to black and then to dark brown-gray as the scattering contribution increased. The size of the particles can be controlled by changing the amounts and ratios of reaction agent, as well as by varying the pH value from the acid solution using NaOH. After several hours of stirring, the particles were washed with water and separated by sedimentation. Silver particles prepared by this method are shown in Fig. 5-21. In Fig. 5-22. commercially available nano-sized spheres are shown.

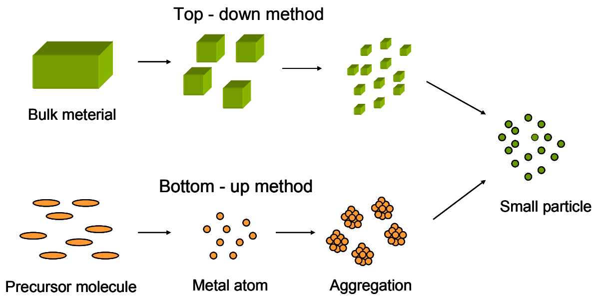

Fig. 5-20: Schematic preparation methods for small particles

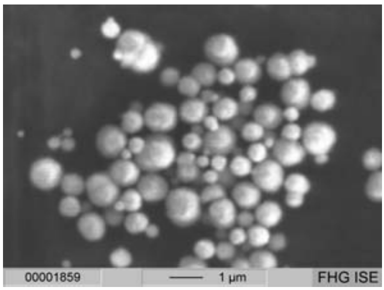

Fig. 5-21: SEM-image of small silver spheres, prepared at ISE

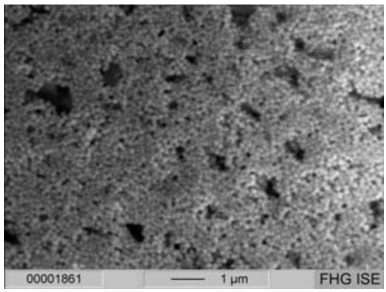

Fig. 5-22: SEM-image of almost monodisperse sub-micrometer spheres

As the amount of silver particles necessary for the fabrication of a metal ink exceeds our production capacity, we purchased silver powders in the required size range of <1 µm from Alfa Aesar and Heraeus.

The first inks were prepared using basic lab equipment like beaker glass and spatulas. The solvents were first poured in the beaker and the solids were slowly added under ultra sonic dispersion. By this method, it was possible to prepare 20-30 ml of ink, which is a sufficient amount for first aerosol printing tests. The used solvents should have a low vapor pressure, at least lower than 32 Pa, which is the vapor pressure of 1-Methyl-2-pyrrolidon, a solvent with a low viscosity and a relatively high boiling point. Other solvents used for aerosol inks are glycol ether or terpineol. In general, a low vapor pressure is important to get a constant atomization and to avoid a drying of the ink inside the atomizer. Additionally, all organic ink compounds should either evaporate during a drying step of the printed substrate at T=250°C or they should totally combust into CO_2 and H_2O during the firing step - typically at temperatures below T<600°C.

The quality of the ink can be further improved, especially by amending deagglomeration of the solid particles, which in particular is necessary for highly solid loaded inks. Therefore, we are now using dispersing tools such as a three-role mill and an ultrasonic horn. The solvents and the inorganic powders are mixed together using an agitator, or better an Ultra Turax. The viscosity of the ink at this stage is still too high, as many of the particles are still agglomerated. A low viscosity can be achieved when the ink is homogenized on a three mill chair. Finally, the remaining agglomerates are solved using an ultrasonic horn and the final ink is stirred at room temperature for 24 hours before it is used in the printing system. Now the ink preparation is more reproducible and higher quantities can be produced as well.

5.3 Chapter summary

Metal aerosol jet printing is demonstrated to be a reliable technique to create a seed layer for the front side contacts of silicon solar cells. Several parameters are determining the quality of the deposited line and the printing process itself. Next to the system settings like the ratio of aerosol flow to sheath gas flow, substrate temperature and nozzle diameter, the ink is the most important parameter for a good printing result. It has to fulfil the requirement of a contact ink for a solar cell and the requirement of the printing system. Up to now it is beneficial for the contact performance, if the ink contains solid metal particles, from which an electrical contact is formed in a firing step. For the atomization and the printing a particle free ink would be beneficial. An upper limit for the particle size used in an aerosol ink was found to be at d<0.5 µm. In general, the smaller the size distribution, the better the printing results. Additionally, it is beneficial for the atomization and the printing, if the particles are well homogenized and dispersed into a low viscous ink (η_{vis}<1 Pa s) at a low sheer rate. The more aerosol can be generated from an ink, the more ink can be deposited and the higher is the printing speed. If the well homogenized, sub-micrometer particles are dispersed in a nonvolatile solvent, and if the solid load is higher 50m% and the viscosity at low sheer rates is lower 0.5 Pas, a stable printing of well-defined lines is possible. The printed line width is above all defined by the nozzle opening, and is about 5 times smaller than the nozzle opening itself - e.g. line widths below 20 µm can be deposited using a 100 µm nozzle.

6 Light-induced plated contacts

All metal contacts studied within this work have one thing in common: they are all seed layer contacts and therefore they need to be thickened in a second metallization step. The light-induced plating (LIP) is a plating technique which is used at Fraunhofer ISE to thicken the seed contact layer and to increase the line conductivity of front contacts [8]. LIP has been used at Fraunhofer since 1992 to establish the second layer of a two-layer contact, the conductive layer, on high-efficiency p-type solar cells [102]. In a subsequent growth step, the seed layer is reinforced by means of an electrochemical deposition of a highly conductive metal (e.g. silver, copper). The light-induced plating utilizes the photovoltaic effect of the solar cell for the metal deposition on the front side contact. The cell is immersed into the electrolytic plating bath and irradiated at the front side, which leads to a very homogeneous current density in the front side grid. Only the rear side of the cell has to be contacted and connected to a metal-anode, which is much easier than individually contacting the fine front side lines. This simplifies the process considerably – and the plating technique could be transferred from the laboratory into industry. In 2005 an in-line plating machine was developed in cooperation with, an equipment fabricator (Schmid GmbH) and a chemical supplier (Rohm & Haas). The main difference between the in-line LIP and the LIP equipment applied for lab-type solar cells is the electrolyte used. It can be distinguished between two types of electrolyte solutions, a cyanide bath and a cyanide-free bath. In order to minimize the health risk, the cyanide-free baths are favorable for an industrial application. However, until recently the best plating results, in homogeneity and especially in line conductivity, could only be achieved using the cyanide bath. During this work, two different cyanide-free plating solutions were tested and the results on large area mc-Si solar cells are compared with the results achieved using a cyanide bath. The difference in cell performance weather a cyanidic or a cyanide free plating solution is used, can be neglected especially for new electrolytes. The line conductivity for all three baths is measured and the differences are explained using SEM images. Additionally, the total loss of a solar cell that is induced by the front side grid is simulated for different line conductivities and the optimum is determined. Finally, large area (15.6x15.6 cm²) mc-Si solar cells were produced and gradually plated, using cyanide and a cyanide-free bath. The measured IV-parameters are discussed in detail.

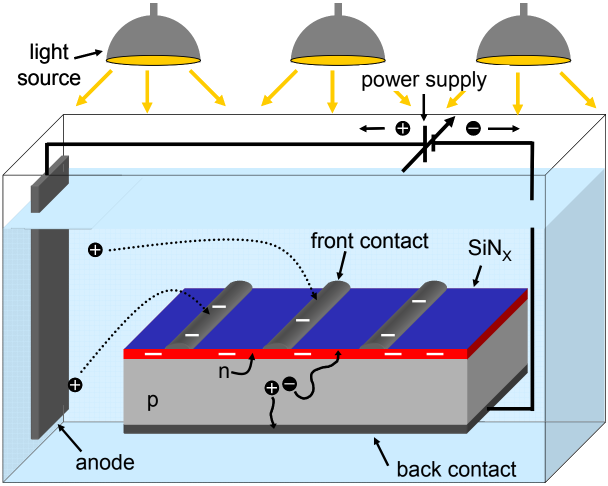

Fig. 6-1: Schematic drawing of the LIP process. The positively charged metal cations are deposited onto the negative n-doped front surface (cathode), induced by the photovoltaic effect under illumination [8].

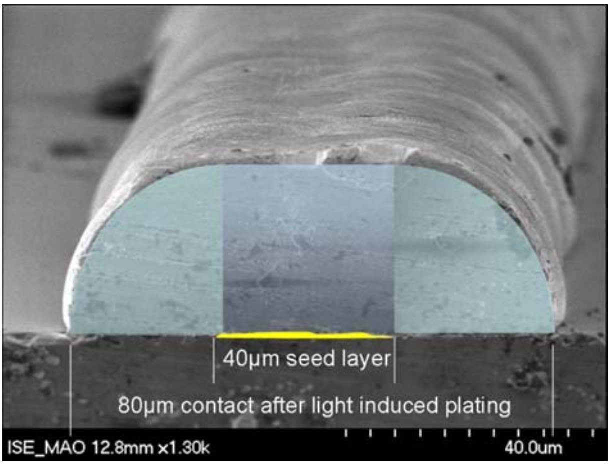

Fig. 6-2: Cross section of an aerosol printed and light induced plated contact. The contact width increases during plating by two times the plating height. The seed layer as well as the geometric structures used to describe the contact is highlighted.

6.1 Working principle

The solar cell, as a photovoltaic device, generates electrons under illumination. This effect is directly used in a light-induced plating process. In the case of a *p-type* solar cell with an n-doped emitter, the solar cell surface is negatively charged under illumination and the positively charged silver ions are attracted by the solar cell front side potential and deposited along the metal fingers, see Fig. 1-1. The insulating antireflection layer therefore acts as a mask, while the seed layer contact acts as the cathode. Silver is therefore locally deposited to form the front contact grid. In order to close the current circuit, the rear side of the cell is electrically connected with the silver anode. Silver atoms from the anode are oxidized to Ag^+-ions; the cations are transported by the electrolyte towards the solar cell surface, where they are reduced to silver by photo-generated electrons. The driving force is the electrochemical potential between the Ag-anode and the cell surface (cathode). In total, three potentials have to be considered: the potential of the anode, of the front and the rear side of the solar cell. The plating condition can be controlled primarily by two parameters; by an external voltage applied at the rear side, and the light intensity, which controls the potential at the front side. For a deposition with an optimum current flow from the anode to the cathode (I_{LIP}), the potentials have to be adjusted, so that the voltage drop between rear side and anode is slightly above half the voltage drop between anode and front side [25]. In this case, silver is oxidized at the anode, at the cell rear side (along the silver pads) it is both oxidized and reduced, and at the front side it is reduced. At the rear side, the dissolution and deposition of silver is balanced and at the front side, silver is only deposited. The current density, which is equal to the number of silver ions deposited per unit area, determines the morphology and the plating quality – with high current densities resulting in a fast, however often inhomogeneous deposition [103]. Therefore it has to be adjusted by limiting the current I_{LIP}. For a cyanide bath, an optimum current density of j_{LIP}=1.1A/dm² was determined by Mette [25]. The current I_{LIP} can be calculated by:

$$I_{LIP} = j_{LIP} \cdot A_{metal\_area} \qquad \text{6-3}$$

where A_{metal_area} is the area of the front side grid (size of the cathode).

Further parameters which influence the plating quality are the pH-value and the temperature of the plating bath; both are defined by the used electrolyte and the used complex agent respectively. The complex agent is responsible for stabilizing the oxidized silver ions in the electrolyte bath and to avoid their precipitation. At the same time, the complex agent influences the reduction of the silver ions and therefore the deposition in terms of morphology, deposition rate, and finally line conductivity. Although the silver deposition from a cyanide (complexing ion) bath runs produces the best results so far, the toxicity is a big disadvantage. Understanding the mechanism behind the deposition and finding adequate replacements for the cyanide bath are subjects of current research [103]. Meanwhile, several cyanide-free plating baths are commercially available. Their influence on the contact quality, even if deposited under optimum conditions, can be seen in Fig. 6-5. The resulting line conductivity and the influence of the line conductivity on the cell parameters are studied below.

6.2 Simulation

The respective influences of the line conductivity or resistivity on the total loss of a solar cell can be simulated. Total loss means the combination of series resistance losses and shading losses caused by the front contact grid. The individual loss mechanism can be found in chapter 3, and an extensive overview, including all equations and further simulations is given by Mette [25]. The contact structure used for the simulation is shown in Fig. 6-2. The contact cross section is simplified to a square with the width of the seed layer, and two half circles with a radius equal to the contact height. Assumed is a growth of 1:2 (height:width), which means the contact grows one unit in height and simultaneously two units in width. The simulation, shown in Fig. 6-3 was performed for an infinitely thin and 30 µm wide seed layer with a resistivity of ρ_c=1 mΩcm² on an emitter with the sheet resistance R_{SH}=60 /sq. The simulated grid has 80 fingers and 3 bus bars (1.5 mm each) on a 15.6 cm x 15.6 cm mc-Si solar cell. The total loss is plotted as a function of contact width (seed width + plating) and plating height (left) and as a function of the contact distance (right). Additionally, the calculated minimum between optical losses and electrical losses is marked. At small plating heights, the total loss p_{tot} is dominated by electrical losses and is strongly dependent on the amount of deposited silver. At large plating heights the loss mechanism is dominated by optical losses, due to an increased line width. The total loss curve is not symmetric, i.e. beyond the optimal plating height the dependence of the total loss is higher at smaller finger heights. Thus, concerning the total cell loss, it is more favorable to plate too much silver than too little. The solar cell efficiency is very stable over a broad range of plated silver mass (see below). High line conductivity of the plated silver, or in general of the front contacts, is beneficial in two ways: the total losses were diminished, and the amount of required silver is smaller. For example, if the line resistivity is reduced from $\rho_f = 3\times10^{-8}$ Ωm, which is a reasonable value for a standard screen-printed contact, to $\rho_f = 1.9\times10^{-8}$ Ωm, which is a good value for plated silver, the optimum line height can be reduced from 14 µm to 11 µm, which is a reduction of 21%, the line width shrinks by 10%, and the cross section from 730 µm² to 520 µm². As the cross section is nearly directly proportional to the amount of plated silver, 28% less silver is consumed and at the same time p_{tot} is reduced by approximately half percent. Compared to the plating height, the finger spacing (distance) is hardly dependent on the line resistivity. While the line resistivity is reduced by more than 100%, the finger distance only varies in a range of 5% (0.1 mm). The line distance is therefore negligible for the calculation of the optimum plating height. Parameters that have a strong influence on the line distance are the resistivity of the metal-semiconductor contact, the emitter sheet resistance and the seed layer width. Appropriate simulations for the line distance can be found by Mette [25] or in chapter 11.

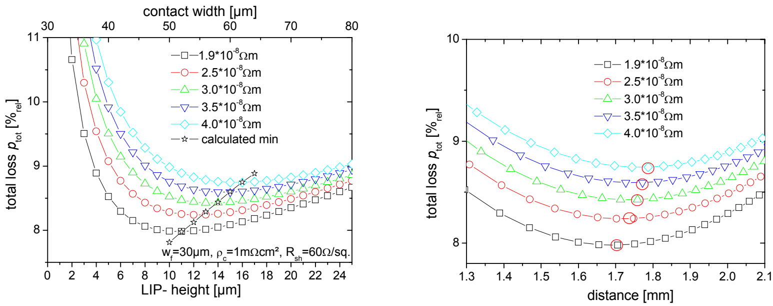

Fig. 6-3: Simulation of the optimum plating height for a specific seed layer. The total loss as a function of plating height and different line resistivities is plotted (left) and as a function of line distance for different line resistivities (right).

6.3 Structure and conductivity

The line resistivity of aerosol-printed and subsequent light-induced plated fingers is shown in Fig. 6-4. The aerosol seed layer is thin enough (<1 µm) and its contribution to the resistivity is negligible, as the plated silver has a height of 15 µm. The growth mechanism and the morphology of the LIP-silver depend, among other factors, on the used electrolytes. Three different plating solutions were tested, one cyanidic and two non-cyanidic electrolytes. The plating parameters, such as light intensity, applied potential, pH-value, and temperature were kept in an optimized range for each electrolyte. The strong influence of the used electrolyte on the line resistivity can be explained by SEM-images (see Fig. 6-5). Also, the influence of an annealing step becomes clear. Both the macroscopic shape of the plated finger and the microcrystalinity are influenced by the different electrolytes. The silver layer deposited from the NCN1-electrolyte shows a botryoidal morphology. The several clusters can reach the value of the height of the finger, thus, more than 10 µm in diameter. The clusters, although very fine grained, can be distinguished. As the resistivity is determined by the smallest cross section, the current flow is mainly limited by these deep incisions. For the measurement of the resistivity we determined an average cross section and the botryoidal structure is levelled. Assuming that the resistivity of a single cluster is high and in the range of bulk silver, due to the rough morphology and the cluster boundaries, the line resistivity is limited, even if the contact losses across the cluster boundaries can be reduced by annealing. Thus, a large fraction of plated silver does not contribute to the current flow.

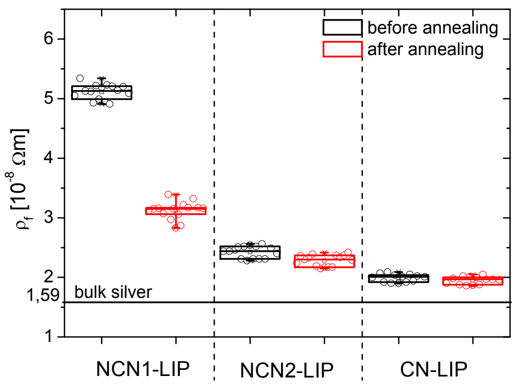

Fig. 6-4: Line resistivity for three different plating baths, two non-cyanide and one cyanide bath, before and after an annealing step of 10 min at T=350°C.

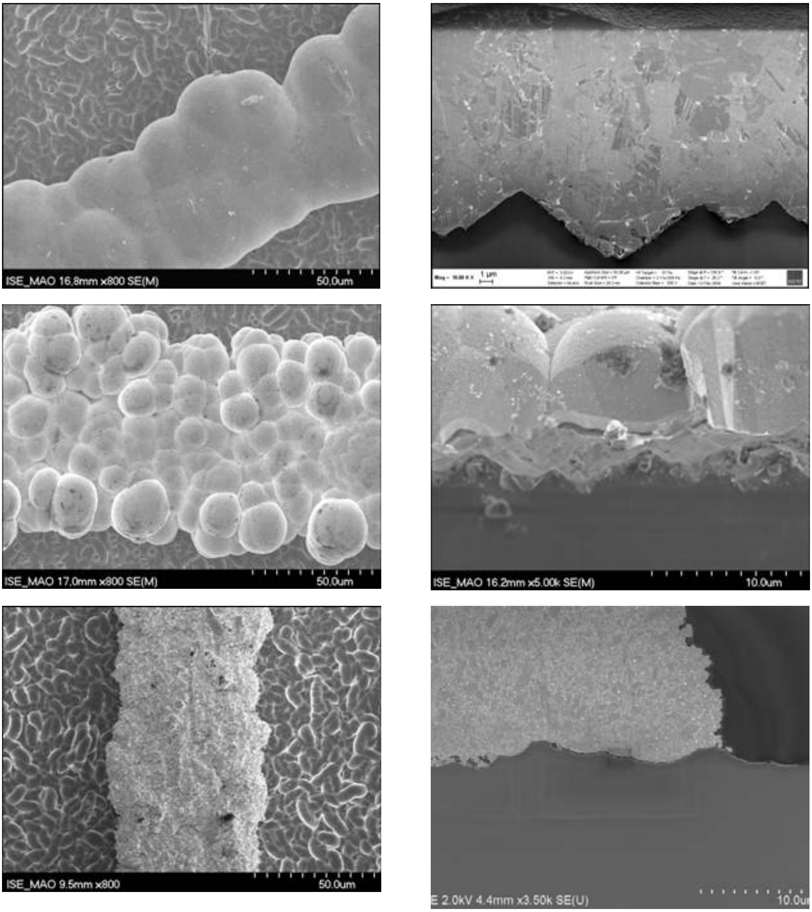

Fig. 6-5: SEM images of contact fingers, plated in different electrolyte solutions, from top to bottom: CN, NCN1, NCN2. The left column shows a top view of the contacts and the right column close-up views.

In case of the NCN2-solution, the several Ag-clusters are pyramidal or trigonal to some extent. They are much smaller, below 1 µm and deep incisions which would reduce the cross section and the measured resistivity are not visible. The LIP-silver grows homogeneously at the surface at the ratio of 1:2 (height:width), resulting in a roundish-shaped contact. The surface roughness is determined by the small Ag-clusters and almost all the plated silver contributes to the current flow. The measured resistivity of $\rho_f = 2.2\times10^{-8}$ Ωm can only slightly be improved by an annealing step, indicating the dense silver deposition and the excellent conductivity between the single Ag-grains.

The best values for line resistivity can be achieved with the cyanidic electrolyte. The measured average value of $\rho_f = 1.9\times10^{-8}$ Ωm is already close to the resistivity of bulk silver ($\rho_f = 1.59\times10^{-8}$ Ωm). The surface is smooth, i.e. Ag-clusters can no longer be distinguished. The structure would possibly reveal single Ag-grains in a SEM-image of a polished cross section. The grain boundaries between the grains are hardly visible, and an influence of an annealing step on the resistivity is barely measureable. However, further investigations have to be performed to reveal the correlation between layer structure (on different scales) and electrical properties.

In conclusion, the cyanidic plating solution is the best choice in terms of electrical and optical properties. Also the process stability is much higher for cyanidic electrolytes. However, the health risks in industrial production have to be taken into account. A good alternative to the cyanidic electrolyte is the plating solution NCN2, which results in a line resistivity close to that of cyanidic plating.

6.4 Solar cell results for differently plated cells

The simulation in Fig. 1.3 illustrates the importance of the line resistivity of plated silver. In order to study the influence of the line resistivity on the IV-parameters of a real solar cell, mc-Si solar cells were processed up to the front side metallization. The front side of the 15.6 cm x 15.6 cm mc-Si solar cells were aerosol-printed and fired, and then the contacts were successively plated in two different LIP-solutions. The CN and the NCN1 plating solutions are used as they showed the largest difference in line resistivity, see above. The front contact grid consists of 80 fingers and 2 bus bars, each 2 mm in width. The cell IV-parameters were measured and the fill factor (*FF*), as well as the series resistance (R_s), in dependence on the mass of LIP-silver is shown in Fig. 6-6. A continuous increase of the *FF* with the mass of plated silver was observed, together with a steady decrease in R_s. In the case of the CN solution the *FF* reached its saturation at a silver mass of approximately 100 mg per wafer, whereas similar *FFs* were reached for the NCN1 solution at about 130 mg. The line resistance is continuously reduced with the quantity of deposited LIP silver and both the values for R_s and for the *FF* are improved. When a LIP-silver mass of about 200 mg is exceeded, an improvement for both electrolytes was hardly measureable and the *FFs* were constant in the tested range.

The short-circuit current density (j_{sc}) is quite sensitive to the mass of plated silver and decreases linearly with the deposited silver amount (see Fig. 6-7). For both plating-solutions a slope of about -1.6 (mA/cm^2)/g was observed. From the measured current densities, $j_{\mathrm{sc\_ini}}$ (after a short LIP-dip, the seed layer became conductive without a significant increase in line width), and $j_{\mathrm{sc\_LIP}}$ (after final LIP), an effective finger width (w_{eff}) can be calculated. If the area of the seed layer metallization is known (A_{active_ini}), the initial non-metalized area (A_{active_cell}) and the corresponding *optically effective* metalized area for the grid fingers (A_{fi_eff}) for all values of j_{sc} can be determined and transferred into an effective finger width. It is well known that the optical effective width of a contact finger can be considerably smaller than its geometrical width [104, 105].

$$w_{eff} = \frac{A_{fi\_effi}}{l_{fi} \times n_{fi}} \qquad \textit{6-1}$$

with $$A_{fi\_eff} = A_{tot\_cell} - A_{active\_cell} - A_{BB}$$

and $$A_{active\_cell} = \frac{j_{sc\_ini}}{j_{sc\_LIP}} \times A_{active\_ini}$$

In Fig. 6-7 the calculated *effective* finger width for the NCN1-LIP is shown. The real finger width, determined from a microscopic picture, for a contact plated with 360 mg NCN1-LIP is about w=100 µm. Its effective width determined from the current density is about w_{eff}=87 µm, which is a reduction of 13%. This reduction will be even greater if the cells are encapsulated into a module, due to the internal reflection at the glass-air interface [105].

The effective width for CN-LIP contacts is even smaller and the average j_{sc}-values for the CN-LIP are about 0.2 mA/cm^2 above the average current density of the NCN1-LIP, even if they are built up with the same amount of LIP-silver. The 0.2 mA higher j_{sc} values in case of CN-LIP can be translated into a reduction in effective contact width by 10 µm. However, an increased cell efficiency of the CN-LIP cells over the NCN1-LIP could not be observed within reasonable statistics by this experiment as the number of tested cells was limited. The cell efficiency reaches its maximum at about

200 mg for both solutions. Passing this point, the gain in efficiency due to an increasing FF is compensated by the steady decrease in j_{sc}. The cell efficiency is constant over a broad range and starts to decrease due to the growing shading losses at LIP quantities of 350 mg for CN-LIP and 450 mg for NCN1-LIP respectively. As expected from the simulation, the cell efficiency is quite resistant to high quantities of LIP silver.

In a further experiment with more than 20 wafers per LIP-solution, an increase in the cell efficiency of $\Delta\eta$=0.1-0.2% absolute was found, if the cells are plated in a CN-LIP instead of using the NCN1-LIP; for the NCN2-LIP the difference in cell efficiency is negligible.

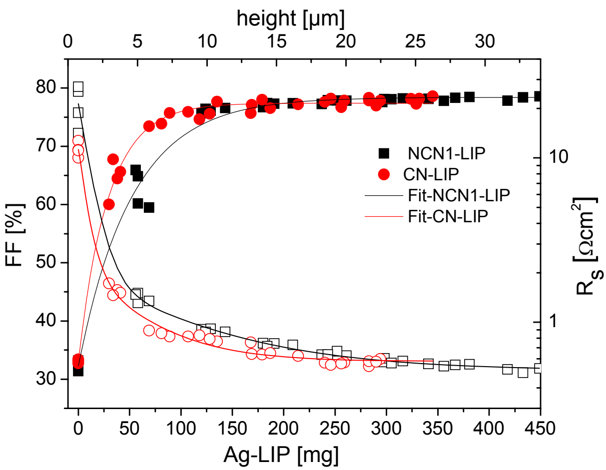

Fig. 6-6: Fill factor (FF) and series resistance (R_s) as a function of the amount of plated silver for both NCN and CN plating solutions.

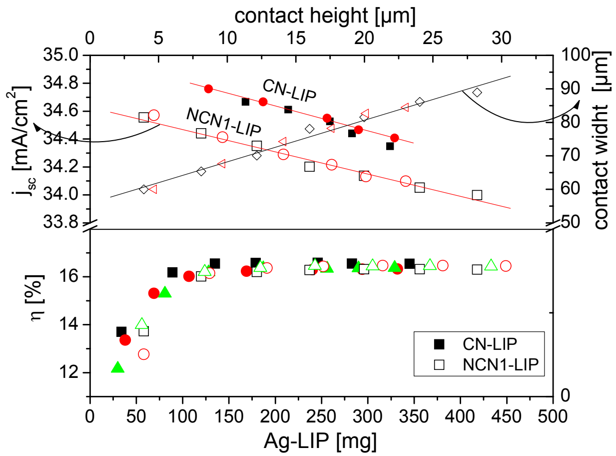

Fig. 6-7: Current density j_{sc} and cell efficiency η as a function of LIP silver mass and contact height from the constant decrease in j_{sc}, an effective contact width is calculated.

6.5 Chapter summary

The thickening of a seed contact is necessary and the used light-induced plating is a quite elegant way to create the conductive layer. The LIP-plating has two advantages: The working principle is quite simple, in that the current generating function of a solar cell is used to build up the front contact grid; therefore it is sufficient to contact the cell only at the rear side. Second, an operating in-line machine is commercially available. Within this chapter, the quality of different plating solutions in terms of electrical contact performance is studied. Different specific line resistivities, from close to bulk silver for contacts plated in a cyanide bath (ρ_f=1.9×10^{-8} Ωm) up to resistivities comparable to screen-printed contacts (NCN1-LIP, ρ_f =3.2×10^{-8} Ωm) were found. The optimum mass of LIP-silver necessary to metalize a solar cell is determined theoretically by simulating the losses of a solar cell that are caused by a front side grid for different line conductivities. A line resistivity of ρ_f =1.9×10^{-8} Ωm compared to ρ_f =3.0×10^{-8} Ωm saves almost 30% of consumed silver. In addition, measuring the short-circuit current of successively plated solar cells as a function of plated silver mass, the effective optical finger width is determined to be about 13% smaller than the geometrical contact width. Finally, the amount of deposited silver was experimentally varied and cell efficiencies over 16% were achieved on large area mc-Si solar cells.

7 Contact formation – Chemical reactions

Before an ink can be designed, the basic reaction of the ink components and the solar cell needs to be understood. The front contact ink typically consists of several components of which each has a special function. The metal, silver, acts as a contact and a conductive material and the glass frit or the metal oxides as a reaction and adhesion promoter. The presence of at least 4 different materials and the relatively short time frame for the contact formation are responsible for the complexity of the process. Within this chapter, the principal chemical reactions, important for the contact formation are clarified. The single ink components are systematically reacted with silicon under controlled condition. The contact firing is therefore simulated using thermal gravimetric - differential thermo analysis (TG-DTA) in combination with mass spectroscopy (MS). From this measurement, the reaction character, endothermic or exothermic, the reaction process, redox reaction or melting, the reaction temperature and the reaction products are studied to reveal the secret of high temperature contact formation. The achieved knowledge is used to interpret the contact formation and to explain some fundamental aspects of contact firing, like the opening of the ARC layer, the etching of silicon and the contact firing under different atmospheres.

Fig. 7-1: Illustrative figure of a silver ink; the image is part of a colored window at the gothic cathedral in Freiburg and shows a miner in the Schauinsland silver mine. Silver and lead is refined from the ore galenite. The material of the window itself is leaded glass. Both the silver and the leaded glass are the main components of a front contact ink.

Fig. 7-1 is an illustrative figure of a silver ink as it shows all important materials used in a front side silver ink. A silver mine worker mines the ore galenite from which silver and lead, both important materials for a contact ink, are gained, and the material, the glass itself, is made of leaded silica glass as it is used for a glass frit. The investigated materials are silver, leaded glass and lead oxide, as they are the main components of the silver front side ink, and silicon and silicon nitride/oxide, which are the solar cell materials. To study the reaction between the single reaction agents, all materials are purchased or milled in powder form. The powdered material as it is experimentally used is shown in Fig. 7-2. The silver was purchased form Alfa Aesar and from Heraeus and has a particle size distribution below 1 µm. The melting point of bulk silver is T=960°C. The melting point can be significantly reduced if the particle size is reduced to nanoscopic dimensions [106]; however, the particles used in our experiment are still too large to reduce the melting point. The silicon powder and the glass frit were prepared in a ball mill. The source for the silicon powder was originally a silicon wafer. The silicon wafer was roughly crushed in a mortar and finally milled to a powder using a ball mill. For the reaction with silicon nitride, silicon powder was sputtered with a 1 µm thick amorphous layer of SiN_x as it is used as a passivation layer on solar cells [107, 108].

Fig. 7-2: material powders as they are used to study the reaction mechanism in a TG-DTA experiment. From left to the right, silver powder, silicon powder and glass powder.

The glass was produced in a furnace from the single oxides SiO_2, PbO, and B_2O_3 at a temperature of 1000°C. At higher temperatures, the glass melts and becomes a clear low viscous liquid. The liquid glass was poured in cold water in order to cool the glass and form millimeter-sized solid glass frits. The fritted glass was then milled in a ball mill to reduce the particle size below d_{90}<1 µm. The silicon oxide determines the glass matrix in which lead and boron are incorporated. The glass formation and the glass structure was first studied by Goldschmidt [109] and Zachariasen [110]. The silicon dioxide forms a three-dimensional glass network which consists of randomly edge connected SiO_4-tetrahedra. SiO_2 is a so-called glass former. Other oxides able to form a glassy network are e.g. GeO_2, P_2O_5, Na_2O, K_2O or CaO. Technical glasses can contain a large amount of basic oxides, so-called glass modifiers which break up the glass structure and separate the tetrahedrons from each other and determine the properties of the glass. The melting point can be reduced from about 1500°C for pure SiO_2-glass to 400°C-800°C. Typical modifiers are Na_2O, MgO, CaO, BaO or K_2O. A detailed overview of the glass chemistry and structure in general is given by Rao [111] and Krebs [112], and more specific for leaded glass as it is used here, by Rabinovich [113]. Lead oxide as it is used in the glass frit can act as a network modifier as well as a network former, depending on the concentration [112]. Also, the conductivity of the glass is influenced by the lead oxide content [114]. In our example, glass, the network is built up by SiO_2 and B_2O_3, whereas PbO is used as both modifier and former, as the concentration is high enough. In general, high amounts of PbO can be solved in the glass systems, e.g. 67 mol% with SiO_2 or even 77 mol% with B_2O_3 [115]. The glass we used contains 61 mol% PbO, 27 mol%, SiO_2, and 12 mol% B_2O_3. The used glass composition is given in Table 7-1. The glass transition temperature is at about 500°C-600°C. High amounts of lead or lead oxide are necessary as it is the key material for the contact formation; therefore the fraction of lead in the glass is as high as possible. The boron oxide is used to define the glass transition temperature and the viscosity, and to increase the chemical stability.

glass	Si [at%]	Pb [at%]	O [at%]	Ag [at%]	B [at%]
Original	10	24	57	-	9
EDX1	36.5	8.3	55	0.2	-
EDX2	25.5	12.9	61.3	0.3	-

Table 7-1 Original glass composition in at% in comparison to the glass composition after the redox reaction.

Material	Melting point [°C]	Eutectic temp. [°C]	properties	ref
Ag	961	(Ag-Si) 937	Contact metal	[116, 117]
PbO	884	(Ag-PbO) 825		[118]
Bi_2O_3	824			[116]
Pb	327.5	(Pb-Ag) 300	Glass modifier	[119] [117]
Bi	271	(Bi-Ag) 250	Glass modifier	[119] [117]
Si	1410		Cell material	[119]
Si_3N_4	1900		ARC	[116]
SiO_2	1610		ARC, glass former	[118, 119]

Table 7-2: Melting points and eutectic temperatures for the used materials and compositions.

7.1 Experiments, based on lead oxide

The powders are weighted and filled in the Alumina crucible of the DTA-sample holder. The ratio and the mass of the single reaction agents are given below, where the reactions are described in detail. The temperature is determined by a thermocouple (type S). The TG-DTA measurements are carried out under inert conditions, apart from the reaction where the influence of oxygen on the contact formation is studied. The used inert gases are nitrogen with a flow rate of 70 ml/min and argon (40 ml/min). Argon is used for the experiments where the TG-DTA measurement was coupled with MS-measurements [120] in order to detect the evolving nitrogen from the reaction with SiN_x. Two different temperature programs were used. For the reaction with abundant silver, the reaction agents were heated up to T=900°C with a heating rate of 10 K/min and a cooling rate of 20 K/min. The relaxation time at the start of heating was 5 min at RT. In order to accommodate for the possible presence of silver, the peak temperature was reduced to T=830°C, below the eutectic temperature of silver and silicon of $T_{eut.}$=836°C, as the temperature at contact firing is typically below the Ag-Si eutectic. After a relaxation time of another 5 min, the reaction agents were heated at a rate of 10 K/min up to a temperature of 830°C. This temperature was kept constant for 15 min before the samples were cooled at a rate of 20 K/min to RT. The reaction products are analyzed with SEM/EDX measurements and the equation for the redox reactions between lead oxide and silicon or lead oxide and silicon nitride are given.

In a first experiment, the reaction between glass/PbO and silicon was studied in order to explain why the reactive component is lead oxide and why it is typically incorporated into a glass matrix. In a second experiment, silver was added as a third reaction agent in order to simulate the contact formation. In a third experiment the question was answered of how the antireflexion coating is opened and why it is difficult to form a low ohmic contact on a surface passivated with a thick thermal oxide. Finally, the influence of different firing atmospheres is explained and also the importance of redox reactions for the contact formation.

7.1.1 Reaction between silicon and glass frit - metal oxides

For the contact formation between silver and silicon at high temperatures just below the silver –silicon eutectic, a glass frit is needed [23, 58, 61, 62, 121, 122]. The glass frit etches through the passivation layer into the silicon surface, it promotes the silver crystallite growth and it increases the adhesion of printed silver contacts. The commonly used glass frits can consist of a variety of different metal oxides as SiO_2, Al_2O_3, MgO, Na_2O, CaO, K_2O, P_2O_5, TiO_2, Bi_2O_3, PbO, ZnO, B_2O_3…[123] [124], whereas the reactive components are lead oxide and/or Bismuth oxide [58] [60] [47]. Mertens already contacted solar cells by using the pure oxide PbO or Bi_2O_3 in combination with silver particles in a contact ink [47]. To understand the contact formation we used pure PbO and a quite simple glass frit with the composition: SiO_2, PbO and B_2O_3, as proposed by Schubert [23], see Table 7-1. Both the reactions of pure lead oxide and the reaction of the glass frit with silicon were studied. A ratio of glass/PbO:Si of 1:1 was chosen and therefore 50 mg silicon and 50 mg of lead oxide or glass frit was filled in the DTA-sample holder in the following order: silicon below, and lead oxide or glass above, similar to a printed contact on a solar cell. In Fig. 7-3, both reactions between silicon and lead oxide and silicon and glass frit can be seen. In the case of lead oxide, an abrupt exothermal reaction takes place at about 680°C. At that temperature, far below the melting point of PbO, the lead oxide reacts with silicon under the formation on lead and silicon oxide, as the SEM analysis of the reaction products reveals. For a reaction in the case of the lead glass, a distinct starting point can not be given. The reaction with the glass probably starts at about 500°C with the melting of the glass, followed by a redox reaction between the embedded lead oxide and the silicon at about 600 to 700°C. For a more detailed analysis, the glass frit is separately measured and the DTA-signal is plotted together with the glass frit-silicon signal in one diagram, see Fig. 7-4. Therefore, 70 mg glass frits are filled in the DTA-crucible and heated up twice. During the first heating, the glass frit components are still reacting with each other or the single milled frits are melting at different temperatures, visible as endothermic peaks at 350°C and 500°C. During the second heating, only a small peak at 400°C is visible, which might indicate the glass-transition temperature, and from a temperature beginning at 570°C in both heating cycles, a broad endothermic peak appears which is related to a continuous melting of the glass. If silicon is present at the first heating cycle, both signals, the pure glass signal and the glass-silicon signal have the same shape up to a temperature of T=570°C. Up to this temperature, the DTA-signal is dominated by the reactions in the glass frit itself. At higher temperatures the DTA-signal for the glass-silicon mixture is further reduced (exothermic reaction) in two steps – the glass frit reacts with silicon. It is very likely the lead oxide from the glass frit, which reacts with silicon between 570°C and 680°C.

During cooling small exothermic signals are visible for both mixtures (PbO-Si and glass-Si) at a temperature T=320°C, which can be attributed to the melting point (condensation) of lead, which was produced during the reaction. Together with the SEM analyses of the reaction products, we are able to confirm the redox reaction 7-1 as proposed by Young and Schubert [58] [23].

$$2PbO + Si \rightarrow 2Pb + SiO_2 \tag{7-1}$$

It looks like the reactive component in a contact metal paste is the glass frit, in particular the lead oxide, incorporated in a glass. Usually, a glass frit is used in contact inks instead of the pure reactive oxide. The idea to transfer the lead oxide into a glass frit, instead of using the oxide directly, has several advantages. On the one hand, the glass becomes liquid at a lower temperature than the pure oxide melts, it wets the entire contact area homogenously, and the reactive oxide or oxides are brought in close contact with the silicon, whereas on the other hand the redox reaction given in 7-1 occurs in a broad range of temperatures, making the contact formation during a fast firing step more controllable.

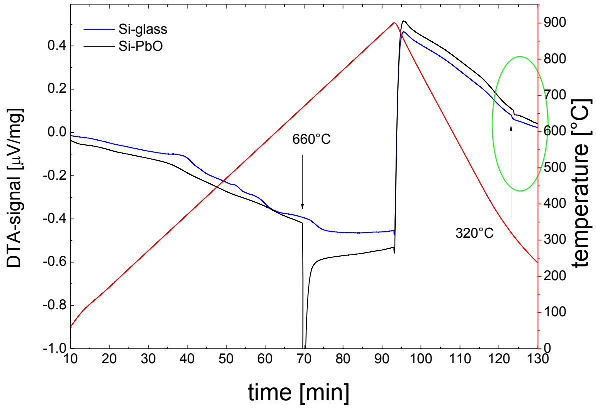

Fig. 7-3: Reaction between Si-PbO and Si-glass$_{PbO}$, The abrupt jump in the DAT-signal when the temperature changes e.g. from heating to cooling is related to the measurement and can be neglected.

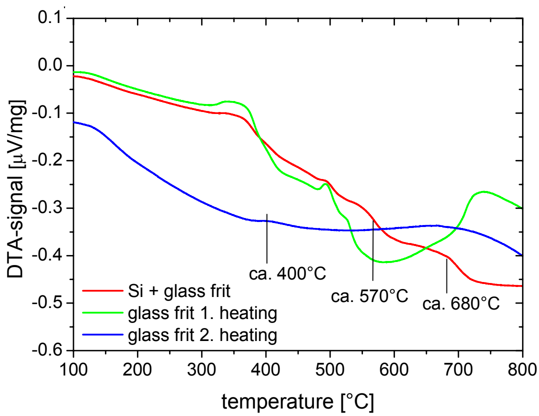

Fig. 7-4: Reactions during heating for the pure glass and in combination with silicon.

In order to verify 7-1, the reaction products were analyzed by SEM and EDX. In Fig. 7-5 and Fig. 7-6 SEM images of the reacted silicon-glass sample are shown. The reaction agents glass and silicon are sintered together and a solid ball consisting of not reacted silicon particles and spherical inclusions, which are glued together with glass, has been formed. The EDX analyses, see Fig. 7-7, confirmed exactly the mentioned redox reaction. The spherical precipitates are pure silver, which initially was not present but was produced by a reduction of lead oxide (glass frit). At the same time, silicon needs to be oxidized to silicon dioxide. The EDX analyses from the glass gives a composition of: 9.2at% (Pb), 34.2at% (Si) and 56.6at% (O). In comparison to the original composition, see Table 7-1, the lead content is reduced (originally 24at%) and at the same time the silicon content is increased (originally 10at%). The composition has changed according to the reaction 7-1.

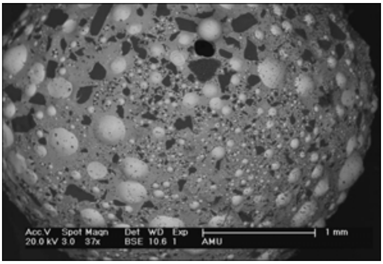

Fig. 7-5: SEM image of the crucible content. The glass frit has react with silicon.

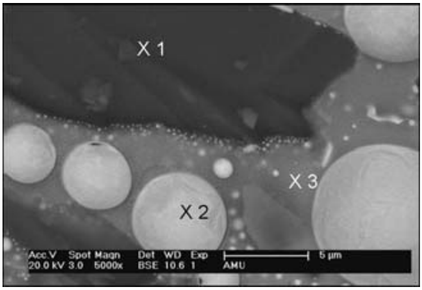

Fig. 7-6: Close up view of image Fig. 7-5. Labeled are positions where EXD was measured.

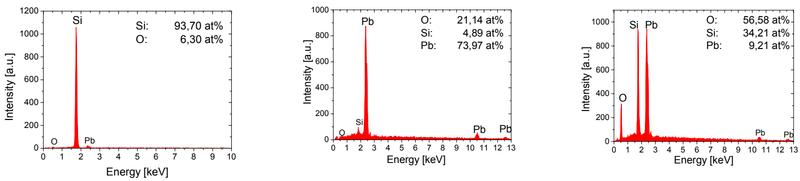

Fig. 7-7: EDX measurements from the reaction products (glass-silicon), see Fig. 7-6. From left to right: position 1(silicon), position 2(lead), position 3(Si-rich glass)

7.1.2 Reaction between silicon, metal oxides and silver

In a second experiment the reaction of a simple contact ink (lead oxide/glass + silver) with silicon was investigated. Therefore 176 mg of the milled glass frit, 49 mg silver powder, and 25 mg silicon were filled in the reaction crucible in the following order: first silicon, second glass frit, and final silver. For the reaction with the pure oxide, the glass frit was replaced by 150 mg of lead oxide. In both experiments, the content of lead oxide, either pure or in the form of a glass frit is kept constant at 150 mg. The used ratio of glass/oxide:silver of 3:1 is quite different from the composition in a contact ink/paste (silver:glass ~15:1). For distinct DTA-signals, the glass/PbO content should be as high as possible and with a realistic ratio; the glass content was too small for a clear signal, as the capacity of the DTA-sample holder was limited - larger sample holders having the disadvantage that the measurement is less accurate. In a comparison measurement the influence of different silver:glass(oxide) ratios was 1:3 and 9:1. The peak positions in the DTA-signal were exactly at the same temperatures. As the peak size is less important in this experiment, a ratio of 1:3 (silver:glass/oxide) was chosen in order to get a good signal to noise ratio. In Fig. 7-8 the TG-DTA signals for the Ag-PbO-Si and Ag-glass-Si compositions are shown.

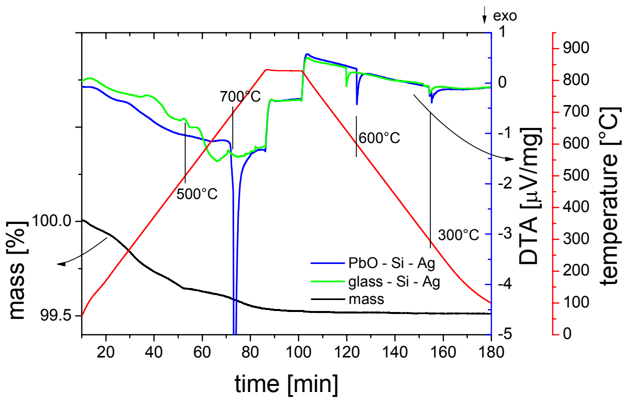

Fig. 7-8: DTA-measurement of the reaction agents PbO (150 mg), Si (25.5 mg), Ag (49.6 mg) and glass$_{PbO}$ (176.5 mg), Si (25.5 mg), Ag (49.6 mg). Additionally, the mass signal and the temperature profile are shown. Next to the labeled reaction peaks, steps in the measured DTA-signal are visible every time the heating rate changes. These steps can be neglected as they are related to the measurement unit.

The DTA-signal during heating up to 830°C has a similar shape as the DTA-signal from the experiment without silver and is dominated by the reactive glass. The influence of silver becomes visible during cooling.

Two further exothermic peaks are visible in both signals, at 300°C and at 600°C. The peaks in the Ag-PbO-Si sample are larger than the peaks where $glass_{PbO}$ is used instead of pure PbO, even if in both samples the content of PbO and also the mass of silver and silicon was the same. This indicates that during the reaction between Si and PbO, more energy is released compared to the reaction of Si and glass, and therefore higher amounts of metals can be solved, which condensates during cooling (exothermic peaks). The two exothermic peaks are in close relation to the Ag-Pb phase diagram. A lead-rich eutectic exists at T_{Eu}=304°C and a silver-rich phase with a lead content between 1% and 3% exists in a temperature range of 300°C-961°C, the melting point of silver. The experiment with Ag-PbO-Si was repeated three times; see Fig. 7-10 under the same conditions (temperature program, measurement setup, gas atmospheres and sample mass) in order to prove the reproducibility.

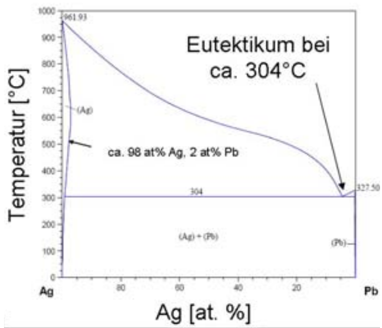

Fig. 7-9: Phase diagram Ag-Pb. A lead-rich phase condensates in the eutectic point at T_{Eu}=304°C and a silver-rich phase between 300°C and 961°C depending on the lead content. [117]

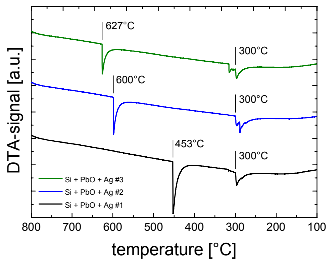

Fig. 7-10: Repetitions of the experiment with Ag-PbO-Si. The used masses and also the reaction parameters were kept constant as good as possible.

The peak position for the silver-rich phase can vary in a range of 480-700°C repeating the experiment, whereas the peak at 300°C is fixed. The origin for the different silver condensation temperatures is not clear and might be related to the reaction dynamic, whereas the lead-rich phase always condensates at the eutectic point.

The measured mass signal does not show a significant change, as the reaction agents are not volatile in the measured temperature range; the slight initial mass loss is related to the evaporation of water and the combustion of carbon-components from the glass frit. The reaction occurs under inert conditions, and oxidation can be excluded.

In both experiments, Ag-PbO-Si (sample1) and Ag-glass$_{PbO}$-Si (sample2), the content of the crucible was analyzed by SEM images and EDX measurements. When the DTA-crucible after the reaction was opened, two separated phases were found for both samples, a metal phase shown in Fig. 7-11 and a silicon-glass phase shown in Fig. 7-12, Fig. 7-13 and Fig. 7-14. The metal phase consists of silver and lead, which are again separated in an Ag-rich and a Pb-rich phase. It is noticeable that all the silver has been molten even if the temperature is kept far below the melting point of silver and below the silver-silicon eutectic. The energy necessary to solve the silver has to be provided by the exothermic reaction between PbO and Si. The silver-rich phase re-crystallizes in the form of cubic silver crystallites within the amorphous lead-rich Ag-Pb eutectic. The EDX analysis of the reaction products are in good agreement with the expected Ag-Pb phase according to the Ag-Pb phase diagram, see Fig. 7-9. For the silver-rich phase a content of 98.1at% Ag is found, and for the Pb-rich eutectic a composition of Ag:Pb of 3.9:96.1at%.

The silicon-glass phase is characterized by silicon particles and metal precipitates embedded in a glass matrix. The glass in sample1 has been formed during the redox reaction and for sample2, where glass is already present, its composition has changed, see Table 7-1. The glass close to the silicon particles has a reduced lead content and increased silicon content, whereas the glass in the middle of two Si-particles contains a higher lead content. During the redox reaction, silicon is oxidized to silicon dioxide, which is incorporated into the already existing glass layer (increased Si content). At the same time, lead oxide is reduced to lead and an Ag-Pb phase can be formed. The Ag-Pb melt condensates in the form of silver–lead precipitates which, in case of larger precipitates, can consist of the above described two metal phases. A layer of small metal precipitates is found in the glass layer, especially in the vicinity of silicon particles quite large Ag-Pb precipitates are homogenously distributed over the glass phase.

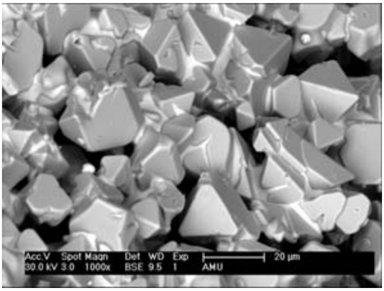

Fig. 7-11: SEM image of the condensed Ag-Pb melt. The silver-rich phase re-crystallizes in cubic structures, whereas the lead-rich phase condensates amorphously and fills the gaps between the Ag crystals.

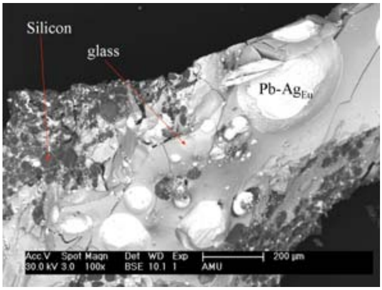

Fig. 7-12: Silicon-rich phase of the Ag-PbO-Si sample1. Silicon particles are still visible, PbO is reduced toPb (metallic Pb-Ag$_{Eu}$ precipitates) and a glass layer gluing everything together has been formed.

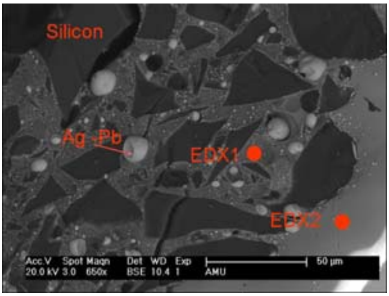

Fig. 7-13: Silicon-phase of sample2 (Ag-glass$_{PbO}$-Si). The EDX positions are labeled and summarized in Table 7-1.

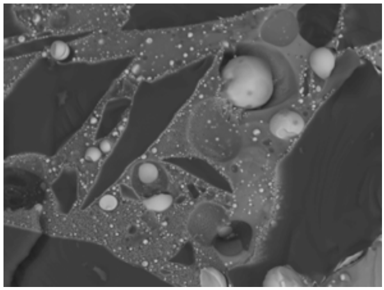

Fig. 7-14: SEM image of the glass and silicon-rich phase from the same crucible. Silicon pieces are still visible. The Si is embedded in a glass layer. Around the Si particles, a thin layer of small Ag-Pb precipitates are visible. Between them, larger, mainly Pb precipitates are found.

7.1.3 Opening of the anti-reflection coating

In general, the metal paste or ink is deposited on the antireflection or passivation layer and not on silicon directly [125], [126]. Before a contact corresponding to the above mentioned reaction can be formed, the dielectric layer first needs to be opened. The ARC is opened during the firing step by a reaction between the ink components and the dielectric layer. Most industrially produced solar cells are coated with a silicon nitride layer. For some high efficiency applications, silicon dioxide is used to passivate the cell surface. The reaction between lead oxide (glass frit) and both coatings, silicon nitride and silicon dioxide, has been studied by DTA measurements. In case of SiN_x, shown in Fig. 7-15, a strong exothermic reaction similar to the reaction with pure silicon is observed, whereas for the reaction of lead oxide and silicon dioxide only a small endothermic peak is visible, see Fig. 7-16. According to the binary phase diagram for the system PbO-SiO_2, introduced by Geller et al. [127], the system PbO-SiO_2 melts in the eutectic temperature of T_{Eu}=710°C and re-crystallizes at T=800°C. For a thick SiO_2 layer (d>100 nm) the described contact formation is hardly possible as the only possible mechanism to open the thick oxide during a firing step is a melting process. The formation of silver crystallites, important for the electrical contact, could not be observed on a SiO_2-passivated solar cell and contact resistant measurements were not possible. To achieve a good electrical contact on a solar cell passivated with a thick SiO_2 layer, the dielectric layer either needs to be opened in advance or the firing temperature has to be increased. Experiments have shown that in a combination of a thin oxide and thick nitride layer, used as a thermally stable passivation layer [128-130], the reaction energy released from the opening of the nitride is enough to penetrate the thin silicon dioxide (d<15 nm) and to form an electrical contact under standard firing conditions.

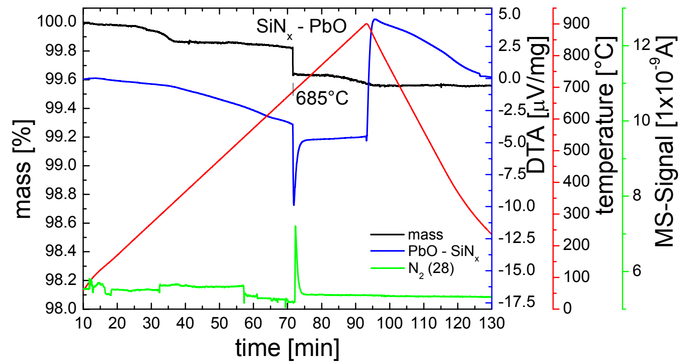

Fig. 7-15: DTA – MS measurement of SiN_x and PbO. A strong exothermic reaction at 685°C under the evolution of nitrogen is responsible for the opening of the ARC-layer.

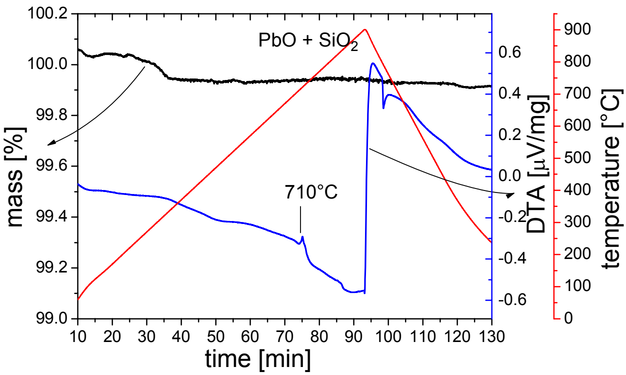

Fig. 7-16: DTA-measurement of PbO and SiO_2.

The reaction between the PbO (glass) and SiN_x is given as

$$4PbO + 2SiN_x \rightarrow 4Pb + 2SiO_2 + xN_2(\uparrow) \qquad \text{7-2}$$

To prove the evolution of nitrogen, the exhaust gasses are analyzed by mass spectroscopy measurements (MS). The signals for nitrogen (28) and for oxygen (32) are detected. The oxygen signal is used to exclude any external effects on the measurements and did not show a signal. Simultaneously with a sharp decrease in the mass signal, a peak in the N_2-signal indicates the evolution of nitrogen gas. For the case where $glass_{PbO}$ instead of pure PbO (as shown here) is used, the N_2-signal was not a sharp peak but a broad signal between T=570°C and T=800°C. The starting temperature for the evolution of nitrogen is consistent with the temperature where $glass_{PbO}$ starts to react with silicon, see Fig. 7-4. The silicon nitride is oxidized under the evolution of nitrogen and lead oxide is consecutively reduced to lead.

The opening of a silicon nitride layer during a firing step is based on the same redox-reaction 7-2 as the contact formation itself, whereas the opening of the SiO_2 layer is more a melting process and therefore unlikely. As the reaction mechanism for these two investigated dielectric layers already show significant differences, it is worthwhile to study the reaction mechanism for further passivation layers like TiO_2, SiC, Si-rich SiN_x, a-Si or Al_2O_3.

7.1.4 Different firing atmospheres

The firing of solar cells in industrial production occurs mainly under ambient air atmosphere. A positive impact of excess oxygen during the firing step on the electrical contact is reported by Huljic and Grupp [131] [132]. They studied the contact resistance as a function of the oxygen concentration during firing. They fired solar cells in a rapid thermal furnace (RTP) under different atmospheres, from inert conditions (100% N_2) up to 100% oxygen and plotted the IV-parameter as a function of the O_2 content. For elevated O_2 concentrations they found the best cell results, whereas for cells fired under inert conditions especially the fill factor was drastically reduced. These results can be explained by DTA-measurements under different atmospheres. The presence of oxygen has not, as it was expected, a detrimental influence on the contact performance, due to the oxidation of ink components and the formation of an insulating layer, but rather it is even necessary for the contact formation itself. The reaction mechanism for both the opening of the dielectric layer and the contact formation on silicon is based on a redox reaction, which is supported in an oxidizing atmosphere. One of the suggested contact mechanisms is the etching of silicon under the influence of a reactive lead-silver melt [23]. In order to investigate this mechanism we tested the system Ag-Pb-Si in a TG-DTA-measurement under inert and oxidizing atmospheres. For a better understanding of the reaction, we initially studied the system Pb-Ag as both metals contribute to the contact formation. The reactions between Ag (49.5 mg) and Pb (139.7 mg) under different atmospheres are shown in Fig. 7-17. Under inert conditions (N_2) the observed reactions are quite clear: The first endothermic peak at T=327°C corresponds to the melting point of lead (T_{mp}=326°C), and at a temperature of about 300°C the melt re-crystallizes at the eutectic temperature for Ag-Pb (T_{Eu}=304°C). The eutectic has probably been formed around 500°C; a distinct point can not be given. The mass signal is more or less constant. An oxidation is not possible and both agents are not volatile in the measured range of temperature. The reaction mechanism for the same system Ag-Pb under synthetic air looks quite different. At temperatures between 150°C and 320°C, silver oxides, formed already at RT and especially when the sample is heated, are thermally reduced to silver, and for temperatures above 320°C only metal silver is present. During cooling, at around 300°C where the Ag-Pb eutectic is expected, only a small signal can be observed. The formation of an Ag-Pb eutectic is not possible, as most of the lead is oxidized. The mass signal confirms the observed reactions from the DTA-signal. Initially, when heating starts the sample mass is increased due to an oxidation of lead and silver. Up to a temperature of 320°C the mass is almost constant as the oxidation of lead and the reduction of silver oxide are balanced. From a temperature of 320°C up to the beginning of cooling at T_{max}=830°C, the mass is constantly increased due to the oxidation of lead to lead oxide.

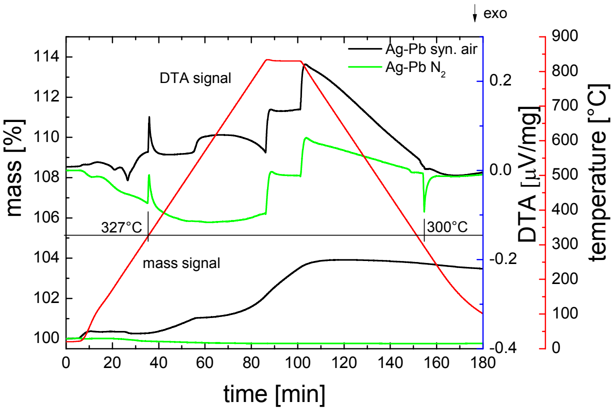

Fig. 7-17: Reaction between Pb and Ag under inert and oxidizing atmosphere.

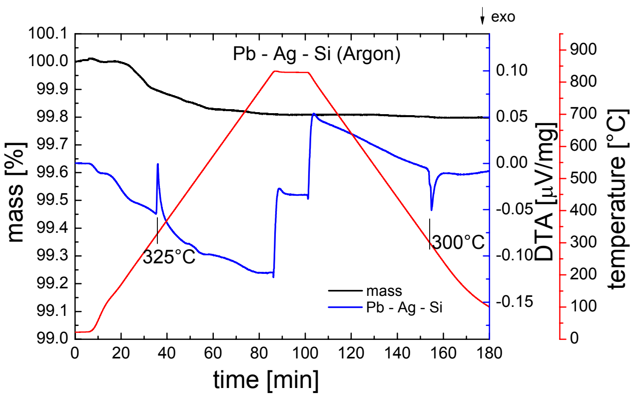

Fig. 7-18: DTA-measurement of the reaction agents Pb – Ag – Si, tempered under inert atmosphere.

In the next experiment, where the contact formation on silicon under different atmospheres was studied, silicon was added to the mixture of lead and silver. Therefore, a mixture of lead (139.7 mg) and silver powder (49.5 mg) with the same ratio and mass as in the previous experiment are brought into reaction with silicon (25.6 mg) in a crucible and the DTA-signal and the mass-signal are monitored. From the phase diagrams of Ag-Si and Pb-Si, a reaction can not be expected within the studied range of temperature (T<850°C). If a reaction between the liquid Ag-Pb melt occurs, it should be visible in the DTA-signal. Fig. 7-18 shows the reaction of the three agents under inert (N_2) atmosphere and Fig. 7-19 under ambient air.

Under inert conditions, the melting of lead at 325°C is visible, probably the formation of a Ag-Pb melt from 500°C-800°C, and the condensation of the Ag-Pb melt at the eutectic point at 300°C. The DTA-signal is the same as for the pure metals and a direct reaction between the liquid Ag-Pb phase and silicon could not be observed. Therefore, an etching of the Ag-Pb melt into the silicon can be excluded. The same reaction agents (same ratio and mass) heated up under synthetic air behave completely different and the signal looks like a combination of Ag-Pb (under air) in Fig. 7-17 and Ag-PbO-Si (N_2) in Fig. 7-8. It starts with a small exothermic peak, which indicates the reduction of naturally formed silver oxide, followed by the melting of lead. At a temperature of around 500°C a broad endothermic peak is visible, similar to the Ag-Pb system, which is abruptly interrupted by a strong exothermic reaction which starts around 700°C. Lead oxide reacts according to 7-1 and 7-2 and both lead and silicon dioxide are formed. The reduced lead can again be oxidized and the oxidation of silicon is continued or lead oxide is added to the silica glass which is formed during the reaction. The additional amount of oxygen becomes visible in the mass signal. Responsible for the gain in mass is the oxidation of lead to lead oxide and the oxidation of silicon, which ends either due to the consumption of one agent or because of the start of cooling. In case of the material system Ag-Pb the gain in mass is 4% whereas the gain in mass for the system Ag-Pb-Si is almost 7%. Oxygen from air is transported via the oxidized lead to the silicon and forms SiO_2.

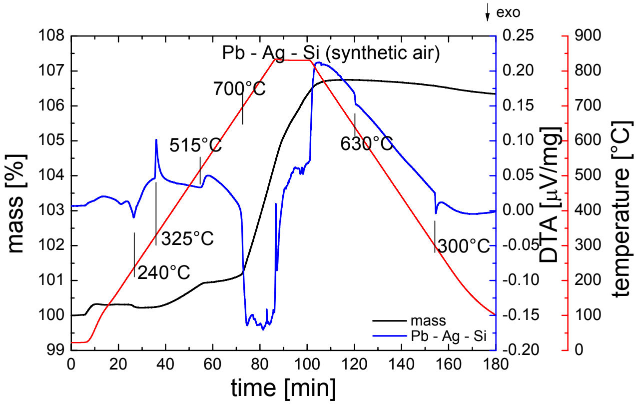

Fig. 7-19: DTA-measurement of the mixture Pb – Ag – Si tempered under synthetic air. The temperature profile, the mass signal and the DTA-signal are shown.

During cooling two peaks are observed: one is characteristic for the formation of Ag-crystallites and a second for the Ag-Pb eutectic at 300°C. The size of the peak at 300°C is smaller than the eutectic-peak Ag-Pb (N_2) but larger than the peak Ag-Pb (syn. air), see Fig. 7-17. That means that metallic silver and lead are still present. One part, the silver-rich phase, re-crystallizes around 630°C and another part in the form of the Ag-Pb eutectic at 300°C. It is interesting that the peak at around 600°C is only visible in all DTA-measurements if oxygen either in form of lead oxide or lead in an oxidizing atmosphere is present during the reaction with silver and silicon. Lead oxide together with silicon forms a glass, which is probably responsible for the separation of the Ag-Pb melt in two phases, a silver-rich phase and the Ag-Pb eutectic.

In conclusion, the presence of oxygen during the firing step promotes the contact formation and enhances the growth of silver crystallites. Ag-crystallites are found on silicon samples, contacted with a mixture of metal silver and lead, and fired under ambient air [23].

7.2 Reaction with bismuth oxide

Due to the health and environmental risks with the use of heavy metals like lead, cadmium or mercury, the EU-commission announced the directive "Restriction of the use of certain hazardous substances in electrical and electronical equipment – RoHS"[133], which in general regulates the use of hazardous substances. Currently, a maximum concentration of 0.1 m% lead (in homogenous materials) is accepted for the production of electronic components. As the amount of lead used in silicon solar cells exceeds this value, solar cells have been excepted from this directive until now. In 2006, when the EU-directive was published, paste manufacturers worked on the development of lead-free contact pastes [123, 134]. A detailed survey is given by Hoornstra und Schubert [60], who developed a lead-free front and rear side paste. However, since then, only little work on this topic has been published and also the industrially used contact inks/pastes still contain lead. In the future, it is very likely that solar cells will be included in the directive and lead-free alternatives are unavoidable. In particular solar cell producers, as suppliers of sustainable energy, should seriously be interested in using environmentally friendly and sustainable materials for the production of their products.

Lead oxide incorporated in a glass frit is in common screen print pastes the key component in terms of contact formation. In most lead-free pastes, the leaded glass is substituted by bismuth glass. Bismuth oxide can be used to replace the toxic lead in the contact inks as it has similar properties to lead oxide [115]. In order to obtain a deeper understanding of the role of a low melting oxide during the front contact formation in a firing step, the basic reaction between Bi_2O_3 and Si/SiN_x together with silver are studied in TG-DTA measurements; additionally, metal inks based on silver and bismuth oxide were prepared and tested on solar cells, see chapter 8.

The reaction between bismuth oxide and silicon or silicon nitrite is investigated by TG-DTA and compared with the reactions of lead oxide and Si or SiN_x, respectively. In Fig. 7-20 and Fig. 7-21 the reactions are illustrated. Bismuth oxide reacts in a similar way with Si or SiN_x as with lead oxide. The reaction temperature in the case of Bi_2O_3 is slightly higher and approximately shifted by 30-60°C. The exothermic character of the reactions is similar. As soon as the activation energy is reached, a strong exothermic reaction between the metal oxides and the Si or SiN_x occurs. Bismuth oxide can be used to open the passivation coating (SiN_x) and it reacts with silicon, which is the precondition for the formation of contact Ag-crystallites. Therefore, Bi_2O_3

is a possible substitute for lead oxide in a front contact paste and the reaction mechanisms can be given as:

Reaction with silicon

$$2Bi_2O_3 + 3Si \rightarrow 4Bi + 3SiO_2 \tag{7-3}$$

Reaction with silicon nitride

$$2Bi_2O_3 + 3SiN_x \rightarrow 4Bi + 3SiO_2 + \tfrac{3}{2}XN_2(\uparrow) \tag{7-4}$$

Silicon or silicon nitride are oxidized by the metal oxide, which is reduced to metallic bismuth at the same time. The oxidized silicon probably forms a glass layer, whereas the metallic bismuth helps to solve high amounts of silver. The solved silver can re-crystallize in the form of Ag-crystallites, which are needed for a high quality contact. The elemental formula of lead oxide and bismuth oxide are different and for the oxidation of silicon or silicon nitride, 1/3 more oxygen is present compared to the reaction with PbO. In theory, the metal lead content in the contact paste can be reduced by 1/3. Reduced glass content results in a thinner insulating glass layer at the metal-semiconductor interface and a lower contact resistance can be expected.

In order to prove the capability of bismuth oxide to act as a contact promoter in a contact ink, its reaction with silver needs to be investigated as well, in particular the re-crystallization during cooling. In Fig. 7-22 the reaction between the metal oxides (PbO or Bi_2O_3) with silicon and silver is shown. The reaction with lead oxide is used as a reference as it is known that a good electrical contact can be formed by this reaction. The DTA-sample holder is filled with Si (25.5 mg), Bi_2O_3 (156.7 mg) and Ag (29.6 mg). The molar mass is the same as for the experiment with lead oxide. The contact formation starts during cooling with the condensation of Ag-crystallites. Similar to the reaction with lead oxide, mainly two exothermic peaks are visible, at temperatures around 600°C and at temperatures below 230°C. The peak at 600°C agrees with the Ag-Bi phase diagram, which is quite similar to the diagram of Ag-Pb, see Fig. 7-23.

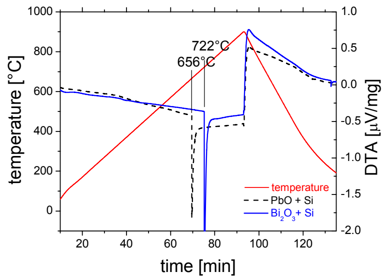

Fig. 7-20: Reaction between Bi_2O_3 and Si under inert conditions. The reaction with lead oxide is given as well (dashed line).

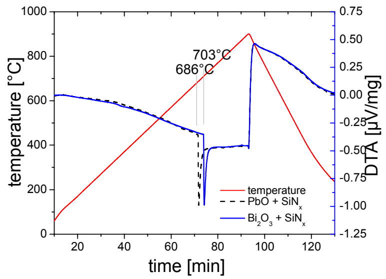

Fig. 7-21: Reaction between Bi_2O_3 and SiN_x under inert conditions. The corresponding reaction with lead oxide is given as well (dashed line).

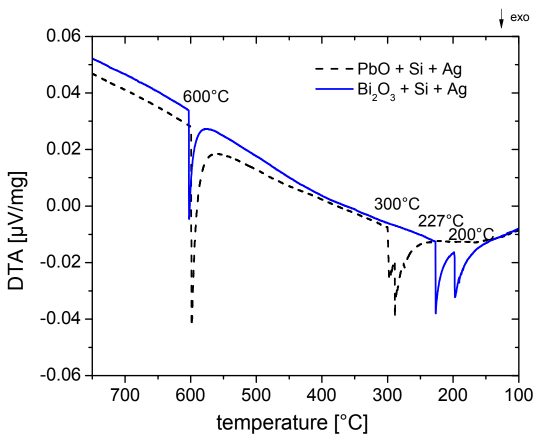

Fig. 7-22: Re-crystallization of Ag-Pb phases (silver rich and lead rich) and of Ag-Bi phases (silver rich and bismuth rich).

A silver-rich phase exists in a broad range of temperatures, depending on the bismuth content. At 600°C a composition Ag:Bi of 96:4 is expected. In the SEM/EDS analysis two metal phases were found, a silver-rich 96 at% (Ag) and a bismuth-rich phase 90 at% (Ag). For the silver-rich phase, the composition of 96:4 Ag:Bi corresponds to the re-crystallization at 600°C, whereas the Bi-Ag eutectic contains a higher amount of silver than expected. The condensation temperature of the bismuth-rich phase is too low compared to possible theoretical values; nevertheless, they are probably related to the eutectic temperature of Ag-Bi (250°C) and/or to the melting point of bismuth (271°C). It is not clear as to why the temperature of the assumed melting point and eutectic is shifted by 50°C to lower temperatures. The condensation temperature of bismuth in the experiment Bi_2O_3-Si was 214°C, which is also below the expected melting point for bismuth of 271°C.

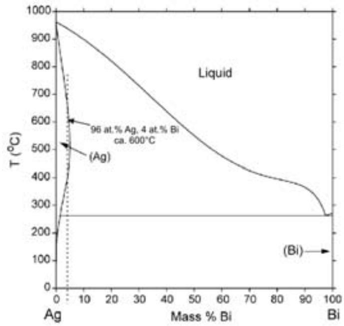

Fig. 7-23:Phase diagram for the system Ag-Bi [117]

The performed measurement indicates the usability of Bi_2O_3 as a contact promoter in a silver ink, even if the reaction temperatures are slightly higher and the temperature for the re-crystallization lower compared to lead oxide. The reaction mechanism seems to be similar to the reaction with lead oxide and the contact formation with a lead free ink should be based on the same mechanism as for a lead containing ink. To prove this result, front contact inks, based on silver and bismuth oxide, were prepared and tested on silicon solar cells (see next chapter).

7.3 Presence of phosphorous in the contact ink

An often-discussed topic is the formation of a selective emitter during the firing step. It would combine the advantages of a lowly doped emitter, (see chapter 9) with the necessity of a high emitter doping for the contact formation using printed silver contacts. The addition of phosphorous components or elemental P to the front contact pastes would be the easiest way to form a highly doped region directly under the contact. Ideally, the P diffuses during the firing step in the lowly doped emitter region and decreases the emitter sheet resistivity and increases locally the surface doping concentration N_D. Actually, some commercially available contact pastes contain phosphorous for this reason [123] and Hilali [135] and Rohatgi [136] presented slightly improved cell efficiencies if self-doping contact pastes are used. However, in both experiments the silver pastes were fired above the silver-silicon eutectic (835°C). Rohatgi has proven by SIMS measurements that P is incorporated into the silicon surface if P containing silver pastes are fired above the eutectic for 2 min. Higher P surface concentrations are found for pastes without a glass frit, which is in agreement with the results from Meier [137].

We tried to test whether elemental P, as part of silver paste or directly deposited on a silicon solar cell, with both a lowly and highly doped emitter can influence the emitter sheet resistivity. The used samples were shiny etched Cz-wafers with emitter sheet resistivities of R_{SH}=50 Ω/sq. (N_D=6×10^{20} cm^{-3}) and R_{SH}=120 Ω/sq. (N_D=7×10^{18} cm^{-3}). On each sample, three different inks were deposited, pure phosphorous, phosphorous mixed with a front side silver ink and phosphorous mixture with pure silver powder. In the case of the mixtures, the phosphorous content was 3 m% by mass. The samples were fired in an in-line furnace at a temperature of 800°C (below the Ag-Si eutectic of 835°C) and at 850°C, above the Ag-Si eutectic. The peak temperature is applied for less than 5 sec. The fired wafers were cleaned in nitric acid in order to remove the silver and dipped in a low concentration HF (5%) solution for 5 min at RT to remove the formed phosphorous glass layer. The emitter sheet resistance was analyzed by 4-point probe measurements, sheet resistance imaging and inductive sheet resistance measurements before the inks were deposited and fired, and afterwards the samples were cleaned.

The results were quite surprising, as with none of the used methods we found an indication for an increased P content in the samples. Independent of the initial doping concentration, firing temperature and ink, the sheet resistance was not reduced after the firing step. To the contrary, phosphorous seems to diffuse out of the emitter into the formed phosphorous glass and the measured R_{SH} was even reduced. The diffusion of P at room temperature into a native oxide layer is reported by [138]. During cleaning in HF the native oxide layer is removed and probably some of the surface phosphorous as well. The measurement methods we used are not sensitive to the surface; therefore, a local diffusion into the silicon surface can not be excluded even if it is very unlikely.

The diffusion coefficient for P in silicon even at 1100°C is ~10^{-13} cm²/s [139] and therefore more than 10000 times lower than the diffusion coefficient for silver in silicon (2.7×10^{-9} cm²/s) [140]. The formation of a selective emitter by diffusion is not possible during a fast firing step. The formation of a selective emitter from a P containing silver ink is only possible at high temperatures (>835°C) applied for a long temper period, as reported by Meier and Porter [137, 141-143]. They proved the presence of a selective emitter due to the formation of an Ag-Si-P melt where P is incorporated during re-crystallization. Additionally, they found that the formation of a selective emitter was not possible if glass was already present in the contact ink, as the P is absorbed by the liquid glass and incorporated into the glass layer instead of the silicon. As almost all front side contact inks contain a glass frit (necessary for the opening of the ARC coating and for the contact formation below the Ag-Si eutectic), the addition of P in a standard Ag paste is not useful for the formation of a selective emitter. The addition of P might have an influence on the properties of the glass frit during firing and therefore on the contact formation, as phosphorous tends to be oxidized to P_2O_5, which is known as a glass former. However, the formation of a thick glass layer on the contact interface has more a detrimental than a positive effect on the electrical contact quality. Solar cells contacted with inks which contain elemental phosphorous show quite indifferent results. The IV-parameters were either not affected by the addition of P or they changed for the worse; at the least a positive effect on the electrical contact properties could not be observed. In general, the mechanical adhesion was improved, which promotes the theory that from the additional P a thicker glass layer is formed.

7.4 Chapter summary

The fundamental reactions between a silver contact ink and an n-type silicon surface are investigated by thermal gravimetric - differential thermo analysis (TG-DTA). Contact inks are mainly consisting of silver particles and a lead-oxide glass frit. The important components for the contact formation are lead oxide as a contact promoter and silver as a contact metal. The reaction mechanisms between lead oxide and silicon and with dielectric coatings like (SiN_x and SiO_2) are clarified. Lead oxide reacts exothermically with Si or SiN_x at a temperature of about 680°C, the contact formation with silicon is actively promoted, and silver contact crystallites are formed from liquid Ag-Pb. This is hardly the case if SiO_2 is used as a passivation layer as the reaction of PbO with SiO_2 is a slow melting process. The presence of oxygen during the firing step is unavoidable, as the opening of the passivation layer as well as the etching of silicon are based in reduction and oxidation processed. It is even possible to form an electrical contact to silicon under oxidizing atmosphere using only the metals silver and lead. It is also shown, that the toxic lead oxide can be replaced by bismuth oxide. The general reaction mechanisms, important for the contact formation are similar. Bismuth oxide reacts exothermically with silicon and SiN_x at slightly higher temperatures than lead oxide does. Finally, the presence of phosphorous is studied, in order to prove the possibility of forming a selectively doped emitter during the firing of the front side paste. However under no condition a measureable impact of P present in the silver ink could be found. Based on these basic results different contact inks were fabricated and tested on silicon solar cells, see next chapter.

8 Metallization inks – tested on solar cells

Relatively simple contact inks were produced in order to test the chemical reaction studied above on a real wafer and to understand the contact formation. First, a two component system based on silver and bismuth oxide was used to prepare aerosol inks, which were than deposited on solar cells. Bismuth oxide was used as a reactive metal oxide as it is nontoxic and has similar properties as the toxic lead oxide. Solar cells, contacted with "homemade" inks, were already produced by Mertens [47]. He tested different silver particles, spheres and flakes, together with different oxides (PbO and Bi_2O_3) or glass-based inks where lead oxide or bismuth oxide were part of the glass composition. In his study, the best cells contacted with bismuth oxide-based inks performed almost as good as the best cells, contacted with a commercial silver ink. In our experiments we could confirm that bismuth oxide is a good alternative to lead oxide. The etching behavior seems to be more aggressive resulting in an increased saturation current density j_{02} and a reduced shunt resistance R_p. However, as soon as the pure oxide is incorporated in a glass system, the reaction of contact formation seems to be more moderate and the firing step is less critical. For an ink, based on a leaded glass system, the optimum glass content was determined. This ink is used for all further studies and called "seed layer ink for the metallization of solar cells" (SISC).

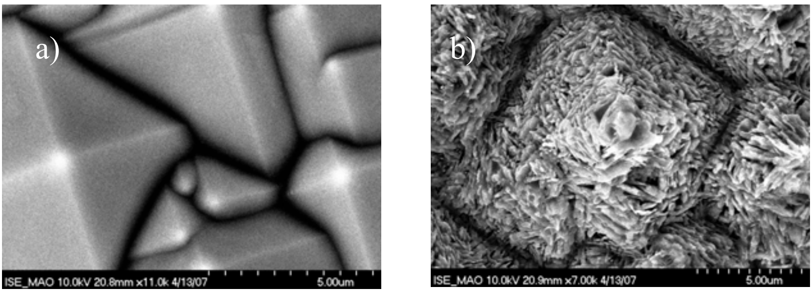

Fig. 8-1: SEM images of a textured Si-wafer surface (left a) and of the same Si-surface after the deposition of bismuth oxide, firing and cleaning (right b). The deposited and fired ink (pure Bi_2O_3-powder) has been removed by chlorine and fluoric acid.

8.1 Experiment

Two component contact inks, based on silver and bismuth oxide, were prepared with different Bi_2O_3 concentrations, from 0 mass% (pure silver ink) up to inks with 90 m% Bi_2O_3. The solid content for all inks was kept constant at 67 m%. Ag-powder and Bi_2O_3-powder were the only inorganic components used. Organic solvents and dispersant agents were used to adjust the ink rheology. In total six inks were prepared with different ratios of Ag:Bi_2O_3 and labeled AgBi_x, see *Table 8-1*. Ag-powder from Alfa Aeser and bismuth oxide powder from Sigma Aldrich, both with a mean particle size below 1 µm, necessary for the aerosol print [144], were mixed. The solids were dispersed in a mixture of glycol ether and n-methylpyrrolidone using an ultrasonic bath.

name	Bi_2O_3 [m%]	Ag [m%]
AgBi0	-	100
AgBi10	10	90
AgBi30	30	70
AgBi50	50	50
AgBi70	70	30
AgBi90	90	10

Table 8-1: Composition of the silver-bismuth oxide inks

The inks were deposited on 5x5 cm² Cz-silicon wafers. The cells' front sides were textured and passivated with a PECVD-SiN_x layer with the emitter sheet resistance of R_{SH}=50 Ω/sq. The rear side was metalized with an Al screen print paste. The front side grid was printed using the aerosol jet technology. The aerosol-printed front side contacts were co-fired with the screen-printed Al-rear side in an RTP furnace at different temperatures, followed by a thickening step in a light-induced plating bath. The printed contact width was w_c<50 µm and after plating of 12 µm in height, the contact width was increased to w_f=75 µm. Five cells of each ink were fabricated and fired at 5 different temperatures between 700°C and 820°C with a delta of 30°C. Finally, the cell performance is determined by IV-measurements and the contact resistance was analyzed using the transfer length model (TLM). The contact microstructure and the contact interface are studied by SEM/EDX measurements of etched contacts and on an ion-polished cross section. The etching behavior of AgBi_x inks was studied on polished samples by AFM measurements. Therefore, polished 2x2 cm² samples are aerosol-printed with the different inks, fired in an RTP furnace, and finally cleaned by an HNO_3/HF etching sequence.

One of the successfully studied AgBi_x inks was used to process large-area 15.6x15.6 cm² mc-Si solar cells. The ink consists of 90 m% Ag-powder and 10 m% Bi_2O_3, called AgBi10. The cells were aerosol-printed, co-fired in an in-line furnace at different temperatures, thickened by LIP and characterized by IV, TLM-measurements and SEM images. The samples, used for all further experiments on large-area multi-crystalline silicon solar cells, had an acidic textured front side, passivated by a PECVD-SiN_x coating, Al-screen printed rear including Al-Ag connectors, and the $POCl_3$-diffused emitter had a sheet resistance of either 65 Ω/sq or 80 Ω/sq. As the contact formation with pure oxide inks is quite temperature dependent, the metal oxides were incorporated into a glass frit. Two glasses, one based on lead oxide, called $glass_{PbO}$ and one based on bismuth oxide, called $glass_{Bi2O3}$, were produced and milled into a glass frit which then could be added to a silver ink, similar to the pure oxides. Several seed layer inks with different $glass_{PbO}$-contents were produced and deposited on mc-Si solar cells in order to study the dependence of the glass content on the contact performance. Again, the IV-parameters were compared with the contact resistance and structure and the optimum $glass_{PbO}$ content was determined. Finally, a lead-free seed layer ink based on a bismuth $glass_{Bi2O3}$ was produced (with the optimum glass content) and deposited on solar cells, which then were fired at different temperatures.

8.2 Seed layer inks, based on silver and bismuth oxide

The impact of pure Bi_2O_3 on a textured solar cell, fired under typical conditions (ambient air T=800°C) is shown in Fig. 8-1a) before and b) after firing. The reaction is very aggressive and the silicon surface is heavily attacked by the bismuth oxide. The etching, or better the oxidation of silicon to silicon dioxide by a metal oxide is the prerequisite for the use of the metal oxide, as the reactive component in a silver contact ink, assuming the current contact model is valid. Six inks with different Bi_2O_3 contents (see Table 8-1) are therefore deposited by aerosol printing on 5x5 cm² samples and fired at different temperatures. The IV-results are summarized in Fig. 8-2. Surprisingly, the cell performance is almost independent of the Bi_2O_3 concentration; even inks with a Bi_2O_3 content of 90 m% gave comparably good IV-results. Only for the ink AgBi0 (pure silver ink) a contact formation on silicon was not possible. The contacts did not adhere and the total front side grid was lifted off after contact firing or during the LIP step. The silver particles sinter together and form a conductive layer, but as expected silver does not form a metal silicide and a direct or even intimate connection between silver and silicon is not possible, at least for the used firing conditions (below the Ag-Si eutectic). The presence of a contact promoter like bismuth oxide is necessary as it is able to solve/etch the silicon in a redox reaction and forms a glass layer which improves the contact adhesion. At the same time, Ag-crystallites are epitaxial re-crystallized and a close contact between silver and silicon is formed.

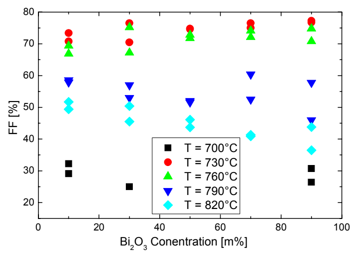

Fig. 8-2: Fill factor of all processed cells as a function of the Bi_2O_3 concentration and firing temperature

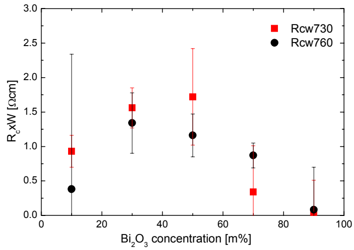

Fig. 8-3: Values for the normalized contact resistance $R_c xW$ as a function of the Bi_2O_3 concentration for contacts fired at 730°C and 760°C.

Bi_2O_3	T	V_{oc}	J_{sc}	FF	η	j_{01}	n_1	j_{02}	n_2	R_S	R_P
[m%]	[°C]		[mA/cm²]		[%]	[pA/cm²]		[nA/cm²]		[Ωcm²]	[Ωcm²]
90	730	605	32.4	77.3	15.2	1.24	1	374	2.48	0.52	1270
70	730	594	35.8	76.5	16.3	1.77	1	258	2.25	0.69	2855
50	730	598	35.9	74.8	16.1	1.42	1	53.7	2	1.24	2639
30	730	598	35.7	76.5	16.3	1.67	1	32.3	2	1.02	3215
10	730	595	35.8	73.4	15.6	1.53	1	72.9	2	1.28	2407

Table 8-2: IV-parameter for 5x5 cm² Cz-Si solar cells, contacted with different AgBi_x inks and fired at 730°C.

The solar cell IV-parameters are strongly dependent on the firing temperature and the optimized firing temperature is in a quite small window around 730°C. If the firing temperature is reduced by only 30°C to 700°C, the activation energy for the redox reaction Eq.7-1 is too low and a contact formation is not possible, independent of the Bi_2O_3 content. At 30°C higher temperatures (760°C), the FFs are already slightly reduced, not due to a reduced contact quality but more likely due to a dark saturation current in the space charge region j_{02}, see Fig. 8-4 where the IV-dark curves are plotted for different firing temperatures. Solar cells fired at 700°C have an increased series resistance (no contact formation) and with an increasing temperature, the "ideal" two-diode curve is more and more determined by an increased recombination and reduced parallel resistance. Only for the solar cells fired at 730°C a reliable fit of the dark IV-parameter (R_s, R_p, j_{01}, j_{02}) was possible; the data for this are given in Fig. 8-4 and Fig. 8-5. With increased bismuth oxide content, the series resistance is reduced but at the same time, the values for j_{02} are slightly increased as well. High oxide contents seem to be beneficial for the contact quality but detrimental for the pn-junction. The strong dependence of the dark saturation current density on the firing temperature is evidence for the diffusion of metal impurities into the contact. As the only materials present are silver and bismuth oxide, it is either the bismuth or the silver which diffuses into the silicon surface and the related damage in the crystal structure increases the recombination and therefore the saturation current density. Silver can diffuse, especially if no glass layer is initially present at the interface, which acts as a diffusion barrier for impurities [145]. The influence of an annealing step can be seen in Fig. 8-6 and Fig. 8-7. The cell efficiencies of optimum fired cells (T=730°C) is more or less unaffected by the annealing. However, the cells fired at too high temperatures are very sensitive to the additional tempering step. The recombination is strongly reduced during an annealing step of 10 min at 400°C under forming gas and the gain in efficiency is proportional to the firing temperature. Crystal defects introduced during firing in the space charge region seemed to be annealed e.g. a cell fired at 790°C had an efficiency of η=12% after firing and of η=16.6% after the annealing. The gain is based on an increased voltage from V_{oc}=582 mV to V_{oc}=611 mV and an increased fill factor from 57% to 75%. The gain in the FF can also be based on an improved contact interface, as studied by Nakajima and by Schubert [146, 147], however, in this case the series resistance was unaffected and the improved cell parameters are related to a reduction in the dark saturation current density j_{02}. In conclusion, the cell efficiency is more affected by the firing condition than by the bismuth oxide content.

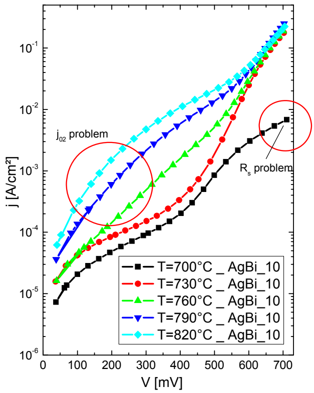

Fig. 8-4: Dark IV-curves for solar cells, contacted with the 10 m%-containing Bi_2O_3 ink, fired at different temperatures.

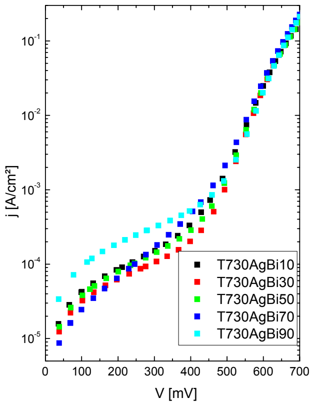

Fig. 8-5: Dark IV-curves for solar cells, fired at a constant temperature of T=730°C and contacted with different Bi_2O_3- inks

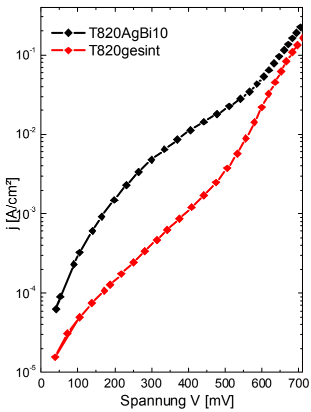

Fig. 8-6: Dark IV-curves before and after FGA annealing at 350°C of a cell, fired at T=820°C and contacted with a 10 m% Bi_2O_3 ink.

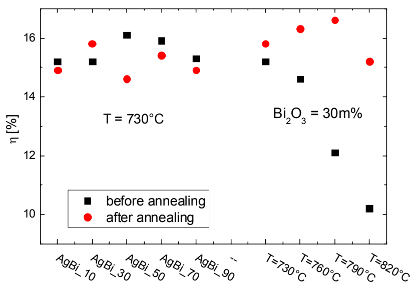

Fig. 8-7: Solar cell efficiencies before and after annealing, for both cells with a constant firing temperature and a varying Bi_2O_3 concentration (left), and for different firing temperatures and a constant Bi_2O_3 content (right).

The fact that the IV-parameters are not affected by the bismuth oxide content can be explained by contact resistance measurements and by the microstructure of the contact interface, see Fig. 8-8. The contact resistance has a maximum at bismuth oxide concentration of 30 m%-50 m% and is reduced for lower and higher bismuth concentrations. One explanation is the number of Ag-crystallites and the assumed thickness of a formed glass layer. As the inks do not contain any glass, the only insulating glass present at the contact interface was formed during the contact formation. Bismuth oxide etches silicon under the formation of a bismuth-silica glass. That means, the more the silicon is etched, the thicker is the glass layer. The printed contact height for all contacts is the same and in the range of 1 µm. The amount of Bi_2O_3 per contact area is therefore defined by the ink composition. For a low oxide concentration, the contact interface is only slightly etched and some Ag-contact crystallites are visible and the SiN_x layer seems to be hardly etched by the oxide. The glass layer therefore is quite thin and an effective contact between the crystallites and the bulk silver is possible, as demonstrated in the following chapter. With an increasing Bi_2O_3 content, the SiN_x layer as well as the silicon is etched more strongly, and even if more Ag-crystallites are visible, the contact resistance is increased as the glass layer is probably too thick. At even higher Bi_2O_3 concentrations, the contact resistance is reduced again. The surface is etched even more and more glass is produced. But now, almost the whole contact area is covered by silver crystallites and the probability for a contact between Ag-crystallite and bulk silver is increased. The best values for the contact resistance could be achieved with high oxide concentrations; however, the adhesion of the contacts containing high amounts of Bi_2O_3 is strongly reduced and the diffusion of impurities is increased with the Bi_2O_3 content. Therefore, for all further investigations, the ink AgBi10 with an oxide content of 10m% was used.

8.2.1 Contact analysis and microstructure

The different etching behavior of the inks was studied by taking SEM-images of the contact interface. The structure of the interface helps to interpret the IV-parameters measured above and to obtain a better understanding of the contact formation. Therefore, the metal contacts were etched successively in nitric acid to remove the bulk silver and in fluoric acid to remove the formed SiO_2-glass. The Ag-crystallites as long as they were formed during contact firing, remained. The number and size of the crystallites can be used to interpret the quality of a contact. In Fig. 8-8 the influence of the firing temperature on the contact interface, formed using ink AgBi10, is shown as well as the influence of the bismuth oxide content on the contact interface at a constant firing temperature of 730°C. At 700°C no Ag-crystallites are visible and an electrical contact could not be measured; the measured surface roughness is due to ink components which could not be removed during the etching steps but the SiN_x-coating on the cell surface was not affected. At 730°C Ag-crystallites grown into the silicon surface are visible and the SiN_x coating is locally removed, which indicates that the redox reaction between bismuth oxide and silicon starts at this temperature. The redox reaction also seems to be responsible for the crystallite growth. With increasing temperature the size of the crystallites is increased even more, and at the same time diffusion of impurities is an issue. The same trend as shown for an increasing temperature can be found on interfaces produced with varied oxide contents. The more oxide is present at the interface, the larger is the density of Ag-crystallites. Both an increase in temperature and oxide content supports the redox reaction responsible for the contact formation.

T=700°C 10 m%

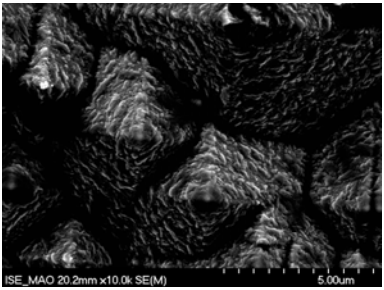

T=730°C 10 m%

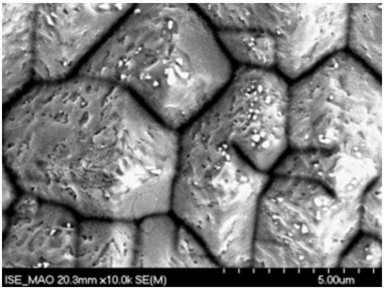

T=730°C 10 m%

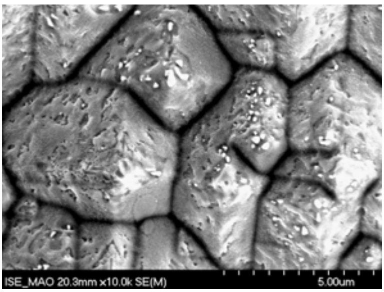

T=730°C 30 m%

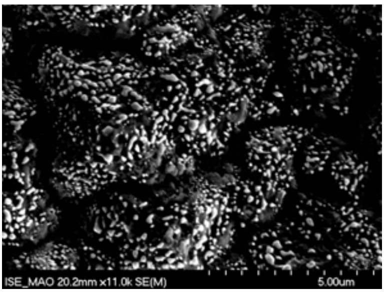

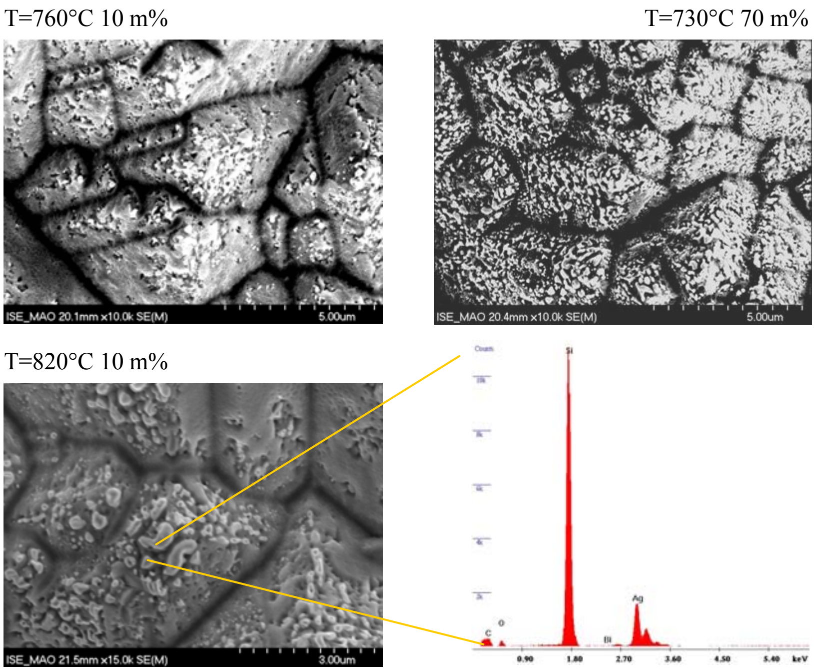

Fig. 8-8: SEM images of contact interfaces. The bulk silver and the glass layer were removed and the silver-crystallites are left over. The dependency on the firing temperature (left) and on the bismuth oxide concentration (right) is shown together with an EDX analysis of one of the silver-crystallites.

On a cross section of the metal-semiconductor interface, the distributions of the elements and the contact structure are studied by EDX-analysis. A cross section was produced from a contact printed with the ink AgBi10 and AgBi70. The contact was first cut by a dicing saw, the cross section was mechanically polished and finally treated in an ion polisher. An image of a total contact cross section can be seen in Fig. 8-9 and a close up view in Fig. 8-11. The different contact layers are given additionally in different colors. The contact cross section for the contact AgBi10 was analyzed by EDX-mapping of the elements silver, bismuth, oxygen and carbon. Both contacts were fired at 730°C and have similar cell results and also similar contact resistances, nevertheless, their interfaces are quite different, see Fig. 8-10 and Fig. 8-11. In both cases, the plated silver is clearly visible as it has a dense and homogenous structure, whereas the seed layer consists of more phases and additionally roundish cavities are present. The cavities are formed during the firing step, and they are either grown from the evaporation of nitrogen from the SiN_x coating or more likely from the combustion of hydrocarbons, the organic ink components. The EDX analyses revealed an increased concentration of carbon around the cavities, see Fig. 8-13. The combustion of the organic ink components is not perfect and occurs at temperatures that are too high where the glass layer is already liquid, and the formed combustion gasses (CO_2 and water) are not able to evaporate, resulting in cavity formation.

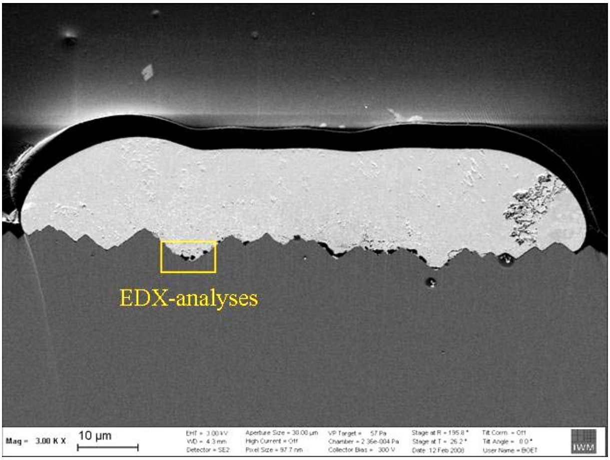

Fig. 8-9: Contact cross section of a seed layer printed and light induced plated contact. The contact was fired at T=760°C and printed with the ink AgBi10 (10 m% Bi_2O_3). The cross section was prepared by ion polishing. The EDX analyzed area is labelled.

The seed layer in the case of AgBi70 mainly consists of non-reacted or re-crystallized bismuth oxide, as it is the main component of the layer. The Bi_2O_3 grains have a geometric structure, which is more characteristic for a crystallite than for a glass layer. This more than 1 µm-thick layer (thickness of the printed seed layer) separates the Ag-crystallites from the bulk silver and the LIP-silver. Ag-crystallites are clearly visible and almost the whole contact surface, see also Fig. 8-8, is covered by the crystallites. The Ag-crystallites are covered by a thin glass layer, which has been formed during the contact formation. In case of the ink AgBi10, silver crystallites are hardly visible in the cross section even if they are present, as we know from Fig. 8-8. The layer on the interface to the silicon also consists of Bi_2O_3, which again is either pure re-crystallized bismuth oxide or a $glass_{Bi2O3}$. The thickness of the Bi_2O_3 layer is comparably thin and it looks like if at some positions a direct contact between bulk silver and silicon surface is possible. In the EDX-mapping of the contact cross section, bismuth is only found in the presence of oxygen. Pure Bi is probably not present on the contact interface and is either present in the form of crystalline Bi_2O_3 or in the form of a $glass_{Bi2O3}$ layer.

For both inks, AgBi10 and AgBi70, a quite low contact resistance $R_cxW<1\ \Omega$ cm was measured. This was not expected, as the interfaces, especially the thickness of the Bi_2O_3-layer is totally different. The thickness of the oxide layer under contacts printed with ink AgBi70 is almost 1 µm thick. The low values for the contact resistance can either be explained by the overcompensation for the negative effect of a thick Bi_2O_3 layer by an extremely high density of Ag-crystallites or by the conductivity. The conductivity of a crystalline bismuth oxide layer seems to be better than the conductivity of a $glass_{Bi2O3}$ layer as otherwise an electrical contact would not be possible. For this investigation, further studies are necessary.

Even if the contact resistance is improved for higher bismuth oxide contents, it is preferable to keep the fraction of oxide as low as possible, as the electrical cell parameter j_{02} and R_p are negatively influenced. Additionally, a boundary between the seed layer and the plated silver is visible for the ink AgBi10, whereas the boundary becomes a gap of a view nm in the case of contact ink AgBi70. The LIP silver preferable growth on silver and not on oxide. As only a little amount of silver is present at the contact, the LIP-growth is not homogenous, see Fig. 8-10. This interface reduces the mechanical adhesion with increased bismuth oxide content.

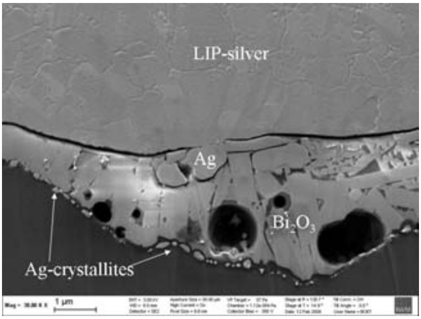

Fig. 8-10: Cross section of contact, printed with the ink AgBi70 (70 m% Bi_2O_3). Most of the seed layer consists of re-crystallized bismuth oxide.

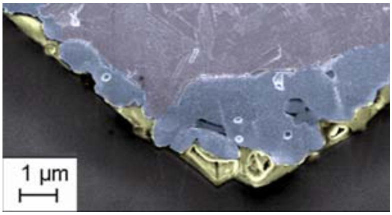

Fig. 8-11: Close up view of Fig. 8-9. The formed glass$_{Bi2O3}$ layer, the bulk silver and the LIP silver are colored, most of the seed layer consists of silver and the formed glass layer is quite thin.

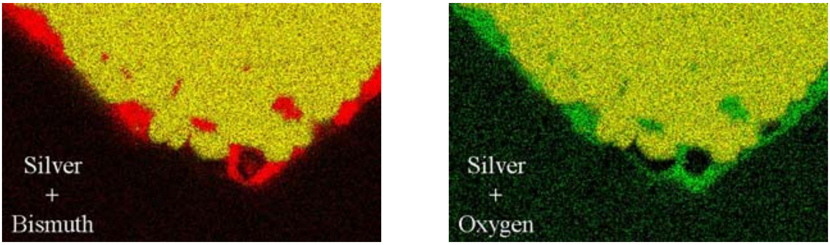

Fig. 8-12: EDX-mapping for the elements silver (yellow) together with bismuth (red)-(left) and oxygen (green) (right). Evidence for the presence of pure bismuth was not found, but bismuth exists together with oxygen.

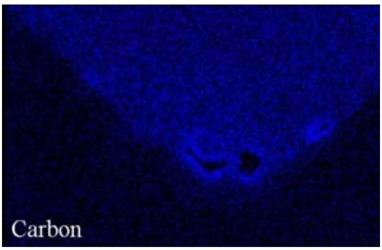

Fig. 8-13: EDX-mapping for the element carbon. In the surrounding cavities, an increased carbon concentration indicates the formation of the hollows due to an incomplete combustion of the organic ink components.

8.2.2 AFM-measurements

The etch depth of Bi_2O_3 into silicon was investigated by AFM-measurements. Therefore 2 cm x 2 cm, diffused silicon samples with a polished (100)-oriented surface were used, as a deeper etching on (100)-Si surfaces is expected. The junction depth on the studied samples is about ~0.4 µm. The reported etching depth of Ag-crystallites for optimum fired contacts on a (100)-Si surface is in the range of 100-150 nm [56] and therefore about twice as deep as on samples with a (111)-Si surface [62].

The samples were printed with the different AgBi_x inks, fired, and cleaned, so that only the imprints in the silicon surface were measured. All samples were fired at the optimum firing temperature of T=730°C in an RTP furnace. A representative area of 5 µm x5 µm was profiled and the maximal etching depth was determined by measuring the difference between the highest and lowest points. The samples were covered by a nitride layer and the highest point under the contact, still covered by the nitride layer, was leveled by measuring the height next to the contact where the surface (SiN_x coating) is not affected by the ink. The highest point was set to zero and the deepest point was found by line scans of the total investigated area. In Fig. 8-14 an SEM image of the profiled region together with one line scan is given.

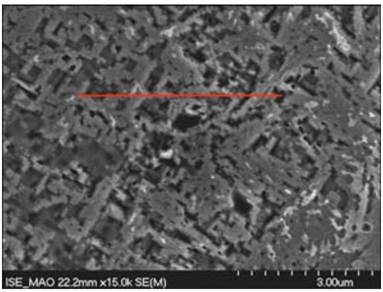

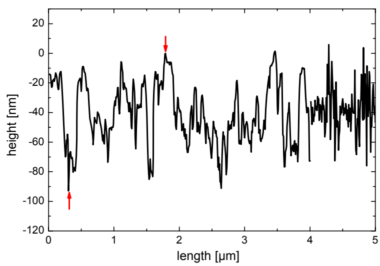

Fig. 8-14: SEM image of a polished (100)-Si surface with an emitter sheet resistance of R_{SH}=90 Ω/sq, after the ink AgBi90 was fired and removed. The surface is heavily attacked and the geometric footprints of the removed Ag-crystallites are visible.

The etching depths depending on the Bi_2O_3 concentrations are summarized in Table 8-3. A relation between the etching depth and the oxide concentration was found and the imprints for the ink AgBi90 are, with a depth of 128 nm, twice as deep as for the ink AgBi10 (62 nm). This explains the reduction of R_p and probably the increased j_{02}, as the surface is stronger etched with increasing Bi_2O_3 contents, albeit the etching depth is for all inks below the junction depth of ~0.4 µm and direct evidence for the penetration of the emitter was not found; however, it can not be excluded as only a limited area of the contact was analyzed.

The etching depth of Ag-crystallites on samples with a different diffusion was studied as well. In Table 8-3 the results for samples with emitter sheet resistances of R_{SH}=55, 70, and 90 Ω/sq is summarized. The samples were metalized with ink AgBi30 and fired at T=730°C. A relation between the emitter doping and the imprint depth was not found. The etching depth is for all emitters in the same range of 80-100 nm. The sample surfaces, independent of the emitter sheet resistance, are heavily attacked and a dense network of geometric footprints of Ag-crystallites is found. The doping profiles can be seen in chapter 9 Fig. 9-14. The thickness of a defect-rich layer at the sample surface, caused by the phosphorus diffusion, obviously does not influence the etching if pure bismuth oxide is used. Also the number of imprints seems not to be dependent on the emitter diffusion, at least not in the studied range. Bismuth oxide is therefore a very effective contact promoter and even on emitters with a high sheet resistance it should be possible to perform a low ohmic contact.

ink	etching depth [nm]
AgBi_10	61,6
AgBi_30	93,2
AgBi_50	99,7
AgBi_70	104,9
AgBi_90	128,9

Table 8-3: Etching depths for different inks, fired on a 55 Ω/sq emitter at the optimized temperature of T=730°C

R_{SH} [Ω/sq]	etching depth [nm]
55	89
70	82
90	97

Table 8-4: Etching depth of Ag-crystallites on (100)-oriented silicon with different emitter sheet resistances. The emitters were contacted with the ink AgBi30 and fired at T=730°C.

8.2.3 IV-results on 15.6x15.6 cm² mc-Si solar cells

Motivated by the results obtained on small 5 cm x 5 cm Cz-silicon solar cells the performance was tested of ink AgBi10 on large-area mc-Si solar cells. The ink with the lowest oxide content was used, as comparably good values for the contact resistance of $R_c x W$<1 Ω cm were obtained by a moderate etching of the contact interface. The cells with an emitter sheet resistance of R_{SH}=65 Ω/sq were metalized by aerosol seed layer printing and light-induced plating. In advance of the plating step, the cells were co-fired in an in-line furnace in order to prove the industrial feasibility. Five cells were fabricated at each temperature.

The efficiency, the series resistance (R_s) and the shunt resistance (R_p) are plotted as a function of the firing temperature in Fig. 8-15. The cell performance is again strongly dependent on the firing temperature and a maximum was found for a furnace set temperature at T=880°C. Up to temperatures of 880°C the cell efficiency is increasing due to an improved series resistance. As all cells have the same base material, the same amount of plated silver, and are fabricated under the same conditions, the series resistance represents the contact resistance and therefore the contact quality. With increasing firing temperature the contact quality seems to be improved as the series resistance drops, but at the same time, the shunt resistance is reduced as well. For firing temperatures below T=880°C, the values for R_p are above 5000 Ωcm² and a detrimental effect on the cell efficiency is barely visible. For firing temperatures T>880°C the shunt resistance drops to values of only R_p=2000 Ωcm² whereas the series resistance remains constant, therefore reducing the cell efficiency. The best solar cell, fired at the optimized temperature of T=880°C, achieved an efficiency of η=16.3% and had a FF of 77.9%.

The metallization of an industrial solar cell and the formation of a low ohmic contact with a simple two-component ink (silver + bismuth oxide) is possible. On the one hand, bismuth oxide is an effective contact promoter with a strong etching behavior. A high density of Ag-crystallites can be formed on the contact interface if Bi_2O_3 is present and the formed glass layer is thin enough to guarantee a low ohmic contact. On the other hand, the etching of the ink is almost too strong and with increasing firing temperature the IV-parameter j_{02} and R_p are worsened. The production window for a good electrical contact is very small and solar cells have to be fired at an accurate temperature with a deviation of only ΔT=20°C. As soon as an electrical contact has been formed, the shunt resistance is additionally reduced to values of R_p<7 kΩcm².

In a further experiment, the bismuth oxide was incorporated into a glass system. The exact composition of the glass system is proprietary. According to the basic chemical reaction between silicon and a glass frit, the reaction is supposed to be less aggressive and occurs also in a broader range of temperatures. Solar cells, metalized with an ink based on silver and glass, should have a wider production window in terms of being less sensitive to the temperature variation. During firing, the glass frit becomes liquid at moderate temperatures below the contact formation temperature, wetting the silicon surface. The reactive glass components are homogenously distributed on the contact interface and the redox reaction can be better controlled. Improved values especially for the shunt resistance and j_{02} are expected, as the etching depth should be reduced and the glass frit additionally acts as a diffusion barrier for metal impurities.

Large-area mc-Si solar cells with an emitter sheet resistance of R_{SH}=80 Ω/sq were produced and metalized. The seed layer ink was a lead-free ink, based on silver and a bismuth based glass$_{Bi2O3}$ frit. The cells were fired in a belt furnace with a temperature deviation of ΔT=100°C. Four cells at each temperature were fired, starting from T=850°C to 950°C. As it is expected that a shunting of the cell is strongly reduced due to the presence of the glass frit, the temperatures are higher than in the previous experiment where an effective contact formation was observed for set temperatures T>820°C. The efficiency and the *FF* as a function of the temperature and the dark *IV* curves for different temperatures are shown in Fig. 8-16. The *FF* and also the efficiency are less dependent on the temperature compared to the results using the pure oxide. The dark *IV* characteristic does not show either a connection between j_{02} and firing temperature. The *FF* are on a quite high level of 78% with a standard deviation of 0.3%, and the efficiency is constant at around 16.5% ($\Delta\eta$=0.1%) for solar cells fired at T=880°C-920°C. For higher and lower firing temperatures (T=850°C and T=950°C), the values for FF and η are only slightly reduced. For temperatures below T=850°C, the activation energy, necessary for the contact formation, is too low and for high temperatures T>950°C the contact formation is too effective; the density and size of Ag-crystallites is increased but simultaneously the formed glass layer is getting too thick and therefore the contact performance is decreased. This experiment clearly demonstrates the advantages of using a glass frit instead of the pure oxide.

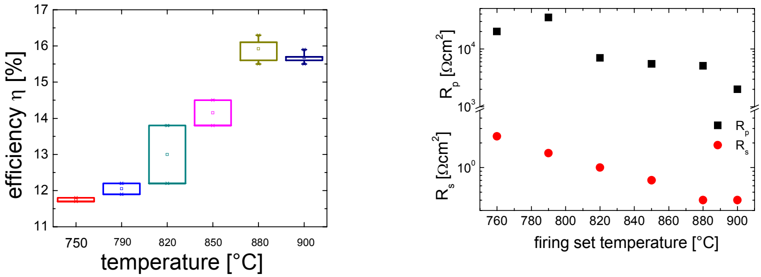

Fig. 8-15: Cell efficiency as a function of the firing (set temperature) for large area mc-Si solar cells contacted with a seed layer ink based on pure bismuth oxide and silver (left) and the values for R_s and R_p as a function of the temperature (right).

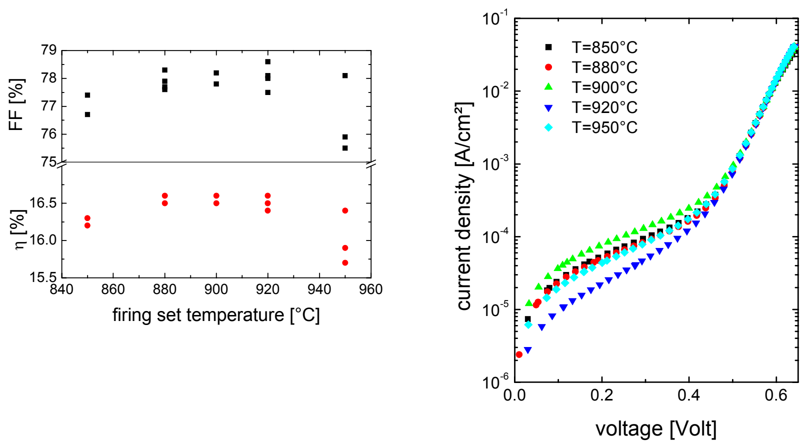

Fig. 8-16: Lead-free seed layer ink, based on glass$_{Bi2O3}$. Results from a illuminated IV measurement (left) and the corresponding dark IV curves (right).

The use of a glass system instead of the pure metal oxide improves the cell results and also the process stability. The next section answers the question of how much glass can be added to a contact ink. The glass system used to study the dependence of the glass amount on the contact quality is based on leaded $glass_{PbO}$. As the optimum firing temperature for a silver ink containing a glass frit has its optimum on a broad plateau around T=900°C, it was kept constant at this temperature for all different inks with different glass contents.

8.3 Seed layer inks, based on silver and glass system

As the reactive component in a front contact paste/ink is the metal oxide, here incorporated in a glass frit, the amount of $glass_{PbO}$ used in an ink influences the contact formation. With an increasing glass content, the size and the number of Ag-crystallites and also the fraction of the opened SiN_x-layer is increased, see SEM images from Fig. 8-19. These images show that increased glass content has a similar effect on the contact interface as increased bismuth oxide content. An improved contact performance with increased glass content can be expected, albeit the TLM and also the IV-measurements show a different image (see Fig. 8-17 and Fig. 8-18). These results are comparable to the results of the experiment where the Bi_2O_3 content was varied, apart from the fact that in the case of the bismuth oxide experiment, the contact resistance was reduced with increasing glass content which is not the case for the glass frit experiment. The contact resistance is increased as soon as more than 10 m% of glass is added to the silver ink. The increased glass content supports the redox reaction and more Pb is formed, more Ag can be solved, the number and the size of Ag-crystallites are increased but at the same time, SiO_2 is formed and the thickness of the insulating glass layer is increased. If too little glass <1m% (of the total ink) was present, no crystallites were formed, the SiN_x-layer was hardly opened and the measurement of a value for the contact resistance was not possible. For glass loadings of more than >30m% the SiN_x-coating was totally removed, a high number of large Ag-crystallites was found, which were covered by a thick insulating glass layer, and again high contact resistances were measured. The optimum glass content, represented by a sufficiently large number of Ag-crystallites and a possible thin glass layer, is found somewhere in between. No significant difference in the contact resistance is observable in the range of 2 m% to 10 m% of $glass_{PbO}$. Remarkable is the broad range in which the glass content can be varied. The contact and the cell performance are quite stable between 2 m% and 30 m%. Even if one third of the ink consists of glass, *FFs* of more than 78% were measured. Similar to the experimental results for high oxide contents, the values for j_{02} and R_p are reduced with increasing glass content, albeit on a higher level and the effect is less detrimental for the cell efficiency.

The glass content has of course an influence on the mechanical adhesion; it is the adhesion promoter, the “glue”, for fired silver contacts. As the contact consists of two layers, the seed layer and the plated LIP-silver and has therefore two bonds, where the contact can be detached in a pull test. It has to be distinguished whether the junction between seed layer and wafer and/or between LIP-silver and seed layer silver is the weak bond. For low glass contents <2m% the adhesion was reduced as well as for contacts where the glass contents exceeds 20m%. In the first case the contacts were detached under a tape test on the interface seed-silicon thus, the total contact was removed. The amount of glass was just too little and the adhesion between seed layer and silicon is too weak. For the contacts with high glass content, the weak bond is the junction seed layer-LIP silver. In this case, the problem with adhesion is the same as for the contacts with high oxide loadings, see above, the seed layer contains too high amount of non-metallic materials and the LIP-silver can not form an intimate metallic bond. Therefore, also for the mechanical adhesion the optimum glass content seems to be somewhere between 2% and 10%.

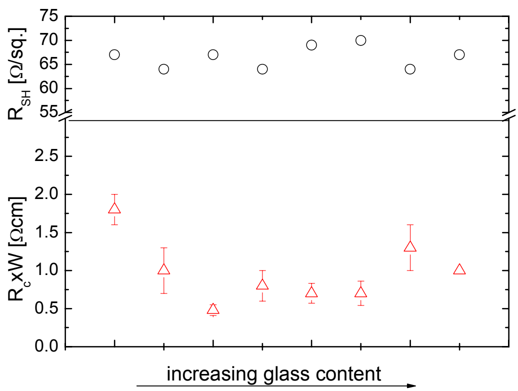

Fig. 8-17: Contact resistance (normalized) as a function of the glass$_{PbO}$ content. The emitter sheet resistance is plotted as a control parameter for the measurement.

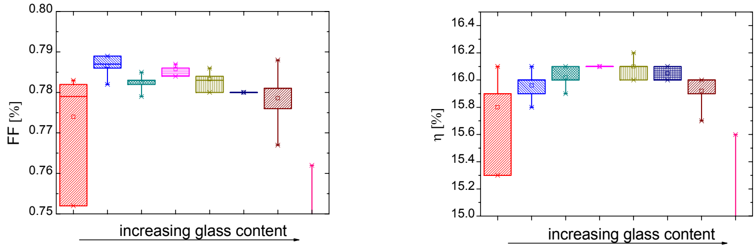

Fig. 8-18: IV-parameter for large area mc-Si solar cells contacted with a seed layer ink, based on leaded glass$_{PbO}$ as a function of the glass concentration.

The experimental data determined an optimum value for the glass content of 2 m% - 10 m%. The glass is necessary to form the electrical contact; however, too much glass is detrimental to the electrical performance. The thickness of the glass$_{PbO}$ layer is dependent on the glass content in the ink and also on the contact height. What is the necessary height of the glass layer? In order to give a lower bound for the glass content, the glass frit theoretically consists only of lead oxide. Assuming a seed layer printed contact with a height of 1 µm, printed with an ink containing 5 m% pure PbO (density ρ_{PbO}=9.53 g/cm³) and 95m% silver (ρ_{Ag}=10.49 g/cm³), the resulting glass layer thickness can be calculated as d_{glass}=58 nm, which is hardly sufficient to open the ARC coating. Theoretically, only for the opening of the 70 nm thick SiN_x-layer according to Eq.7-2, a layer of at least 60 nm pure PbO would be necessary. The 70 nm thick SiN_x-layer (density $\rho_{(PECVD)}$=2.4 g/cm³) is oxidized, resulting in an 76 nm thick amorphous SiO_2-layer (density $\rho_{(a\text{-}SiO2)}$=2.2 g/cm³), which is solved and added to the glass layer. In total, an insulating glass layer of more than 100 nm after the reaction is present if the whole SiN_x coating is opened. This means that an ohmic contact is impossible. If a glass frit is used instead of the pure oxide, the resulting insulating layer is even thicker. How is it possible that even with inks, containing less than 5 m% of glass frit, low ohmic contacts can be achieved? Fortunately, the contact formation is quite inhomogeneous and the thickness of the glass layer at the contact interface varies strongly, from a few nm up to several 100 nm. On areas with a thick glass layer, an electrical contact between bulk silver and emitter is impossible, whereas on contact points (grown Ag-crystallites), the glass layer is quite thin and either a direct or a tunnel contact is possible. Additionally, it is not necessary to open the whole passivation layer to create a low ohmic contact, as shown in the next chapter. Using the ink developed here an maximum efficiency of 16.8 % was achieved for large-area multicrystalline silicon solar cells see also chapter 11.

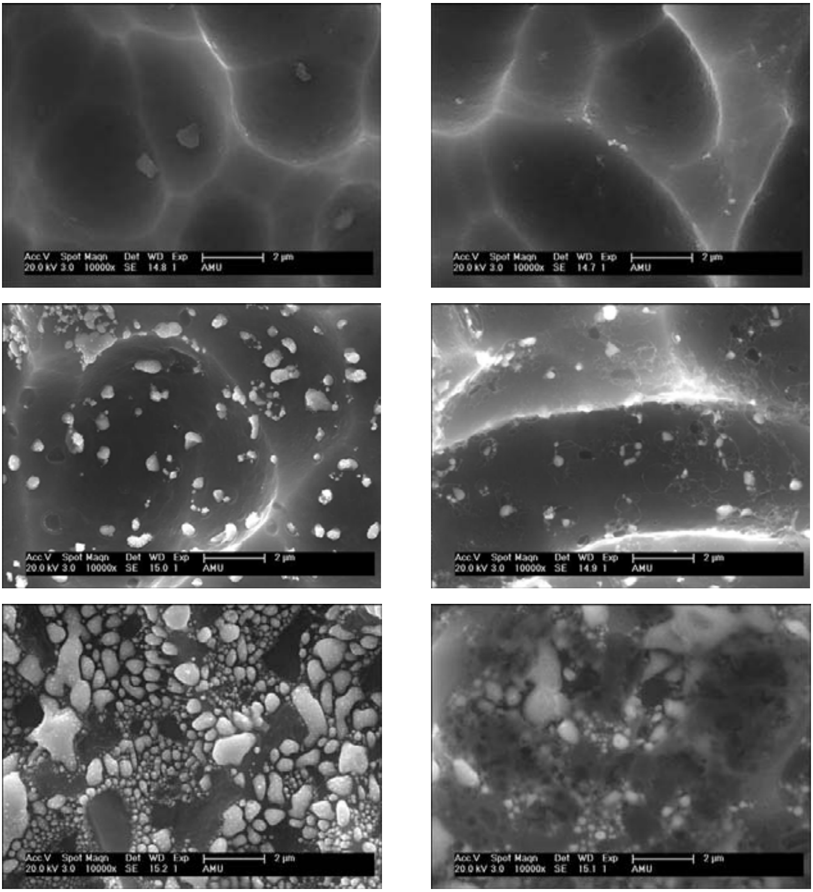

Fig. 8-19: SEM images of the contact interfaces for increasing glass content top to bottom. The pure Ag-crystallites (left) are visible if silver and the insulating glass layer are removed in an acid bath. On the right pictures the increasing glass thickness is visible.

8.4 Chapter summary

In the present chapter, different contact inks have been fabricated and tested on silicon solar cells. The inks only contain as solid components silver and a metal oxide or a glass system. In the first part of the chapter the influence of a reactive metal oxide, bismuth oxide, on the metal-silicon interface is studied by microscopic analysis. The electrical contact and cell parameters are used to interpret the observation. Bismuth oxide as an additive to silver is a rather effective contact promoter, the etching of silicon is even too strong and finding the right firing parameter is difficult. The formed contacts tend to shunt the pn-junction and/or defects are generated in the space charge region resulting in a strongly increased value for j_{02}. Never the less it was possible to fabricate multi-crystalline silicon solar cells with an efficiency of η=16.3%. The used ink was based only on silver and bismuth oxide. Further more the advantages of using a glass frit instead of the pure oxide was tested for both, leaded glass and bismuth oxide based glass. It was found, that the cell results are less dependent on the firing temperature which can be explained by the moderate reaction between the bismuth glass and the silicon. The contact formation occurs in a broader range of temperature and the values for j_{02} and R_p are not related to the temperature. Finally the optimum glass content is determined for an ink using a leaded glass system. For a seed layer application where the deposited ink height is only 1µm, the glass content is less critical and can vary in a broad range of 2-20m%. Using the ink developed here a maximum efficiency of 16.8 % was achieved for large-area multicrystalline silicon solar cells.

9 Contact formation and electrical properties

The properties of fine-line printed, fired, and plated (SFP) contacts are investigated in this chapter. The investigated contacts are two layer contacts which are formed by a combination of fine-line aerosol print and light-induced plating (LIP). For seed layer print the optimized ink SISC (**s**eed layer ink for the metallization of **s**olar **c**ells), developed during this work is used. A cross section image of a SFP contact is shown in Fig. 9-2. The thinly printed seed layer is different from the LIP silver due to its coarse structure; it is additionally highlighted in a red circle. The contact is composed of conductive LIP-silver, printed bulk silver, a glass layer, and a layer of silver crystallites grown through the dielectric layer into the emitter. Unfortunately, the metalized area is not equal to the contact area; therefore the effective contact area needs to be determined. In the first part of this chapter the interface between seed layer and silicon surface is discussed. Responsible for an electrical contact are small silver crystallites, formed directly on the interface. The Ag-crystallites are in direct contact with silicon. In Fig. 9-1 a schematic drawing of two types of crystallites is shown. In case of type1 the silver crystallite is isolated from the bulk silver by a thin glass layer. In case of type2 the crystallite is in direct contact with the silver finger. The two types of contacts are used to explain the discrepancy between the theoretically expected and experimentally determined resistivity, which is about a factor of 10^5.

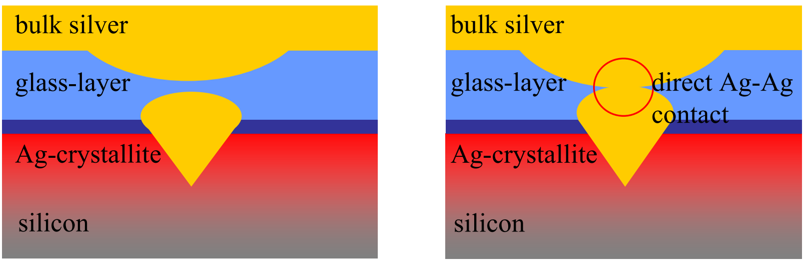

Fig. 9-1: Model of the microscopic contact area. The electrical contact is determined by a small contact area between Ag-crystallite and bulk silver, both of which are usually separated by a thin glass layer (type1, left). Crystallite and bulk silver can also be in direct contact (type2, right).

The microscopic analysis is additionally used to learn more about the growth mechanism of silver crystallites in silicon. The SEM and TEM images are interpreted based on the results of chapter 7. Possible current paths are discussed and compared to the results with thick film contacts. The most efficient and in many cases the only possible current path is via Ag-crystallites. Additionally, the influence of the emitter doping on the growth of silver crystallites is investigated. From standard screen printed solar cells it is known that a slightly reduced doping concentration makes an effective contact formation impossible. In case of the SISC ink it was possible to contact solar cells with an emitter sheet resistance R_{SH} of more than 120 Ω/sq. In general, effective crystallite growth is observed on a $POCl_3$ diffused emitter as long as the surface concentration is higher than $N_D > 10^{19}$ cm^{-3}. It is suggested that a defect-rich layer on the surface of the emitter, consisting of SiP clusters, is responsible for the growth of Ag-crystallites.

In the second part of the chapter, the influence of the contact geometry, especially the seed layer height on the electrical contact properties like line conductivity and contact resistance, is investigated before and after plating. The question of how much ink per contact area is required in order to achieve a low ohmic contact on a standard silicon solar cell is answered. The relationship between contact resistance and contact height is measured by using the transfer length model (TLM). By taking SEM images of the metal-semiconductor interface, it is then proven that a contact height of less than 1 µm or a minimum total ink amount of only 4-6 mg is sufficient to contact a large area (15.6 cm x 15.6 cm) silicon solar cell. It was found that a possible thin contact layer is beneficial for both: the finger conductivity, as the fraction of LIP silver is increased, and the contact resistance, as the contact formation is more effective. Finally, the results are summarized, the main aspects are highlighted, and outlook for further work is given.

9.1 Contact formation and microstructure

The contact formation for fine-line printed contacts is principally the same as for thick-film contacts. A detailed analysis of the contact formation using thick film pastes is given by G. Schubert [23, 54] and a review is given by Refs. [66, 148]. However, there are some distinct differences. For fine-line contacts, both the line width and the line height are reduced. The amount of ink necessary to contact a 15.6 cm x 15.6 cm large solar cell is about 20 times lower than the amount of paste deposited in a screen print process, meaning as well, that the amount of ink per contact area is more than 10 times lower as the contact area is smaller; therefore, the contact formation needs to be more effective. The reduced ink density has the advantage that more oxygen, which promotes contact formation, can reach the interface. At the same time, volatile reaction products like nitrogen from the SiN_x coating, and carbon dioxide and water, formed by the combustion of organic ink components, can be released easier. Furthermore, due to the reduced contact height (reduced ink density), less reaction partners per contact area are present and the ink composition, i.e. the ratio of silver:glass, must be adjusted. The main difference between these contacts, however, is the different application. Whereas a thick-film contact has to have a high lateral conductivity, and at the same time a low resistivity, the seed layer printed contact only has to be optimized for superior contact properties as the lateral conductivity is done in a further process step. In this chapter the contact formation of a seed layer printed, fired and plated (SFP) contact is described. SEM and TEM images are used to investigate the microstructure in order to understand the contact mechanism and current transport on an optimized SFP contact. In Fig. 9-2: a cross section of a SFP contact is shown. The relation of seed layer thickness, especially after firing, to LIP thickness illustrates the negligible contribution of the seed layer to the line conductivity.

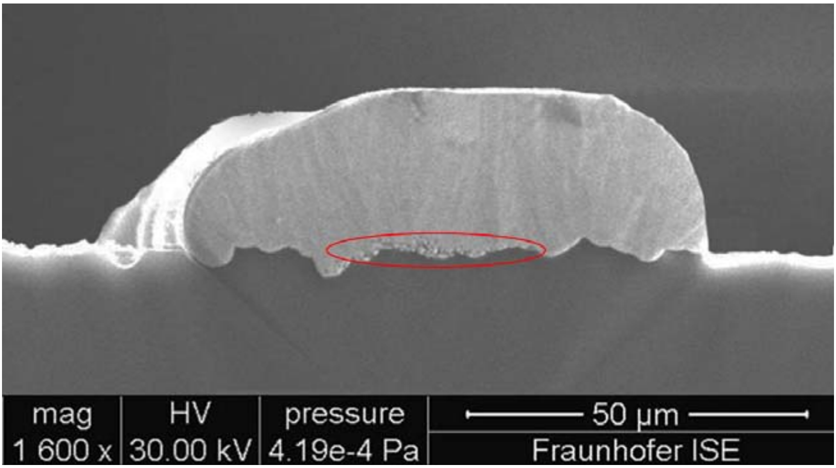

Fig. 9-2: SEM image of a SFP-contact cross section. The aerosol printed, fired seed layer is marked. More than 97% of the contact consists of LIP silver.

The contact formation and the microstructure can be investigated by taking SEM or TEM images of the contact interface either from a top view or from a cross section image. The sample preparation for a top view of the contact interface is shown in Fig. 9-3 a)-e): the different layers of an SFP were removed by a HNO_3/HF sequence. We start with a complete finger Fig. 9-3 a) and remove the formed contact layers stepwise.

Fig. 9-3 a) and b) are untreated samples, b) is after firing of the seed layer and a) after light induced plating. No further sample preparation is necessary for taking SEM images. The bulk silver (printed and fired silver + plated silver) can be removed in nitric acid. Therefore, the samples are etched in HNO_3 69% at 90°C for 10 min, the result can be seen in Fig. 9-3c). The contact silver crystallites, which are protected by the glass layer, are remaining and are visible through the thin glass layer. In a further etching step the glass layer is removed in fluoric acid (HF 5%) at room temperature (RT) within 4 min. During this HF etch, the SiN_x-coating can be thinned as well [149], therefore, all samples saw the same etching sequence, additionally it was proven by SEM images that next to the contact area the SiN_x-coating is still present. The remaining silver crystallites are now clearly visible, including their geometric structure, see Fig. 9-3 d). The silver crystallites can be removed by immersing the sample in nitric acid again (HNO_3, 69%) at 90°C for 10 min followed by a further HF dip (HF, 5%) at RT for 1min. Fig. 9-3 e) shows the plain silicon surface with the footprints of the removed Ag-crystallites.

a)

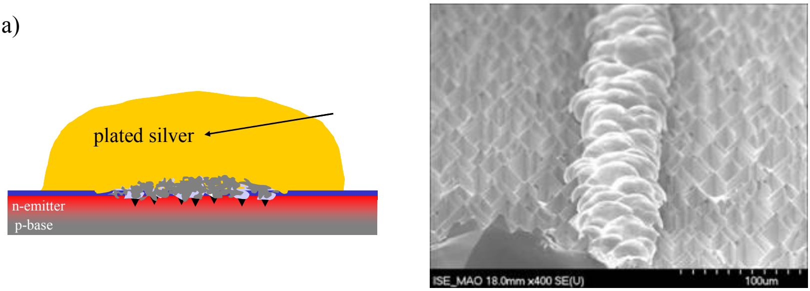

b)

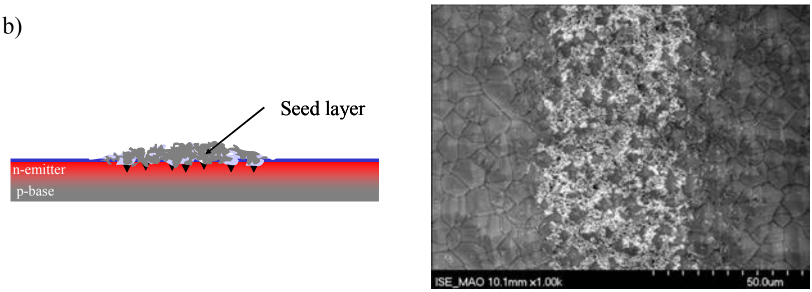

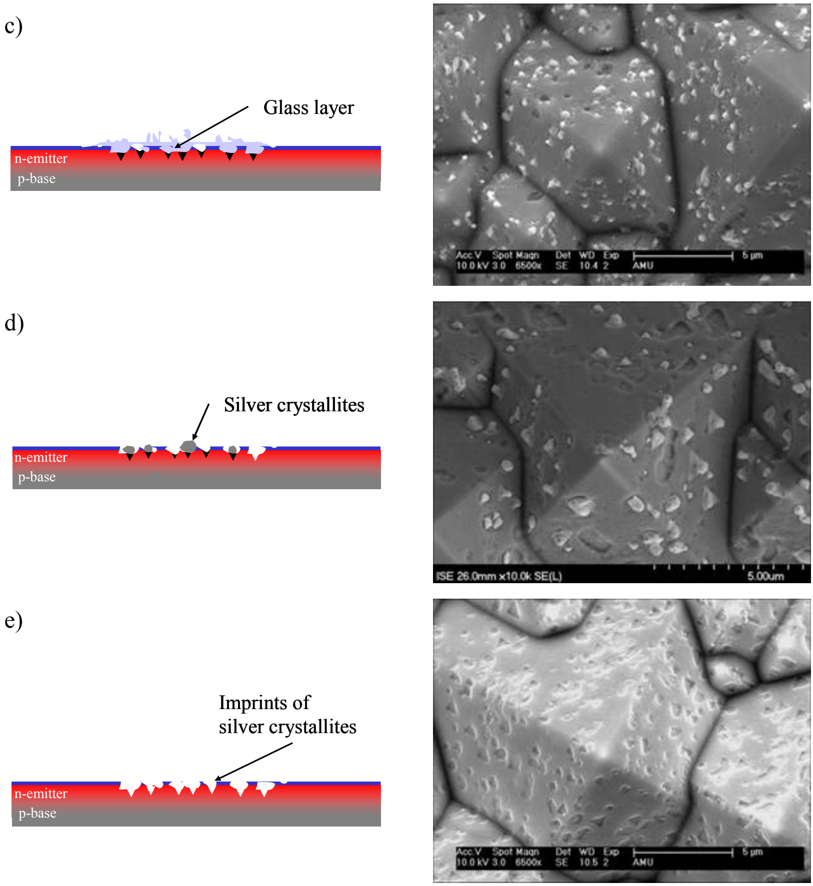

Fig. 9-3: SEM-images of the contact interface; the contact layers are sequentially removed

9.1.1 Effective contact area

The theoretical value for the resistivity of silver with n-type silicon is in the range of ρ_c~1x10^{-7} Ω cm²-1x10^{-8} Ω cm² for doping concentrations above N_d>1x10^{20} cm^{-3} [23]. The measured values for ρ_c for printed and fired contacts on highly doped emitters are in the range of ρ_c~1x10^{-3} Ωcm². The resistivity for a single silver crystallite on a 35 Ω/sq emitter was determined by Ballif and Huljic [55, 150], using conductive AFM and found to be ρ_c=2x10^{-7} Ωcm². According to these measurements, only 0.01% of the contact area needs to be covered by Ag-crystallites in order to explain the measured values, which are on the order of $1x10^{-3}$ Ωcm², see Fig. 9-4. However, about 1-20% of the contact area is typically covered by Ag-crystallites. In Fig. 9-5 the silicon surface after removal of the silver contacts is shown. The geometric imprints are the footprints of contact Ag-crystallites; their shape is dependent on the crystal orientation [62, 65]. On (111)-oriented silicon surfaces, the Ag-crystallites have a triangle foot print and a flat, lens-shaped appearance. On (100)-silicon surfaces, the footprint is square-like and the crystallite has the shape of an inverted pyramid. The top of the crystallites (outside the silicon surface) is randomly mostly spherically shaped, except for when they are in close contact with the bulk silver.

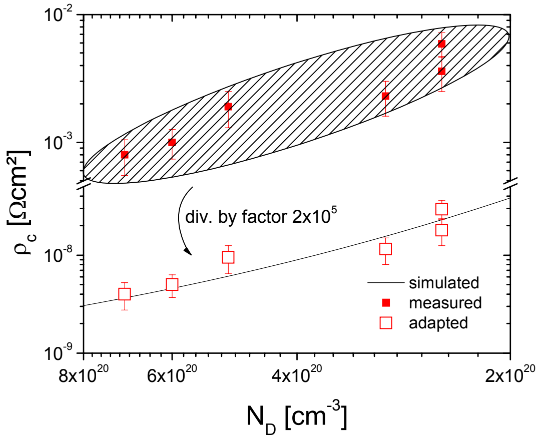

Fig. 9-4: Resistivities of SFP contacts as a function of N_D, determined from TLM-measurements. The theoretical ρ_c is illustrated by the bold line. The red squares are the real measurements (small squares) divided by a factor of $2x10^5$.

In the example given, about 10% of the contact area is covered by silver crystals. Assuming these 10% consist of direct silver-semiconductor junctions (type2), the measured values for ρ_c should be much lower. To explain the discrepancy in ρ_c, theoretically and experimentally determined by TLM measurements, as seen in Fig. 9-4, TEM images on a contact cross section were performed. To give an estimation of the real effective contact area, a TEM measurement of a contact cross section was performed. The TEM image of a metal-silicon interface can be seen in Fig. 9-7. The contact crystallites, which are grown through the anti-reflection coating into the silicon surface, are either of type2 and in direct contact with the conductive silver (bulk silver), or, more likely, of type1 and covered by an insulating glass layer. The measureable contact is either a metal-insulator-metal-semiconductor junction, where contact resistance is determined by the tunneling process of the charge carriers through the glass, or a metal-semiconductor junction with a very small contact area. The presence of a glass layer between the contact crystallites and the contact bulk silver was reported by several authors [22, 54, 56, 59, 61, 62, 65, 66, 146, 151]. In this work the resistances of SFP contacts were measured, which were processed on emitters with different surface doping concentrations N_D (see below). The measured values show the expected dependence on N_D, however, at a much higher level than predicted. A factor of $2x10^5$ separates the theoretical values from the experimental values. This discrepancy can be explained by taking the *effective* contact area into account. The TLM-measured value for ρ_c implies that the actual metal-semiconductor contact area is equal to the metalized area. However, for the investigated SFP contact this is not the case, see Fig. 9-5.

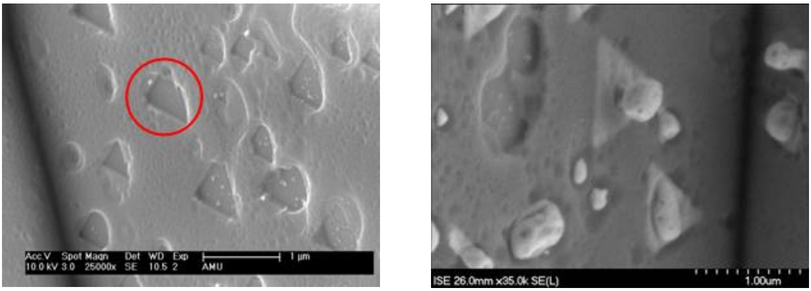

Fig. 9-5: SEM image of the Ag-crystallite (right) and imprints (left) in a (111)-oriented surface, after removing the metal contact. The SiN_x-layer is still present apart from the positions where an Ag-crystallite has grown through the nitride and into the silicon.

Direct contact is only possible on very distinct positions. The size of the crystallite imprints on the silicon surface were determined by taking several SEM images on 6 different contact positions, randomly distributed over one solar cell. In total, 40 footprints were analyzed and the average contact size was determined to be

A_{cr}=0.156 µm², together with an area density of about 0.77 crystallites per µm², which is a coverage fraction of about 10%. In Fig. 9-6 an SEM image is shown on one of the investigated contact interfaces. Only the contact silver was removed; nevertheless, some of the Ag-crystallites were removed as well, which means that not all of the crystallites are covered by an insulating glass layer, but rather some are potentially type2 contacts. Type2 contact points cover about 1% of the contact area and if the area of the foot prints is used for the calculation, the resistivity is still too low to explain the discrepancy of 10^5. However, if we are assuming that the potential contact area between bulk silver and silver crystallite is not defined by the footprints (silver-silicon junction) but by the direct silver-silver junction, the difference of $2x10^5$ can be explained. The area for a direct silver-silver junction is approximated by a circle with a radius of 10-20 nm from a TEM image Fig. 9-7. As the determination of the direct contact area is quite inaccurate, the only conclusion which can be drawn is that the relatively small number of type2 contacts is already sufficient to explain the measured contact resistance. All type1 crystallites are either inactive or their contribution to the current flow is rather small. Not only the crystallite size and density, but moreover the thickness and conductivity of the intermediate glass layer is important for type1 contacts. G. Schubert [23] has proven that the contact resistance is strongly limited by the intermediate glass layer. When the layer is removed and the Ag-crystallites are contacted directly by liquid conductive silver, all crystallites are type2 contacts and a resistivity could be measured in the range of the theoretical expectations.

Additionally, it must be taken into account that if all the current is flowing over such a small area, it is very likely that the contact resistance is also determined by the spreading resistance under these contacts [37].

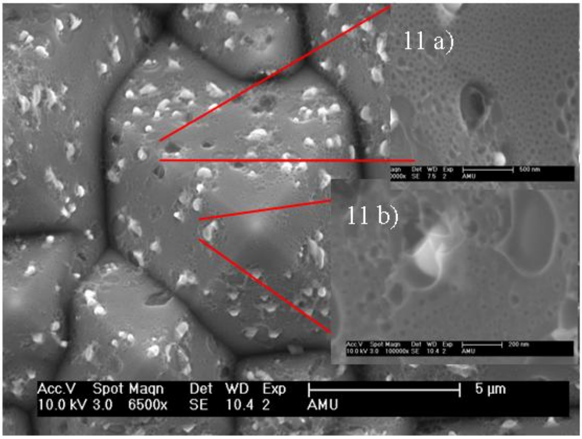

Fig. 9-6: SEM image of the contact interface. The bulk silver is removed in nitric acid and the contact Ag-crystallites covered by a thin glass layer are visible a). On some positions where no glass layer is present, the Ag-crystallites are also removed and a direct contact to the bulk silver was possible.

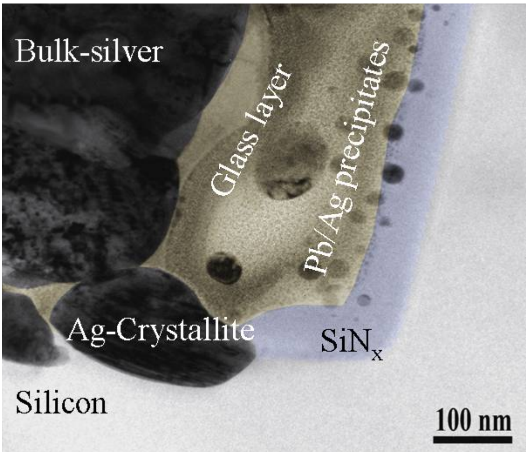

Fig. 9-7: TEM image of a seed layer printed and fired contact. Visible is the Si-substrate; the SiN_x-coating, penetrated by the contact Ag-crystallites; a glass layer, filled with Ag-Pb precipitates; and the bulk silver, which is in close contact with the Ag-crystallites. Only in the position where an Ag-crystallite has grown, an electrical contact is possible.

9.1.2 Silver crystallite growth

For the growth mechanism of Ag-crystallites two theories predominate. The first possible mechanism describes the growth of silver crystallites from silver which is solved in the liquid glass and transported to the silicon interface [47, 56, 150]. During cooling, the silver from the glass and the solved silicon re-crystallize and the geometrically shaped silver crystallites, which grow epitaxial on the silicon lattices, are formed [56]. The second proposed reaction mechanism is the "etching" of silicon by a redox reaction Eq.7-2 and Eq.7-3 where silicon is oxidized by a metal oxide and the produced silicon oxide is solved in the glass, while the reduced lead can solve high quantities of silver, which re-crystallizes during cooling in the form of Ag-crystallites in the opened, previously etched silicon position [58].

The origin of Ag-crystallites is very likely the condensation of liquid silver from a liquid Ag-Pb phase, which has been formed during an exothermic reaction between PbO and either Si or/and SiN_x. The amount of lead produced during the contact formation of a single crystallite can be estimated: The footprint of a single Ag-crystallite was determined by averaging the size of 100 footprints from SEM images to be 0.156 μm^2. The shape of the footprint is simplified as a cycle and the shape of the crystallite as a half dome with a volume of $V_{Ag\text{-}Cy}=2.3\times10^{-20}$ m^3. The average mass of a single crystallite can than be calculated to $m_{Ag\text{-}Cry}=2.43\times10^{-13}$ g (density $\rho_{Ag}=10.5$ g/cm^3).

The amount of lead, which is formed during the "etching" of SiN and silicon for one Ag-crystallite can also be estimated: The depth of the imprints is the thickness of the SiN_x coating plus approximately 50 nm of dissolved/etched silicon; in total 120 nm. The single volumes are $V_{SiN}=1.1\times10^{-14}$ m^3 and $V_{Si}=0.78\times10^{-14}$ m^3 which is equivalent to a mass of $m_{SiN}=2.6\times10^{-14}$ g and $m_{Si}=1.8\times10^{-14}$ g. During the contact formation, according to Eq.7-2 two mol Pb are formed while 1 mol Si (M=28 g/mol, $\rho_{Si}=2.33$ g/cm^3) or SiN_x (M=42 g/mol, $\rho_{SiN}=2.4$ g/cm^3) are oxidized. The amount of formed lead is therefore in total $m_{Pb}=5.3\times10^{-13}$ g, which is almost two times more than the mass of silver necessary to form a single Ag-crystallite. Therefore, sufficient lead is present and together with the contact silver, an Ag-Pb phase can be formed.

Another option for the silver source, from which the Ag-crystallites can be grown, is silver that has been solved in the glass. Glass was heated together with silver up to 800°C and kept at this temperature for 30 min. The hot liquid glass was poured in cold water to freeze the solved silver in the glass. A content of 1.7at% of silver could be solved in the glass. Other authors found similar results with 3at% at 900°C [54] and 8.5at% at 1000°C (2 hours) [23]. As the reaction time for the contact formation is only a few seconds and not several minutes or hours, the content of solved silver in the glass is negligible. For a seed layer contact (height 1 µm, width 50 µm, printed with an ink containing 5m% PbO_{glass}), about 17m% of silver has to be solved in the glass to form the observed number of Ag-crystallites (Ag-crystallite density 0.77 μm^{-2}, crystallite volume $V_{Ag\text{-}cry}=2.3\times10^{-20}\ m^3$). This is by far too much to explain the crystallite formation by silver solved in glass. The formation of Ag-crystallites from silver rich glass, reported by [61] is a possible mechanism; however, it can be excluded as the main source of silver for the Ag-crystallite growth.

Proposed is a combination of these two effects for the reaction mechanism. The source for the Ag-crystallites is definitely the silver-lead melt, which can be incorporated into the liquid glass. The Ag-Pb melt is formed during the redox reaction of lead oxide with Si/SiN_x. The PbO from the glass frit reacts exothermically with the SiN_x layer or directly with the silicon. During the redox reaction, silicon is anisotropically etched (see Fig. 9-8). The formed SiO_2 is dissolved in the glass, together with the highly reactive lead, allowing a high amount of silver to be solved due to the high lead content. It is especially silicon from defect-rich surfaces which tends to be oxidized and solved; see below. In Fig. 9-10a)-d), our understanding of the crystallite formation is explained. The Ag-crystallites are formed from the liquid Ag-Pb-glass phase. They crystallize during cooling, corresponding to the Si-lattices, and an intimate contact with the silicon is formed. An explanation for the formation of a direct silver-silicon contact, as observed in high resolution TEM studies by Refs. [56], [62], can be given by the formation of a local Ag-Si eutectic. Even if the reaction temperature is below the eutectic temperature of 835°C, a formation is possible, due to the additional energy supplied by the exothermic redox reaction. Another explanation is the dissolution of silicon into the reactive Ag-Pb-glass melt. During cooling, the locally solved silicon re-crystallizes along the Si-lattice in a diamond structure at the same time silver recrystallizes as face-centered cubic and forming a direct Si-Ag junction. The lead and the glass on top of the Ag-crystallite are still liquid at this point and silver, solved in the Ag-Pb-glass, diffuses towards the crystallite and grows on top of the silver seed crystal. The diffusion of silver in liquid glass is quite high [54]. The more silver is solved, either in the glass or in the form of the Ag-Pb eutectic, the larger the crystal grows. The bulk silver is solid at each state of the firing step, as the temperature is far below the melting point of silver. The crystallites are increased until the bulk silver limits the growth or until the viscosity of the glass phase is too high and a further diffusion of silver to the crystallites becomes impossible. The silver-lead phase crystallizes in the form of small precipitates in the glass layer. The crystallites, if they reach the bulk silver, have a flat surface and appear to be in close contact with the bulk silver above, but a small glass layer is usually present. Otherwise, all Ag-crystallites would have been removed during a HNO_3 etch, rather than just a few (see Fig. 9-9 and Fig. 9-6).

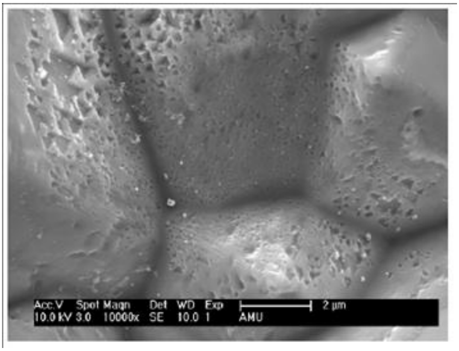

Fig. 9-8: Glass-frit ink on textured (111)-Silicon: etching of the pure glass is visible after the samples were tempered for 5 min at 800°C in a box furnace. The glass layer was removed by fluoric acid (HF 5% at RT for 30 min)

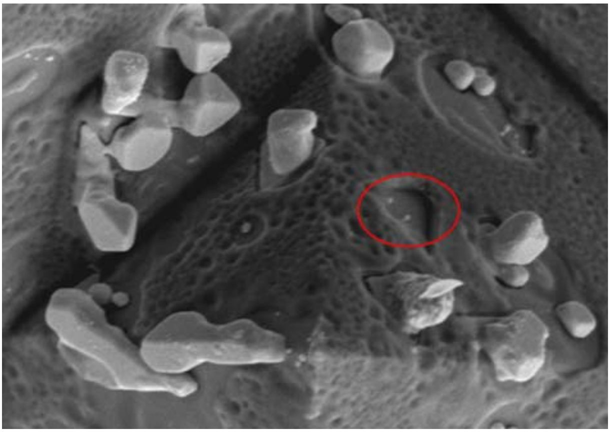

Fig. 9-9: Silver crystallites and footprint of silver crystallites at the contact interface, after removing the bulk silver in an HNO3 etching step. The growth of most Ag-crystallites seems to be limited by the bulk silver, as they have levelled surfaces

In Fig. 9-9, all described Ag-crystallite characteristics are visible: locally opened SiN_x layer, mostly circles of differing diameters, remaining silver crystallites with a flat surface, and an imprint from a crystallite, removed in a single HNO_3 etching step. These results can also explain the improved contact resistance if a slow cooling after fast firing of a contact is applied [152][23]. This step gives the crystallites more time to grow, as the solidification of the glass layer is reduced and more silver is able to diffuse from the glass to the crystallites.

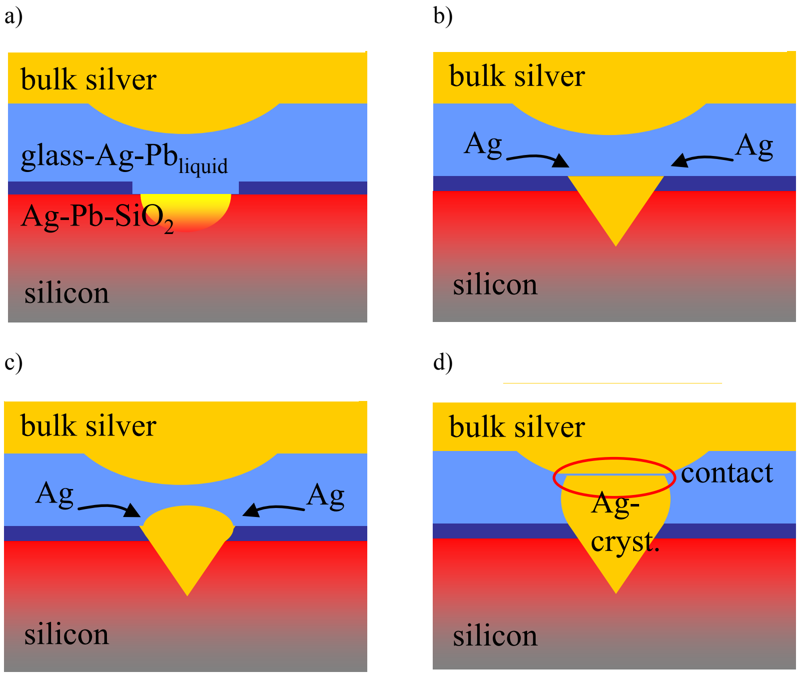

Fig. 9-10: Schematic drawing of contact formation. a) At temperatures above 700°C the glass is liquid and the redox reaction Eq.7-1 takes place. The formed SiO_2 is added to the glass melt together with the liquid lead. High quantities of silver are dissolved. During cooling, at temperatures <600°C the dissolved silver recrystallizes epitaxial on the Si-lattice. Dissolved silver diffuses toward the Ag-crystallite, the size of which is enhanced. d) The viscosity of the glass melt is too high, diffusion has become impossible, the Ag-crystallite is in close contact with the bulk silver, separated by a thin glass layer.

An additional proof of the redox-reaction theory can be given by using the results from chapter 7 with emphasis on the crystallite growth. The Ag-crystallites are formed during cooling at temperatures around 500-700°C, indicated by an exothermic peak in the DTA-signal. In Fig. 9-11 different examples are given for reactions between Ag-PbO/glass-Si. The eutectic is formed in all cases as expected at around 300°C. The second peak at higher temperatures, which is responsible for the crystallite formation, is only visible under the presence of oxygen, here in the form of lead oxide. These reactions were carried out under argon gas atmosphere to exclude the influence of gaseous oxygen. The DTA-signals for the reaction with glass or with PbO as a replacement are more or less the same. Both peaks are clearly visible. For the system Si-Pb-Ag, where metal is present but not the metal oxide, only the eutectic can be found. It appears that the reaction, which is responsible for the Ag-crystallite formation, needs the presence of both silicon and a metal oxide. In a further experiment, under the presence of synthetic air (oxygen) the reactions of the metals Pb-Ag and Si are investigated. If the presence of both oxygen and silicon is responsible for the crystallite formation, we would expect no peak for the system Pb-Ag apart from the melting point or eutectic, as silicon is missing. However, we would expect a second peak for the system Pb-Ag+Si. The data can be seen in Fig. 9-12. Even if no metal oxide or glass is initially present, the DTA-signal during cooling shows the same reactions as the system Si-PbO-Ag as during heating under synthetic air; Pb is oxidized to PbO, which then reacts with silicon. Therefore, it is possible to create a contact on a silicon wafer without the initial presence of any glass. G. Schubert fired under ambient air a mixture of lead and silver deposited on a Si-wafer, finding a high density of crystallites at the metal semiconductor interface [23]. Silver inks deposited on a wafer and fired under argon or nitrogen atmospheres, however, do not form a contact on silicon [131, 132].

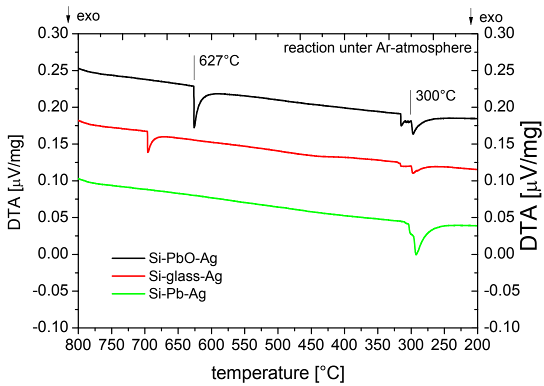

Fig. 9-11: DTA-measurement for different ink compositions under inert conditions during cooling.

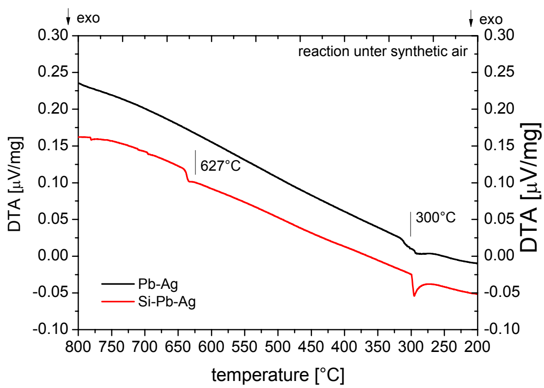

Fig. 9-12: DTA-measurement of Ag-Pb-/Si during cooling from 800°C to RT under synthetic air.

From this we can conclude that for the contact formation of silver on silicon, the presence of a metal oxide, initially present or formed during firing, is necessary. Firing under oxygen atmosphere is essential as it promotes the oxidation reaction. The additional reaction energy, set free from the oxidation of Si to SiO_2, helps to solve silver and is probably also responsible for the solution of Si in an Ag-Si eutectic and for the formation of Ag-crystallites. The redox-reaction theory is supported by the following effects: larger Ag-crystallites with higher crystallite density are found either by higher firing temperatures [153], longer temper times [152], higher $glass_{PbO}$ contents in the ink, oxidizing atmosphere during firing, or the presence of a defect-rich silicon surface (high N_D).

However, the detailed growth mechanism of the crystallites in the silicon surface, either from an anisotropic etching of $glass_{PbO}$ and the crystallization of silver from a Ag-Pb-melt or from a re-crystallized locally solved silicon and the Ag-crystallization from a formed silver-silicon eutectic, is not entirely revealed; especially not for the contact formation on a real solar cell. It is not only a reaction between the materials $glass_{PbO}$, silver and silicon, also structure, surface defects, dopants, and doping concentration on silicon playing an important role for the crystallite formation, as shown below in 9.2.

9.1.3 Current transport

In contrast to the Ag-crystallite formation, it is rather easy to explain the possible current paths on an SFP contact. Several current paths on a fired thick-film contact which is additionally plated are proposed, also see chapter 3. The transport of the charge carriers on a seed layer printed contact can be simplified to one. From our understanding, the main contact points are the Ag-crystallites as these are the only contact points between bulk silver and silicon. The rest of the contact area is covered by a SiN_x coating. The crystallites are homogenously distributed over the whole contact area, covering about 10% (for an optimized contact $R_c \times W < 1\ \Omega cm^2$). Therefore, only 10% of the SiN_x coating needs to be opened, which is advisable for two reasons. First, the more the SiN_x is dissolved, the thicker is the insulating glass layer and the worse is the contact resistance. Additionally, a locally penetrated SiN_x coating helps to reduce the surface recombination, even under the contacts. The glass content or the printing height should be adjusted in such a way as to allow the local opening of the SiN_x coating. The locally opened SiN_x-layer allows us to determine the main current transport mechanism. The only possible contact positions are the Ag-crystallites, as the rest of the contact area is covered by the insulating SiN_x-coating (see Fig. 9-5 and Fig. 9-7). Even if the SiN_x coating is partly or totally removed during the contact formation (see Fig. 9-33 and Fig. 9-34), the contact resistance is not improved.

Therefore, the only effective way for the current to pass from the solar cell emitter into the bulk silver is via the Ag-crystallites. All other current paths can be excluded.

9.1.4 Annealing

An annealing step often helps to improve the contact performance. Direct metal-semiconductor junctions and the contacts where the crystallites are separated by a thin glass layer are probably the positions where the contact can be further improved by an annealing step. In Fig. 9-13 the results of contact resistance measurements for different annealing temperatures and atmospheres are given. One sample is annealed under forming gas (FGA) and another under ambient air for 15 min. After annealing, the quality of both contacts is improved. Even if the contacts are starting at different levels in contact resistance, they reach their lowest values at annealing temperatures of 250°C, independent of the atmosphere. The positive influence of an annealing step under FGA is reported by [23, 154] and can be explained by the reduction of metal oxides on the surface of the glass layer [155, 156]. The number of small precipitates is increased and the conductivity of the insulating glass is improved. It is reported that silver, which is solved in the glass, forms small precipitates and a conductive silver layer on the glass surface [157]. As we find similar results for a contact annealed in air, we believe that in addition, the boundary between Ag-crystallite and the bulk silver is improved, especially for contact positions where the crystallites are in close contact with the bulk silver. The contact resistance for both structures, annealed in air or in FGA ambient, is strongly increased at annealing temperatures above 300°C or 350°C respectively. The temperature range between 300 and 350°C is the temperature where lead, and also the silver-lead eutectic, becomes liquid. At annealing temperatures above 300°C, the eutectic melts and the contact is restructured. It is possible that the liquid eutectic, which is formed close to the silicon surface, diffuses and some large precipitates are formed from many smaller ones or the liquid precipitates are moving from the soft glass into the bulk, reducing the conductivity of the glass layer. It is also possible that the eutectic found on top of an Ag-crystallite, melts and diffuses into the bulk, decreasing the distance between Ag-crystallite and bulk silver [23]. In summary, fine line printed contacts can be improved by an annealing step up to temperatures of 280°C.

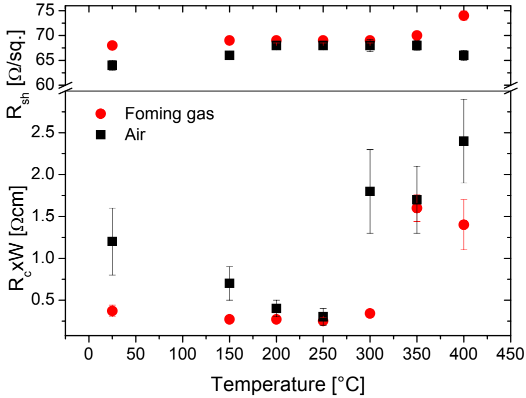

Fig. 9-13: Contact resistance measurements (TLM) of two samples, annealed at different temperatures and different atmospheres. The contacts are two layer contacts (fine line print + LIP).

9.2 Contact formation on different emitters

The full potential of silicon solar cells can be reached if low-ohmic contacts are formed using fine-line printed contacts especially on solar cells with a reduced emitter doping concentration. One of the technological efforts in PV research is to reduce the line width in order to reduce shading and recombination losses. These, however, make the effective contact formation even more complicated. To make use of the advantages of a fine contact structure, on an emitter with a reduced doping concentration, it is necessary to improve the electrical performance of the metal-semiconductor junction. Otherwise, the gain in current (j_{sc}) and voltage (V_{oc}) is overcompensated by a reduced fill factor (*FF*) due to an increased series resistance (R_s).

In this experiment we have investigated the contact performance of the seed layer metallization ink *SISC* on different materials and emitters. Solar cells were produced and analyzed on Cz-wafers with different emitter sheet resistivities. In advance some preliminary studies on silicon samples with different surface doping concentrations and different emitter profiles were performed. A short review of the defects on highly doped silicon samples is given and discussed with our results according to the Ag-crystallite growth.

9.2.1 Emitter doping and Ag-crystallite growth

Important for the formation of low ohmic contacts during a firing step is the number, or better the density, of silver crystallites at the metal-semiconductor interface. The Ag-crystallites have been studied in detail and also their function as main current paths was suggested, but their growth conditions, especially the influence on the emitter surface, are not clear yet. For the metallization of screen printed, or in general printed and fired contacts on solar cells, low sheet resistivities R_{SH}<100 Ω/sq, and high doping concentrations N_D>10^{20} cm^{-3} are necessary [150]. One reason for this is the theoretical dependence of the resistivity on the doping concentration (see chapter 3) but also the reduced number of silver crystallites. Their density seems to be dependent on the emitter sheet resistance and the emitter doping concentration at the surface, respectively [65]. Also the presence of a dielectric layer seems to have an influence on the quality of the contact [48]. In a first experiment, different emitters were prepared in a $POCl_3$ diffusion tube furnace on polished Cz-Si wafers. Four emitters with a shallow error function profile and one emitter with a deep diffused, Gauß-like profile were processed. The emitters with shallow profiles have surface doping concentrations between 2×10^{20} cm^{-3} and $8x10^{20}$ cm^{-3}, resulting in sheet resistances between 50 Ω/sq and 120 Ω/sq. The Gauß profile was achieved in a further diffusion step, also resulting in a sheet resistance of 120 Ω/sq and a surface doping concentration of N_D=7×10^{18} cm^{-3}. Additionally, two further samples were used to study the crystallite growth from a silver front side ink under standard firing conditions. One sample has an epitaxial grown emitter with a surface doping concentration of N_D=10^{20} cm^{-3} and a sheet resistance of 30-40 Ω/sq [158]. The other sample is non-diffused p-type silicon with a doping concentration of 10^{16} cm^{-3}. The profiles of the diffused emitter can be seen in Fig. 9-14 and Fig. 9-15. The surface doping concentration N_D is of special interest for the contact formation and the Ag-crystallite growth. The shallow emitters possess a high N_D, as they are diffused from an infinite P source. During the tube diffusion, a layer of phosphorous silica glass (PSG) is formed on top of the silicon wafer when P_2O_5 or $POCl_3$ was used as a P source. The emitter's surface P concentration even exceeds the amount of P which can be built into the Si-lattice substitutionally. Thus, there is more P present than is electrically active. The total P concentration is determined by secondary ion mass spectroscopy (SIMS) and the amount of electrically active P is determined by measurement of the electrochemical capacitance-voltage (ECV); see Fig. 9-14. The limit for electrically active P is 2-$3x10^{20}$ cm^{-3} [159, 160] (see also Fig. 9-15). With an ECV measurement, only the concentration of electrically active P is determined.

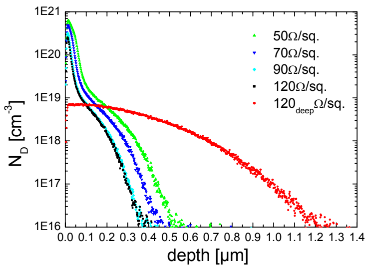

Fig. 9-14: SIMS measurements of the P concentration for different emitter diffusions.

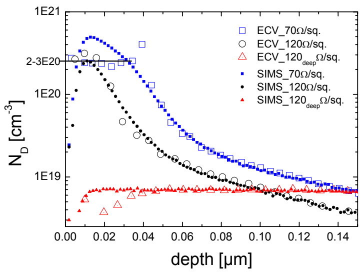

Fig. 9-15: SIMS measurements together with the related ECV profile for two shallow emitter profiles and for the diffused emitter.

The extra phosphorous, which does not sit on a silicon site and acts as a donor, forms small SiP precipitates [160-167] or additionally P-related defects [138]. One of the first studies on SiP-crystallites are the crystallographic investigations from [161]. The form of the SiP precipitates is either orthorhombic [161, 164] or monoclinic, depending on the conditions of growth [164, 165]. For diffused silicon samples, the SiP precipitates grow on the silicon surface on the interface to the PSG layer [166, 168]. The size and the density are dependent on the doping concentration and the diffusion temperature [163]. He found a SiP-crystallite density on the surface of $1x10^{10}$ cm^{-2} for samples with a doping concentration of $2x10^{20}$ cm^{-3}. The average size is about 200 Å. Seibt and Solmi found SiP-structures with a dimension of about 150 nm. If we are comparing this data with the results for the Ag-crystallites (Ag-crystallite density ~$1x10^8$ cm^{-2}, average size d_{Cr}=400 nm), it might be possible that the SiP crystallites are the nucleus for the growth of Ag-crystallites. In Fig. 9-16 and Fig. 9-17, TEM images of SiP-crystallites are shown. Ying *et al.* [169, 170] did some X-ray photoelectron spectroscopy (XPS) measurements on highly doped $POCl_3$ emitters with a surface doping concentration of ~10^{20} cm^{-3}. He observed significant amounts of unoxidized P and a new chemical state of Si, having an unstable bond and a reduced binding energy compared to lattice Si. The detailed structure of the related P or Si defects is not explicitly mentioned, but an overview of the different possibilities of defect states is given. Ying also investigated the oxidation behavior of P-doped and non-doped Si-surfaces and found a thicker native oxide layer for the doped samples, which has grown in a shorter time. Both the faster oxidation and the lower binding energy of Si and P in highly doped Si-surfaces make a relation between Ag-crystallite growth and surface defect density (SiP-precipitates) very likely.

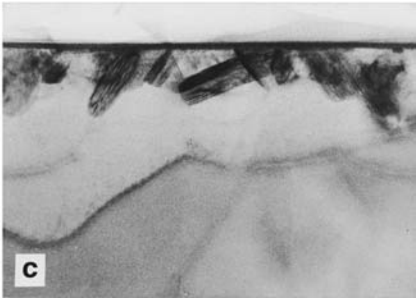

Fig. 9-16: TEM image of SiP crystallites on the surface of a heavily diffused and annealed (100)-Si surface [159]

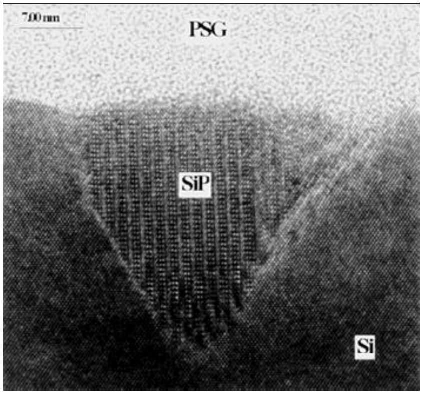

Fig. 9-17: TEM image of a SiP crystallite [166]

The relation between surface defects and doping concentration N_D is experimentally investigated by depositing the seed layer ink SISC on silicon samples with different N_D and firing them in a belt furnace at a wafer temperature of about 800°C. SEM images of the contact interface are shown in Fig. 9-18, where bulk silver and glass layer are removed so that only the Ag-crystallites are present. Especially on the shallow emitter profiles with a high doping concentration, the Ag-crystallite density is high. A difference in density on a sample with an emitter sheet resistance of R_{SH}=120 Ω/sq or R_{SH}=50 Ω/sq is barely observable. Mette [25] found a reduced crystallite density for a contact on a 90 Ω/sq in comparison to a 40 Ωsq emitter. The paste he used was a standard front contact paste and not the SISC ink as it is used here. The density of crystallites on a deep diffused emitter with a surface concentration of N_D=8x10^{18} cm^{-3} is significantly reduced, but crystallites are still present. According to the ECV measurement (Fig. 9-15), all P is active and therefore integrated into the Si-lattice. The presence of SiP crystallites or P-precipitates is rather unlikely. However, as the emitter was also created in a $POCl_3$ diffusion, a high defect density on the surface might still be present and the Ag-crystallite growth during a firing step is possible. Additionally, on a sample where the P concentration at the surface is higher than N_D>1x10^{20} cm^{-3} but the number of defects is reduced, almost no crystallites were found after firing. This silicon sample has an epitaxial grown emitter [158]. Therefore, it is more likely that the number and structure of Si defects, rather than the presence of phosphorus, are responsible for the Ag-crystallite growth. Finally, on n-type bulk silicon with a doping concentration of N_D~10^{16} cm^{-3} (defect etched and polished wafer), some roundish, shallow structures could be found, but no Ag-crystallite. From these results we can conclude that the most important factor for an effective contact formation (high crystallite density) is not the sheet resistance, and only slightly the surface doping concentration, but the way the emitter is produced: the density of surface defects. More detailed studies on the interaction between doping concentration and silver crystallite growth are still necessary, especially for the contact formation on lowly doped emitters.

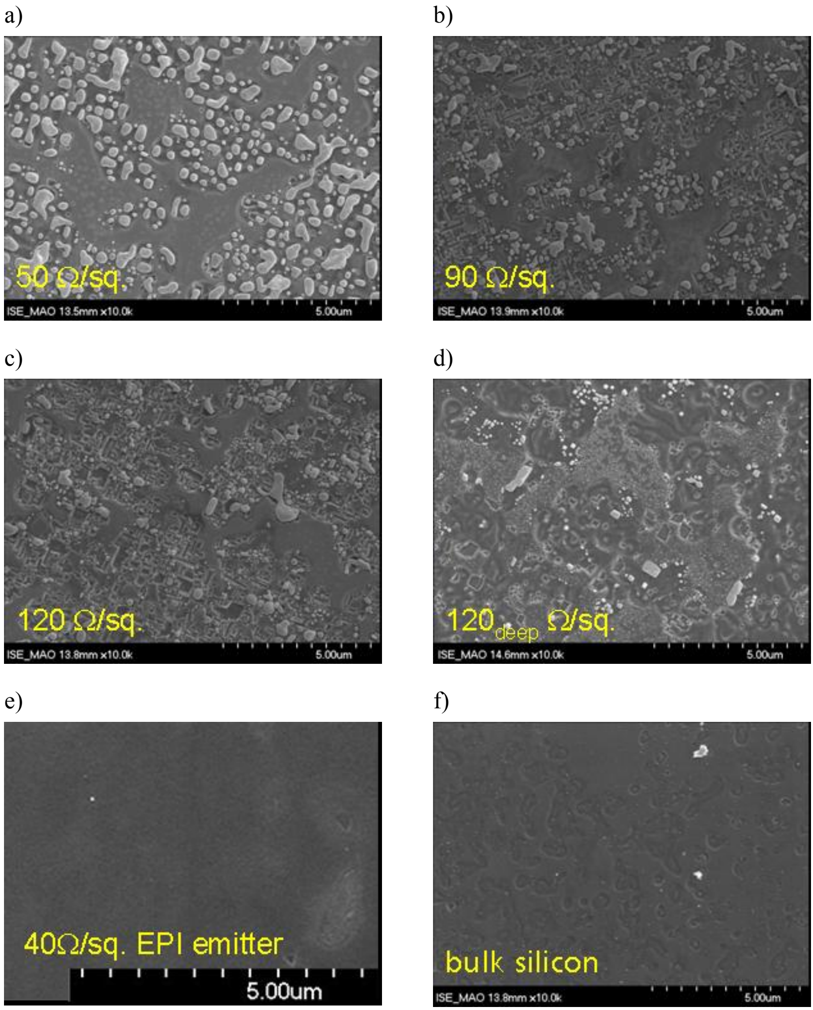

Fig. 9-18: SEM images of the contact interface at surfaces with different emitter sheet resistivities and different surface doping concentration. a)-c) flat $POCl_3$ emitter d) diffused $POCl_3$ emitter e) epitaxial gown emitter f) bulk silicon

9.2.2 AFM-profiles

In a further experiment the size and especially the depth of the Ag-crystallites grown into the silicon were determined. The Ag-crystallites on the above investigated samples were totally removed so that only the footprints were visible. The surface morphology was profiled using atomic force microscopy (AFM). In Fig. 9-19 a 3d-mapping of several AFM line scans is shown. The geometric structure of the inverted pyramids with a square footprint is clearly visible. Small crystallites are forming a perfect inverted pyramid, whereas larger crystallites have the shape of a frustum of pyramid. From a single scan (red line) the crystallite profile can be determined, especially the crystallite depth. The depth strongly depends on the crystallite size. Samples with different doping concentrations were investigated and several crystallites were scanned; however, a clear tendency was not observed. The deviation in crystallite size and depth was too large for a reliable result on all emitters. The surface roughness after firing and etching additionally leads to a strong depth variation. Furthermore, the height of the deposited ink influences the crystallite size. Small crystallites (inverted pyramids) were found in positions where very little ink was deposited, e.g. at the edge of a printed finger. If the crystallite growth was not limited by the material, larger imprints were found. The depth, however, seems to be limited by the wafer material. From a certain pyramidal depth, the crystallites are not found to be growing in depth, but rather in lateral directions; see Fig. 9-20. The crystal depth seems to be related to the thickness of the defect-rich layer at the surface. The deepest crystallite found for all investigated samples had a plateau at a depth of about 150 nm.

a) b)

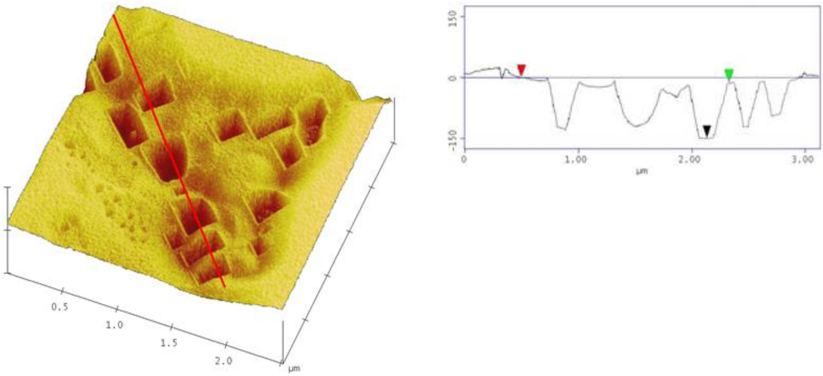

Fig. 9-19: AFM image and line scan of contact imprints a) and the measured profile from the line scan b)

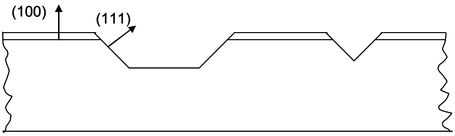

Fig. 9-20: Redraw of [62], Schematic of Ag-crystallite imprints grown into a (100)-Si surface with different depth.

9.2.3 Results on large-area industrial cells on Cz-Si

Silicon solar cells were processed on 12.5 cm x 12.5 cm Cz silicon wafers (ρ_{base}=1-3 Ω cm) with an alkaline texturing, PECVD-SiN_x coating, an Al-BSF rear side, and different emitter sheet resistances (R_{SH}). Half of the cells had seed and plate (SFP) contacts and the other half of the cells were conventionally screen printed (SP), using the silver paste PV 154. The seed layer was aerosol printed with the silver ink SISC, which was developed and fabricated at Fraunhofer ISE and subsequently silver plated in an in-line LIP machine. To investigate the influence of the emitter surface doping concentration on the silver crystallite density and the contact resistance, different emitter profiles were processed in a $POCl_3$ tube furnace. The profiles and the surface doping concentrations are equivalent to the samples above. The sheet resistance and the surface concentration vary from 2×10^{20} - 8×10^{20} cm^{-3}, resulting in sheet resistivities between 40 Ω/sq and 130 Ω/sq The parameters of the cells were determined by measuring the IV-characteristic as well as the electrical contact properties using the transfer-length model (TLM). Further on, the metal contacts were etched off and the crystallite density on the metal-semiconductor interface was determined using SEM images.

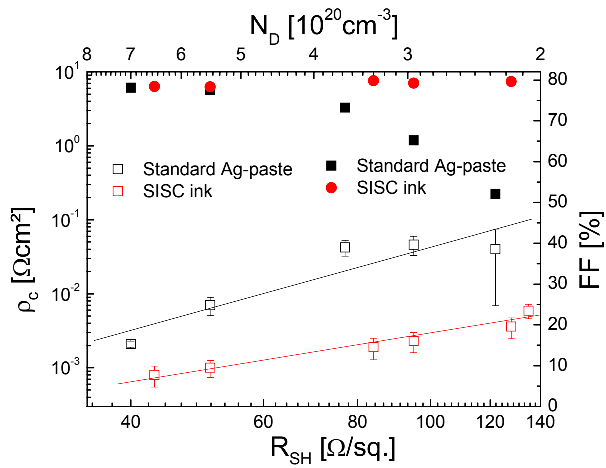

Fig. 9-21: Comparison of measured resistivity and FF of screen-printed (SP) using standard silver paste and SFP contacts using SISC ink on different emitter sheet resistances.

The relation between resistivity ρ_c and the *FF* is shown in Fig. 9-21, where both parameters are shown as a function of the emitter sheet resistance R_{SH} and emitter doping concentration N_D for screen-printed contacts and for SFP contacts. SFP contacts on a 40 Ω/sq emitter have a ρ_c below 1 mΩ cm², whereas the values for the screen-printed contacts are in the range of 2-3 mΩ cm², which is still low enough so that it does not significantly contribute to R_s and therefore the *FF*s are constant at 78%. However, for ρ_c values greater than 6-7 mΩ cm², R_s is increased and thus the fill factor will be reduced. At an emitter sheet resistance of 130 Ω/sq, the values for ρ_c for an SFP contact are 4-5 mΩcm² and the *FF*=78% are still at a high level, whereas the *FFs* for the screen-printed cells are reduced to values around 50%. The resistivity for the screen-printed contacts using standard Ag pastes, increased dramatically for sheet resistivities higher than 60 Ω/sq and the cell *FFs* are reduced. The SFP contacts also depend on N_D, albeit at a much lower level, and emitters with a sheet resistance of 130 Ω/sq can still be contacted without influencing the IV-parameters of a solar cell.

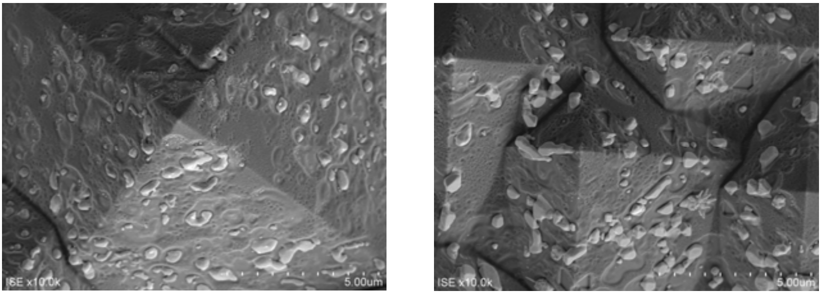

Fig. 9-22: Contact interface on a 40 Ω/sq emitter (left) and 130 Ω/sq (right) metalized with Fraunhofer ISE's SISC ink. The crystallite density on a highly doped and on a lowly doped emitter is more or less constant.

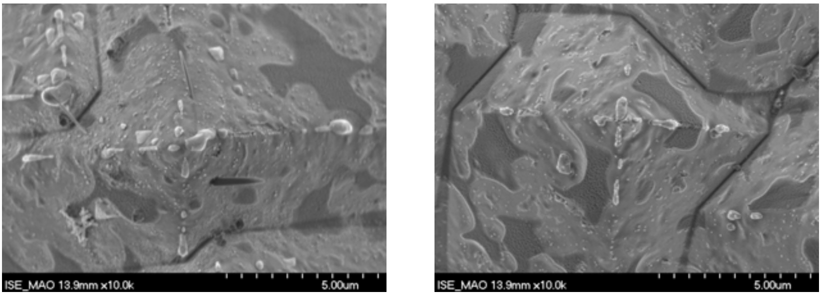

Fig. 9-23: SEM image of the removed contact of a 40 Ω/sq cell (left) and 130 Ω/sq (right) metalized with standard screen-printing paste. A relatively low crystallite density and a widely opened SiN_x layer characterize the contact interface.

The contact interfaces of SP and SFP contacts are shown in Fig. 6-7 for contacts on an emitter with a resistivity of 40 Ω/sq and 130 Ω/sq. The contact interface is different for both contacts. The SFP contacts have a much higher density of Ag-crystallites, which are randomly distributed over the contact area and not concentrated at the pyramid edges. The SiN_x passivation layer is, in the case of screen printed contacts, widely opened whereas the SiN_x coating for the SFP contacts is closed apart from the contact points where an Ag-crystallite has been grown. The crystallite density obviously depends on the used ink and printing method, whereas the doping concentration or the sheet resistance only has a minor influence on the crystallite growth. As the number of crystallites for both contacts is independent of the sheet resistance - at least in the tested range - we can conclude that it is preferable for a low ohmic contact to have a high number of Ag-crystallites instead of having a widely opened SiN_x layer. The current flow from the emitter into the bulk silver is more effective via point crystallites than via a widely opened SiN_x coating. The IV-parameters for average screen-printed solar cells and a solar cell with an SFP contact are shown in Table 1 for emitter sheet resistivities of 40 Ω/sq and 130 Ω/sq.

	R_{sh} [Ω/sq]	w_c [µm]	w_F [µm]	A_c [mm²]	A_a [mm²]	V_{OC} mV	j_{SC} [mA/cm²]	FF [%]	η [%]
SP	40	100	100	10.1	10.1	612	34.7	78.1	16.6
SP	130	100	100	14	14	613	35.4	52.3	11.4
SFP	40	30	70	6.0	9.1	611	35.0	78.4	16.8
SFP	130	30	70	6.3	14.4	625	35.3	79.6	17.6

Table 9-1: IV-parameters for solar cells fabricated on 12.5x12.5 cm², 1-3 Ωcm, p-doped Cz-silicon wafers with Al-BSF, for screen print contacts and seed and plated contacts. The cell thickness is 170 µm.

As expected, the values for V_{oc} and j_{sc} increase with increasing sheet resistance, as the emitter recombination is reduced and the quantum efficiency is increased for short wavelengths, see Fig. 9-24. The difference in j_{sc} and also in V_{oc} for the different printing technique independent of R_{sh} can be explained by the shaded/contacted area, A_s and A_c, where A_s is the area of the total contact finger (seed layer width + plating) and A_c is the area covered by the fired contacts. For screen printed contacts A_s is equal to A_c. The shaded area is of interest in order to interpret the values for j_{sc}, as the current is rather sensitive to the shaded area. For example, the screen-printed cells have a lower j_{sc} on highly doped emitters compared to the SFP contacted cell, which is consistent with a larger A_s for the SP contacts. On lowly doped emitters, the values for j_{sc} for the SP contacts are higher than on SFP cells, as the shaded area is smaller. The contact distance for each solar cell was optimized according to the printed line width and the sheet resistance. The screen-printed lines have a width of about 100 µm and therefore the contact fingers have distances of 2.4 mm (40 Ω/sq) and 1.5 mm

(130 Ω/sq). The contact width for the seed contacts is 30 µm, resulting in finger distances of 2 mm (40 Ω/sq) and 1 mm (130 Ω/sq). Similar cell efficiencies for SP and SFP contacted solar cells can be obtained on highly doped emitters, whereas the cell efficiency on solar cells with a high sheet resistance is dominated by the resistivity, and the SFP contacted cells can benefit from an increased V_{oc} and j_{sc} as the values for the *FF* are on a high level.

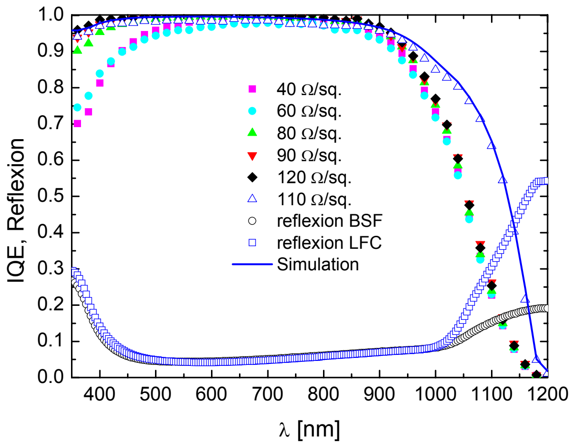

Fig. 9-24: IQE measurements of the best high-efficiency cell on FZ-Si (open triangles) plotted together with IQEs of the Cz-Si cells with different emitter sheet resistivities (closed symbols). The typical reflection is shown for an Al-BSF and a passivated rear solar cell.

The measurement of the internal quantum efficiency as a function of the wavelength reveals the advantages of using an emitter with a high sheet resistance. Due to the flat emitter profile with the relatively high surface doping concentration, all IQEs are reduced at short wavelengths. Nevertheless, there is a strong difference in IQE for the different emitter sheet resistivities. In the short wavelength region, the IQE is increased with increasing values for R_{SH}. The cells with an emitter of R_{SH}=40 Ω/sq and 60 Ω/sq have a very strongly reduced IQE of below 80% for a wavelength of λ=350 nm. The difference in IQE for samples with an R_{SH}>90 Ω/sq can be neglected, as the difference in N_D for these samples is also rather small (R_{SH}=90 Ω/sq, N_D=3x10^{20} cm^{-3} and R_{SH}=120 Ω/sq, N_D=2.5x10^{20} cm^{-3}). The IQE for R_{SH}>90 Ω/sq is above 90%, see Fig.

9-24. For long wavelengths, which represent the rear side of the cell, the IQE is the same. In addition, in Fig. 9-24 the IQE of a high efficiency solar cell with a R_{SH}=110 Ω/sq is shown. This cell has a passivated rear side and a higher optical reflectivity due to the evaporated Al-mirror. On the front side, the IQEs are similar to the described solar cells, however, on the rear side, the advantages of improved passivation (thermal grown oxide with LFC contacts) compared to the Al-BSF are visible. The high efficiency cells are described in detail in chapter 11.

9.3 Contact geometry

An aerosol system was used to deposit the seed layer contact structures on silicon substrates. The line width strongly depends on the used nozzle diameter (see chapter 5). For these experiments a nozzle opening of 200 µm was used, resulting in a line width below 40 µm, as seen in Fig. 9-26. The line height of a single aerosol printed seed contact is in the range of h=1 µm and depends on the initial ink particle size. With nanoscopic inks, line heights below 100 nm are possible as well, and a thick film contact more and more becomes a thin film contact. The impact of the line height on the contact formation is studied below. All the described contacts need to be fired in order to form an electrical contact. The firing step also influences the contact geometry. The contact shrinks, due to the evaporation of solvents and binders and due to the sintering of the silver particles. The single silver particles sinter into clusters and islands and form an interrupted conductive layer. The contact cross section is reduced by about 30%, which correlates with the solid load of the printed ink. Even if the silver particles are in the range of 100 nm and a homogenous silver layer is formed during the firing step, the contact cross section is by far too small for an effective current transport. The cross sectional area of a front side contact needs to be approximately between 500 and 1000 µm² in order to transport the current without significant losses. Here the area is only a few µm² and a thickening (see chapter 6) is unavoidable, if only a single seed contact is deposited. The contact height can be varied by printing at different printing speeds, by multiple path printing, or by using different inks, such as hotmelt inks [90].

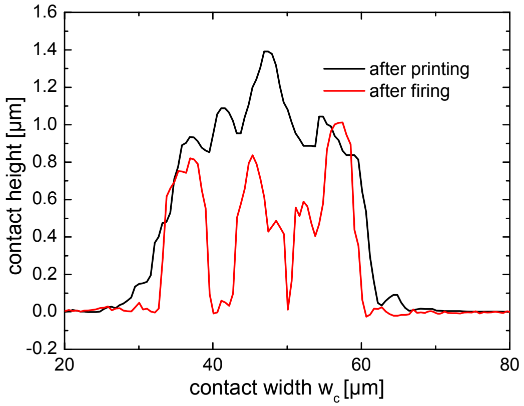

Fig. 9-25: Contact cross section of a single aerosol printed front side contact, before and after firing.

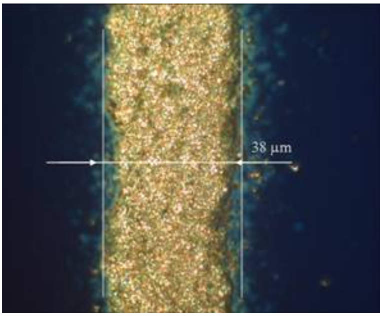

Fig. 9-26: Image of a single aerosol printed front side contact.

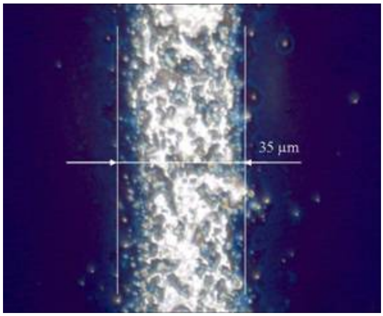

Fig. 9-27: Image of a single aerosol printed and fired front side contact.

The effects of multiple-layer printing on the contact geometry were studied on seed layers, deposited on shiny-etched wafers. The line height was varied by multiple printing (1-15 layers). The printed lines were fired in an in-line furnace and finally plated in a cyanidic (CN) plating bath, using the light-induced plating process. The contact geometry, especially the cross sectional area, was determined by confocal microscopic measurements and verified with microscopic pictures from polished contact cross sections. The contact geometry for multiple aerosol-printed lines can be seen in Fig. 9-28 and Fig. 9-29. The lines were printed on top of each other.

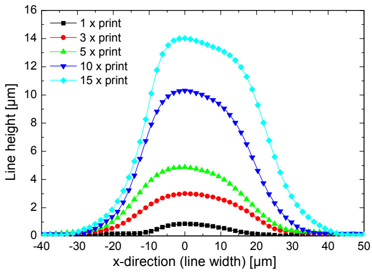

Fig. 9-28: Cross section measurements from 1- to 15-fold (one over each other) printed fingers after the contacts have been fired

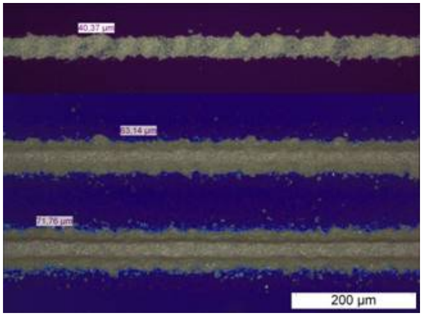

Fig. 9-29: Microscopic pictures of single, 5-layer and 15-layer printed contacts on a polished silicon substrate

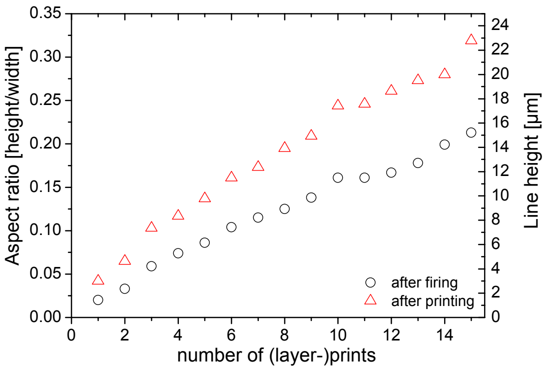

Fig. 9-30: Aspect ratios (finger height:width) for single – 15 layer aerosol printed fingers as printed and after firing.

The height of the single printed line is limited to 1 µm, which is about two times the diameter of the silver powder used in the contact ink. Hence, finer contacts can be obtained with an ink containing finer particles. The lines are deposited at a printing speed of 30 mm/s; at higher speeds the line height can be reduced even more, but line interruptions are unavoidable. Each further printing step increases the line height by another micrometer. The contacts grow faster in height than in width, indicated by a linearly increasing aspect ratio as shown in Fig. 9-30. The line width is increased, as the ink tends to wet the silicon surface. This can be avoided and an ink deposition in layers is possible if the rheology of aerosol inks is further improved.

9.4 Resistance and line conductivity of SFP contacts

The electrical properties like line resistivity ρ_l and resistance $R_c xW$ were investigated on multiple-layer printed seed contacts, too. These parameters are of special interest for the metallization of solar cells, as both contribute directly to the series resistance and therefore to the fill factor [24]. For the determination of the line resistivity, the contacts printed on polished wafers from the geometrical studies are used. The line resistivity is determined after firing and after plating. The line resistance for all contact structures was measured using a 4-probe measurement and the specific line resistivity was calculated, taking into account the determined cross section area.

The resistivity was studied on alkaline textured solar cells in order to get a value for $R_c xW$, dependent on the contact height for industrial solar cells. The resistivity of each contact structure was determined by a TLM measurement. The influence of the ink density on the contact resistance was analyzed by taking SEM images of the metal-semiconductor interface.

9.4.1 Line conductivity

The specific line resistivity was determined from the measured line resistance, taking into account the cross sectional area. For the single printed contact no value can be given, as the contact is not continuous (see Fig. 9-27). For all other contacts, the values are illustrated in Fig. 9-31. A constant growth in the cross section, together with a steady decrease in line resistance, should lead to a constant resistivity; however, the measured resistivity decreases with every printing step. There are two reasons for this phenomenon: first of all, the sintering behavior of the silver particles is supported by a higher ink density, as the silver particles can find a neighbor particle in all directions. The single silver particles do not melt together, as the firing temperatures are usually below the melting point of silver, but they do form metal bonds to intimate neighbor particles. The more particles are in an intimate contact, the higher is the conductivity. Multiple current paths are possible, which reduces the line resistivity. Second, the influence of the glass frit on the line resistivity decreases during the firing step. The glass melts, segregates from the silver, diffuses towards the silicon surface, and the remaining pure silver forms a continuous conductive layer. The contact can be built up line by line and achieve resistivities comparable to screen printed contacts. However, more than 15 lines (15 µm contact height) are necessary until the conductivity is reached which can be compared to screen printed contacts. In conclusion, the higher the seed layers, the lower the specific line resistivity before plating.

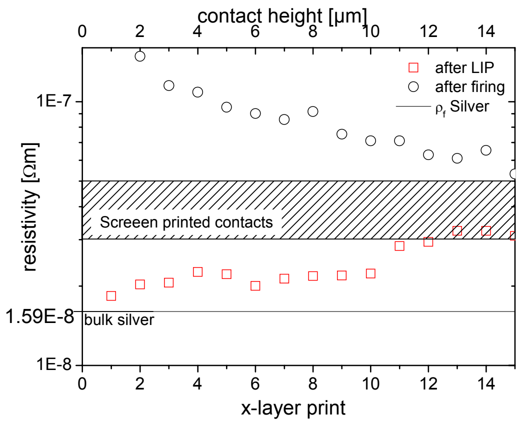

Fig. 9-31: Specific line resistivity as a function of printing layers after firing and after CN-LIP. The dashed line marks the conductivity of bulk silver, and the crosshatched area the resistivity of screen printed contacts.

The contact we are looking for is supposed to be a seed layer, which has to be thickened in an LIP process to reach its final resistivity. Therefore, the multiple printed contacts were plated with the same amount of silver and the line resistivity was measured. In Fig. 9-31 the advantage of a thin, subsequently plated seed layer is obvious. In general, the resistivity for all plated contacts, independent of the seed layer height, is reduced. However, the best conductivity was achieved for the single printed seed layer, which initially was not measureable. Generally, the less material is deposited for the seed layer, the lower is the total line resistivity after plating. In the case of the single printed contact, a line resistivity of ρ_f=1.85×10^{-8} Ωm is measured, which is already close to the value of bulk silver (ρ_f=1.59×10^{-8} Ωm). The resistivity of a contact structure with a flat seed layer is dominated by the conductivity of plated silver. As the conductivity of LIP silver is much higher than the conductivity of printed silver, aerosol- or screen-printed, it is advisable to keep the fraction of printed silver as small as possible. The crosshatched area in Fig. 9-31 represents the resistivity of screen printed contacts. As long as the seed layer height is below 10 µm, the two layer contact structure is superior in resistivity compared to screen printed contacts.

9.4.2 Contact resistance

In a further experiment the influence of the seed layer height on the contact resistance was investigated. Contact structures were printed at different speeds and heights (different ink densities) on randomly textured Cz-wafers. The height of the lines was varied from 1 µm to 9 µm. The height can hardly be measured on textured wafers, as the height of the pyramids exceeds the deposited line height; therefore, the results on polished wafers were used to determine the line height. After printing, the cells were fired in an in-line furnace and subsequently plated by LIP. To be independent of printing parameters like line width, printing speed and, material output, a value for the deposited ink mass, the ink density [g/m²], was defined. For this we measured the ink output of the printer, the line width and the printing speed. From this data an area density can be calculated by (9-1),

$$\rho = \frac{d}{v \times w} \qquad \textit{(9-1)}$$

with (ink density ρ *[g/m²],* throughput *d [mg/min]*, printing speed *v [mm/s],* and line width *w [µm])*.

For example, a 45 µm wide line printed with a speed of 20 mm/s and a material output (dry) of d = 0.2 mg/min, results in an ink density of ρ = 3.7 g/m². A solar cell with an area of 15.6 cm x 15.6 cm and a grid of 80 fingers and 2 busbars (1.5 mm) can be contacted using only 4.4 mg ink. In Fig. 9-32 a top view of such a fired seed contact is shown.

The surface texture is still visible and the contact area is not totally covered by the ink; nevertheless, this is an example for a contact with a normalized contact resistance $R_c xW$ below 0.5 Ωcm. The contact resistance was measured using the transfer length model (TLM) [34, 37]. The measured resistance was multiplied by the width (W) of the test structure in order to get the normalized contact resistance $R_c xW$ [37], which is independent one the dimension of the TLM test sample and only dependent on the contact width w. All measured contact resistances are shown in Fig. 9-33.

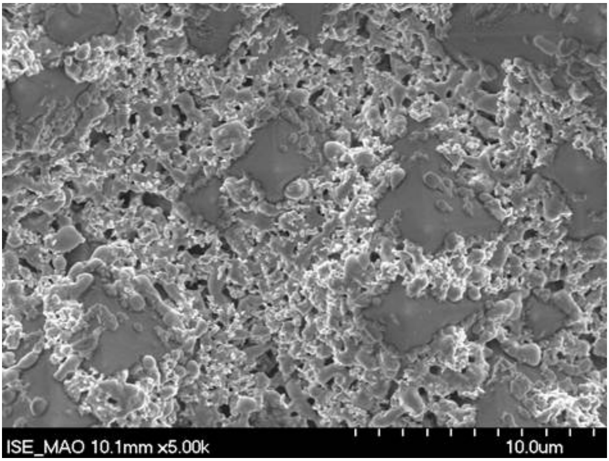

Fig. 9-32: Image of a single printed and fired seed contact Even with an incompletely covered contact surface a normalized contact resistance $R_c xW<0.5\ \Omega cm$ is reached.

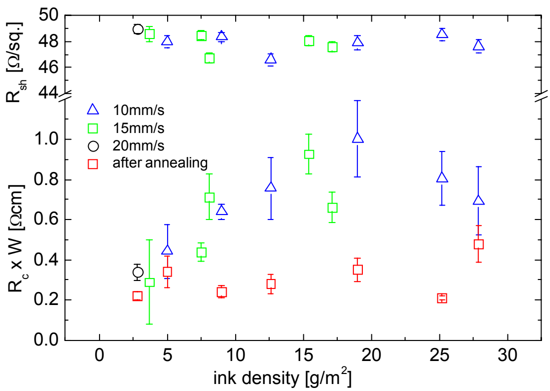

Fig. 9-33: Contact resistance measurements for different ink densities (calculated from line width, material output and printing speed) and contact heights. The emitter sheet resistance is monitored additionally to prove the reliability of the TLM measurement

To check the reliability of the TLM measurement, the emitter sheet resistance, also obtained by TLM measurement, is plotted, too. The measured sheet resistance for every test structure was around 48 Ω/sq +/- 5 Ω/sq, which is consistent with the expected R_{SH} for these cells (45 Ω/sq$<R_{SH}<$50 Ω/sq).

The contact structures were measured after an LIP step. The plated silver is necessary for reliable TLM results, as it is not possible to contact and measure a thin seed layer directly. The contact resistance of the non-plated contacts can only be measured when there is enough ink present and the seed layer height exceeds about 4 µm. In this case, we did not find a difference in contact resistance for plated or unplated fingers. The positive effect of a plating step on a fired seed layer contact [171] could not be investigated in this experiment, as the seed layer is too thin and no leaking glass layer was found next to the contact with additional edge crystallites, which can support the current flow if they are contacted by plated silver.

Although a decrease in the contact resistance with rising ink density was assumed, we found an opposing behavior. The contact quality decreased as the height of printed contacts is increased. With increasing ink mass per contact area, the measured resistance increases. At a contact height of 4-5 µm (corresponding to an ink density of 12 g/m²) or higher, the contact resistance remained at a constant level of (about 0.8 Ω cm), which is comparable with a good screen printed contact. To understand the correlation between ink density and resistance, the contact silver was etched off; Ag and the glass frit were selectively removed by an HNO_3/HF sequence, so that the remaining Ag-crystallites could be investigated. SEM images were taken from the metal semiconductor junction, see Fig. 9-34a)-e). A constantly high density of silver crystallites, which are mainly responsible for a high quality contact, could be found independently of the contact height. Thus, it is not the crystallite density which degrades the contact quality with a rising ink density. Additionally, an increasing opening of the SiN_x-passivation layer was observed, as can be seen in Fig. 9-34. In contrast to the common understanding, the contact resistance increased with increasing opening of the SiN_x-layer [153]. The higher the ink density was, the more SiN_x was etched off. A higher ink density is equivalent to a higher amount of reactive ink components (glass) per contact area. The higher amount of glass at the contact interface has two effects: first, the glass itself forms a thicker insulating layer, and second, the glass etches the SiN_x-layer and an even thicker glass layer is formed during firing. The SiN_x-layer is oxidized to SiO_2 by the metal oxides in the glass. The SiO_2 is solved in the glass and the thickness of the insulating glass layer increases even more. On the one hand, the contact area should be as large as possible (opened ARC); on the other hand, the resulting insulating glass layer should be as thin as possible. In conclusion, a good contact resistance can be achieved by keeping the SiN_x-layer non-etched apart from the points where silver crystallites are formed; see Fig. 9-34a). In this case, the glass layer is very thin and mainly determined by the initial amount of glass, the content of which should be as low as possible. From our experiments we can conclude that the current between solar cell and metal grid can only flow via the Ag-crystallites, while all other suggested current paths seem to be of no significance [25, 55].

Thus, the thinner the printed contact (low ink density) is the lower is the resistance. For a good front side metallization, the ink density of the seed layer should be as low as possible: just enough to form a high density of silver crystallites, achieve a good adhesion, and a good ability for plating. For ink densities below 2.5 g/m², no continuous line could be achieved after LIP. One further interesting aspect is the influence of an annealing step on the contact performance. All annealed cells show a significant reduction in the contact resistance. The annealing was performed at T=300°C under forming gas (FGA). The positive effect of an FGA step on the contact resistance was found by several authors [146, 154, 172-174]. The most likely process is the reduction of metal oxides in the glass layer to metal precipitates at the glass surface, which increases the total conductivity of the glass layer. This theory is quite consistent with our results. As the insulating glass layer is, after an annealing step, no longer the critical barrier for the current transport, the contact resistance is determined by the effective contact area. The number of crystallites is approximately the same for all contact heights, and therefore, the measured contact resistance is almost constant. However, it also can be explained by an improved effective contact between the silver crystallite and the bulk silver just by an improved sintering due to the post anneal (see above).

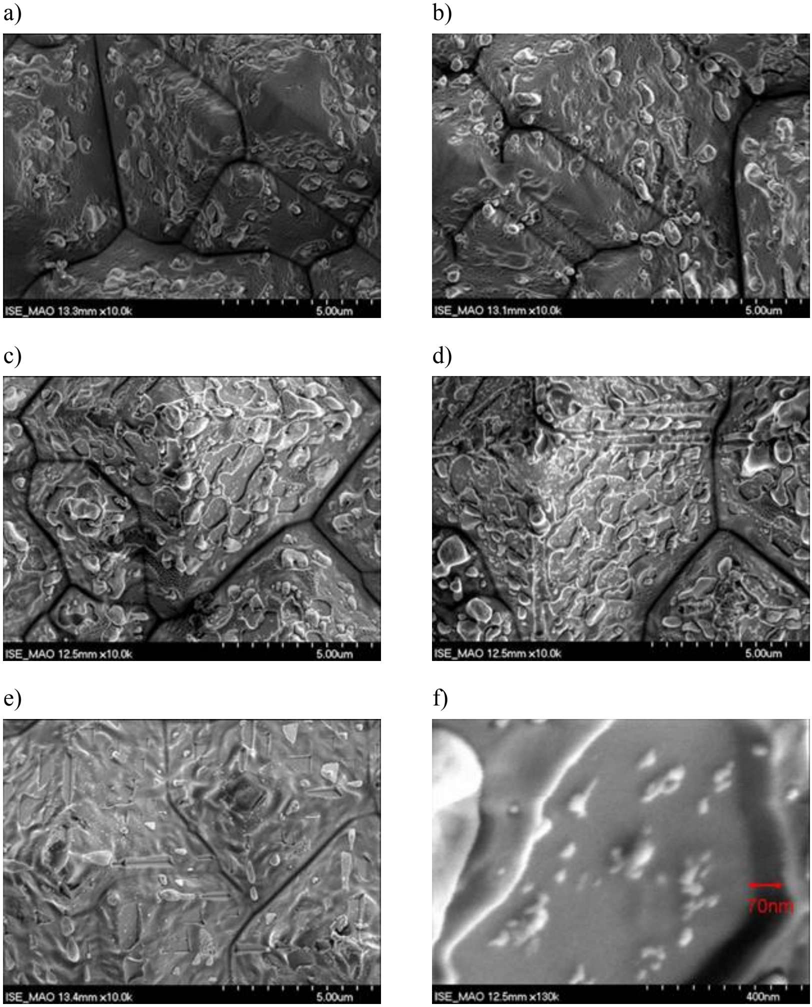

Fig. 9-34 SEM images of silver crystallites on the metal-semiconductor interface a-e with increasing ink density. a) Single printed contact with $v = 20$ mm/s (low ink density <10 g/m²). A high crystallite density is visible, but the SiN_x coating is mainly untouched. c) Medium ink densities (10-20 g/m²), the crystallite density is approximately the same, but additionally the SiN_x coating is strongly etched. e) High ink density (>20 g/m²), the surface and the whole SiN_x-coating is etched away, but the number of silver crystallites or imprints is still constant. f) close-up of (c), showing the opened SiN_x coating.

9.5 Chapter summary

In this chapter the contact formation between contact ink and silicon and the growth mechanism of Ag-crystallites is investigated. The crystallite growth can be summarized briefly as: lead oxide (glass frit) is the reactive component which first opens the SiN_x-layer and reacts with the silicon. During the reaction, lead is formed and silver can be solved. At peak temperatures of about 800°C, the Ag-Pb phase and the glass are liquid. During cooling, first, silver re-crystallizes from the Ag-Pb phase on the opened silicon surface; as the glass is still liquid, silver can easily diffuse to the crystal seeds and the formation of relatively large Ag-crystallites is possible. Second, the glass solidifies and encapsulates the liquid lead, which third, condensates in the form of small lead precipitates. Due to the growth of the Ag-crystallites, the glass layer on top of an Ag-crystallite thins and either a direct or a tunnel contact is possible. The Ag-crystallites are homogenously distributed over the contact area and it can be distinguished between contact of type1 and type2. About 1% of the contact area (silver-silicon) is covered by type2 contacts and about 10% by type1 contacts. Nevertheless, type2 contacts are mainly responsible for the current transport. After the bulk silver is removed in a nitric acid etching, it can be distinguished between type1 and type2. Type1 contacts are protected by the insulating glass layer, whereas from the type2 contacts only the foot prints are visible after etching. The theoretical limit for silver contacts on silicon solar cells is described in dependence of the doping concentration. The huge difference of about 10^5 between the calculated and the measured value for ρ_c is based on the small contact area between Ag-crystallite and bulk silver from type2 contacts. Even after firing, the whole contact interface is covered by an insulating dielectric layer, apart from the position where Ag-crystallite has grown. Therefore, the only possible current path is via silver crystallites, which is rather effective as our studies on different diffused emitters have shown. An effective contact formation with the SISC ink is possible on an emitter with a sheet resistance as high as R_{SH}=130 Ω/sq and *FFs* of *FF*=80% could be achieved.

Regarding the electrical properties of a two layer contact, it is beneficial for both the line resistivity and the contact resistance to keep the seed layer as thin as possible. The best results on 15.6x15.6 cm² wafers were achieved with 2-3 g/m² (ink per contact area), which is equal to only 3-5 mg of ink per wafer. The fraction of the seed layer of the total contact cross section needs to be minimized, while the fraction of the LIP silver should be maximized to achieve the lowest values for the line resistivity of about $\rho_f=1.9\times10^{-8}$ Ωm. Additionally, contact formation between the seed layer and the emitter of a solar cell is more efficient for a thin (h<2 µm) than for a thick (h=2-9 µm) seed layer. In SEM images the influence of the seed layer thickness on the contact interface was investigated. For a low contact resistance it is important to etch very little material from the wafer (SiN_x-layer, Si) for keeping the resulting glass layer as thin as possible. For a good front side metallization, the printed line height of the seed layer should be as low as possible, just enough to form a low ohmic contact, to achieve a good adhesion, and to provide a good ability for plating.

Further work needs to be done in order to understand the relation between SiP clusters or surface defects in general and the Ag-crystallite growth. The number of type2 crystallites can probably also be increased by reducing or changing the glass component and it is worth studying the contact formation on emitters with a strongly reduced surface concentration $N_D<10^{19}$ cm^{-3}.

10 Optical contact properties

One main efficiency loss in industrial solar cells is the shading of the cell caused by the metal front side contacts. With the aerosol-printing technique plus additional light induced plating (LIP), not only the geometrical contact width is reduced compared to screen-printed contacts, but also the shape of the finger changes, which can have an influence on the effective optical width (see Fig. 10-1). The roundish edges of the contact are hardly visible in an optical microscopic top view, as the light is reflected into the cell area, whereas the middle section of the finger is strongly reflective. The geometrical width is visibly reduced to an optical width. In this work the effective shading of different finger types is analyzed with two different measurement methods. The essential parameter for characterizing the finger is the effective width, which can be reduced drastically compared to the geometrical width due to total internal reflection at the glass-air layer and the reflection from the roundish edges of the contact fingers into the cell. This parameter was determined with different methods. It could be shown that for aerosol-printed fingers the effective optical width is only 38% of its geometrical width, while for standard screen-printed fingers it is 47%. The measured values are compared to a theoretical model for an aerosol-printed and plated finger and are in good agreement. Blakers [104, 175] and Stuckings [176] have already analyzed this effect for contact fingers with a seed layer width of 3.5-8 μm and postplated silver, using measurements of the global short-circuit current and global reflection. They have observed a great reduction of the effective optical width of the contacts to about a third of the geometrical width.

The main motivation is to analyze, whether the SFP contact fingers, fabricated with the industrially feasible aerosol jet printing technology, will also show such a dramatic reduction, and to compare the optical performance of these fingers with the standard industrially screen-printed contacts. To achieve this goal, we have used the methods suggested by Stuckings and Blakers, in addition to locally resolved measurements of the reflection.

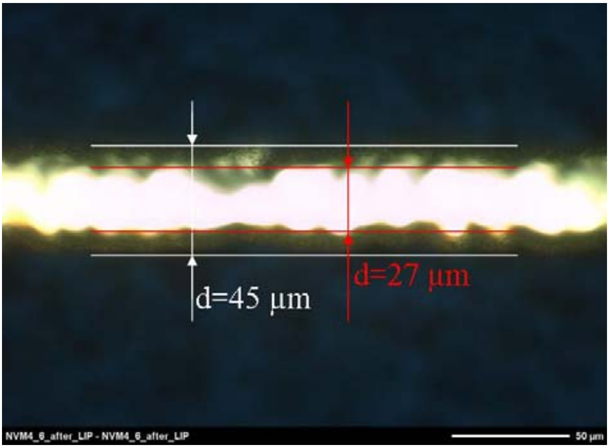

Fig. 10-1: Geometrical width and optical contact width visualized in a microscopic top view image on an SFP contact

10.1 Theoretical Considerations

For the calculation of shading losses of the solar cell, the determining factor for the fingers is not the geometrical width, but the effective (optical) width. It is the fraction of the geometrical (measured) width that actually shades the solar cell. The effective width can be significantly smaller than the geometrical width, because light can be reflected from the finger to the cell and therefore contribute to the power generation.

Blakers [104, 175] has calculated the effective shading of a roughly half-circular encapsulated finger to be 36%. The nearly optimum half-circled shape was achieved by a very narrow seed layer and a subsequent silver electroplating step. He compared this value with j_{sc} measurements of cells covered with isopropanol and found excellent agreement. Stuckings [176] also calculated the theoretical effective width of a half-circular encapsulated finger and found a similar value of 34%. He compared this value to reflection measurements and determined experimental values between 30% and 35%, which is in good agreement with the theoretical value. In this work, on the one hand the finger structures are quite different from the previously investigated ones due to the wider seed layer, and on the other hand the striking question is, whether the aerosol-printed fingers are beneficial compared to the screen-printed ones.

Assuming that the light hits the finger perpendicular to the encapsulated cell (see Fig. 10-2), there are three different cases for the light to be reflected:

- I: direct reflection onto the silicon surface
- II: total reflection can occur at the boundary layer glass-air
- III: the light can be reflected out of the module.

For cases I and II, the light can contribute to current generation and therefore reduce the effective width. In order to determine the lateral x-position for the simple case of a half-circular-shaped finger, where total reflection occurs, the refractive index of the glass has to be measured. In the wavelength range of 600-1000 nm a value of n_{glass} = 1.528 ± 0.007 was determined. With the refractive index for air n_{air} = 1 and Snells law

$$\alpha = \arcsin\left(\frac{n_{air}}{n_{glass}}\right) \tag{10-1}$$

the critical angle for total reflection is α = 40.9°. The (upper) angle β is half of the alternate angle of α, β = 20.4°. This angle can be found as well between the silicon and the tangent of the half circle. The gradient of the tangent is -tan(β) = -0.37 and can be set equal to the derivation of the equation of a half circle ($f(x) = \sqrt{1-x^2}$)

$$f'(x) = \frac{-x}{\sqrt{1-x^2}} = -0.37 \tag{10-2}$$

If the origin is set at the middle of the circle, it follows that the light hitting the finger at a position -0.35 > x > 0.35 (assuming a unit circle) will result in total reflection. The situation changes to case I at a tangent smaller than -1 with an x-position of 0.71. Thus, the fraction of the area of a half-circled finger can be assigned: I = 29.3%, II = 35.8%, and III = 34.9%.

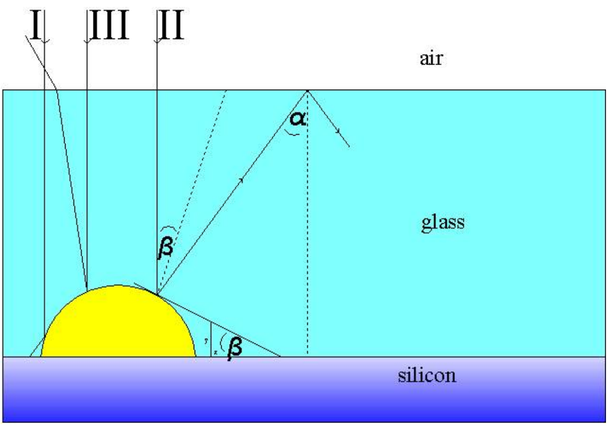

Fig. 10-2: Three different cases for the reflection of the light from the finger. The pottant between the silicon and glass is not illustrated because it has about the same refractive index as the glass and therefore no influence on the optics.

For the seed-printed and plated fingers, however, the cross-section looks slightly different. As can be seen in Fig. 10-3, the flanks are indeed similar to a quarter of a circle, but the finger has a 30 µm wide middle section due to a wider seed layer. Therefore, the model was extended by an additional 4th part, describing this middle section. This shifts the area fractions to: I = 16.7%, II = 20.5%, III = 19.9%, IV = 42.9%.

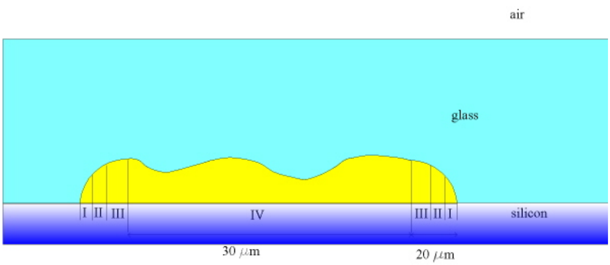

Fig. 10-3: Sketch for the aerosol-printed and plated fingers with the four areas that have different reflection properties

Area IV is assumed to be a lambertian emitter, i.e. in each angle the same amount of light is reflected. The waviness in the micrometer range and also the rough microstructure of the plated silver make the assumption reasonable (see Fig. 10-4**).**

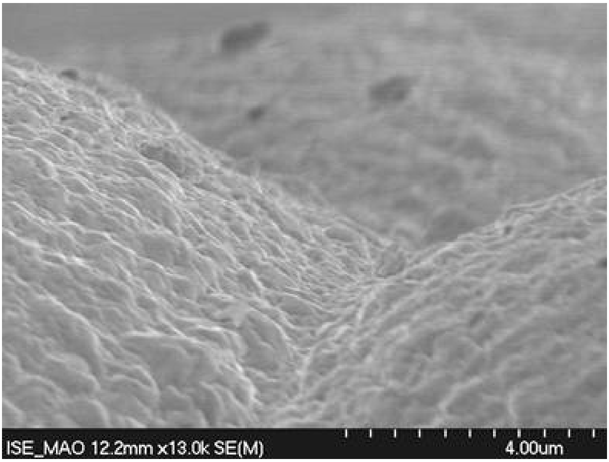

Fig. 10-4: Microstructure of the plated silver surface

Light that is reflected from the metal with an angle > 40.9° hits the glass-air interface and is 100% reflected back to the silicon. In order to calculate the part of the reflected light at smaller angles, the light is divided into two halves: one half is s-polarized and the other half is p-polarized [177]. For the varying angles of incidence φ the Snell's law of refraction is applied:

$$R_{ref} = \left(\frac{\eta_0 - \eta_1}{\eta_0 + \eta_1} \right)^2 \qquad (10\text{-}3)$$

with $\eta_{0,1}$ = H/E the optical admittance and the index 0 for air and 1 for glass. Fig. 10-5 shows that for small angles, the reflection is smaller than 5% and just before $\alpha = 40.9°$ increases rapidly.

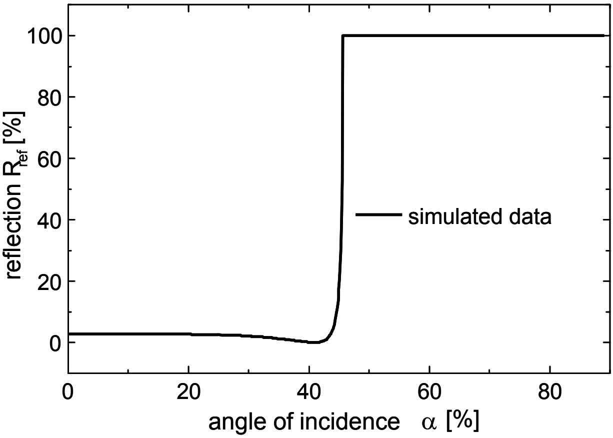

Fig. 10-5: Simulated data for the reflection at the interface glass-air, according to Macloed [177].

The effective width EW illustrates the fraction of the absorption and the loss of reflection of a finger and is 100% minus the light that reaches the silicon. The amount of light that reaches the silicon is 100% minus the losses of area III (L_{III}) and IV (L_{IV}), multiplied by the reflection of the silver:

$$EW = 100\% - \left(100\% - L_{III} - L_{IV}\right) \cdot R_{Ag} \tag{10-4}$$

The fraction of the angle of the light being reflected out of the module is

$$d\alpha = \frac{1}{2\pi}\int_0^{2\pi} d\varphi \int_0^{\alpha} d\vartheta \sin\vartheta = \left[-\cos\vartheta\right]_0^{\alpha} = 0.245 \tag{10-5}$$

with φ, ϑ the spherical coordinates.

With the data of Fig. 10-5 about 96% of the light with an angle <α leaves the module and 42.9% of the covered area of the finger is IV; it results that

$$L_{\mathrm{IV}} = 0.245 \cdot 0.429 \cdot 96\% \,.$$

Because of the rough microstructure, not all of the light of area III leaves the module directly. Half of it is assumed to behave like a lambertian surface, so that

$$L_{\mathrm{III}} = 0.623 \cdot 0.199 \cdot 96\% \,. \qquad \textit{(10-6)}$$

In this model, multiple reflections between finger and the interface are neglected, as well as the absorption within the glass layer. The measurement for the reflection of the plated silver between 600 nm and 1000 nm is shown in the next section and is R_{Ag} = 83.7%. The effective width (EW) of an aerosol-printed and plated finger with an encapsulated glass layer above then results in EW = 34.7% (of the geometrical width).

10.2 Optical contact width – geometrical width

For this experiment, four p-type Cz-silicon textured wafers with industrial emitter (60 Ω/sq) and Al-BSF were processed with different fingers (see Table 10-1). Two cells received a 50 µm wide seed layer with the aerosol printer. Afterwards the fingers were thickened by about 20 µm by LIP. These two cells differed in their finger spacing: one cell had a line spacing of 1.955 mm (Awd); the small spacing was half of it, about 1 mm (Asd). The two screen-printed cells are identical, though one was plated additionally, which is the reason why the geometrical width is greater. The finger widths are based on microscope measurements. After LIP the cells were encapsulated into a module using EVA. Cross section images of the different fingers can be seen in Fig. 10-6.

a) b)

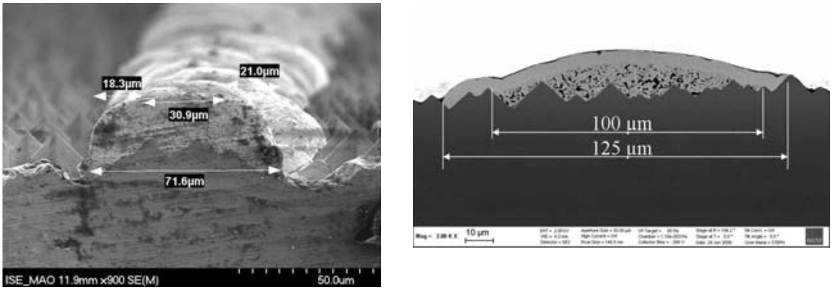

Fig. 10-6: a) Cross-section of an aerosol-printed and plated finger, exhibiting a geometrical width of 72 µm. The seed layer width was approximately 50 µm and the plated silver about 20 µm. b) Cross-section of a screen-printed finger and plated finger. In this example, the screen printed finger exhibits a geometrical width of 100 µm and 125 mm, including a layer of LIP silver.

Abbreviation	Explanation	Geometrical finger width GW [µm]	Fraction of finger coverage of the global measurement area pGW [%]
Awd	<u>A</u>erosol-printed cell with <u>w</u>ide line <u>d</u>istance	65 ± 4.9	3.25
Asd	<u>A</u>erosol-printed cell with <u>s</u>mall line <u>d</u>istance	70.6 ± 4.4	7.06
S	<u>S</u>creen-printed cell	124.8 ± 4.3	6.24
S+LIP	<u>S</u>creen-printed cell <u>+</u> <u>LIP</u>	135.8 ± 3.9	6.79

Table 10-1 Explanation of the four different cells that have been processed

10.3 Global measurement

At this measurement as proposed by Stuckings [176], a 0.5 cm wide and 1 cm high area is illuminated with a wavelength-dependent spectrum between 600 nm and 1000 nm and the reflection is measured. The encapsulated cells have been measured, including 5 horizontally adjusted fingers in the measurement area. For the sample Asd 10 fingers were included. In Fig. 10-7, the wavelength-dependent reflection R_{ref} for the four cell types is plotted. Additionally, the following samples were studied: one sample without metal, one completely covered with screen-printed silver, and one completely of plated silver. As expected, the reflection increases with the covered metal fraction. Comparing the completely covered samples, it can be concluded that the plated silver reflects more light than the screen-printed silver.

The optical loss (OL) of a metal finger can be calculated using the following equation, according to the method of Stuckings [176].

$$OL = R_{ref}(cell) - R_{ref}(without\ metal) A_{ref} + \alpha_{abs} A_{abs} \qquad (10\text{-}7)$$

Optical loss is the reflection of a cell (incl. the metal fingers) minus the reflection without metal plus the absorption of the silver finger α_{abs}. A_{abs} equals 100% - R_{ref}(completely screen-printed silver) respectively R_{ref} (completely plated silver). The reflections are weighted with the covered areas A_{ref} and A_{abs}, which are determined from the microscope pictures. Schematically the calculation is clarified in Fig. 10-9.

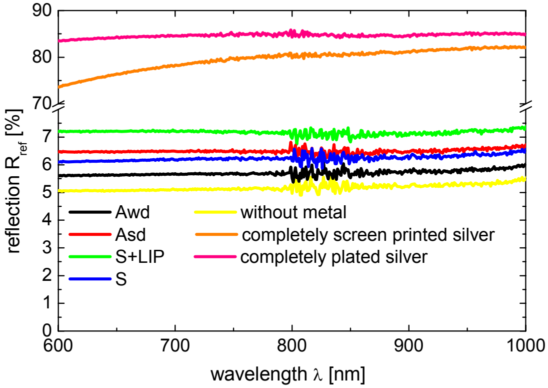

Fig. 10-7: Reflection curves of the global measurement of the four processed cells of Table 1 and additionally one cell without metal, one completely covered with screen-printed silver, and one with completely plated silver

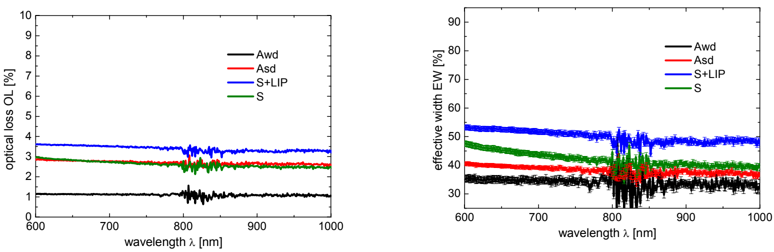

Fig. 10-8: Curves for the optical loss (OL) for the four different cell types (left) that are calculated according to equation (8) and effective width EW for the four different cells (see Table 1) (right)

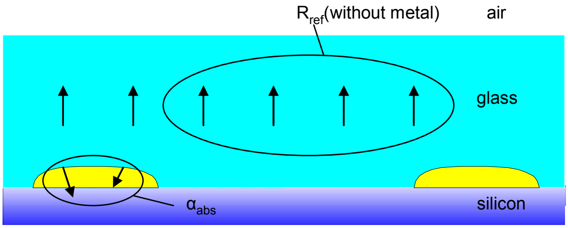

Fig. 10-9: Drawing for clarifying the optical loss OL: the reflection signal of the sample without metal is subtracted and the absorption of the silver is added to the reflection signal of each of the four cells

The data for the optical loss and the according effective width is plotted in Fig. 10-8, showing how much light is lost by each type of area. Regarding the fraction of the optical loss to the reflection of a flat finger that reflects all the light, or differently expressed the fraction of OL to the fraction of the finger coverage (pGW), we receive the effective width (EW).

$$EW = \frac{OL}{pGW} \tag{10-8}$$

The effective widths of all fingers are clearly under 60%, which means that just up to 60% of the finger area is effectively shading the cell and at least 40% of the light striking the finger is still producing current (see Fig. 10-2). Furthermore, the effective widths for the SFP contacts are smaller than for the screen-printed fingers. However, the optical contact area is also reduced significantly for screen-printed fingers. The highest values for the effective width could be found for screen-printed and plated fingers. There are two reasons for this: on the one hand, the reflectivity of the finger surface is increased and also the area is more smooth; therefore, more light is totally reflected in the middle part of the finger and can not be used in the solar cell. The other reason is the geometrical aspect ratio. The width of a screen printed and plated finger is rather ineffectively increased, which means the area (I) and (II) where most of the reflected light is directly used is comparably smaller than areas (III) and (IV) (see Fig. 10-3). Averaging the data, seed layer printed and plated cells have an effective width of 36%, the screen-printed finger 42%, and the additionally plated screen-printed finger has an EW of still only 50%.

10.4 LBIC measurement

Usually the LBIC method is used to measure the spatially resolved IQE by scanning a cell with a laser beam [178]. In this experiment, the laser beam with a wavelength of 833 nm and a diameter of 6 µm scanned a finger (of the four different cells above) 10 times with a displacement of 3.1 µm while measuring the reflection. The data of two fingers is shown in Fig. 10-10. Comparing them, the screen-printed finger looks wider than the aerosol-printed finger and has a higher maximal reflection. The average reflection in the case of the SP contact in the middle of the finger is about 50%, which means even if the light beam illuminates only the metal contact, only 50% is reflected directly. As the plated silver has a higher reflectivity than the screen printed silver (see Fig. 10-7), and the reflection in the middle of the finger is <40%, the optical contact width is probably reduced. The surface roughness is additionally visible from the LBIC measurement. The screen printed contacts have a higher surface roughness than the plated fingers, as the measured signal for the different scans is noisier in the case of the SP contacts.

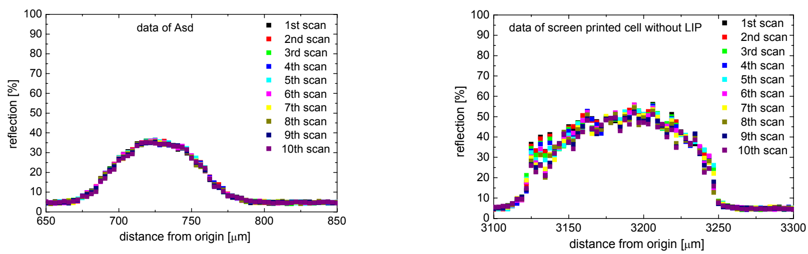

Fig. 10-10: Locally resolved reflection signal using a LBIC setup of an aerosol-printed and plated finger (left) and for a screen-printed, non-plated finger (right).

In order to compare the data with the measurement setup above, the following procedure was applied: The 10 scans were averaged and the signal was integrated and divided by GW. The loss by reflection is shown in Fig. 10-11. Beside the loss by reflection, the loss by absorption of the silver has to be included. The amount is only α_{in}=(100% - loss of reflection)R_{Ag}. Therefore, the effective width is EW =100% -α_{in}, which is plotted in Fig. 10-11 as well. The trend observed for this data is the same as for the global method. The aerosol-printed cells are optically narrower than the screen-printed cells. The aerosol-printed cells have an EW of 43% (average of Awd and Asd) and the screen-printed, as well as those with LIP, have an EW of 52%.

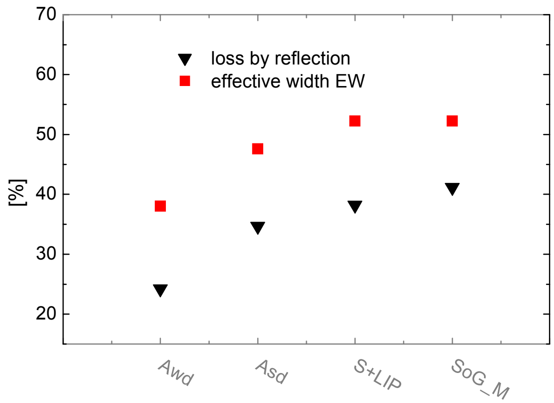

Fig. 10-11: Loss by reflection and effective width EW for the LBIC measurement of the four differently processed cells

Method	Aerosol-printing	Screen-printing
Theoretical value	34.5	-
Global measurement	36.0	41.9
LBIC measurement	42.8	52.3

Table 10-2 Calculated and measured effective widths for the three different methods for the aerosol and screen-printed cells. The screen-printed column includes the mean value for screen-printed cells and those with a plating step.

10.5 Chapter summary

The effective reflection of different types of metal fingers, screen printed and seed and plated (SFP), have been analyzed by theory and experiment. The theory showed that the effective shading area is significantly smaller than the geometrical one for a metalized front side finger. The effective widths for a SFP contact and a screen-printed contact were experimentally determined from LBIC measurements and from reflection measurements. Averaging the values for the SFP contact, the effective width is 38%, which is slightly higher than the values found by Blakers [104, 175] (36%) and Stuckings [176] (30-35%) received for contacts with a very narrow seed layer and electroplating. The effective width of a standard screen-printed contact is significantly reduced as well, and values between 40% and 50% were determined.

11 Results on silicon solar cells

During this work, silicon solar cells were produced on different substrates. The essential results are summarized within this chapter. Industrially relevant large-area multicrystalline silicon solar cells are fabricated as well as high-efficiency lab-type solar cells. All presented cells are metalized on the front side using the ink SISC in order to demonstrate the variety of applications. The contact performance of the ink was already investigated in previous chapters. Here the focus is on the cell design and in particular on the layout of the front side grid. The optimum between shading and electrical losses can be calculated using the simulation tool "GridSim" [25]. The theoretically found results can be confirmed experimentally by printing several different front side patterns on solar cells. The flexibility of the used printing technique, the aerosol print, is a clear benefit for this experiment, as it is possible to print any contact structure more or less directly from a CAD-drawing. The line width can be varied by using nozzles of different diameter. In the first experiment, the solar cell parameters of mc-Si solar cells are studied as a function of the metalized area. The metalized area is successively reduced. A significant reduction of the metalized area is possible if a different cell concept is used, where the front side metallization is partly transferred to the rear side as it is the case for metal-wrap-through (MWT) solar cells [179]. This type of solar cells is predestined for fine line printed contacts. In a last experiment, float zone (FZ) silicon is used to test the ink performance on a high-efficiency cell structure with passivated rear surface.

11.1 Results on large area silicon solar cells

11.1.1 Grid variation on mc-Si – reduced metalized surface fraction

The layout of the front side grid, especially line distance can be optimized with respect on the shading losses by printing thinner contact fingers with increasing the finger distance and on electrical losses by increasing the number of the contact fingers and their line conductivity. The width of a single finger (w_{fi}) is first of all dependent on the seed layer width (w_c) and on the plated silver height (h_{LIP}). The simulations in Fig. 11-1 are based on a large area 15.6x15.6 cm² mc-Si solar cell with a sheet resistance of R_{SH}=60 Ω/sq. The front side grid has three bus bars, a contact resistivity of ρ_c=1 mΩcm² and as an upper estimation for in-line plated silver fingers a line resistivity of ρ_f=3x10^{-8} Ωm. The total loss (p_{tot}), electrical losses and optical losses, is strongly dependent on the seed layer width, the line distance and only little on the LIP-silver height. As already shown in chapter 9, it is hardly possible to deposit too much LIP silver on a contact grid. The finger distance (d_f) can also vary in a range of ±0.5 mm without a significant increase in p_{tot}. For the experiment three different seed layer widths are realized: w_c=20 µm, 30 µm, and 50 µm, see Fig. 11-2. For each seed layer width, the optimum finger distance is calculated and varied around the minimum by ±0.2 mm. The grid layouts are summarized in the caption of Fig. 11-4. Three identical cells are produced resulting in nine cells per group (same seed layer width) and in total 27 solar cells.

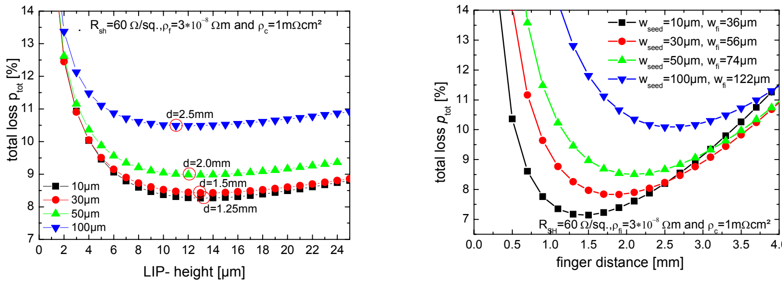

Fig. 11-1: Simulated optical and electrical power losses (p_{tot}) for a large area mc-Si solar cell as a function of the deposited LIP silver and finger distance for different seed layer widths.

The grid was varied on a multicrystalline 15.6x15.6 cm² sized solar cell. The cells have a rear side aluminium BSF and silver contact pads for the interconnectors. The front side is acidic textured and the 80 Ω/sq. $POCl_3$ emitter is passivated by a PECVD SiN_x antireflection coating. After printing, the cells are fired in an inline conveyor belt furnace at a set temperature of T_{set}=900°C and subsequently light-induced plated. The plating height was for all cells around h_{LIP}=12-14 µm. The finger width can be determined by adding two times h_{LIP} to the seed width.

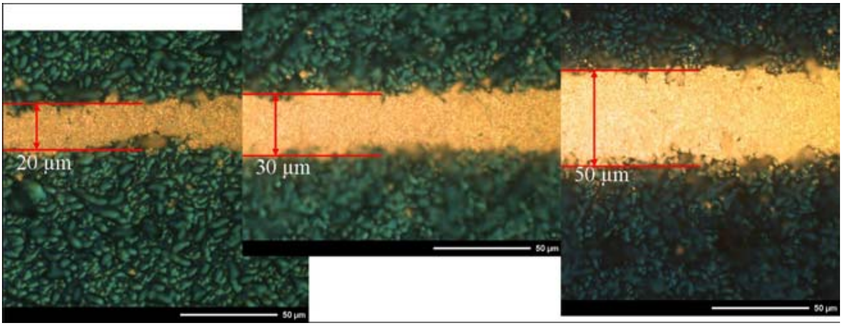

Fig. 11-2: Images of the deposited seed layers. The width was varied from w_c=20 µm to w_c=50 µm by using different nozzle openings.

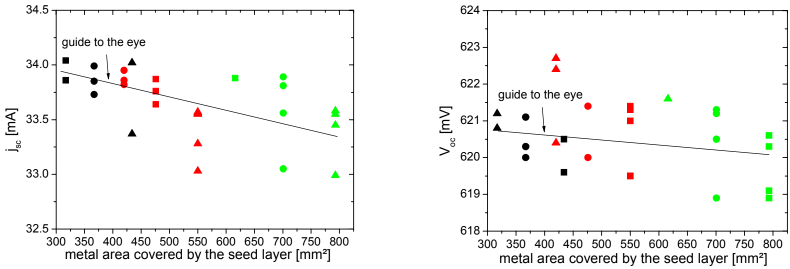

Fig. 11-3: The short circuit current density j_{sc} is strongly dependent on the metalized area whereas V_{oc} is almost constant.

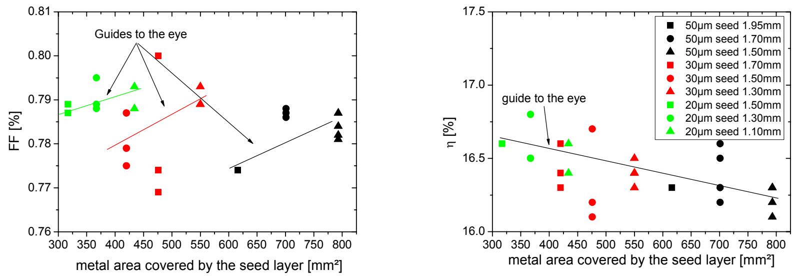

Fig. 11-4: The FF is more dependent on the number of fingers than on the total metalized area. The efficiency η is continuously reduced as the local benefit in FF is overcompensated by a reduced j_{sc}.

The *IV* parameters are shown as a function of the metalized area in Fig. 11-3 and Fig. 11-4. The best correlation can be found between metal area and j_{sc}, as the current density is rather sensitive to shading losses. The open-circuit voltage is slightly reduced with an increasing metallization fraction; however, the average reduction is only within one mV. Thus the higher recombination losses under the metal contacts hardly limit V_{oc}. For the *FF*, the important parameter is not the total amount of silver but the number of fingers which is increased within each group. The *FFs* of each group increased as well as an increased metal fraction is equal to an increased number of fingers. The efficiency, however, is clearly dependent on the metalized area and the gain in *FF* with a larger number of fingers is overcompensated by a reduced current and the overall efficiency is reduced for increased metalized area. In Table 11-1 the results are summarized for the average values for each group and the best cell. The best cell printed with a seed layer width of w_c=20 µm achieved an efficiency of η=16.8%. The quite low contact resistance of only ρ_c=2 mΩcm² together with the high number of fingers (119) allow a fill factor of *FF*=78.5% and in parallel high values for j_{sc}=34 mA/cm². In total, the best way to increase the cell efficiency is to reduce the metalized area, without reducing the number of contact fingers. This appears only to be possible with the deposition of even finer lines. The front side grid can be separated in contact fingers and bus bars. The fraction covered by the fingers is about 40-50% (for fine line printed fingers) of the total metalized area and thus the bus bar covers almost 50%. The shading losses drastically can be reduced if the influence of the bus bars is diminished. This is possible by using a larger number of smaller bus bars [25] or by using a multi-wire electrode as an interconnector as it is the case for the Day4™ technology [180, 181]. The most elegant solution, however, is to remove the bus bars completely from the front side. This is realized in a cell concept called metal-wrap-through solar cell (MWT) [179].

	w_c	f_d	V_{OC}	J_{SC}	FF	η
	[µm]	[mm]	mV	[mA/cm²]	[%]	[%]
Ave	20		621	33.8	79.0	16.6
best cell	20	1.3	621	34.0	79.5	16.8
Ave	30		621	33.8	78.2	16.4
best cell	30	1.5	620	33.6	80.0	16.7
Ave	50		620	33.6	78.4	16.3
best cell	50	1.7	621	33.9	78.7	16.6

Table 11-1: Results for large area mc-Si solar cells, metalized with different contact widths and finger distances.

11.1.2 Metal-wrap-through solar cell on mc-Si

In addition to fine line printing, the metalized fraction on the front side can be reduced by a new cell design called metal wrap through (MWT) solar cells [179]. In this case, the bus bars are transferred from the solar cell front side to the back side. This is realized by drilling small holes, vias in the cell, placed along the former bus bars. The metalized vias are interconnecting the front-side grid with the bus bars at the rear side. In order to avoid shunting of the cell, the emitter region is expanded from the front side through the vias to the bus bar region on the rear and isolated by laser ablation, see Fig. 11-5. On the cell front side, only small metalized holes with a diameter d_{via}<200 µm are contributing to the shading losses, see Fig. 11-6 and Fig. 11-7. The processes and layout of a mc-Si MWT-solar cell developed by Clement [182] are used to test the combination of fine line printing and MWT concept. Due to a design and process sequence which is very similar to that of conventionally processed screen-printed solar cells, the rear contact MWT solar cell is a very promising alternative. The absence of the front bus bars leads to a gain in active cell area and thus an efficiency gain compared with conventionally processed screen-printed solar cells, especially if the front side grid is realized by fine line printing.

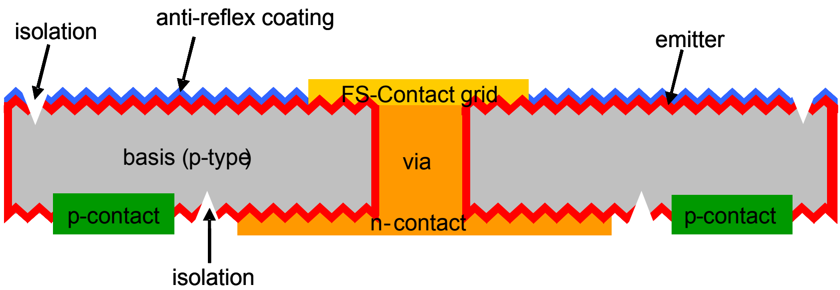

Fig. 11-5: Schematic of a MWT-solar cell from [183].

To achieve fine line printed front contacts different approaches will be discussed. First, a new, readily implementable screen-printing technique [184] which allows a significantly reduced printed finger width on textured surfaces in comparison to conventional screen printing is presented. This can be reached by using a heated print nest that keeps the wafer at a defined temperature while printing, leading to less spreading effects of the printed structure. Second, a two-step metallization process including seed layer printing and light induced inline silver plating [8] is shown. For the seed layer metallization step two different techniques are compared: screen-printing and metal aerosol jet printing [9].

The presented metallisation techniques are applied to conventional and MWT solar cells. For solar cell processing a conventional process flow including Al-BSF as rear metallization is chosen. For MWT solar cells only two additional laser process steps (via hole drilling and rear contact isolation) and one screen-printing step (via hole metallization) compared with the conventional cell process are used.

Fig. 11-6: images of a conventional solar cell (left) and a MWT solar cell (right). Instead of the bus bars, which are covering about 3% of the front side, only hole-contacts (vias) are visible with a negligible contribution to the front side shading [185].

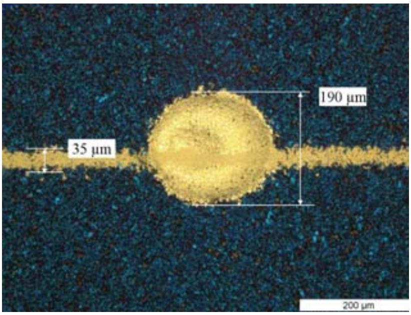

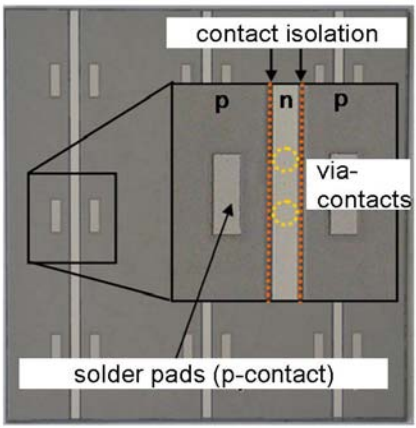

Fig. 11-7: The fine line printed front side contact is deposited on a metalized via in order to connect the front side grid with the rear side (left). Rear side of a MWT-solar cell (right).

With a one step metallization process based on screen-printing cell efficiencies up to 16.4% are reached for MWT solar cells. Front contacts with line widths of about 80 µm and heights over 10 µm are realized. An efficiency gain up to 0.5% absolute is achieved by the use of MWT cells instead of conventional solar cells, see Table 11-2.

By the use of a two-step metallization process efficiencies up to 16.7% are achieved with both, fine line screen-printed and aerosol jet printed seed layers and up to 16.8% for MWT solar cells. For all cells an emitter sheet resistance of about 80 Ω/sq is used. Contact widths of 30 µm to 60 µm are reached before and 70 µm to 100 µm after light-induced silver plating as well as contact heights of 10 µm to 20 µm after light-induced silver plating. The finger geometry depends on the applied metallization technology. However, due to the two-step metallization process a clear efficiency increase is reached compared with the one-step metallization process; visible in the increased current density j_{sc} of about 1 mA. Another increase by 1 mA to a value of j_{sc}=35.9 mA/cm^2 is achieved by applying the two layer metallization to MWT solar cells. Moreover, primary low values of the pseudo fill factor limit the efficiency of MWT cells in comparison with conventional cells, especially for emitters with high sheet resistances. But a further optimization of the via pastes [186] should allow higher pseudo fill factors and thus efficiencies over 17%.

Cell type	**Print-technology**	V_{OC} **mV**	j_{SC} **[mA/cm²]**	FF **[%]**	η **[%]**	FF_0 **[%]**	PFF **[%]**
One-step metallization, R_{SH}=65 Ω/sq							
conv.	Screen-printing	612	33.7	77.3	15.9	83.0	80.9
MWT	Screen-printing	615	34.8	76.8	16.4	83.0	80.6
Two-step metallization, R_{SH}=80 Ω/sq							
conv.	Screen-printing (fine line)	616	34.9	77.9	16.7	83.0	81.0
conv.	Aerosol	615	34.7	78.1	16.7	83.0	80.7
MWT	Aerosol	615	35.9	76.0	16.8	83.0	79.5

Table 11-2: IV parameters of MWT solar cells in comparison with standard solar cells produced on 12.5x12.5 cm² mc-Si wafers. Standard screen printed cells are compared with two sep metalized fine line screen print and aerosol print solar cells [182].

11.2 Results on high-efficiency solar cells

In order to test the performance of fine line printed contacts, the developed SISC ink was deposited on a high-efficiency cell structure, shown in Fig. 11-8. The advantage of a passivated rear side with the benefit of an industrially feasible two-step front side metallization is combined within these cells. Neither the formation of a selective emitter nor the opening on a dielectric layer is necessary which makes the process flow rather simple, compared to photolithographically defined cell structure.

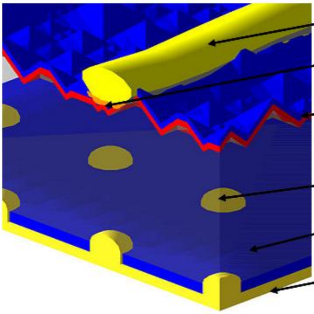

Fig. 11-8: Schematic of the used high efficiency cell structure

The cell structure, used in this experiment, shown in Fig. 11-8 is rather simple and all processes are transferable into an industrial production. Silicon solar cells with different emitter sheet resistance were produced on float zone silicon wafers (thickness 250 µm, p-type, resistivity 0.5 Ωcm). On each wafer seven 4 cm² solar cell were produced. The single diffused shallow n-type emitter was processes in a $POCl_3$ tube furnace. The textured front side is passivated with a 70 nm thick PECVD-SiN_x anti reflection coating on which the front contacts are directly aerosol jet printed. After firing in a conveyer belt furnace at set temperature of about T_{set}=830°C the contacts were plated using LIP. The rear side of the cells is passivated by a 100 nm wet thermally grown silicon dioxide on which a layer of 3 µm aluminium is evaporated. The point contacts on the rear are created by laser contact firing (LFC) [187]. Finally, to improve the passivation of the oxide thermally grown in a wet ambient and to improve the contact performance on the rear and on the front, the cells are annealed under reducing atmosphere for 10 min at a temperature of T=350°C.

The comparison between the new metallization processes of aerosol printed- and plated (LIP) contacts and the standard high efficiency photolithography process presently used in our laboratories is depicted in Fig. 11-9 and shows the reduced complexity of the process.

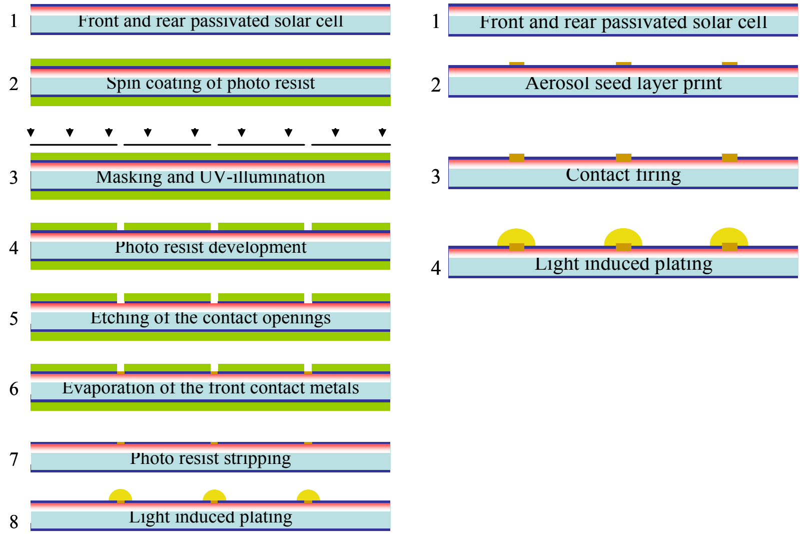

Fig. 11-9: Process flow of a photolithographically defined cell metallization (left) and of fine line printed and fired contacts (right).

11.2.1 Grid optimization

In this experiment, the deposited seed layer width is in the range of 20 µm < w_c < 30 µm. During plating in a cyanide plating bath approximately 20 µm of silver was grown on the fired seed layer resulting in a line width of about 60 µm. A cross section of such a contact structure is depicted in Fig. 11-10. The contact-less printed seed layer has a height of only 2 µm after printing and of 1-2 µm after contact firing, respectively. The contact resistivity on an emitter with a sheet resistivity of R_{SH}=75 Ω/sq. as it is used in this experiment of ρ_c=2 mΩ cm² is measured and for the line resistivity after plating a value of ρ_l=2*10^{-8} Ω m was found.

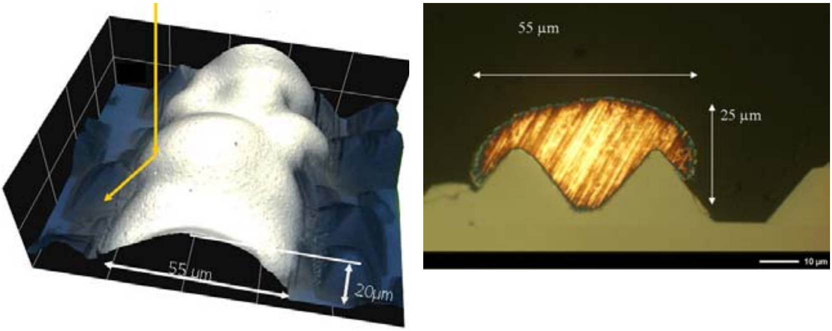

Fig. 11-10: Contact geometry: microscopic 3d image (left) and microscopic image of a cross section (right).

The electrical data together with the grid layout are used to simulate the front side grid in order to determine the optimum finger distance, see Fig. 11-11. The optimum is found around a finger distance of d_f=1.8 mm. Experimentally with 3 identical wafers on which seven solar cells are produced, the finger distance is varied from d_f=1.2 mm to d_f=2.4 mm within Δd_f=0.2 mm steps. The relation between *IV* parameters and finger distance is interesting. While a clear trend between the FF, j_{sc} and the finger distance can be seen, the efficiency is more or less on a constant level, see Fig. 11-12. The increase of the *FF* and the decrease in j_{sc} show a linear behaviour. Using these linear fits and the almost constant open-circuit voltage of V_{oc}=644.6mV (±1.3mV), the calculated efficiency is hardly influenced by the finger distance and a mean value of 19.9% is found. The fact, that an optimum is apparently visible around a finger distance of d_f=1.8-2.0 mm is related to statistical effects and the fact that these cells are predominantly placed in the middle of the wafer. For these cells efficiencies as high as η=20.2% are measured. In conclusion, within the tested range, the finger distance has an influence on *IV* parameters, however, not on the cell efficiency. In order to reduce the amount of silver it is recommended rather to reduce the number of fingers than to increase it.

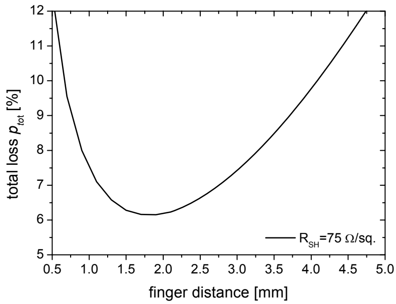

Fig. 11-11: Simulated power loss including optical and electrical losses caused by the front side grid for a 2x2 cm² high efficiency solar cell.

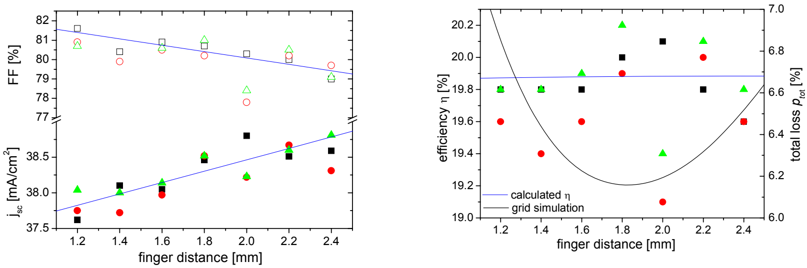

Fig. 11-12: IV parameters for high efficiency solar cells as a function of the finger distance. FF and j_{sc} are strongly dependent on the number of fingers (left) whereas the efficiency is hardly affected as the total loss p_{tot} is varied by less than 1%.

11.2.2 Best solar cell results

The best value for the energy conversion efficiency of η=20.6% was achieved on a 2x2 cm² FZ-Si solar cell with a sheet resistivity of R_{SH}=110 Ω/sq. On each wafer seven 4 cm² cells were aerosol printed. The printed finger width was w_c<20 µm after printing and 45 µm after LIP, respectively. The busbar for all cells has the same shape and covers about 1.5% of the active cell area. In total, an area of 5.6% is covered by the front side grid. Due to the round shape of the plated fingers, incoming light can be reflected from the finger onto the active solar cell area, see Fig. 11-10. Thus, the optical width of the contact is considerably smaller than the geometrical width [104] which decreases the shadowing losses drastically. In chapter 10 it is shown that the optical width of an aerosol-printed and plated contact embedded in a module is only 43% of its geometrical width [188]. The contact resistance is determined by TLM measurements. A contact resistivity on a R_{SH}=110 Ω/sq. emitter of ρ_c =2 mΩ cm² is measured and for the line resistivity after plating a value of ρ_l=2x10^{-8} Ω m was found. The optimized finger distance is calculated including the optical width to d_i=1.1 mm, which is close to the experimentally determined value of d_i=1.0 mm for the best cell.

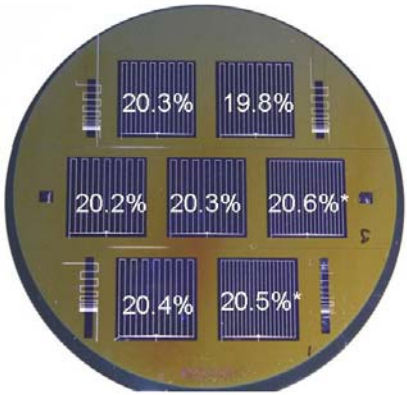

Fig. 11-13: High efficiency wafer with seven aerosol- printed, fired and plated solar cells.

The independently confirmed *IV*-parameters for the best cells are summarized in Table 11-3. The very good values of V_{oc} around 650 mV are due to a high-quality passivated rear, achieved by the wet thermally grown oxide combined with laser-fired point contacts and the reduced contact area at the front side. The values for the short circuit current density j_{sc} have some potential for a further increase. The texturing of the cell front side was not homogenously, see Fig. 11-10 and the amount of plated silver can also be reduced. The low series resistance of R_s=0.5 Ωcm² result in a fill factor of *FF*>80%. The pseudo fill factor of *pFF*=83% indicate, that the quality of the *pn*-

junction is hardly affected by the metallization and the difference between *FF* and *pFF* can be explained by the series resistance losses.

The improved performance of the lower doped emitter is clearly reflected in the short-wavelength region of the quantum efficiency, see Fig. 11-14. The quantum efficiency for the R_{SH}=110 Ω/sq emitter is close to one and thus close to the performance of a high-efficiency lab-type cell. For the simulation of this cell, the emitter profile is defined by a surface doping concentration of $N_D=10^{20}$ cm^{-3}, an error-function like profile and a junction depth of 290 nm. The calculated emitter sheet resistance of R_{SH}=111 Ω/sq. is consistent with the value determined by TLM measurement and 4-point probe measurement. The front side recombination was set to S_F=10000 cm/s which is similar to the values found by Cuevas [189] for oxide-passivated samples. Using this set of parameters the IQE measurement can be described accurately. Also the open-circuit voltage, V_{oc}=660 mV and the short-circuit current j_{sc}=38.4 mA/cm^2 extracted from the simulation under one-sun simulation are consistent with the *IV*-measurements. In order to evaluate the efficiency potential of our front side structure, we set the bulk and rear side recombination to zero in the simulation and found a value for V_{oc}=676 mV, j_{sc}=39.5 mA/cm^2 and a maximum efficiency of η=21.8%. This shows the very high potential of this simple front structure with a single, shallow emitter diffusion, a single passivation layer, and a firing step for the contact formation. The solar cell is not limited by the front side metallization as in the case of industrial standard screen-printing with low sheet resistance emitters and high shading losses.

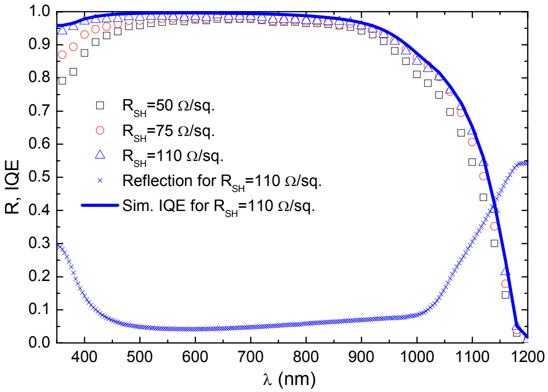

Fig. 11-14: Higher emitter sheet resistances having a higher IQE in the short wavelength region, even if single diffused shallow diffusion profiles are used. The IQE for the R_{SH}=110 Ω/sq. emitter is additionally simulated using PC1D.

No.	**R_{SH}**	**A**	**V_{OC}**	**J_{SC}**	**FF**	**pFF**	**η**	**R_S**	**ρ_c**
	[Ω/sq.]	**[cm²]**	**mV**	**[mA/cm²]**	**[%]**	**[%]**	**[%]**	**[Ωcm²]**	**[mΩcm²]**
21.1*	110	4	661	38.7	80.1	83.2	20.5	0.5	2.0
21.3*	110	4	658	37.5	81.4	82.8	20.6	0.5	2.0

*Table 11-3: IV parameters of the best solar cells, including a printing and firing step for the metallization. *The values are independently confirmed by Callab ISE.*

11.3 Chapter Summary

The best large area 15.6x15.6 cm² mc-Si solar cell produced within this work achieved an efficiency of η=16.8%. The quite low contact resistance of only ρ_c=2 mΩ□cm² together with a high line resistivity of ρ_l=3x10^{-8} Ω m allow a fill factor of FF=78.5% even on an emitter with a sheet resistance of R_{SH}=80 Ω/sq. The finger distance was reduced to d_f=1.3 mm, never the less high values for j_{sc}=34 mA/cm² were realized. This was possible as the metalized area was drastically reduced by depositing seed layers with widths of only w_c=20 µm (finger width w_f=50 µm). Using a standard front side grid, a further reduction of the metalized area is hardly possible as the busbars are covering about half of the contact area. With a new cell design where the busbars are located on the rear side, called metal wrap through (MWT) solar cells [179], fine line printing is predestined. Compared to a standard cell, the current density j_{sc} is increased by 1 mA/cm^2 to a value of j_{sc}=35.9 mA/cm² by applying the two layer metallization to mc-Si MWT solar cells. Fine line printed MWT solar cells on mc-Si material (12.5x12.5 cm²) achieved efficiencies up to η=16.8%. Higher efficiencies are expected for the future as currently the cells are limited by the quality of the via metallization which reduces the *pFF* and therefore the *FF* to a value of *FF*=76%.

The high-efficiency solar cells fabricated on FZ-wafers combine the advantages of an advanced front side metallization with a passivated and local contacted (LFC) rear side. Both processes are industrially feasible. In a first experiment the front side grid was optimized on 2x2 cm² solar cells with a R_{SH}=75 Ω/sq. Within the tested range of finger distances (1.8 mm<d_f<2.5 mm), the cell efficiency is hardly affected as the gain in j_{sc} is compensated by the loss in *FF*. Within this experiment solar cells were produced with an efficiency of η=20.2%.

In order to test the performance of the SISC ink the same high efficiency cell structure was used, however, with an higher emitter sheet resistance of R_{SH}=110 Ω/sq. The reduced contact area together with a negligible contact resistance of only ρ_c=2 mΩ cm² makes it possible to benefit from an increased V_{oc} of 661 mV and j_{sc} of 38.4 mA/cm^2. On 2x2 cm² solar cells with a R_{SH}=110 Ω/sq. emitter record cell efficiencies of η=20.6% were measured and independently confirmed. Thus, using the metal ink developed in this work, it is possible to contact lowly doped emitters with an excellent blue response and high efficiency potential. Up to this point this was only possible using non-industrial techniques as evaporation of Ti or by the use of selective emitter, i.e. a local highly diffused area under the contacts.

12 Summary

In this thesis, the contact formation on the front side of crystalline silicon solar cells is optimized. The cell efficiency is increased and at the same time the amount of consumed contact metal is reduced. In order to achieve this goal the optical and electrical losses had to be reduced by achieving contact fingers with a high aspect ratio (height:width), higher line conductivity and lower contact resistivity. This is only possible if the contact resistivity and the line resistivity are optimized individually as is the case for the two-layer metallization. The conductive layer is produced using the already established technique of light-induced plating (LIP), where line resistivities close to bulk metals can be achieved. The challenge was to develop a seed layer with a reduced contact area and a low contact resistivity, which ideally is deposited on the passivation layer and fired through in a high-temperature step similar to the standard process for screen-printed contacts.

Special attention was paid to improving the aerosol jet printing system used for the contactless deposition of fine lines on silicon solar cells. The system was analyzed to determine the ink requirements, including viscosity, vapour pressure and particle size. Simulation and measurement show that the optimum deposited particle/droplet size is around d_p=0.5 µm. With an optimized ink, contact fingers with a line width w_c below 20 µm were deposited on randomly textured surfaces. Although thinner contact lines will reduce the shadowing losses, the requirements for a low specific contact resistivity are very high due the reduced contact area.

Thus, the main focus of this thesis is on the development of a seed layer ink for low ohmic contacts in particular on *n-type* emitters with a high sheet resistivity (R_{SH}>100 Ω/sq). The fundamental reactions between a silver contact ink and the silicon surface were investigated by thermal gravimetric-differential thermo analysis (TG-DTA). Contact inks are mainly consisting of silver particles and a lead-oxide glass frit. The important components for the contact formation are lead oxide as a contact promoter and silver as a contact metal. The reaction mechanisms between lead oxide and silicon and with dielectric coatings, like SiN_x and SiO_2 were clarified. Both, the opening of the dielectric layer and the “etching” of silicon are redox-reactions, where lead oxide is reduced to the metal and silicon dioxide is formed and added to the glass. Lead oxide reacts exothermically with Si or SiN_x at a temperature of about 680°C and the reduced metal can solve high amounts of silver, which re-crystallizes during cooling in form of a silver- and lead-rich phase according to the phase diagram. As the reactions are temperature-controlled and based on an oxidation process, both high temperatures and the excess of oxygen promote the reaction. In general, low melting oxides like lead oxide or bismuth oxide are responsible for the reaction with silicon and therefore necessary for the contact formation. The observed strong reactivity of the pure metal oxides with silicon can be moderate if the oxides are incorporated into a glass frit that makes the contact formation less sensitive to the firing temperature. It was additionally demonstrated that bismuth oxide is a suitable replacement for the toxic lead oxide as the same reactions occur at similar temperatures.

Based on these principal investigations, contact inks were formulated and fabricated with respect to the requirements for aerosol printing and tested on crystalline silicon solar cells. First the influence of the reactive metal oxide on the contact interface was studied. Inks, based on silver and bismuth oxide, were formulated with different ratios and aerosol jetted on solar cells. The *IV* parameters were rather more sensitive to the firing temperature than to the oxide content. As the printed seed layers are very thin h_c<2 µm, the oxide content is less important but as soon as the firing temperature exceeds the activation energy, a strong reaction between bismuth oxide and silicon occurs. The etching of silicon becomes even too strong, making finding of the right firing parameters difficult. The formed contacts tend to shunt the *pn*-junction and/or metal impurities are diffused into the space charge region, resulting in a strongly increased value for j_{02}. Nevertheless, it was possible to fabricate multi-crystalline silicon solar cells featuring a standard industrial design with an efficiency of η=16.3%. Furthermore, the advantages of using a glass frit instead of the pure oxide were tested for both leaded glass and bismuth oxide-based glass. It was found that the cell results are less dependent on the firing temperature which can be explained by the moderate reaction between glass and silicon. The contact formation occurs in a broader range of temperature and the values for j_{02} and R_p are not related to the temperature. For a seed layer application where the deposited ink height is only 1 µm, the glass content, similar to the bismuth content, is less critical and can also vary between 2-20 m% without a significant reduction in cell performance.

The developed **s**eed layer **i**nk for the metallization of silicon **s**olar **c**ells (SISC) was used to analyze the contact microstructure and the possible current paths on a thin printed contact. The measured contact resistivity was improved by reducing the seed layer height. The contact formation for a thin contact is more efficient than for a thick printed contact, as the reactive ink components are in direct contact with the cell surface and environmental oxygen supports the reaction. High density of silver crystallites, which are responsible for the contact are found, even if less than 5 mg of ink per wafer (15.6 cm x15.6 cm) is deposited, which is only 2-3% compared to screen printed contacts. It was shown that for seed contacts the dielectric layer was only locally opened under the metalized area. The local "etching" has the advantage that only a small amount of glass is formed during the contact formation and the glass layer thickness at the metal-semiconductor interface is rather thin. On each point were the SiN_x coating was opened, a silver crystallite was grown, forming a point contact. The only possible current path is therefore via the silver crystallites, as the rest of the contact area is still covered by the dielectric layer. The contact resistivity for differently doped emitters was experimentally determined and on an emitter with a sheet resistivity of R_{SH}=130 Ω/sq a contact resistivity of ρ_c<5 mΩ cm² was measured, which is an order of magnitude lower compared to a standard thick film contact.

The best large area 15.6x15.6 cm² mc-Si solar cell produced within this work achieved an efficiency of η=16.8%. The quite low contact resistance of only ρ_c=2 mΩcm² together with a high line resistivity of ρ_l=3x10^{-8} Ωm allow a fill factor of *FF*=78.5%, even on an emitter with a sheet resistance of R_{SH}=80 Ω/sq. The finger distance was reduced to d_f=1.3 mm, but nevertheless high values for j_{sc}=34 mA/cm² were realized. This was possible as the metalized area was drastically reduced by depositing seed layer widths of only w_c=20 µm (finger width w_f=50 µm).

The high-efficiency solar cells, fabricated on FZ-wafers combine the advantages of an advanced front side metallization with a passivated and local contacted (LFC) rear side. In a first experiment the front side grid was optimized on 2x2 cm² solar cells with an emitter sheet resistance of R_{SH}=75 Ω/sq.. Within the tested range of finger distances (1.8 mm<d_f<2.5 mm), the cell efficiency is hardly affected as the gain in j_{sc} is compensated by the loss in *FF*. Within this experiment solar cells were produced with an efficiency of η=20.2%.

On the same high efficiency cell structure with an emitter sheet resistance of R_{SH}=110 Ω/sq a contact resistivity of only ρ_c=2 mΩ cm² for a contact width w_c<20 µm was determined and a record cell efficiency for a printed and fired solar cell of η=20.6% and *FF*=81% were measured and independently confirmed.

For future work it would be interesting to study the relation between surface defects and crystallite growth and to answer the question weather the dopants or the crystal defects are responsible for the growth of contact crystallites. Also the role of dopants on the contact formation needs further investigations in particular on p-type emitters. Additionally, a replacement for the contact and conductive material silver is needed. A promising and intensively studied contact material is Nickel, however only little information about Nickel as a high temperature contact metal can be found in literature so far.

Deutsche Zusammenfassung

In der vorliegenden Arbeit wurde das Vorderseitenkontaktgitter von kristallinen Siliciumsolarzellen optimiert. Dabei wurden durch schmalere Kontaktstrukturen die metallisierte Fläche und damit die Abschattungsverluste verringert, ohne jedoch die elektrischen Verluste zu erhöhen. Dies ist möglich, indem eine zweistufige Vorderseitenmetallisierung verwendet wird, bei der im ersten Schritt eine dünne Kontaktschicht aufgebracht wird, welche in einem zweiten Schritt galvanisch verstärkt wird. Dies hat den Vorteil, dass der Kontaktwiderstand unabhängig von der lateralen Fingerleitfähigkeit optimiert werden kann. Die Herausforderung bei dieser Arbeit war es, eine Kontaktschicht zu entwickeln, die trotz stark reduzierter Kontaktfläche einen geringen elektrischen Widerstand aufweist und idealerweise, ähnlich einer Standard-Siebdruckmetallisierung, in einem Hochtemperaturschritt, durch die dielektrische Passivierungsschicht gefeuert werden kann.

Die dünnen Kontakte wurden mit einem Aerosol-Drucker aufgebracht. Dieses neuartige kontaktlose Druckverfahren wurde speziell für die Metallisierung von kristallinen Solarzellen optimiert, hinsichtlich hoher Abscheideraten (Druckgeschwindigkeit), Druckstabilität und des Druckes dünner Linien auf texturierten Substraten. Die Anforderungen für eine Aerosol Tinte wie Viskosität, Partikelgröße, geeignete Lösemittel wurden untersucht und fließen bei der Tintenformulierung mit ein. Simulation und Messung ergaben, dass die optimale Tröpfchengröße und damit maximale Partikelgröße bei 0.5 µm liegt, ebenso wurde eine obere Grenze für die Viskosität gefunden, die 1 Pas bei geringen Scheerraten nicht überschreiten sollte. Mit einer angepassten Tinte konnten auf alkalisch texturierten Solarzellen Linienbreiten von weniger als w_c<20 µm gedruckt werden. Obwohl schmalere Kontaktstrukturen die optischen Verluste reduzieren, steigen dadurch die Anforderungen an den spezifischen Kontaktwiderstand, da nur eine reduzierte Kontaktfläche zur Verfügung steht.

Deshalb ist der Schwerpunkt der Arbeit die Entwicklung einer Kontakttinte zur Verbesserung des Kontaktwiderstandes am Metall-Halbleiterübergang auf n-Typ Silizium vorzugsweise bei einer reduzierten Dotierkonzentration bzw. einem erhöhten Schichtwiderstand (R_{SH}>100 Ω/sq) des Emitters. Zunächst wurden die fundamentalen Reaktionen zwischen Kontaktmaterialien und Solarzelle mittels differentieller Thermoanalyse untersucht. Eine Vorderseitenmetalltinte besteht maßgeblich aus Silberpartikel und einem niederschmelzendem Glas, wobei der Hauptbestandteil der Glasfritte Bleioxid oder Wismutoxid ist. Das Öffnen der Antireflexschicht und auch das „Ätzen" der Kontakttinte in Silicium basiert auf Redoxreaktionen, bei denen Blei- bzw. Wismutoxid zum Metall reduziert und Silizium bzw. Siliziumnitrid bei Temperaturen um T=680°C zu Siliziumdioxid oxidiert werden. Das entstandene metallische Blei oder Wismut löst Silber und die entstandene Si-Pb/Bi Phase erstarrt beim Abkühlen, entsprechend den Phasendiagrammen. Das bei der Reaktion entstandene SiO_2 verbleibt in der Glasschicht an der Kontaktgrenzfläche. Je mehr Silicium oxidiert wird, desto dicker ist später die isolierende Glasschicht und umso höher der Kontaktwiderstand. Weiterhin wirken sich Temperatur und Sauerstoffgehalt der Umgebung reaktionsfördernd aus. Am stärksten verlaufen die Kontaktbildungsreaktionen wenn reine Oxide (PbO, Bi_2O_3) verwendet werden, was eine kontrollierte Kontaktbildung nahezu unmöglich macht. Um die Kontaktbildung besser kontrollieren zu können, werden die Oxide in ein Glassystem überführt und damit der Reaktionsbereich, bei dem eine Kontaktbildung stattfinden kann, auf 100°C erweitert. Es wurde auch gezeigt, dass Wismutoxid in der Lage ist, das giftige Bleioxid zu ersetzen, da dieselben chemischen Reaktionen bei ähnlichen Temperaturen ablaufen.

Bei der Auswahl der Prozessparameter und vor allem der Tintenformulierung ist ein Gleichgewicht zwischen guter Kontaktbildung und geringer Schädigung der Emitterschicht zu finden. Basierend auf den Reaktionsmechanismen bei der Kontaktbildung, wurden Aerosoltinten hergestellt und auf Siliciumsolarzellen getestet. Bei allen untersuchten Tinten wurde ein Zusammenhang zwischen Kontaktwiderstand, Zellparameter und Kontaktstruktur (REM-Aufnahmen) hergestellt. Untersucht wurde der Einfluss des Oxid/Glasanteils auf die Kontaktbildung bei verschiedenen Temperaturen. Bei Tinten, die im Wesentlichen aus Silber und Wismutoxid bestehen, ist die Kontaktbildung vor allem von der Feuertemperatur und weniger vom Oxidgehalt abhängig. Die Auftragshöhe der Kontakttinte ist sehr gering (1-2 µm) und daher ist der Oxidanteil im Vergleich zu einem Dickschichtkontakt weniger kritisch, sobald jedoch die Aktivierungsenergie für die Reaktion zwischen Bi_2O_3 und Silicium erreicht ist, wird die Zelloberfläche unter den Kontakten stark angegriffen. Die *IV* Parameter der Solarzellen werden daher sehr von der Feuertemperatur beeinflusst und eine Schädigung des pn-Übergangs und lokale Kurzschlüsse sind kaum zu vermeiden. Dennoch ist es gelungen, multikristalline Silicium-Solarzellen auf großer Fläche (15.6x15.6 cm²) und industriellem Design mit einem Wirkungsgrad von η=16.3% herzustellen. Der Vorteil eines Glassystems im Vergleich zum reinen Metalloxid wurde mit zwei Gläsern, eines basierend auf Bleiglas das andere auf Wismutglas bestätigt. Sobald das Oxid im Glas gebunden war, konnten stabile Zellergebnisse über einen Bereich von mehr als 100°C unabhängig von der Feuertemperatur gemessen werden. Der Glasanteil hat ähnlich wie der Wismutoxidanteil nur einen geringen

Einfluss auf den Kontaktwiderstand und variiert im Bereich von 2-20gew% ohne signifikante Auswirkung auf die Zellparameter zu haben.

Die in dieser Arbeit entwickelte Kontakttinte mit der Bezeichnung SISC dient dazu, um die Kontaktbildung, die Mikrostruktur und mögliche Strompfade an schmalen Kontakten zu untersuchen. Es wurde gezeigt, dass sich der Kontaktwiderstand durch den verringerten Auftrag reduziert. Die reaktiven Tintenbestandteile sind näher an der Zelloberfläche und auch Sauerstoff aus der Umgebungsluft kann besser die Grenzschicht zwischen Tinte und Zelle erreichen. Bei optimal gefeuerten Kontakten ist die Dichte der Silberkristallite am Kontakt trotz geringer Auftragshöhe sehr hoch und bedeckt ca. 10% der Kontaktfläche. So ist z.B. zur Kontaktierung eines 15.6x15.6 cm² großen Wafers eine Tintenmasse von lediglich 5 mg notwendig. Die geringe Auftragshöhe hat zur Folge, dass die Antireflexschicht unter den Kontakten nicht vollständig, sondern nur lokal geöffnet ist, wobei jede Öffnung durch einen Silberkristallit gefüllt ist. Für den Strom vom Emitter in den Kontaktfinger ergibt sich somit nur ein möglicher Strompfad über die Silberkristallite, da die übrige Kontaktfläche von der Passivierschicht bedeckt ist. Der Kontaktwiderstand ist zum einen von der Flächendichte der Silberkristallite als auch von der Dicke der Glasschicht zwischen Kristallit und Silberfinger abhängig, weshalb der Glasanteil in der Tinte tendenziell gering sein sollte. Der Einfluss des Emitterschichtwiderstandes auf den Kontaktwiderstand wurde für verschieden dotierte n-Typ Emitter ($40\ \Omega/sq<R_{SH}<130\ \Omega/sq$) experimentell bestimmt. Auf einen Emitter mit einem Schichtwiderstand von $R_{SH}=130\ \Omega/sq$ und einer Oberflächenkonzentration von $N_D=2\times10^{20}\ cm^{-3}$ wurde ein Wert von $\rho_c<5\ m\Omega cm^2$ gemessen. Das anhand von Verlustrechnungen gezeigte Ergebnis, dass es günstiger ist, viele schmale Kontaktstrukturen zu drucken, als wenige, dafür breitere, wurde experimentell bestätigt. Die beste industrielle großflächige (15.6 cm x 15.6 cm) Solarzelle, bestehend aus multikristallinem Material, die in diesem Experiment produziert wurde, erzielte einen Wirkungsgrad von $\eta=16.8\%$. Der dabei erreichte Kontaktwiderstand von nur $\rho_c=2\ m\Omega cm^2$ und laterale Fingerwiderstand von $\rho_f=3*10^{-8}\ \Omega m$ ermöglicht einen Füllfaktor von $FF=78.5\%$ auf einem Emitter mit einem Schichtwiderstand von $R_{SH}=80\ \Omega/sq$. Aufgrund der reduzierten Kontaktbreite $w_c=20\ \mu m$ und damit auch Fingerbreite $w_f=50\ \mu m$ wurde bei einem Fingerabstand von $d_f=1.3\ mm$ ein Kurzschlussstrom von $j_{sc}=34\ mA/cm^2$ erreicht.

Hocheffizienz-Solarzellen aus FZ-Silicium wurden dazu verwendet, das Potential der entwickelten Tinte zu demonstrieren. Die 2x2 cm² großen Zellen besitzen eine passivierte, mit LFC kontaktierte Rückseite, einen flachen $POCl_3$ Emitter und eine einfache SiN_x Passivierung. Zunächst wurde auf diesen Zellen mit einem Emitterschichtwiderstand von R_{SH}=75 Ω/sq das Vorderseitenkontaktgitter optimiert. Dabei hat sich gezeigt, dass der Fingerabstand im Bereich von 1.8 mm<d_f<2.5 mm verändert werden kann, ohne dass sich der Wirkungsgrad verändert, da der Gewinn im Kurzschlussstrom j_{sc} durch die Verluste im *FF* für größere Fingerabstände kompensiert wird. Wirkungsgrade von η=20.2% wurden erreicht. Auf Hocheffizienzzellen mit gleicher Zellstruktur, nur mit einem erhöhten Emitterschichtwiderstand von R_{SH}=110 Ω/sq, wurde ein Kontaktwiderstand von ρ_c=2 mΩcm², bei einer Kontaktbreite w_c<20 µm und einem Fingerabstand von d_f=1 mm, bestimmt. Daraus resultiert ein Füllfaktor von *FF*=81% und ein Wirkungsgrad von η=20.6%, welches den höchsten bisher veröffentlichten Wert für eine gedruckte und gefeuerte Solarzelle darstellt.

List of symbols, acronyms, indices and constants

symbol	description	unit
μ	dynamic viscosity	Pa s
A_f	cross section area of finger	m²
d_p	Particle diameter	m
d_{noz}	Nozzle diameter	m
d_{jet}	diameter of aerosol jet	m
E_{00}	characteristic energy for metal semiconductor interface	eV
E_C	energy level of conduction band edge	eV
E_F	Fermi- energy level	eV
E_T	energy level of trap	eV
E_V	energy level of valence band edge	eV
h	height	m
I	electric current	A
j	current density	A m^{-2}
$j_{01,}$	recombination current density in emitter and base	A m^{-2}
j_{02}	recombination current density in space charge region	A m^{-2}
j_a	current density of the active cell area	A m^{-2}
j_{Lip}	current density of bath	A m^{-2}
j_{mpp}	current density at maximum power point	A m^{-2}
$j_{mpp,a}$	current density at mpp of the active cell area	A m^{-2}
j_{ph}	photo-generated current density	A m^{-2}
j_{sc}	short-circuit current density	A m^{-2}
W	contact length for ρ_c test structure	m
w_f	finger width	m
w_c	contact width (seed layer width)	m
m	mass	kg
n	density of free electrons	m^{-3}
n_1,n_2	diode ideality factors	
d_{cr}	crystallite density	m^{-2}

N_D	concentration of donor atoms	m^{-3}
p	power loss fraction	%
p_c	fraction of front side covered by metallization pattern	%
p_e	electrical loss fraction	%
P_{loss}	electric power loss	$W\ m^{-2}$
P_{max}	power gain of corresponding unit cell	$W\ m^{-2}$
P_{mpp}	electric power density at maximum power point	$W\ m^{-2}$
p_s	shading fraction caused by front metallization pattern	%
q	elementary charge	C
r	area weighted resistance	$\Omega\ m^2$
R	resistance	Ω
R_c	contact resistance (in this work R_c always corresponds to the resistance for a contact of side length l_c = 1 cm)	Ω
R_{eff}	effective series resistance	Ω
R_{line}	resistance of the contact finger per unit length	$\Omega\ m^{-1}$
r_p	shunt (or parallel) resistance	$\Omega\ m^2$
r_s	series resistance	$\Omega\ m^2$
R_{sh}	emitter sheet resistance	Ω/sq
$r_{Si/SiN}$	coverage fraction of silicon to SiN	
$r_{Si/SiNx}$	ratio of etched SiN area	
R_{sk}	sheet resistance under contact	Ω/sq
s	finger separation distance	m
S	surface recombination velocity	$m\ s^{-1}$
S_{back}	surface recombination velocity on the rear	$m\ s^{-1}$
S_{eff}	effective surface recombination velocity	$m\ s^{-1}$
S_{front}	surface recombination velocity on the front	$m\ s^{-1}$
t	time	s
T	temperature	°C or K
t_b, t_f	transparency factor of busbar; finger	
T_{boil}	boiling temperature of hotmelt paste	°C
$t_{f,ez}$, $t_{f,mz}$	transparency factor finger edge zone and middle zone	
T_{paste}	temperature of hotmelt paste	°C
T_{plate}; T_{nest}	temperature of printing plate; nest	°C
T_{screen}	screen temperature	°C

V	voltage	V
V_a	voltage active cell area	V
V_{bi}	built-in voltage	V
$V_{mpp,a}$	voltage at maximum power point of active cell area	V
V_n	voltage between conduction band and Fermi level	V
V_{oc}	open-circuit voltage	V
V_{paste}	theoretical paste volume	m^{-3}
V_{rs}	voltage drop at the series resistance	V
v_{print}	velocity of print through process	m/s
v_{th}	thermal velocity	$C\cdot m\ s^{-1}$
w	width	m
x	distance, penetration depth	m
X_{suns}	number representing the irradiance in suns	
Φ	incident power density of photons	$W\ m^{-2}$
χ_S	electron affinity of the semiconductor	eV
ε_S	dielectric constant of the semiconductor	$C^2\ J^{-1}\cdot m^{-1}$
ϕ_{Bn}	potential barrier to n-silicon	
ϕ_M	potential barrier of metal	
ϕ_{gas}	gas flow rate	cm^3/min
ϕ_d	throughput of dry ink	$g\ m^{-1}$
η	efficiency of solar cell	
η_{bath}	efficiency of plating bath	
φ	potential	
λ	wavelength	m
ρ_f,	line resistivity	Ω m
ρ_c	contact resistivity	$\Omega\ m^2$
ρ_p	particle density	m^{-3}
ρ_A	area density of material (ink per contact area)	$kg\ m^{-2}$
ρ°	density of material	$kg\ cm^{-3}$
τ	minority carrier lifetime	s
τ_{shear}	shear stress	s^{-1}

constant	description	value
A^*	effective Richardson constant	$(m^*/m_0)\cdot 120$ A m^{-2} K^{-2}
c	velocity of light	299792458 m s^{-1}
F	Faraday constant	96485 C mol^{-1}
h	Planck's constant	$6.62608\cdot 10^{-34}$ J s
k	Boltzmann's constant	$1.3806\cdot 10^{-23}$ J K^{-1}
m^*	effective electron mass	$1.08\cdot m$
M_{Ag}	molar mass of silver	107.87 g mol^{-1}
N_C	effective density of states of conduction band	$2.84\cdot 10^{19}$ cm^{-3}
n_i	intrinsic carrier density	$1.00\cdot 10^{10}$ cm^{-3}
N_V	effective density of states of valence band	$2.68\cdot 10^{19}$ cm^{-3}
q, m	elementary charge of electrons	$1.602\cdot 10^{-19}$ C
z_{Ag}	oxidation number of silver	1

acronym	description
AFM	atomic force microscopy
Al-BSF	aluminium back surface field
AM1.5g	air mass 1.5 global spectrum
AR	aspect ratio (height to width)
ARC	antireflection coating
Cz	monocrystalline silicon produced with the **Cz**ochralsky method
D	diode
TG-DTA	differential thermogravimetric analysis
EDX	energy dispersive X-ray
FE	field emission
FIB	focused ion beam
FZ	monocrystalline silicon produced with the **f**loating **z**one method
IV	current-voltage
LFC	laser-fired contacts
PECVD	plasma enhanced chemical vapour deposition
PSG	phosphorus silicate glass

SEM	scanning electron microscope
SIMS	secondary ion mass spectroscopy
SP	screen printed
TE	thermionic emission
TFE	thermionic field emission
TEM	transmission electron microscope
TGA	Thermogravimetric analysis

Publications

[1] Hörteis, M., et al. "Further progress in metal aerosol jet printing for front side metallization of silicon solar cells", *Proc. 22nd EU PVSEC*. 2007. Milan, Italy.

[2] Hörteis, M., P.L. Richter, and S.W. Glunz. "Improved front side metallization by aerosol jet printing of hotmelt inks", *Proc. 23rd EU PVSEC*. 2008. Valencia, Spain.

[3] Hörteis, M. and S.W. Glunz "Fine line printed silicon solar cells exceeding 20% efficiency", *Progr. Photovolt.*, **16** 2008, pp. 555-60.

[4] Hörteis, M., et al., "Electrical properties of fine line printed and light-induced plated contacts on silicon solar cells", *Progress in Photovoltaics: Research and Applications*, in print 2009.

[5] Hörteis, M., et al., "High temperature contact formation on n-type silicon: basic reactions and contact model for seed layer contacts", *Advanced Functional Materials*, online available 2009.

[6] Hörteis, M., et al. "Fine line printed and plated contacts on high ohmic emitters enabling 20% cell efficiency", *Proc. 34th IEEE PVSC*. 2009. Philadelphia, USA.

[7] Hörteis, M., et al. "Different aspects of seed layer printed and light-induced plated front side contacts", *Proc. 24th EU PVSEC* 2009. Hamburg, Germany.

[8] Hörteis, M., P. Richter, and S. Glunz, Verfahren zur Metallisierung von Solarzellen, Hotmelt-Aerosol-Tinte und Aeorosol-Jet-Drucksystem, in *DE 10 2007 058 972 A1*. publication date: 2009, Fraunhofer Gesellschaft: Germany.

[9] Deenapanray, P., M. Hörteis, and D. MacDonald, "Minority Carrier Lifetime Properties of Reactive Ion Etched p-Type Float Zone Si", *Electrochemical and Solid-Status Letters*, **8** 2005, pp. G78-G81.

[10] Mette, A., et al., "Metal aerosol jet printing for solar cell metallization", *Progr. Photovolt.*, **115** 2007, pp. 621-7.

[11] Grote, D., et al. "Analyzing the effects of laterally varying emitter sheet resistance in combination with contact resistance", *Proc. 23rd EU PVSEC*. 2008. Valencia, Spain.

[12] Glunz, S.W., et al. "Progress in advanced metallization technology at Fraunhofer ISE", *Proc. 33rd IEEE PVSC*. 2008. San Diego, USA.

[13] Woehl, R., M. Hörteis, and S.W. Glunz. "Determination of the effective optical width of screen-printed and aerosol-printed and plated fingers", *Proc. 23rd EU PVSEC*. 2008. Valencia, Spain.

[14] Woehl, R., M. Hörteis, and S.W. Glunz "Analysis of the optical properties of screen-printed and aerosol-printed and plated fingers of silicon solar cells", *Advances in OptoElectronics*, 2008.

[15] Schmiega, C., et al. "Large-area n-type Silicon Solar Cells with Printed Contacts and Aluminium-alloyed Rear Emitter", *Proc. 24th EU PVSEC* 2009. Hamburg, Germany.

[16] Kontermann, S., et al., "Spatially resolved contact-resistance measurements on crystalline silicon solar cells", *Physica Status Solidi A*, **1-6** 2009.

Oral presentations

[1] Hörteis, M., et al. "Further progress in metal aerosol jet printing for front side metallization of silicon solar cells", *Proc. 22nd EU PVSEC*. 2007. Milan, Italy.

[2] Hörteis, M. "Neue Metallisierungsverfahren für Silizium Solarzellen", *Materials Valley*. 2008. Hanau, Germany.

[3] Hörteis, M. "Fine line printed silicon solar cells exceeding 20% efficiency", *Crystalclear workshop: Metallization*. 2008. Utrecht, The Netherlands.

[4] Hörteis, M. "Aerosol-Druck mit fortgeschrittenen Tinten", *Silicon Forest*. 2009. Falkau, Germany.

[3] Hörteis, M., et al. "Fine line printed and plated contacts on high ohmic emitters enabling 20% cell efficinecy", *Proc. 34th IEEE PVSC*. 2009. Philadelphia, USA.

[6] Hörteis, M., et al. "Different aspects of seed layer printed and light-induced plated front side contacts", *Proc. 24th EU PVSEC* 2009. Hamburg, Germany.

References

[1] Europas Industrie setzt auf Solarstrom made in Afrika. 2009; Available from: http://www.spiegel.de/.

[2] Hayward, T. BP Statistical Review of World Energy. 2009; Available from: www.bp.com/statisticalreview.

[3] EU, 20 20 by 2020 Europe's climate change opportunity. 2008: Brussels.

[4] Kearney, A.T. Set For 2020. 2009; Available from: http://www.epia.org.

[5] eurostat. Available from: http://epp.eurostat.ec.europa.eu/portal/page/portal/energy.

[6] Glunz, S.W., et al. "New concepts for the front side metallization of silicon solar cells", *Proc. 21st EU PVSEC*. 2006. Dresden, Germany.

[7] Glunz, S.W., et al. "Progress in advanced metallization technology at Fraunhofer ISE", *Proc. 33rd IEEE PVSC*. 2008. San Diego, USA.

[8] Mette, A., et al. "Increasing the efficiency of screen-printed silicon solar cells by light-induced silver plating", *Proc. 4th WCPEC*. 2006. Waikoloa, Hawaii, USA.

[9] Mette, A., et al., "Metal aerosol jet printing for solar cell metallization", *Progr. Photovolt.*, **115** 2007, pp. 621-7.

[10] Green, M.A., "Solar cells: operating principles, technology and system applications". 1998, Kensington: The University of New South Wales.

[11] Goetzberger, A., B. Voß, and J. Knobloch, "Sonnenenergie: Photovoltaik, Physik und Technologie der Solarzelle". 2nd ed. 1997, Stuttgart: Teubner. 261.

[12] Green, M.A., "Solar cells: operating principles, technology and system applications". 1986, Kensington: UNSW.

[13] Glunz, S.W., Ladungsträgerrekombination in Silicium und Siliciumsolarzellen, in *Fakultät für Physik*. 1995, Universität Freiburg: Freiburg. p. 166.

[14] Sinton, R.A. and A. Cuevas. "A quasi-steady-state open-circuit voltage method for solar cell characterization", *Proc. 16th EC PVSEC*. 2000. Glasgow, UK: James & James, London, UK, 2000.

[15] Pysch, D., et al. "Detailed analysis of fine line printed and planted solar cell contacts", *Proc. 22nd EU PVSEC*. 2007. Milan, Italy.

[16] Nielsen, L.D., "Distributed series resistance effects in solar cells", *IEEE Trans. Electron Devices*, **ED-29** 1982, pp. 821-7.

[17] Aberle, A.G., S.R. Wenham, and M.A. Green. "A new method for accurate measurements of the lumped series resistance of solar cells", *Proc. 23rd IEEE PVSC*. 1993. Louisville, Kentucky, USA: IEEE; New York, NY, USA.

[18] Rohatgi, A., et al., "The impact of molybdenum on silicon and silicon solar cell performance", *Solid-State Electron.*, **23** 1980, pp. 1185-90.

[19] Goetzberger, A., B. Voß, and J. Knobloch, "Sonnenenergie: Photovoltaik - Physik und Technologie der Solarzelle". Vol. 2., B. G. Teubner Stuttgart 1979. 261.

[20] McIntosh, K.R., Lumps, humps and bumps: Three detrimental effects in the current-voltage curve of silicon solar cells, in *Centre for Photovoltaic Engineering*. 2001, University of New South Wales: Sydney, Australia. p. 180.

[21] Cotter, J.E., et al. "Combined emitter and groove diffusion in buried contact solar cells", *Proc. 16th EC PVSEC*. 2000. Glasgow, UK: James & James, London, UK.

[22] Huster, F., et al. "Shunts in silicon solar cells below screen printed silver contacts", *Proc. 19th EC PVSEC*. 2004. Paris, France: WIP-Munich, ETA-Florence.

[23] Schubert, G., Thick film metallisation of crystalline silicon solar cells 2006, Universität Konstanz: Konstanz. p. 142.

[24] Pysch, D., A. Mette, and S.W. Glunz, "A review and comparison of different methods to determine the series resistance of solar cells", *Solar Energy Materials & Solar Cells*, **91** 2007, pp. 1698-706.

[25] Mette, A., New concepts for front side metallization of industrial silicon solar cells, in *Fakultät für Angewandte Wissenschaften*. 2007, Universität Freiburg: Freiburg. p. 231.

[26] Braun, F., "Über die Stromleitung durch Schwefelmetalle", *Ann. Phys. Chem.*, **153** 1874, pp. 556.

[27] Schottky, "Halbleitertheorie der Sperrschicht", *Naturwissenschaften*, **26** 1938.

[28] Schottky, W., "Zur Halbleitertheorie der Sperrschicht- und Spitzengleichrichter", *Z. Physik*, **113** 1939, pp. 367-414.

[29] Bardeen, J., "Semiconductor research leading to the point contact transistor", *Nobel Lecture*, 1956.

[30] Bardeen, J., "Surface states and rectification at a metal semi-conductor contact", *Physical Review*, **71** 1947, pp. 717-27.

[31] Cowley, A.M. and S.M. Sze, "Surface states and barrier height of metal-semiconductor systems", *J. Appl. Phys.*, **36** 1965, pp. 3212-20.

[32] Sze, S.M., "Physics of Semiconductor Devices". 2nd ed. 1981, New York: John Wiley & Sons. 868.

[33] Rhoderick, E.H. and R.H. Williams, "Metal-semiconductors contacts". 1988, Oxford: Claren-don Press (University-Press).

[34] Meier, D.L. and D.K. Schroder, "Contact resistance: its measurement and relative importance to power loss in a solar cell", *IEEE Trans. Electron Devices*, **ED-31** 1984, pp. 647-53.

[35] Tove, P.A., "Simple dipole model for barrier heights of silicide-silicon and metal-silicon barriers", *Surf. Sci.*, **132** 1983, pp. 336-43.

[36] Crowell, C.R., H.B. Shore, and E.E. LaBate, "Surface-state and interface effects in Schottky barriers at n-type silicon surfaces", *J. Appl. Phys.*, **36** 1965, pp. 3843-50.

[37] Schroder, D.K. and D.L. Meier, "Solar cell contact resistance - a review", *IEEE Trans. Electron Devices*, **ED-31** 1984, pp. 637-47.

[38] Yu, A.Y.C., "Electron tunneling and contact resistance of metal-silicon contact barriers", *Solid-State Electron.*, **13** 1970, pp. 239-47.

[39] Varahramyan, K. and E.J. Verret, "A model for specific contact resistance applicable for titanium silicide-silicon contacts", *Solid State Electronics*, **39** 1996, pp. 1601-7.

[40] Crowell, C.R. and V.L. Rideout, "Normalized thermionic-field (T-F) emission in metal-semiconductor (schottky) barriers", *Solid-State Electron.*, **12** 1969, pp. 89-105.

[41] Padovani, F.A. and R. Stratton, "Field and thermionic-field emission in Schottky barriers", *Solid-State Electron.*, **9** 1966, pp. 695-707.

[42] Ng, K.K., "Barrier heights and contact resistances: Metal/Si", *Properties of Silicon*, **Chapter 20** 1987, pp. 799-845.

[43] Ralph, E.L. "Recent advancements in low cost solar cell processing", *Proc. 11th IEEE PVSC*. 1975. Scottsdale, Arizona, USA.

[44] Frisson, L., et al. "Screen printed contacts on silicon solar cells with low series resistance", *Proc. 13th IEEE PVSC* 1978.

[45] Lin, H.C., D.P. Spittlehouse, and Y.W. Hsueh. "Contact resistance of silver ink on solar cell", *Proc. 13th IEEE PVSEC*. 1978.

[46] Riemer, D.E. "Evaluation of thick film materials for use as solar cell contacts", *Proc. 13th IEEE PVSC*. 1978. Washington DC, USA.

[47] Mertens, R., et al. "Critical processing parameter optimization for screen printed semicrystalline silicon solar cells", *Proc. 17th IEEE PVSC*. 1984. Kissimmee, Florida, USA.

[48] Cheek, G.C., et al., "Thick-film metallization for solar cell applications", *IEEE Trans. Electron Devices*, **ED-31** 1984, pp. 602-9.

[49] Abdi, Y., et al., "Silicon nano-crystalline structures fabricated by a sequential plasma hydrogenation and annealing technique", *Thin Solid Films*, **516** 2008, pp. 3172-8.

[50] Narasimha, S., A. Rohatgi, and A.W. Weeber, "An optimized rapid aluminum back surface field technique for silicon solar cells", *IEEE Trans. Electron Devices*, **46** 1999, pp. 1363-70.

[51] Sopori, B.L., et al., "Hydrogen in silicon: a discussion of diffusion and passivation mechanisms", *Sol. Ener. Mater. Sol. Cells*, **41/42** 1996, pp. 159-69.

[52] Aberle, A., T. Lauinger, and R. Hezel. "Remote PECVD silicon nitride - a key technology for the crystalline silicon PV industry of the 21st century?" *Proc. 14th EC PVSEC*. 1997. Barcelona, Spain.

[53] Duerinckx, F., et al. "Simple and efficient screen printing process for multicrystalline silicon solar cells based on firing through silicon nitride", *Proc. 14th EC PVSEC*. 1997. Barcelona, Spain.

[54] Prudenziati, M., et al., "Ag-based thick-film front metallization of silicon solar cells", *Active and passive electronic components*, **13** 1989, pp. 133-50.

[55] Huljic, D.M., et al. "Microstructural analyses of Ag thick-film contacts on n-type silicon emitters", *Proc. 3rd WCPEC*. 2003. Osaka, Japan: WCPEC-3 Organizing Committee, December 2003.

[56] Ballif, C., et al. "Nature of the Ag-Si interface in screen-printed contacts: a detailed transmission electron microscopy study of cross-sectional structures", *Proc. 29th IEEE PVSC*. 2002. New Orleans, Louisiana, USA.

[57] Schubert, G., F. Huster, and P. Fath. "Current transport mechanism in printed AG thick film contacts to an n-type emitter of a crystalline silicon solar cell", *Proc. 19th EC PVSEC*. 2004. Paris, France: WIP-Munich, ETA-Florence.

[58] Young, R.J.S. and A.F. Carroll. "Advances in front-side thick film metallisations for silicon solar cells", *Proc. 16th EC PVSEC*. 2000. Glasgow, UK: James & James, London, UK.

[59] Hilali, M.M., et al., "Effect of glass frit chemistry on the physical and electrical properties of thick-film Ag contacts for silicon solar cells", *J. Electron. Mater.*, **35** 2006, pp. 2041-7.

[60] Hoornstra, J., et al. "Lead free metallisation paste for crystalline silicon solar cells: from model to results", *Proc. 31st IEEE PVSC*. 2005. Orlando, USA.

[61] Schubert, G., B. Fischer, and P. Fath. "Formation and nature of AG thick film front contacts on crystalline silicon solar cells", *PV in Europe - From PV Technology to Energy Solutions*. 2002. Rome, Italy.

[62] Khadilkar, C., et al. "Effect of glass chemistry and silicon orientation on the front contact microstructure formation in a silicon solar cell", *Proc. 20th EC PVSEC* 2005. Barcelona, Spain.

[63] Hilali, M.M., et al., "Effect of Ag particle size in thick-film Ag paste on the electrical and physical properties of screen printed contacts and silicon solar cells", *Journal of the Electrochemical Society*, **153** 2006, pp. A 5-11.

[64] Thuillier, B., et al., "Transmission electron microscopy and EDS analysis of screen-printed contacts formation on multicrystalline silicon solar cells", *Mater. Sci. Eng. B*, **B102** 2003, pp. 58-62.

[65] Pysch, D., et al., "Comprehensive analysis of advanced solar cell contacts consisting of printed fine-line seed layers thickened by silver plating", *Progr. Photovolt.*, **17** 2009, pp. 101-14.

[66] Hilali, M.M., B. To, and A. Rohatgi. "A review and understanding of screen-printed contacts and selective-emitter formation", *Proceedings of the 14th Workshop on Crystalline Silicon Solar Cells and Modules NREL*. 2004. Winter Park, Colorado, USA.

[67] Khadilkar, C., et al. "Characterization of front contact in a silicon solar cell", *Proc. 14th PVSEC*. 2004. Bangkok, Thailand.

[68] Roy, B. and D. Chakravorty, "Electrical conductance of silver nanoparticles grown in glass-ceramic", *J. Phys.: Condens. Matter*, **2** 1990, pp. 9323-34.

[69] Berger, H.H., "Contact resistance and contact resistivity", *Journal of the Electrochemical Society*, **119** 1972, pp. 507-14.

[70] Schroder, D.K., "Semiconductor Material and Device Characterization". 1990, New York: John Wiley & Sons. 599.

[71] Pysch, D., Analyse von neuartigen Kontakten für die Vorderseite von Solarzellen, in *Fakultät für Physik*. 2007, Universität Karlsruhe: Freiburg. p. 118.

[72] Proctor, S.J. and L.W. Linholm, "A direct measurement of interfacial contact resistance", *IEEE Electron. Dev. Lett.*, **3** 1982, pp. 294-6.

[73] Melczarsky, M., et al. "Contact Resistance Measurement Techniques for Ag Thick-Film Screen-Printed Contacts to Solar Cells", *IEEE PVSC*. 2009. Philadelphia, USA.

[74] Shockley, W., "Research and Investigation of Inverse Epitaxial UHF Power Transistor ". Technical Report No. AL-TDR-64-207. 1964, Ohio: Air Force Atomic Laboratory, A i r Force Systems Command, Wright-Patterson Air Force Base,.

[75] Berger, H.H. "Contact resistance on diffused resistors", *IEEE International Solid-State Circuits Conference*. 1969.

[76] Murrmann, H. and D. Widmann, "Current crowding on metal contacts to planar devices", *IEEE Trans. Electron Devices*, **16** 1969, pp. 1022-4.

[77] Berger, H.H., "Models for contacts to planar devices", *Solid-State Electron.*, **15** 1972, pp. 145-58.

[78] Murrmann, H. and D. Widmann, "Messung des Übergangswiderstandes zwischen Metall und Diffusionsschicht in Si-Planarelementen", *Solid-State Electron.*, **12** 1969, pp. 879-86.

[79] Wolf, M. and H. Rauschenbach, "Series resistance effects on solar cell measurements", *Advanced Energy Conversion*, **3** 1963, pp. 455-79.

[80] Alonso, J., et al. "Progress on high efficiency silicon solar cells", *Proc. 10th EC PVSEC*. 1991. Lisbon, Portugal.

[81] Franke, R., Netzsch Gerätebau GmbH, in *Simultaneous Thermal Analysis - Methods, Functional principles*.

[82] King, B., "Maskless mesoscale materials deposition", *Electronic Packaging and Production*, 2003, pp. 18-20.

[83] Sears, J.W. and J. Colvin, "Applying nanoparticels via direct-write technology for industrial applications", *Adv. Powder. Metall. Part. Mater.*, **1** 2005, pp. 17-31.

[84] Richter, P., Abscheiden der Vorderseitenkontakte von Solarzellen mittels eines metallhaltigen Aerosol-Strahls – Evaluierung und Prozessoptimierung. 2005, Hochschule Bremen - University of Applied Sciences. p. 109.

[85] Raabe, O., The generation of aerosols of fine particles, in *Inhalation Toxicology Research Institute*: Albuquerque.

[86] Renn, M. and B. King, Direct write system, in *Patent Application Publication*, U. States, Editor. 2007, Optomec Design company: US.

[87] Collison, W.E., "Inhalation Therapy Techniques". 1935, London: Heinemann.

[88] Chen, B.T. and H.C. Yeh, "An Improved Virtual Impactor: Design and Performance", *J. Aerosol Sci.*, **18** 1987, pp. 203-214.

[89] Liu, B.Y.H., R.N. Berglund, and J.K. Agarwal, "Experimental studies of optical particle counters", *Atmos. Environ.*, **8** 1974, pp. 717-32.

[90] Hörteis, M., P.L. Richter, and S.W. Glunz. "Improved front side metallization by aerosol jet printing of hotmelt inks", *Proc. 23rd EU PVSEC*. 2008. Valencia, Spain.

[91] Akhatov, I.S., J.M. Hoey, and O.F. Swenson, "Aerosol flow through a long micro-capillary: collimated aerosol beam", *Microfluid Nanofluid* **5**2008, pp. 215-224.

[92] Akhatov, I.S., J.M. Hoey, and O.F. Swenson, "Aerosol focusing in micro-capillaries: Theory and experiment", *Journal of aerosol science*, **39** 2008 pp. 691-709.

[93] Saffman, P.G., "The lift on a small sphere in a slow shear flow - Corrigendum", *Journal of Fluid Mechanics*, **31** 1968, pp. 624.

[94] Poiseuille, J.L.M., *Annales des Sciences Naturallas*, **5** 1836, pp. 111.

[95] Schulz, D.L., J.M. Hoey, and D. Thompson. "Collimated Aerosol Beam Deposition: Sub 5-µm reolution of Printed Actives and Passives", *Flexible Electronics and Displays Conference and Exhibition* 2008.

[96] Hinds, W.C., "Aerosol Technology". second ed. 1998, New York: John Wiley&Sons.

[97] Bönnemann, H. and R.M. Richards, "Nanoscopic Metal Particles - Synthetic Methods and Potential Applications", *Eur. J. Inorg. Chem.*, 2001pp. 2455-2480.

[98] Pileni, M.P., "Reverse Micelles as Microreactors", *J. Phys. Chem.*, **97** 1993, pp. 6961-6973.

[99] Faraday, M., "The Bakerian Lecture: Experimental Relations of Gold (and Other Metals) to Light", *Philos. Trans. r. Soc. London*, **147** 1857, pp. 145-153.

[100] Schmid, G., "Nanoparticles - From Theory to Application". 2003, Weinheim: Wiley-VCH.

[101] Velikov, K.P., "Synthesis and Characterization of Large Colloidal Silver Particles", *Langmuir*, **19** 2003, pp. 1384-1389.

[102] Glunz, S.W., et al. "Comparison of different dielectric passivation layers for application in industrially feasible high-efficiency crystalline silicon solar cells", *Proc. 20th EC PVSEC* 2005. Barcelona, Spain.

[103] Radtke, V., et al. "Understanding the electrochemical mechanisms of light induced plating by means of voltametric techniques", *Proc. 23rd EU PVSEC*. 2008. Valencia, Spain.

[104] Blakers, A.W., "Shading losses of solar-cell metal grids", *J. Appl. Phys.*, **71** 1992, pp. 5237-41.

[105] Woehl, R., M. Hörteis, and S.W. Glunz "Analysis of the optical properties of screen-printed and aerosol-printed and plated fingers of silicon solar cells", *Advances in OptoElectronics*, **2008** 2008.

[106] Buffat, P. and J.-P. Borel, "Size effect on the melting temperature of gold particles", *Phys. Rev. A*, **13** 1975, pp. 2287-2298.

[107] Wolke, W., et al. "Surface passivation for solar cells by large scale inline sputtering of silicon nitride", *Proc. 20th EC PVSEC* 2005. Barcelona, Spain.

[108] Wolke, W., et al. "SiN:H anti-reflection coatings for c-Si solar cells by large scale inline sputtering", *Proc. 19th EC PVSEC*. 2004. Paris, France: WIP-Munich, ETA-Florence.

[109] Goldschmidt, V.M., "Geochemische Verteilungsgesetze der Elemente," *VIII. Vid. Akad. Ser. Oslo*, **Nr. 8,** 1926.

[110] Zachariasen, W.H., "The atomic arrangement in glass", *Journal of the American Chemical Society*, **54** 1932, pp. 3841-3851.

[111] Rao, K.J., "Structural Chemistry of Glasses". 1 ed. 2002, Oxford: Elsevier Science & Technology584.

[112] Krebs, H., "Über den strukturellen Aufbau von Gläsern", *Angew. Chem.*, **78** 1966, pp. 577-587.

[113] Rabinovich, E.M., "Review Lead in glasses", *Journal of Materials science*, **11** 1976, pp. 925-948.

[114] El-Damrawi, G. and E. Mansour, "Electrical properties of lead borosilicate glasses", *Physica B*, **364** 2005, pp. 190-198.

[115] Imaoka, M. "Adv. in glass Technol.," *4. Congress on Glass*. 1962. Washingtion: Plenum Press, New York.

[116] Riedel, E., "Anorganische Chemie". Vol. 3. 1994, Berlin, New York: Walter de Gruyter. 911.

[117] FACT. 2009; Available from: http://www.crct.polymtl.ca/FACT/documentation/.

[118] Shao, Z.B. and K.R. Liu, "Equilibrium Phase Diagrams in the Systems PbO-Ag and CuO-Ag", *Jounal of the American Ceramic Society*, **76** 1993, pp. 2663-2664.

[119] Stöcker, H., "Taschenbuch der Physik". 2000, Frankfurt: Harri Deutsch.

[120] Hanss, J., A. Kalytta, and A. Reller. "Potentials and limitations of lthe Skimmer MS-System", *5th SKT Hyphenated Techniques in Thermal Analysis*. 2003. Bad Orb.

[121] Hilali, M., et al. "Understanding and development of Ag pastes for silicon solar cells with high sheet-resistance emitters", *Proc. 19th EC PVSEC*. 2004. Paris, France: WIP-Munich, ETA-Florence.

[122] Mertens, R.P., R.J. van Overstraeten, and K.U. Leuven, "Solar cell fabrication techniques for single and semicrystalline silicon substrates", *International Journal of Solar Energy*, **2** 1983, pp. 121-40.

[123] Sridharan, S., Lead Free Solar Cell Contacts, in *Patent Application Publication*. 2006, Ferro Corporation: US.

[124] Christensen, C.J., Metallizing Composition, U.S.P. Office, Editor. 1949, Bell Telephone Laboratories: US.

[125] Kumar, B., et al. "Commercialization of a silicon nitride co-fire through (SINCOFT) process for manufacturing high efficiency mono-crystalline silicon solar cells", *Proc. 29th IEEE PVSC*. 2002. New Orleans, LA, USA.

[126] Soppe, W., et al. "Cost-effective mc-Si cell processing by screenprinting on remote-PECVD layers", *Proc. 2nd WCPEC*. 1998. Vienna, Austria.

[127] Geller, R.F., A.S. Creamer, and E.N. Bunting, "The System: PbO-SiOz", *J. Research Natl. Bur. Stand.*, **13** 1934, pp. 237-244.

[128] Jin, H., Characterization of Silicon / Silicon Dioxide / LPCVD Silicon Nitride stacks for solar cell application. 2007, Australian National University. p. 194.

[129] Schultz, O., et al. "Silicon oxide / silicon nitride stack systems for 20% efficient silicon solar cells", *Proc. 31st IEEE PVSC*. 2005. Orlando, Florida, USA.

[130] Schmidt, J., M. Kerr, and A. Cuevas, "Surface passivation of silicon solar cells using plasma-enhanced chemical-vapour-deposited SiN films and thin thermal SiO_2/plasma SiN stacks", *Semicond. Sci. Technol.*, **16** 2001, pp. 164-70.

[131] Grupp, G., Charakterisierung der Dickfilm-Kontaktierung texturierter kristalliner Siliziumsolarzellen, in *Fakultät für Mathematik und Physik*. 2004, Universität Freiburg: Freiburg. p. 1-111.

[132] Huljic, D.M., et al. "Comprehensive study of rapid thermal firing for industrial production of crystalline silicon thick-film solar cells", *Proc. 19th EC PVSEC*. 2004. Paris, France: WIP-Munich, ETA-Florence.

[133] Directive 2002/95/EC on the restricion of the use of certain hazardous substances in electrical and electronic equipment. 2003, European Union. p. 19-23.

[134] Sridharan, S. and S. Kim. "Lead Free Silver Front Contact Pastes for SiNx Coated Polycrystalline Silicon Solar Cells", *PVSEC-15*. 2005. Shanghai, China.

[135] Hilali, M., et al. "Optimization of self-doping Ag paste firing to achieve high fill factors on screen-printed silicon solar cells with a 100 Ω/sq. emitter", *Proc. 29th IEEE PVSC*. 2002. New Orleans, Louisiana, USA.

[136] Rohatgi, A., et al. "Self-aligned self-doping selective emitter for screen-printed silicon solar cells", *Proc. 17th EC PVSEC*. 2001. Munich, Germany.

[137] Meier, D.L., et al. "Self-doping contacts to silicon using silver coated with a dopant source", *Proc. 28th IEEE PVSC*. 2000. Anchorage, USA.

[138] Ying, W.B., et al., "The chemical composition changes of silicon and phosphorus in the process of native oxide formation of heavily phosphorus doped silicon", *Appl. Surf. Sci.*, **181** 2001, pp. 1-14.

[139] Moynagh, P.B. and P.J. Rosser, "Diffusion of P in Si", *Properties of Silicon*, 1987, pp. 348-367.

[140] Weber, E.R., "Diffusion of Ag in Si", *Properties of Silicon*, 1988, pp. 411-415.

[141] Porter, L.M., A. Teicher, and D.L. Meier, "Phosphorus-doped, silver-based pastes for self-doping ohmic contacts for crystalline silicon solar cells", *Sol. Ener. Mater. Sol. Cells*, **73** 2002, pp. 209-19.

[142] Meier, D.L., et al. "Self-doping, screen-printed silver contacts applied to IBC and phostop dendritic web silicon solar cells", *Proc. 17th EC PVSEC*. 2001. Munich, Germany: WIP-Renewable Energies, Munich, GermanyETA, Firenze, Italy.

[143] Meier, D.L., et al. "Self-doping contacts and associated silicon solar cell structures", *Proc. 2nd WCPEC*. 1998. Vienna, Austria: European Commission, Ispra, Italy, 1998.

[144] Hörteis, M., et al. "Further progress in metal aerosol jet printing for front side metallization of silicon solar cells", *Proc. 22nd EU PVSEC*. 2007. Milan, Italy.

[145] Van Craen, M., L. Frisson, and F.C. Adams, "SIMS study of the penetration of metallic secondary impurities in screen-printed silicon solar cells", *Surf. Interface Anal.*, **6** 1984, pp. 257-60.

[146] Nakajima, T., A. Kawakami, and A. Tade, "Ohmic contact of conductive silver paste to silicon solar cells ", *The International journal for hybrid microelectronics*, **6** 1983, pp. 580-8.

[147] Schubert, G., F. Huster, and P. Fath. "Physical understanding of printed thick film front contacts of crystalline Si solar cells: review of existing models and recent developments", *Technical Digest of the 14th International Photovoltaic Science and Engineering Conference*. 2004. Bangkok, Thailand.

[148] Schubert, G., F. Huster, and P. Fath, "Physical understanding of printed thick-film front contacts of crystalline Si solar cells—Review of existing models and recent developments", *Solar Energy Materials & Solar Cells*, **90** 2006, pp. 3399-406.

[149] Witvrouwa, A., et al. "A comparison between wet HF etching and vapor HF etching for sacrificial oxide removal", *SPIE proc. Micromachining and microfabrication process technology*. 2000. Santa Clara.

[150] Ballif, C., et al., "Silver thick-film contacts on highly doped n-type silicon emitters: structural and electronic properties of the interface", *Appl. Phys. Lett.*, **82** 2003, pp. 1878-80.

[151] Sridharan, S., et al. "Characterization of silver/glass/silicon front contact interface in a silicon solar cell", *13th NREL Workshop on Crystalline Silicon Solar Cell Materials and Processes*. 2003. Vail, Colorado, USA.

[152] Grupp, G., et al. "Analysis of silver thick-film contact formation on industrial silicon solar cells", *Proceedings of the 31st IEEE Photovoltaics Specialists Conference (PVSEC)*. 2005. Orlando, Florida.

[153] Grupp, G., et al. "Peak firing temperature dependence of the microstructure of ag thick-film contacts on silicon solar cells - a detailed afm study of the interface", *Proc. 20th EC PVSEC* 2005. Barcelona, Spain.

[154] Kontermann, S., et al. "Investigations on the influence of different annealing steps on silicon solar cells with silver thick film contacts", *Proc. 22nd EU PVSEC*. 2007. Milan, Italy.

[155] Gzowski, O., L. Murawski, and K. Trzebiatowski, "The surface conductivity of lead glasses", *Journal of physics*, **15** 1982, pp. 1097-1101.

[156] Chybicki, M., J. Liwo, and K. Trzebiatowski, "Electrical surface conductivity modifications of lead-silicate glasses", *Phys. Status Solidi A*, **115** 1989, pp. K185-9.

[157] Kaganovskii, Y., et al., "Formation of nanoclusters through silver reduction in glasses: the model", *J. Non-Cryst. Solids*, **353** 2007, pp. 2263-71.

[158] Schmich, E., et al. "Screen-printed and evaporated crystalline silicon thin-film solar cells with epitaxial emitters", *Proc. 22nd EU PVSEC*. 2007. Milan, Italy.

[159] Solmi, S., et al., "Dopant and carrier concentration in Si in equilibrium with monoclinic SiP precipitates", *Physical Review B*, **53** 1996, pp. 7836-41.

[160] Nobili, D., et al., "Precipitation as the phenomenon responsible for the electrically inactive phosphorus in silicon", *J. Appl. Phys.*, **53** 1982, pp. 1484-91.

[161] Beck, C.G. and R. Stickler, "Crystallography of SiP and SiAs single crystals and of SiP precipitates in Si", *J. Appl. Phys.*, **37** 1966, pp. 4683-6.

[162] Armigliato, A. and P. Werner, "High resolution electron microscopy observations of precipitates in p-supersaturated silicon", *Ultramicroscopy*, **15** 1984, pp. 61-69.

[163] Finetti, M., et al., "Electrical properties and stability of supersaturated phosphorus-doped silicon layers", *J. Electrochem. Soc.*, **128** 1981, pp. 1313-7.

[164] Servidori, M. and A. Armigliato, "Electron microscopy of silicon monophosphide precipitates in p-diffused silicon", *Journal of Materials Science*, **10** 1975, pp. 306-13.

[165] Solmi, S., et al., "Predeposition in silicon as affected by the formation of orthorhombic SiP and cubic $SiO_2 \cdot P_2O_5$ at the PSG-Si interface", *Journal of the Electrochemical Society*, **123** 1976, pp. 654-60.

[166] Seibt, M., et al., "Phosphorus diffusion gettering of platinum in silicon: formation of near-surface precipitates", *phys. stat. sol. (b)*, **222** 2000, pp. 327-36.

[167] Solmi, S. and D. Nobili, "High concentration diffusivity and clustering of arsenic and phosphorus in silicon", *J. Appl. Phys.*, **83** 1998, pp. 2484-90.

[168] Schröter, W., et al., "Mechanisms and computer modelling of transition element gettering in silicon", *Sol. Ener. Mater. Sol. Cells*, **72** 2002, pp. 299-313.

[169] Ying, W.B., et al., "Evaluation of the initial oxidation of heavily phosphorus doped silicon surfaces using angle-dependent X-ray photoelectron spectroscopy", *Thin Solid Films*, **343-344** 1999, pp. 393-6.

[170] Ying, W.B., et al., "Annealing behavior of phosphorus in native oxide films on heavily phosphorus doped silicon", *Appl. Surf. Sci.*, **100/101** 1996, pp. 556-60.

[171] Pysch, D., et al., "Comprehensive analysis of advanced solar cell contacts consisting of printed fine-line seed layers thickened by silver plating", *Progr. Photovolt.*, 2008, pp. published online.

[172] Rohatgi, A., et al., "Understanding and implementation of rapid thermal technologies for high-efficiency silicon solar cells", *IEEE Trans. Electron Devices*, **46** 1999, pp. 1970-7.

[173] Ebong, A., M. Hilali, and A. Rohatgi. "Rapid photo-assisted forming gas anneal (FGA) for high quality screen-printed contacts for silicon solar cells", *Proc. 28th IEEE PVSC*. 2000. Anchorage, Alaska, USA.

[174] Schubert, G., J. Horzel, and S. Ohl. "Investigations on the mechanism behind the beneficial effect of a forming gas anneal on solar cells with silver thick film contacts", *Proc. 21st EU PVSEC*. 2006. Dresden, Germany.

[175] Blakers, A.W. "Low loss metallisation of solar cells", *Proc. 23rd IEEE PVSC*. 1993. Louisville, Kentucky, USA.

[176] Stuckings, M.F. and A.W. Blakers, "A study of shading and resistive loss from thefingers of encapsulated solar cells", *Solar Energy Materials & Solar Cells*, **59** 1999, pp. 233-42.

[177] Macleod, H.A., "Thin-film optical filters". 1986: Adam Hilger.

[178] Rinio, M., H.J. Möller, and M. Werner. "LBIC investigations of the lifetime degradation by extended defects in multicrystalline solar silicon", *Beam Injection Assessment of Defects in Semiconductors. 5th International Workshop*. 1998. Schloss Wulkow, Germany: Diffus. Defect Data B, Solid State Phenom. (Switzerland), Switzerland: Balaban Publishers; Scitec Publications.

[179] van Kerschaver, E., et al. "A novel silicon solar cell structure with both external polarity contacts on the back surface", *Proc. 2nd WCPEC*. 1998. Vienna, Austria: European Commission, Ispra, Italy, 1998.

[180] Schneider, A., L. Rubin, and G. Rubin. "Solar cell efficiency improvement by new metallization techniques the day4^{TM} electrode concepts", *Proc. 4th WCPEC*. 2006. Hawaii, USA.

[181] Rubin, L.B. and G.L. Rubin, Elektrode für fotovoltaische Zellen, fotovoltaische Zelle und fotovoltaischer Modul, in *Deutsches Patent (DE 10239845 C1)*. 2003, Day4Energy Inc., Vancouver, Canada: Germany.

[182] Clement, F., "Die Metal Wrap Through Solarzelle", in *Fakultät für Angewandte Wissenschaften*. 2009, Universität Freiburg: Freiburg. p. 244.

[183] Clement, F., et al. "Industrially feasible multi crystalline metal wrap through (mwt) silicon solar cells exceeding 16% efficiency", *Technical Digest of the*

17th International Photovoltaic Solar Energy Conference. 2007. Fukuoka, Japan.

[184] Erath D., Clement, F., et al., Proc. 17th International Material Research Congress, 2008 Cancún, México

[185] Clement, F., et al. "Industrially feasible mc-Si metal wrap through (MWT) solar cells with high emitter sheet resistances exceeding 16% efficiency", *Proc. 23rd EU PVSEC*. 2008. Valencia, Spain.

[186] Neidert, M., Clement, F., et al., "Development of via pastes for high efficiency MWT cells with a low shunting behaviour" *Proc. 24th EU PVSEC* 2009. Hamburg, Germany.

[187] Schneiderlöchner, E., et al., "Laser-fired rear contacts for crystalline silicon solar cells", *Progr. Photovolt.*, **10** 2002, pp. 29-34.

[188] Woehl, R., "Analyse von aerosolgedruckten Kontakten für die Vorderseite von Solarzellen", in *Fakultät für Mathematik und Physik*. 2008, Universität Freiburg: Freiburg. p. 109.

[189] Cuevas, A., et al. "Extraction of the surface recombination velocity of passivated phosphorus-doped silicon emitters", *Proc. 1st WCPEC* 1994. Waikoloa, Hawaii, USA

Danksagung

Zu Beginn meiner Promotion wurde mir schnell klar, dass allein die Idee, die Welt ein wenig zu verbessern und die Begeisterung am Forschen schwer ausreichen, um diese Arbeit zu erstellen. Erst die Zusammenarbeit vieler Einzelner führte zu dem vorliegenden Ergebnis, und mein Dank gilt allen, die dazu beigetragen haben, dass dieses Projekt realisiert werden konnte. Namentlich möchte ich mich bedanken bei Herrn Prof. Gerhard Willeke für das Ermöglichen dieser Arbeit und das Erstellen des Erstgutachtens. Herrn Prof. Giso Hahn gilt mein Dank für seine kurzentschlossene und spontane Zusage, das Zweitgutachten zu erstellen.

Mein besonderer Dank gilt Stefan Glunz für seine Unterstützung bei allen Belangen dieser Arbeit, für sein Vertrauen, das eine freie und kreative Arbeitsweise erst ermöglicht hat. Seine offene und humorvolle Art, sein Pragmatismus beim Lösen von Problemen waren mir stets Hilfe und Beispiel.

Prof. Armin Reller, Andreas Kalytta, Jan Hanss, möchte ich danken, dass ich am Lehrstuhl für Chemie der Universität Augsburg immer offene Türen und Antworten auf so manche chemische Frage fand.

Insbesondere darf ich mich bei meinen Diplomanden, Master und Bachelor Studenten, Robert Woehl, Sebastian Binder, Christian Seitz, Tobias Gutberlet, Jan Jäger, Kristine Drew, Janis Jeanne Merkel bedanken, die mit ihren hervorragenden Arbeiten einen wesentlichen Beitrag zu dieser Arbeit geleistet haben.

Weiterhin gilt mein Dank Judith Woehl und Wesley Dopkins für das zuverlässige Korrekturlesen vor allem der englischen Texte.

Ebenfalls eine große Unterstützung waren Johannes Spannagel, Sergio Feo und Thomas Cuber, die als wissenschaftliche Hilfskräfte viele Stunden zum Gelingen dieser Arbeit im Labor standen.

Meinen aktuellen und ehemaligen Zimmerkollegen: Mónica Alemán, Jan Benick, Filip Granek, Christian Reichle und Ansgar Mette ein herzliches Danke, für viele angenehme Stunden innerhalb und außerhalb des ISE, für ihre Geduld beim Beibringen der ISE-Bürokratie und für ihr nahezu grenzenloses Verständnis für mein Verhältnis zum Telefon.

Für die großzügige Versorgung mit Wafern, anregende Diskussionen und eine kollegiale und freundschaftliche Projektarbeit möchte ich mich bei Ansgar Mette, Anke Belitz und Matthias Gunderman von Q-Cells bedanken.

Allen genannten und nicht genannten Kollegen vielen Dank für hilfreiche Diskussionen und eine kreative Arbeitsatmosphäre, ohne die das Arbeiten am ISE lange nicht so viel Freude bereitet hätte: Andreas Fell, Andreas Grohe, Annerose Knorz, Daniel Biro, Daniela Roth, Denis Erath, Dirk Reinwand, Dominic Suwito, Evelyn Schmich, Florian Clement, Gernot Emanuel, Holger Habernich, Jan-Frederic Nekarda, Jochen Hohl-Ebinger, Jonas Bartsch, Kuno Meier, Luca Gautero, Marc Hoffmann, Martin Hermle, Martin Schuber, Martin Zimmer, Matthias Künle, Nico Mingurelli, Pierre Saint-Cast, Stefan Janz, Stefan Kontermann, Sybille Hopmann, Thomas Roth, Valentin Radtke, Winfried Wolke, Wolfram Kwapil und Christian Schmiga

Ebenso möchte ich mich bei Antonio Leimenstoll, Sonja Seitz, Felix Schätzle und Ines Druschke für die zuverlässige Prozessierung von Solarzellen im Reinraum bedanken.

Elisabeth Schäffer für ihre beneidenswerte Ausdauer beim Messen von zahlreichen, mitunter auch missglückten, Solarzellen und Jutta Zielonka für so manches REM-Bild und Christian Schetter für sein unermüdliches Engagement, alle wichtigen Prozesse und Maschinen am Laufen zu halten, herzlichen Dank.

Vielen Dank an alle Beteiligten rund um den Aerosoldruck, im Besonderen Aleksander Filipovic für seine große Hilfe bei allen Druckaufgaben, Philipp Richter (jetzt bei Solarworld) für sein Engagement, den Aersosoldrucker drucken zu lassen, Daniel Schmidt für seine Unterstützung im Metallisierungslabor und Sebastian Binder für das Organisieren zahlreicher Druckaufträge. Jonas Bartsch und Anke Herbolzheimer vielen Dank für das Aufbringen der zweiten Metallschicht in der Licht-induzierten Galvanik.

Meiner Familie danke ich, dass sie immer an mich geglaubt und mich bedingungslos weit über diese Arbeit hinaus unterstützt haben. Zuletzt und von ganzem Herzen möchte ich meiner Frau Monika für ihre Liebe und unserem Sohn Ferdinand für das Ablenken von der Arbeit Danke sagen.